UNIVERSITAT DE BARCELONA

Reconstrucció climàtica dels darrers 2.700 anys a la Mediterrània occidental: sediments marins i estalagmites

Mercè Cisneros Bermejo

CAPÍTOL 3
RESULTATS

"Ets una partícula en el temps. Descendeixes amb innumerables semblants per la foscor silenciosa, una partícula d'aigua freda, salada, cansada i pesada després del viatge que ha consumit la teva calor pujant des del tròpic fins aquesta regió inhòspita, fins a reunir-se totes en les conques de Groenlàndia i de Noruega, en una gran piscina d'aigua gelada. Des d'allà et vesses per la serralada submarina que va de Groenlàndia, Islàndia i Escòcia a la conca de l'Atlàntic. És un viatge infinit fins a l'abisme, per munts de lava i depòsits de sediment. Aquesta corrent poderosa formada per tu i per les demés partícules, prop de Terranova rep reforços de masses d'aigua de la mar del Labrador, que són menys denses i fredes. A l'alçada de les Bermudes s'apropen unes altres, com ovnis rodons que creuen l'oceà des de la Mediterrània, en remolins d'aigua càlida extremadament salada que procedeix de l'Estret de Gibraltar. De la Mediterrània, del Labrador, de Groenlàndia; totes aquestes aigües es mesclen i segueixen cap al sud pel fons de la mar. Ets testimoni de com la Terra es crea a si mateixa"

Frank Schätzing, El Cinquè Dia
(títol original en alemany: Der Schwarm –L'Eixam-)

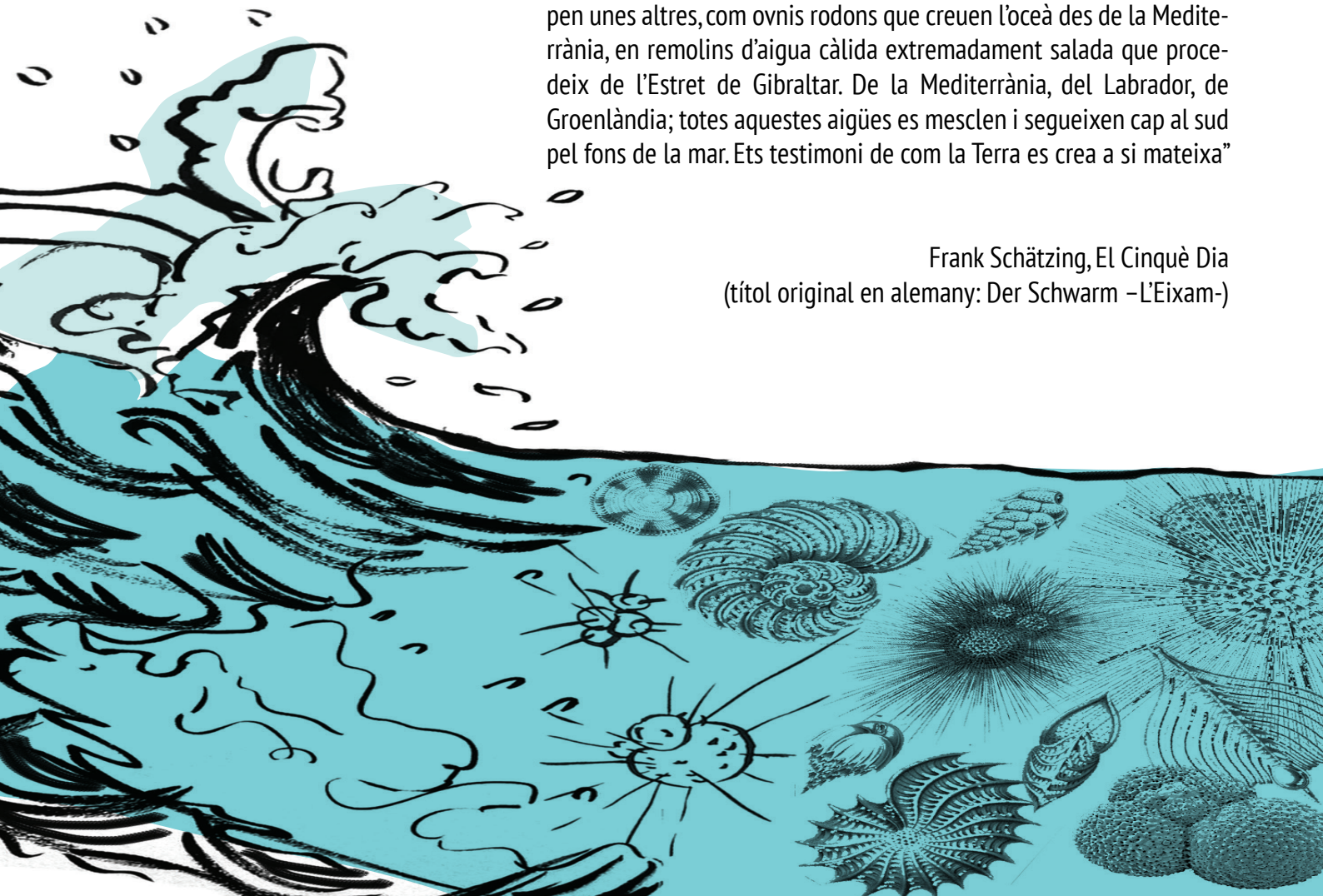

3.1 SEA SURFACE TEMPERATURE VARIABILITY IN THE CENTRAL-WESTERN MEDITERRANEAN SEA DURING THE LAST 2700 YEARS: A MULTI-PROXY AND MULTI-RECORD APPROACH

Mercè Cisneros[1], Isabel Cacho[1], Jaime Frigola[1], Miquel Canals[1], Pere Masqué[2,3,4], Belen Martrat[5], Marta Casado[5], Joan O. Grimalt[5], Leopoldo D. Pena[1], Giulia Margaritelli[6], and Fabrizio Lirer[6]

[1]GRC Geociències Marines, Departament de Dinàmica de la Terra i de l'Oceà, Facultat de Geologia, Universitat de Barcelona, Barcelona, Spain

[2]Institut de Ciència i Tecnologia Ambientals & Departament de Física, Universitat Autònoma de Barcelona, Bellaterra, Spain

[3]School of Natural Sciences and Centre for Marine Ecosystems Research, Edith Cowan University, Joondalup, Australia

[4]Oceans Institute and School of Physics, The University of Western Australia, Crawley, Australia

[5]Institut de Diagnosi Ambiental i Estudis de l'Aigua (IDAEA), Consell Superior d'Investigacions Científiques (CSIC), Barcelona, Spain

[6]Istituto per l'Ambiente Marino Costiero (IAMC)–Consiglio Nazionale delle Ricerche, Calata Porta di Massa, Interno Porto di Napoli, 80133, Naples, Italy

Climate of the Past 12, 849-869, 2016
www.clim-past.net/12/849/2016/
doi:10.5194/cp-12-849-2016

3.1.1 Abstract

This study presents the reconstructed evolution of sea surface conditions in the central-western Mediterranean Sea during the late Holocene (2700 years) from a set of multi-proxy records as measured on five short sediment cores from two sites north of Minorca (cores MINMC06 and HER- MC-MR3). Sea surface temperatures (SSTs) from alkenones and *Globigerina bulloides* Mg/Ca ratios are combined with $\delta^{18}O$ measurements in order to reconstruct changes in the regional evaporation–precipitation (E–P) balance. We also revisit the *G. bulloides* Mg/Ca–SST calibration and readjusted it based on a set of core-top measurements from the western Mediterranean Sea. Modern regional oceanographic data indicate that *Globigerina bulloides* Mg/Ca is mainly controlled by seasonal spring SST conditions, related to the April–May primary

productivity bloom in the region. In contrast, the alkenone–SST signal represents an integration of the annual signal.

The construction of a robust chronological framework in the region allows for the synchronization of the different core sites and the construction of "stacked" proxy records in order to identify the most significant climatic variability patterns. The warmest sustained period occurred during the Roman Period (RP), which was immediately followed by a general cooling trend interrupted by several centennial-scale oscillations. We propose that this general cooling trend could be controlled by changes in the annual mean insolation. Even though some particularly warm SST intervals took place during the Medieval Climate Anomaly (MCA), the Little Ice Age (LIA) was markedly unstable, with some very cold SST events mostly during its second half. Finally, proxy records for the last centuries suggest that relatively low E–P ratios and cold SSTs dominated during negative North Atlantic Oscillation (NAO) phases, although SSTs seem to present a positive connection with the Atlantic Multidecadal Oscillation (AMO) index.

3.1.2 Introduction

The Mediterranean is considered one of the most vulnerable regions with regard to the current global warming (Giorgi, 2006). This high sensitivity to climate variability has been evidenced in several studies on past natural changes (Rohling et al., 1998; Cacho et al., 1999a; Moreno et al., 2002; Martrat et al., 2004; Reguera, 2004; Frigola et al., 2007; Combourieu Nebout et al., 2009). Palaeo-studies focussed mostly on the rapid climate variability in the last glacial period have shown solid evidence of a close connection between changes in North Atlantic oceanography and climate over the western Mediterranean region (Cacho et al., 1999b, 2000, 2001; Moreno et al., 2005; Sierro et al., 2005; Frigola et al., 2008; Fletcher and Sanchez-Goñi, 2008). Nevertheless, climate variability during the Holocene, and particularly during the last millennium, is not so well described in this region, although its understanding is crucial for placing the nature of the 20th century trends in the recent climate history (Huang, 2004).

Some previous studies have already proposed that the Holocene centennial climate variability in the western Mediterranean Sea could be linked to the North Atlantic

Oscillation (NAO) variability (Jalut et al., 1997, 2000; Com- bourieu Nebout et al., 2002; Goy et al., 2003; Roberts et al., 2012; Fletcher et al., 2012). In particular, nine Holocene episodes of enhanced deep water convection in the Gulf of Lion (GoL) and surface cooling conditions have been de- scribed in the region (Frigola et al., 2007). These events have also been correlated to intensified upwelling conditions in the Alboran Sea and tentatively described as two-phase scenar- ios driven by distinctive NAO states (Ausín et al., 2015).

A growing number of studies have revealed considerable climate fluctuations during the last 2 kyr (Abrantes et al., 2005; González-Álvarez et al., 2005; Holzhauser et al., 2005; Kaufman et al., 2009; Lebreiro et al., 2006; Martín-Puertas et al., 2008; Pena et al., 2010; Kobashi et al., 2011; Nieto- Moreno et al., 2011, 2013; Moreno et al., 2012; PAGES2K Consortium, 2013; Esper et al., 2014; McGregor et al., 2015). However, there is no agreement on the exact time span of the different climatic periods defined, such as the Medieval Climatic Anomaly (MCA), a term coined originally by Stine (1994).

The existing Mediterranean climatic records for the last 1 or 2 kyr are mostly based on terrestrial archives such as tree rings (Touchan et al., 2005, 2007; Griggs et al., 2007; Esper et al., 2007; Büntgen et al., 2011; Morellón et al., 2012), speleothem records (Frisia et al., 2003; Mangini et al., 2005; Fleitmann et al., 2009; Martín-Chivelet et al., 2011; Wassenburg et al., 2013), or lake reconstructions (Pla and Catalan, 2005; Martín-Puertas et al., 2008; Corella et al., 2011; Morellón et al., 2012). All of these archives can be good sensors of temperature and humidity changes, but it is often diffi- cult to disentangle the effect of both variables in the proxy records. Recent efforts focussed on integrating these 2 kyr records into regional climatic signals reveal complex regional responses and evidence the scarcity of marine records to form a more complete picture (PAGES, 2009; Lionello, 2012).

Marine records are often limited by the lack of adequate time resolution and/or robust chronologies for detailed comparison with terrestrial records. However, marine records provide a wider range of temperature-sensitive proxies. There are few marine palaeoclimate records available for the last 2 kyr in the Mediterranean Sea (Schilman et al., 2001; Versteegh et al., 2007; Piva et al., 2008; Taricco et al., 2009, 2015; Incarbona et al., 2010; Fanget et al., 2013; Grauel et al., 2013; Lirer et al., 2013, 2014; Di Bella et

al., 2014; Goudeau et al., 2015) and they are even more scarce in the western basin. Unfortunately, the existing pool of marine proxy data in the Mediterranean for the last two millennia is too sparse to recognize common patterns of climate variability (Taricco et al., 2009; Nieto-Moreno et al., 2011; Moreno et al., 2012, and references therein).

The aim of the present study is to characterize changes in surface water properties from the Minorca margin in the Catalan–Balearic Sea (central-western Mediterranean) in order to contribute to a better understanding of the climate variations in this region during the last 2.7 kyr. Sea surface temperature (SST) has been reconstructed by means of two independent proxies, Mg/Ca analyses on the planktonic foraminifera *Globigerina bulloides* and alkenone-derived SST (Villanueva et al., 1997; Lea et al., 1999; Barker et al., 2005; Conte et al., 2006). The application of *G. bulloides* Mg/Ca as a palaeothermometer in the western Mediterranean Sea is tested through the analysis of a series of core-top samples from different locations of the western Mediterranean Sea and the calibration reviewed consistently. Mg/Ca thermometry is applied in conjunction with $\delta^{18}O$ in order to evaluate changes in the evaporation–precipitation (E–P) balance of the basin, which are ultimately linked to salinity (Lea et al., 1999; Pierre, 1999; Barker et al., 2005).

One of the intrinsic limitations of studying the climate evolution of the last 2 kyr is that the magnitude of climatic oscillations is often below the sensitivity of the selected proxies. In order to overcome this limitation we have produced “stack” proxy records from multicores in the same region. The stack record captures the first-order climatic variability from the proxy records and removes the noise, therefore allowing for a more robust identification of regional climatic variability.

The studied time periods have been defined as follows (years expressed as BCE, before common era, and CE, com- mon era): the Talaiotic Period (TP, ending in 123 BCE), Ro- man Period (RP, from 123 BCE to 470 CE), “Dark Middle Ages” (DMA; from 470 until 900 CE), Medieval Climate Anomaly (MCA, from 900 to 1275 CE), and Little Ice Age (LIA, from 1275 to 1850 CE), with the Industrial Era (IE) as the most recent period. The limits of these periods are not uniform across the Mediterranean (Lionello, 2012), and here the selected ages have been chosen according to historical events in Minorca and to the classic climatic ones defined in the literature (i.e. Nieto-Moreno et

al., 2011, 2013; Moreno et al., 2012; Lirer et al., 2013, 2014).

3.1.3 Climatic and oceanographic setings

The Mediterranean Sea is a semi-enclosed basin located in a transitional zone between different climate regimes, from the temperate zone in the north to the subtropical zone in the south. Consequently, the Mediterranean climate is char- acterized by mild wet winters and warm to hot, dry summers (Lionello et al., 2006). Interannual climate variability is very much controlled by the dipole-like pressure gradient between the Azores (high) and Iceland (low) system, known as the North Atlantic Oscillation (NAO; Hurrell, 1995; Lionello and Sanna, 2005; Mariotti, 2011; Ausín et al., 2015). However, the northern part of the Mediterranean region is also linked to other mid-latitude teleconnection patterns (Lionello, 2012).

The Mediterranean Sea is a concentration basin (Béthoux, 1980; Lacombe et al., 1981) and the excess of evaporation with respect to freshwater input is balanced by water ex- change at the Strait of Gibraltar (i.e. Pinardi and Masetti, 2000; Malanotte-Rizzoli et al., 2014). The basin-wide circulation pattern is predominantly cyclonic (Millot, 1999). Three convection cells promote the Mediterranean deep and intermediate circulation: a basin-wide open cell and two separated closed cells, one for the western part of the basin and one for the eastern part. The first one connects the two basins of the Mediterranean Sea though the Strait of Sicily, where water masses interchange occurs at intermediate depths. This cell is associated with the inflow of Atlantic Water (AW) at the Strait of Gibraltar and the outflow of the Levantine Intermediate Water (LIW) that flows below the first (Lionello et al., 2006).

In the north-western Mediterranean Sea, the Northern Current (NC) represents the main feature of the surface circulation transporting waters alongshore from the Ligurian Sea to the Alboran Sea (Fig. 3.1a). North-east of the Balearic Promontory a surface oceanographic front separates Mediter- ranean waters transported by the NC from the Atlantic waters that recently entered the Mediterranean (Millot, 1999; Pinot et al., 2002; André et al., 2005).

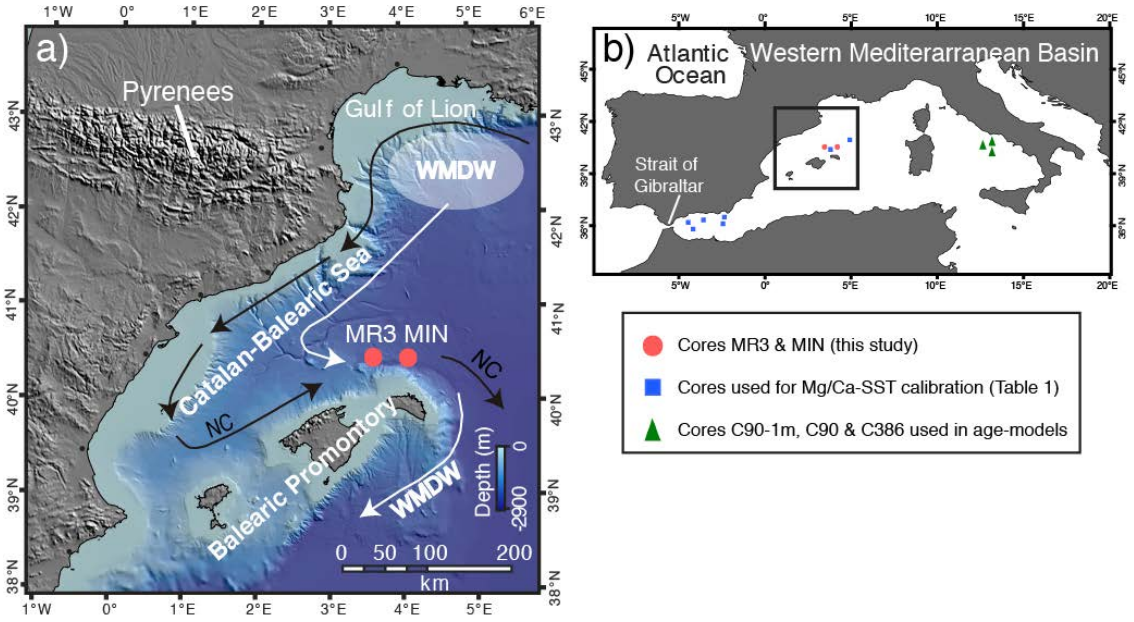

Figure 3.1. Location of the studied area. (a) Central-western Mediterranean Sea: cores MIN and MR3 (red dots). NC: Northern Current (surface). WMDW: Western Mediterranean Deep Water. (b) Cores used in 1

Deep convection occurs offshore of the GoL due to the action of persistent cold and dry winter winds such as the tramontana and the mistral. These winds cause strong evaporation and cooling of surface water, thus increasing their density, sinking to greater depths and leading to Western Mediterranean Deep Water formation (WMDW; MEDOC, 1970; Lacombe et al., 1985; Millot, 1999). Dense shelf water cascading (DSWC) in the GoL also contributes to the sink of large volumes of water and sediments into the deep basin (Canals et al., 2006).

The north-western Mediterranean primary production is subject to an intense bloom in late winter–spring, when the surface layer stabilizes, and sometimes to a less intense bloom in autumn, when the strong summer thermocline is progressively eroded (Estrada et al., 1985; Bosc et al., 2004; D'Ortenzio and Ribera, 2009; Siokou-Frangou et al., 2010). SST in the region evolves accordingly with the seasonal bloom, with minima SST in February, which subsequently increases until maximum SST values during August. After- wards, a SST drop can be observed in October, although with some interannual variability (Pastor, 2012).

3.1.4 Material and methods

Sediment core description

The studied sediment cores were recovered from a sedi- ment drift built by the action of the southward branch of the WMDW north of Minorca (Fig. 3.1). Previous studies carried out at this site have already described high sedimentation rates (> 20 cm kyr^{-1}; Frigola et al., 2007, 2008; Moreno et al., 2012), suggesting that this location was suitable for a detailed study of the last millennia. The cores were recovered with a multicore system in two different stations lo- cated at about 50 km north of Minorca. Cores MINMC06-1 and MINMC06-2 (henceforth MIN1 and MIN2; 40◦ 291 N, 04◦ 011 E; 2391 m water depth; 31 and 32.5 cm core length, respectively) were retrieved in 2006 during the HERMES 3 cruise onboard the R/V *Thethys II*. The recovery of cores HER-MC-MR3.1, HER-MC-MR3.2, and HER-MC-MR3.3 (henceforth MR3.1, MR3.2, and MR3.3; 40◦ 291 N, 3◦ 371 E; 2117 m water depth; 27, 18, and 27 cm core length, respectively) took place in 2009 during the HERMESIONE expedition onboard the R/V *Hespérides*. The distance between MIN and MR3 cores is ~ 30 km and both stations are located at an intermediate position within the sediment drift, which extends along a water depth range from 2000 to 2700 m (Frigola, 2012; Velasco et al., 1996; Mauffret, 1979). The MIN cores are from sites that are about 300 m deeper than the MR3 ones.

MIN cores were homogeneously sampled at 0.5 cm resolution in the laboratory. In the MR3 cores a different strat- egy was followed. MR3.1 and MR3.2 were initially subsampled with a PVC tube and split into two halves for X-ray fluorescence (XRF) analyses in the laboratory. Both halves of core MR3.1 (MR3.1A and MR3.1B) were used for the present work as replicates of the same core, and records for each half are shown separately. All MR3 cores were sam- pled at 0.5 cm resolution in the upper 15 cm and at 1 cm in the deeper sections, with the exception of MR3.1B that was sampled at 0.25 cm resolution. The MR3 cores were com- posed of brown–orange nannofossil and foraminifera silty clay, which was lightly bioturbated and contained layers enriched in pteropods and fragments of gastropods as well as some dark layers.

Additionally, core-top samples from seven multicores col- lected at different locations in the western Mediterranean have also been used for the correction of the Mg/Ca–SST

calibration from *G. bulloides* (Table 3.1; Fig. 3.1).

Table 3.1. Core tops included in the calibration's adjustment. $\delta^{18}O_c$ and Mg/Ca have been obtained from *G. bulloides* (Mg/Ca procedure has been performed without reductive step).

Core	Location	Latitude	Longitude	Mg/Ca (mmol mol^{-1})	$\delta^{18}O$ (‰ VPDB)
TR4-157	Balearic Abyssal Plain	40°30.00' N	4°55.76' E	3.36	0.53
ALB1	Alboran Sea (W. Med.)	36°14.31' N	4°15.52' W	3.2	0.8
ALBT1	Alboran Sea (W. Med.)	36°22.05' N	4°18.14' W	3.44	0.65
ALBT2	Alboran Sea (E. Med.)	36°06.09' N	3°02.41' W	3.63	0.57
ALBT4	Alboran Sea (E. Med.)	36°39.63' N	1°32.35' W	3.72	0.93
ALBT5	Alboran Sea (E. Med.)	36°13.60' N	1°35.97' W	3.38	0.64

Radiocarbon analyses

Twelve 14 C AMS dates were measured in cores MIN1, MIN2, and MR3.3 (Supplement Table 3.2) using 4–22 mg samples of the planktonic foraminifer *Globorotalia inflata* handpicked from the > 355 μm fraction. The ages were calibrated with the standard marine correction of 408 years and the regional average marine reservoir correction (*L\R*) for the central-western Mediterranean Sea using Calib 7.0 software (Stuiver and Reimer, 1993) and the MARINE13 calibration curve (Reimer et al., 2013).

Radionuclides ^{210}Pb and ^{137}Cs

The concentrations of the naturally occurring radionuclide ^{210}Pb (Supplement Fig. 3.10) were determined in cores MIN1, MIN2, MR3.1A, and MR3.2 by alpha spectroscopy (Sanchez-Cabeza et al., 1998). The concentrations of the an-thropogenic radionuclide 137 Cs in core MIN1 (Fig. 3.10) were measured by gamma spectrometry using a high-purity intrinsic germanium detector. The ^{226}Ra concentrations were determined from the gamma emissions of ^{214}Pb that were also used to calculate the excess ^{210}Pb concentrations. The sediment accumulation rates for the last century (see Supplement Information) were calculated using the CIC (constant initial concentration) and the

CF:CS (constant flux:constant sedimentation) models (Appleby and Oldfield, 1992; Krish- naswami et al., 1971), constrained by the ^{137}Cs concentration profile in core MIN1 (Masqué et al., 2003).

Bulk geochemical analyses

The elemental composition of cores MR3.1B and MR3.2 was obtained with an Avaatech XRF core-scanner system (CORELAB, University of Barcelona), which is equipped with an optical variable system that allows determining the length (10–0.1 mm) and the extent (15–2 mm) of the bundle of X-rays in an independent way. This method allows obtaining qualitative information of the elementary composition of the core materials. The core surfaces were scraped, cleaned, and covered with a 4 μm thin SPEXCertiPrep Ultralene foil to prevent contamination and minimize desiccation (Richter and van der Gaast, 2006). Sampling was performed every 1 cm and scanning took place at the split core surface directly. Among the several elements measured in this study, the Mn profile was used for the construction of the age models (see Supplement for age model development).

Planktonic foraminiferal analyses

Planktonic foraminifera specimens of *Globigerina bulloides* were picked together from a size range of 250–355 μm, crushed, and cleaned separately for Mg/Ca and $\delta^{18}O$ measurements. In core MR3.1B, picking was often performed in the < 355 μm fraction due to the small amount of material Additionally, quantitative analysis of planktonic foraminiferal assemblages was carried out in MR3.3 core and on the upper part of MR3.1A core by using the fraction size above 125 μm. The 42 studied samples showed abundant and well-preserved planktonic foraminifera. The ~300 samples for trace elements analyses consisted of ~45 specimens of *G. bulloides* that were crushed under glass slides to open the chambers. Foraminifera cleaning consisted of clay removal and oxidative and weak acid leaching steps (Pena et al., 2005). Samples from MR3.1A core were also cleaned including the “reductive step”. Elemental ratios were measured on an inductively coupled plasma mass spectrometer (ICP-MS, Perkin Elmer ELAN 6000) in the Scientific and Technological Centers of the University of Barcelona (CCiT- UB). A standard solution with known elemental ratios was used for sample standard bracketing (SSB) as a correction for instrumental drift. The average reproducibility of Mg/Ca

ratios, taking into account the known standard solutions concentrations, was 97 and 89% for MIN1 and MIN2 cores, and 99 and 97% for MR3.1A, MR3.1B, and MR3.3 cores, respectively.

Procedural blanks were routinely measured to detect any potential contamination problem during cleaning and dissolution. The Mn/Ca and Al/Ca ratios were also always measured to identify potential contaminations due to the presence of manganese oxides and/or aluminosilicates (Barker et al., 2003; Lea et al., 2005; Pena et al., 2005, 2008).

To avoid the overestimation of Mg/Ca–SST by diagenetic contamination, Mn/Ca values >0.5 mmol mol^{-1} were discarded from MR3.1B core and only those higher than 1 mmol mol^{-1} were removed from MIN1 and MR3.3. Samples suspected to have detrital contamination with elevated Al/Ca ratios were also removed. No significant correlation exists between Mg/Ca and Mn/Ca or Al/Ca ratios after data filtering ($r < 0.29$, p value = 0.06).

The Mg/Ca ratios were transferred into SST values using the calibration proposed in the present study (Section 3.1.6). In the case of the MR3.1A record, which was cleaned using the reductive procedure, and as was expected (Barker et al., 2003; Pena et al., 2005; Yu et al., 2007), the Mg/Ca ratios were about 23% lower than those measured in MR3.1B core without the reductive step. The obtained percentage of Mg/Ca lowering is comparable to or higher than those percentages previously estimated for different planktonic foraminifera, although data from *G. bulloides* have not been previously reported (Barker et al., 2003). Mg/Ca-SST in MR3.1A core was calculated after the Mg/Ca correction of this 23% offset by application of the calibration used with the other records.

Stable isotope measurements were performed by means of sonication on 10 specimens of *G. bulloides* after methanol cleaning to remove fine-grained particles. The ~300 samples analyses were performed in a Finnigan MAT 252 mass spectrometer fitted with a Kiel-IV carbonate microsampler in the CCiT-UB. The analytical precision of laboratory standards for $\delta^{18}O$ was better than 0.08‰. Calibration to Vienna Pee Dee Belemnite (VPDB) was carried out by means of NBS-19 standards (Coplen, 1996).

Seawater $\delta^{18}O$ ($\delta^{18}O_{sw}$) was obtained after removing the temperature effect on the *G. bulloides* $\delta^{18}O$ signal using the Mg/Ca-SST records of the Shackleton palaeotemperature equation (Shackleton, 1974). The results are expressed in the SMOW (Standard Mean Ocean Water) water standard ($\delta^{18}O_{sw}$) after the correction of Craig (1965). The use of specific temperature equations for *G. bulloides* was also considered (Bemis et al., 1998; Mulitza et al., 2003), but the core-top estimates provided $\delta^{18}O_{sw}$ values of 2.1-1.5‰ SMOW (Table 3.1), which were significantly higher than those measured in water samples from the central-western Mediterranean Sea (~1.2‰ SMOW) (Pierre, 1999). After application of the empirical Shackleton (1974) palaeotemperature equation, the core-top $\delta^{18}O_{sw}$ estimates averaged 1.1‰ SMOW and were closer to the actual seawater measurements. Thus, it was decided that this equation provided more realistic oceanographical conditions in this location.

Stable isotope measurements were performed by means of sonication on 10 specimens of *G. bulloides* after methanol cleaning to remove fine-grained particles. The ~300 samples analyses were performed in a Finnigan MAT 252 mass spectrometer fitted with a Kiel-IV carbonate microsampler in the CCiT-UB. The analytical precision of laboratory standards for $\delta^{18}O$ was better than 0.08‰. Calibration to Vienna Pee Dee Belemnite (VPDB) was carried out by means of NBS-19 standards (Coplen, 1996).

Seawater $\delta^{18}O$ ($\delta^{18}O_{sw}$) was obtained after removing the temperature effect on the *G. bulloides* $\delta^{18}O$ signal using the Mg/Ca-SST records of the Shackleton palaeotemperature equation (Shackleton, 1974). The results are expressed in the SMOW (Standard Mean Ocean Water) water standard ($\delta^{18}O_{sw}$) after the correction of Craig (1965). The use of specific temperature equations for *G. bulloides* was also considered (Bemis et al., 1998; Mulitza et al., 2003), but the core-top estimates provided $\delta^{18}O_{sw}$ values of 2.1-1.5‰ SMOW (Table 3.1), which were significantly higher than those measured in water samples from the central-western Mediterranean Sea (~1.2‰ SMOW) (Pierre, 1999). After application of the empirical Shackleton (1974) palaeotemperature equation, the core-top $\delta^{18}O_{sw}$ estimates averaged 1.1‰ SMOW and were closer to the actual seawater measurements. Thus, it was decided that this equation provided more realistic oceanographical conditions in this location.

Alkenones

Measurements of the relative proportion of unsaturated C_{37} alkenones, namely the $U^{k'}_{37}$ index, were carried out in order to obtain SST records for the studied cores. Detailed information about the methodology and equipment used can be found in Villanueva et al. (1997). The precision of this palaeothermometry tool has been determined to be about ±0.5 °C (Eglinton et al., 2001). Furthermore, taking into account duplicate alkenone analysis carried out on MR3.3 core, the precision achieved results better than ±0.8 °C. The reconstruction of SST records was based on the global calibration of Conte et al. (2006), which considers an estimation standard error of 1.1 °C in surface sediments.

3.1.5 Age model development

Obtaining accurate chronologies for each of the studied sed- iment cores is particularly critical to allow intercomparison and produce a stack record that represents the regional cli- matic signal. With this objective, a wide set of parameters have been combined in order to obtain chronological mark- ers in all the studied sedimentary records, including absolute dates and stratigraphical markers based on both geochemi- cal and micro-palaeontological data (Tables 3.3 and 3.5). The methodology of age model development is explained in detail in the Supplement.

3.1.6 Sea surface temperatures and $\delta^{18}O$

Mg/Ca-SST calibration

The Mg/Ca ratio measured in *G. bulloides* is a widely used proxy to reconstruct SST (Barker et al., 2005), although the calibrations available can provide very different results (Lea et al., 1999; Mashiotta et al., 1999; Elderfield and Ganssen, 2000; Anand et al., 2003; McConnell and Thunell, 2005; Cléroux et al., 2008; Thornalley et al., 2009; Patton et al., 2011). Apparently, the regional Mg/Ca-temperature response varies due to parameters that have not yet been identified (Patton et al., 2011). A further difficulty arises from the questioned Mg/Ca thermal signal in high-salinity regions such as the Mediterranean Sea, where anomalously high Mg/Ca values have been observed (Ferguson et al., 2008). This apparent high salinity sensitivity in foraminiferal Mg/Ca ratios is under discussion and has not been supported by recent culture experiments (Hönisch et al., 2013), which, in addition, could be attributed to diagenetic overprints

(Hoogakker et al., 2009; van Raden et al., 2011). In order to test the value of the Mg/Ca ratios in *G. bulloides* from the western Mediterranean Sea and also review its significance in terms of seasonality and depth habitat, a set of core-top samples from different locations of the western Mediterranean Sea have been analysed. Core-top samples were recovered using a multicorer system, and they can be considered representative of present conditions (Masqué et al., 2003; Cacho et al., 2006). The studied cores are located in the 35-45º N latitude range (Table 3.1 and Fig. 3.1) and mostly represent two different trophic regimes, defined by the classical spring bloom (the most north-western basin) and an intermittent bloom (D'Ortenzio and Ribera, 2009).

The resulting Mg/Ca ratios have been compared with the isotopically derived calcification temperatures based on the $\delta^{18}O$ measurements performed also in *G. bulloides* from the same samples. This comparison was performed after use of the Shackleton (1974) palaeotemperature equation and the $\delta^{18}O_{water}$ data published by Pierre (1999), always considering the values of the closer stations and the top 100 m. The resulting Mg/Ca-SST data have been plotted together with those of *G. bulloides* from North Atlantic core tops previously published by Elderfield and Ganssen (2000). The resulting high correlation (r^2 = 0.92; Fig. 3.2) strongly supports that the Mg/Ca ratios of the central-western Mediterranean Sea are dominated by a thermal signal. Thus, the new data set from the Mediterranean core tops improves temperature sensitivity range over the warm end of the calibration. The resulting exponential function indicates ~9.4% Mg/Ca per ºC sensitivity in the Mg uptake with respect to temperature, which is in agreement with the range described in the literature (i.e., Elderfield and Ganssen, 2000; Barker et al., 2005; Patton et al., 2011). The new equation for the Mg/Ca-SST calibration including data from the western Mediterranean Sea and the Atlantic Ocean is as follows:

$$Mg/Ca = 0.7045(\pm 0.0710)e^{0.0939(\pm 0.0066)T}$$

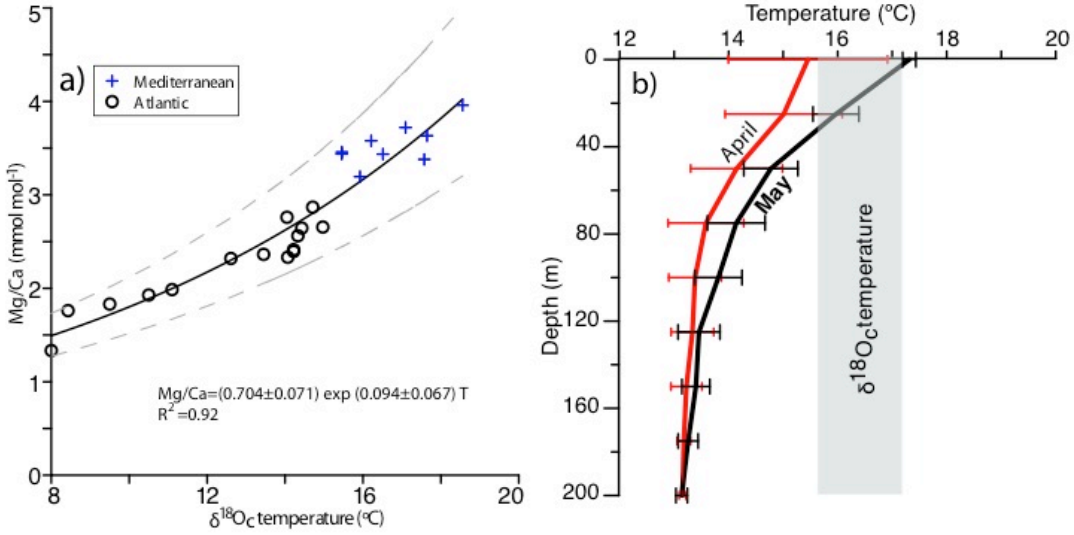

Figure 3.2. Mg/Ca-SST calibration. **a)** Exponential function and correlation between $\delta^{18}O_c$ temperatures and Mg/Ca. Dashed lines show the 1 confidence limits of the curve fit. The standard error of our temperature calibration taking into account each $\delta^{18}O_c$ temperature from core tops (Table 3.1) is ±0.6 C. Error of temperature estimates based on our *G. bulloides* calibration for the western Mediterranean is ±1.4 °C. These uncertainties are higher but still in the range of ±0.6 C obtained for the Atlantic Ocean in Elderfield and Ganssen (2000) and also 1.1 °C in *G. bulloides* culture data (Lea et al., 1999). **b)** April (red) and May (black) temperature profiles of the first 200 m measured during years 1945-2000 in stations corresponding to the studied core tops (MEDAR GROUP, 2002). The $\delta^{18}O_c$ average temperature of all cores is shown (grey, vertical band).

The Mg/Ca-SST signal of *G. bulloides* has been compared with a compilation of water temperature profiles of the first 200 m measured between years 1945 and 2000 in stations close to the studied core tops (MEDAR GROUP, 2002). Although significant regional and interannual variations have been observed, the obtained calcification temperatures of our core-top samples show the best agreement with temperature values of the upper 40 m during the spring months (April–May; Fig. 3.2). This water depth is consistent with preferential depth ranges for *G. bulloides* found by plankton tows in the Mediterranean (Pujol and Vergnaud-Grazzini, 1995) and with results from multiannual sediment trap monitoring in the Alboran Sea and the GoL, where maximum *G. bulloides* percentages were observed just before the beginning of thermal stratifications (see Bárcena et al., 2004; Bosc et al., 2004; Rigual-Hernández et al., 2012). Although the information available about depth and seasonality distribution of *G. bulloides* is relatively fragmented, this species is generally found in intermediate or even shallow waters (i.e. Bé and Hutson, 197; Ganssen and Kroon, 2000; Schiebel et al., 2002; Rogerson et al., 2004; Thornalley et al., 2009). However, *G. bulloides* has also been observed at deeper depths in some western Mediterranean Sea sub-basins (Pujol and Vergnaud- Grazzini, 1995). Extended data with enhanced spatial and seasonal coverage

are required in order to better characterize production, seasonality, and geographic and distribution patterns of live foraminifera such as *G. bulloides*. Nevertheless, the obtained core-top data set offers solid evidence on the seasonal character of the recorded temperature signal in the Mg/Ca ratio.

A regional stack for Mg/Ca-SST records

The Mg/Ca-SST profiles obtained from our records are plotted with the resulting common age model in Fig. 3.3. The average SST values for the last 2700 years ranged from 16.0 ± 0.9 to 17.8 ± 0.8 °C (uncertainties of average values represent 1σ; uncertainties of absolute values include analytical precision and reproducibility and also those derived from the Mg/Ca-SST calibration).

SST records show the warmest sustained period during the RP, approximately between 170 BCE and 300 CE, except in MIN2 core, since this record ends at the RP-EMA transition. In addition, all the records show a generally consistent cooling trend after the RP with several centennial-scale oscillations. The maximum SST value is observed in MR3.3 core (19.6 ± 1.8 °C) during the MCA (Fig. 3.3c) and the minimum is recorded in MIN1 core (14.4 ± 1.4 °C) during the LIA (Fig. 3.3e). Centennial-scale variability is predominant throughout the records. Particularly, during MCA some warm episodes reached slightly higher SST than the averaged SST maximum (i.e. 19.6 ± 1.8 °C at ~1021 CE). These events were far shorter in duration compared to the RP (Fig. 3.3). The highest frequency of intense cold events occurred during the LIA and, in particular, the last millennium recorded the minimum average Mg/Ca-SST (15.2 ± 0.8 °C). Four of the five records show a pronounced SST drop after 1275 CE, coinciding with the onset of the LIA. Based on the different Mg/Ca-SST patterns, the LIA period has been divided into two subperiods, an early warmer interval (LIAa) and a later colder interval (LIAb) by reference to the 1540 CE boundary.

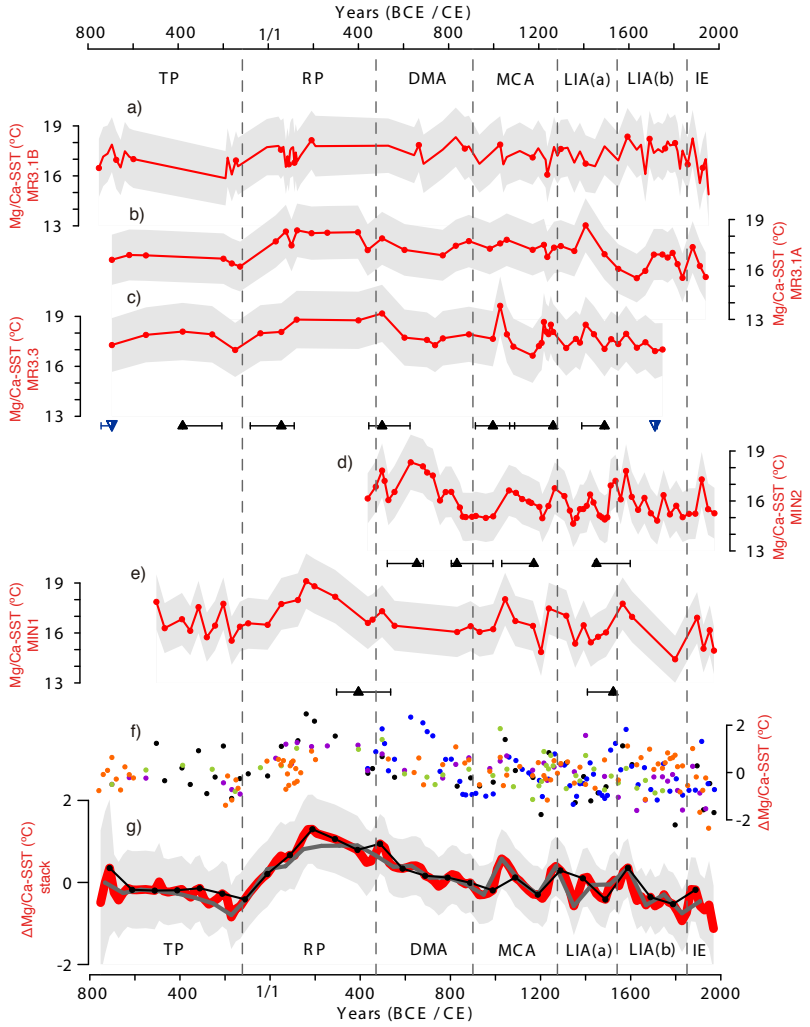

Figure 3.3. SST obtained from Mg/Ca for cores **a)** MR3.1B, **b)** MR3.1A, **c)** MR3.3, **d)** MIN2, and **e)** MIN1. The grey shaded areas integrate uncertainties of average values and represent 1σ of the absolute values. This uncertainty includes analytical precision and reproducibility and the uncertainties derived from the *G. bulloides* core-top calibrations for the central-western Mediterranean Sea developed in this paper. **f)** All individual SST anomalies on their respective time step (MR3.1B: orange; MR3.1A: purple; MR3.3: green; MIN2: blue; MIN1: black dots). **g)** 20 yr cm^{-1} stacked temperature anomaly (red plot) with its 2σ uncertainty (grey band). The 80 yr cm^{-1} (grey plot) and the 100 yr cm^{-1} (black plot) stacks are also shown. The triangles represent ^{14}C dates (black) and biostratigraphical dates based on plank- tonic foraminifera (blue) and are shown below the corresponding core, including their associated 2 errors. Period DMA (Dark Middle Ages) correspond to EMA (Early Middle Ages).

One of the main difficulties with SST reconstructions in the last millennia is the internal noise of the records due to sampling and proxy limitations, which is of the same amplitude as the targeted climatic signal variability. In this sense, we have constructed an Mg/Ca-SST anomaly stack with the aim to detect the most robust climatic structures along the different records and reduce the individual noise. First, each SST record was converted into a SST anomaly record in relation to its average temperature (Fig. 3.3f). Secondly, in order to obtain a common sampling interval, all records were interpolated. Interpolation at three different resolutions did not result in significant differences (Fig.

3.3g). Subsequently, we selected the stack that provided the best resolution offered by our age models (20 yr cm^{-1}) since it very well preserves the high-frequency variability of the individual records (Fig. 3.3g). The obtained SST anomaly stack allows for a better identification of the most significant features at centennial timescales. Abrupt cooling events are mainly recorded during the LIA (-0.5 to -0.7 °C 100 yr^{-1}), while abrupt warmings (0.9 to 0.6 °C 100 yr^{-1}) are detected during the MCA.

Events of similar magnitude have been also documented during the LIA-IE transition. When considering the entire SST anomaly record, a long-term cooling trend of about -1 to -2 °C is observed. However, focussing on the last 1800 years, since the RP maxima, the observed cooling trend was far more intense, at about -3.1 to -3.5 °C (-0.3 to -0.8 °C kyr^{-1}). This is consistent within the recent 2 kyr global reconstruction published by McGregor et al. (2015; estimation of the SST cooling trend, using the average anomaly method 1 for the period 1–2000 CE: -0.3 to -0.4 °C kyr^{-1}).

δ^{18}O

The oxygen isotopes measured on carbonate shells of *G. bulloides* ($\delta\ ^{18}O_c$) and their derived $\delta\ ^{18}O_{sw}$ after removing the temperature effect with the Mg/Ca-SST signals are shown in Fig. 3.4. $\delta\ ^{18}Oc$ and their derived $\delta^{18}O_{sw}$ profiles have been respectively stacked following the same procedure for the Mg/Ca-SST stack (Section 3.1.6). In general terms, all the records present a highly stable pattern during the whole period with a weak depleting trend, which is al- most undetectable in some cases (i.e. MIN1 core).

The average $\delta\ ^{18}O_c$ values range from 1.2 to 1.4 ‰ VPDB and, in general, the MR3 cores show slightly higher values (~1.4 ‰ VPDB) than the MIN cores (~1.2 ‰ VPDB). Regarding to the internal variability of the split samples from core MR3.1 (MR3.1A and MR3.1B), $\delta^{18}O_C$ records and the calculated $\delta^{18}O_{SW}$, averages of the obtained differences have been ±0.05 VPDB‰ and ±0.10 SMOW‰, respectively. The lowest $\delta\ ^{18}O_c$ values (1.0 to 1.2 ‰ VPDB) mostly occur during the RP, although some short, low excursions can also be observed during the end of the MCA and/or the LIA. The highest values (1.4 to 1.8 ‰ VPDB) are mainly associated with short events during the LIA, the MCA, and over the TP-RP transition. A significant increase in $\delta^{18}O_c$ values is observed at the LIA-IE transition, although a sudden drop is recorded at the end of the stack

record (after 1867 CE), which could result from a differential influence of the records (i.e. MIN1) and/or an extreme artefact (Fig. 3.4g).

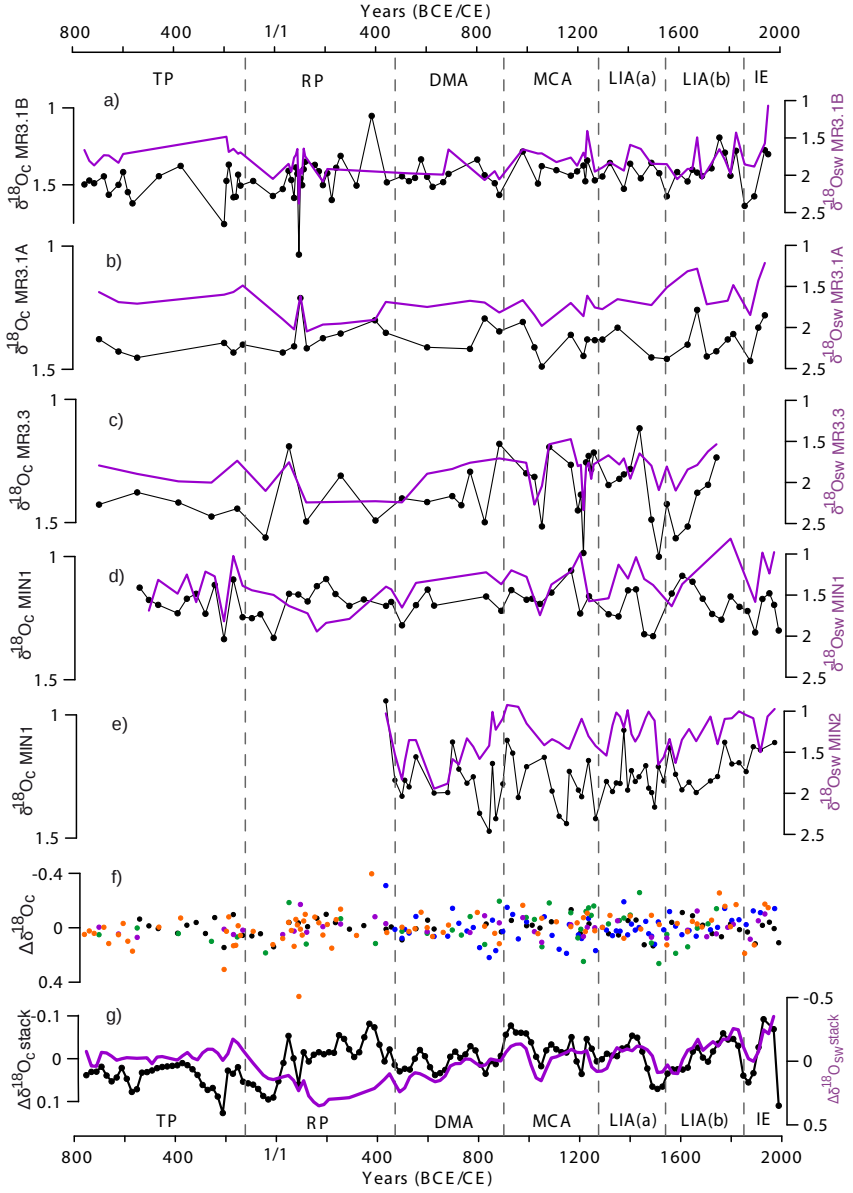

Figure 3.4. Oxygen isotope measured on carbonate shells of *G. bulloides* ($\delta^{18}O_c$ ‰ VPDB, in black) and their derived $\delta^{18}O_{SW}$ (purple) for cores: **(a)** MR3.1B, **(b)** MR3.1A, **(c)** MR3.3, **(d)** MIN2, and **(e)** MIN1. **(f)** Individual $\delta^{18}O_c$ (‰ VPDB) anomalies on their respective time step. **(g)** $\delta^{18}O_c$ and $\delta^{18}O_{SW}$ anomaly stacked records (‰ VPDB and ‰ SMOW, respectively). Period DMA (Dark Middle Ages) correspond to EMA (Early Middle Ages).

After removing the temperature effect from the $\delta^{18}O_c$ record, the remaining $\delta^{18}O_{sw}$ record mainly reflects changes in E-P balance, thus resulting in an indirect proxy of sea surface salinity. The average $\delta^{18}O_{sw}$ values obtained for the period studied ranged from 1.3 to 1.8 ‰ SMOW. The highest $\delta^{18}O_{sw}$ values (from 2.4 to 1.9 ‰ SMOW) are recorded during the RP, when the longest warm period is also observed, and some

values are notable during the MCA too. Enhancements of the E–P balance ($\delta^{18}O_{sw}$ higher values) coincide with higher SST. The lowest $\delta^{18}O_{sw}$ values (from 0.8 to 1.5 ‰ SMOW) are recorded particularly during the onset and the end of the LIA and also during the MCA. A drop in the E-P balance has been obtained from approximately the end of LIA to the most recent years. The most significant changes in our $\delta^{18}O_{sw}$ stack record correspond to increases in the most recent times and around 1200 CE (MCA) and to the decrease observed at the end of the LIA (Fig. 3.4).

Alkenone-SST records

The two alkenone ($U^{k'}_{37}$)-derived SSTs of MIN cores have already been published in Moreno et al. (2012), while the records from MR3 cores are new (Fig. 3.5). The four alkenone–SST records show a similar general cooling trend during the studied period and they have also been integrated in a SST anomaly stack (Fig. 3.5e). The general cooling trend involves about -1.4 °C when the entire studied period is considered and about -1.7 °C since the SST maximum recorded during the RP. The mean SST uncertainties in this section have been estimated as ±1.1 °C, taking into account the estimated standard error.

Previous studies have interpreted the alkenone–SST signal in the western Mediterranean Sea as an annual average (Ternois et al., 1996; Cacho et al., 1999a, b; Martrat et al., 2004). The average alkenone-SST values for the studied period (last 2700 years) ranged from 17.0 to 17.4 °C.

The coldest alkenone temperatures (~16.0 °C) have been obtained in core MIN2 during the LIAa and the warmest (~18.4 °C) in core MR3.3 during the MCA. Values near the average of maxima SST (from 17.9 to 18.4 °C) are observed more frequently during the TP, RP, and MCA, while temperatures during the onset of MCA and LIA show many values closer to the average of minima SST (ranging from 16.0 to 16.2 °C). Abrupt coolings are observed during the LIA and some events during MCA (-0.8 °C 100 yr^{-1}) and to a lesser extent during the LIA–IE transition (-0.5 °C 100 yr^{-1}). The highest warming rates are recorded during the MCA (0.4 °C 100 yr^{-1}) and also during the RP.

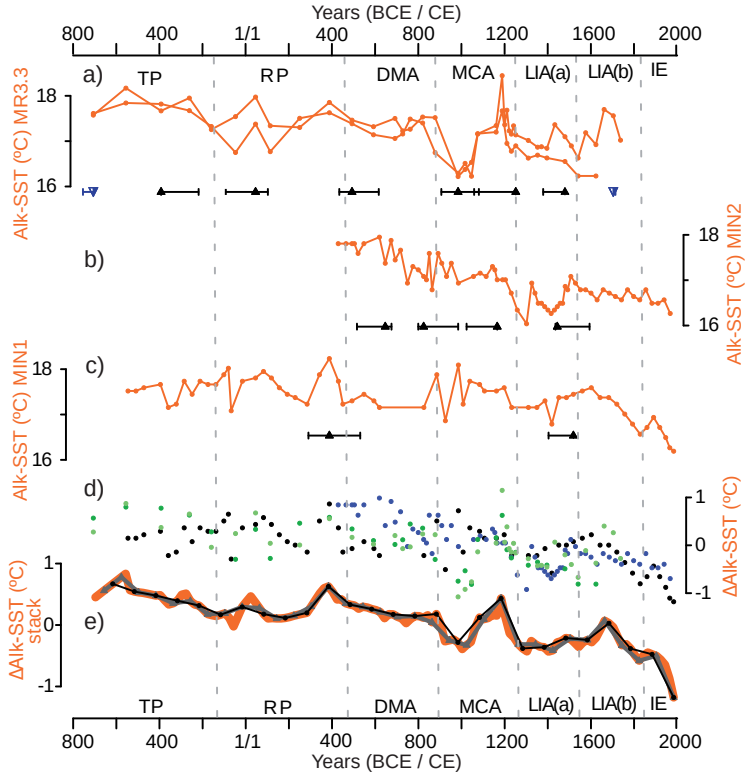

Figure 3.5. Alkenone temperature records from Minorca (this study) for cores **a)** MR3.3, **b)** MIN2, and **c)** MIN1. Triangles represent ^{14}C dates (black) and biostratigraphical dates based on plank-tonic foraminifera (blue) and are shown below the corresponding core with their associated 2σ errors. **d)** Individual alkenone-derived SST anomalies in their respective time step (MR3.3: green; MIN2: blue; MIN1: black dots). **e)** 20yr cm^{-1} stacked temperature anomaly (orange plot). The 80 yr cm^{-1} (grey plot) and the 100 yr cm^{-1} (black plot) stacks are also shown. Period DMA (Dark Middle Ages) correspond to EMA (Early Middle Ages).

Mg/Ca-SST vs. Alkenone-SST records

In this section, the uncertainties of the alkenone, 1.1 °C, have been calculated from the estimated standard error of the calibration and those of Mg/Ca-SST include the analytical precision and reproducibility and the standard error of the calibration. The measured Mg/Ca–SST and alkenone-SST averages are identical within error (16.9 ± 1.4 °C vs. 17.2 ± 1.1 °C), but the temperature range of the Mg/Ca records shows higher amplitude.

The similarity in SST averages of both proxies does not reflect the different habitat depths, since alkenones should mirror the surface photic layer (< 50 m), with relatively warm SST, while *G. bulloides* has the capability to develop in a wider and deeper environment (Bé, 1977; Pujol and Vergnaud-Grazzini, 1995; Ternois et al., 1996; Sicre et al., 1999; Ganssen and Kroon, 2000; Schiebel et al., 2002; Rogerson et al., 2004; Thornalley et al., 2009), where lower SST would be expected.

The enhanced Mg/Ca–SST variability is reflected in the short-term oscillations, at centennial timescales, which are larger in the Mg/Ca record with oscillations over 0.5 °C. This larger Mg/Ca–SST variability could be attributed to the highly restricted seasonal character of the signal, which purely reflects SST changes during the spring season. However, the coccolith signal integrates a wider time period from autumn to spring (Rigual-Hernández et al., 2012, 2013) and, consequently, changes associated with specific seasons be- come more diluted in the resulting averaged signal.

The annual mean SST corresponding to a Balearic site is 18.7 ± 1.1 °C, according to the integrated values of the upper 50 m (Ternois et al., 1996; Cacho et al., 1999a) of the GCC-IEO database between January 1994 and July 2008. Our core-top records represent the last decades and show SST values closer to the annual mean in the case of alkenone–SST, whereas the Mg/Ca–SST record shows slightly lower values.

The $U^{k'}_{37}$-SST records in the western Mediterranean Sea have been interpreted to represent annual mean SST (i.e. Cacho et al., 1999a; Martrat et al., 2004) but seasonal variations in alkenone production could play an important role in the $U^{k'}_{37}$-SST values (Rodrigo-Gámiz et al., 2014). Considering that during the summer months the Mediterranean Sea is a very stratified and oligotrophic sea, reduced alkenone production during this season could be expected (Ternois et al., 1996; Sicre et al., 1999; Bárcena et al., 2004; Versteegh et al., 2007; Hernández-Almeida et al., 2011). This observation is supported by results from sediment traps located in the GoL showing very low coccolith fluxes during the summer months (Rigual-Hernández et al., 2013), while they exhibit higher values during autumn, winter, and spring, reaching maximum fluxes at the end of the winter season, during SST minima. In contrast, high fluxes of *G. bulloides* are almost restricted to the upwelling spring signal, when coccolith fluxes have already started to decrease (Rigual-Hernández et al., 2012, 2013). This different growth season can explain the proxy bias in the SST reconstructions, with more smoothed alkenone-SST signals.

Both Mg/Ca–SST and $U^{k'}_{37}$-SST records show consistent cooling trends of about -0.5 °C kyr^{-1} during the studied period (2700 years), which is consistent with the recent 2kyr global reconstruction (McGregor et al., 2015). The recorded cooling since the RP SST maxima (~200CE) is more pronounced in the Mg/Ca–SST (-1.7 to -2.0 °C kyr^{-1}) than in the alkenone signal (-1.1 °C kyr^{-1}). These coolings are larger than those

estimated in the global reconstruction (McGregor et al., 2015) for the last 1200 years (average anomaly method 1: -0.4 to -0.5 °C kyr^{-1}). It should be noted that the global reconstruction includes alkenone–SST from MIN cores (data published in Moreno et al., 2012).

The detailed comparison of the centennial SST variability recorded by both proxy stacks consistently indicates a puzzling antiphase. Although the main trends are -31 consistently parallel in both alkenone and Mg/Ca proxies (r = 0.5; p value = 0) as observed in other regions, short-term variability appears to have an opposite character. Statistical analysis of these differences examined by means of Welch's test indicates that the null hypothesis (means are equal) can be discarded at the 5% error level: $t_{observed}$ (12.446) > $t_{critical}$ (1.971). This a priori unexpected proxy difference outlines the relevance of the seasonal variability for climate evolution and suggests that extreme winter coolings were followed by more rapid and intense spring warmings. Nevertheless, regarding the low amplitude of several of these oscillations, often close to the proxy error, this observation needs to be supported by further constraints as a solid regional feature.

3.1.7 Discussion

Climate patterns during the last 2.7 kyr

The SST changes in the Minorca region have implications for the surface air mass temperature and moisture source regions that could influence on air mass trajectories and ultimately precipitation patterns in the western Mediterranean region (Millán et al., 2005; Labuhn et al., 2015). Recent observations have identified SST as a key factor in the development of torrential rain events in the western Mediterranean Basin (Pastor et al., 2001), constituting a potential source of mass instability that transits over these waters (Pastor, 2012). In this context, the combined SST and $\delta^{18}O_{sw}$ records can provide information on the connection between thermal changes and moisture export from the central-western Mediterranean Sea during the last 2.7 kyr.

The oldest period recorded in our data is the so-called Talaiotic Period (TP), which corresponds to the ages of antiquity such as the period of ancient Greece in other geographic areas. Both Mg/Ca-SST and alkenone-SST records are consistent in showing a general cooling trend from ~500 BCE and reaching minimum values by the

end of the period (~120 BCE; Fig. 3.6a–b). Very few other records are available from this time period, which make comparisons of these trends at regional scale difficult.

One of the most prominent features in the two SST reconstructions, particularly in the Mg/Ca–SST stack, is the warm SST that predominated during the second half of the RP (150–400 CE). The onset of the RP was relatively cold and a ~2 °C warming occurred during the first part of this period. This SST evolution from colder to warmer conditions during the RP is consistent with the isotopic record of the Gulf of Taranto (Taricco et al., 2009) and peat reconstructions from north-west Spain (Martínez-Cortizas et al., 1999), and to some extent with SST proxies in the south- eastern Tyrrhenian Sea (Lirer et al., 2014). However, none of these records indicates that the RP was the warmest period of the last 2 kyr. Other records from higher latitudes such as Greenland (Dahl-Jensen et al., 1998), and northern Europe (Esper et al., 2014), North Atlantic Ocean (Bond et al., 2001; Sicre et al., 2008), as well as speleothem records from northern Iberia (Martín-Chivelet et al., 2011) and even the multiproxy PAGES 2K reconstruction from Europe, suggest a rather warmer early RP than late RP and, again, none of these records highlights the Roman times as the warmest climate period of the last 2 kyr. Consequently, these very warm RP conditions recorded in the Minorca Mg/Ca–SST stack seem to have a regional character and suggest that climate evolution during this period followed a rather heterogeneous thermal response along the European continent and surrounding marine regions.

Moreover, the observed $\delta^{18}O_{sw}$ stack of the RP suggests an increase in the E-P ratio (Fig. 3.6a) during this period, which has also been observed in some nearby regions like the Alps (Holzhauser et al., 2005; Joerin et al., 2006). In contrast, a lake record from southern Spain indicates relatively high water levels when the $\delta^{18}O_{sw}$ stack indicates the maximum in E-P ratio (Martín-Puertas et al., 2008). This information is not necessarily contradictory, since enhanced E-P balance in the Mediterranean could be balanced out by enhanced precipitation in some of the regions, but more detailed geographical information is required to interpret these proxy records from distinct areas.

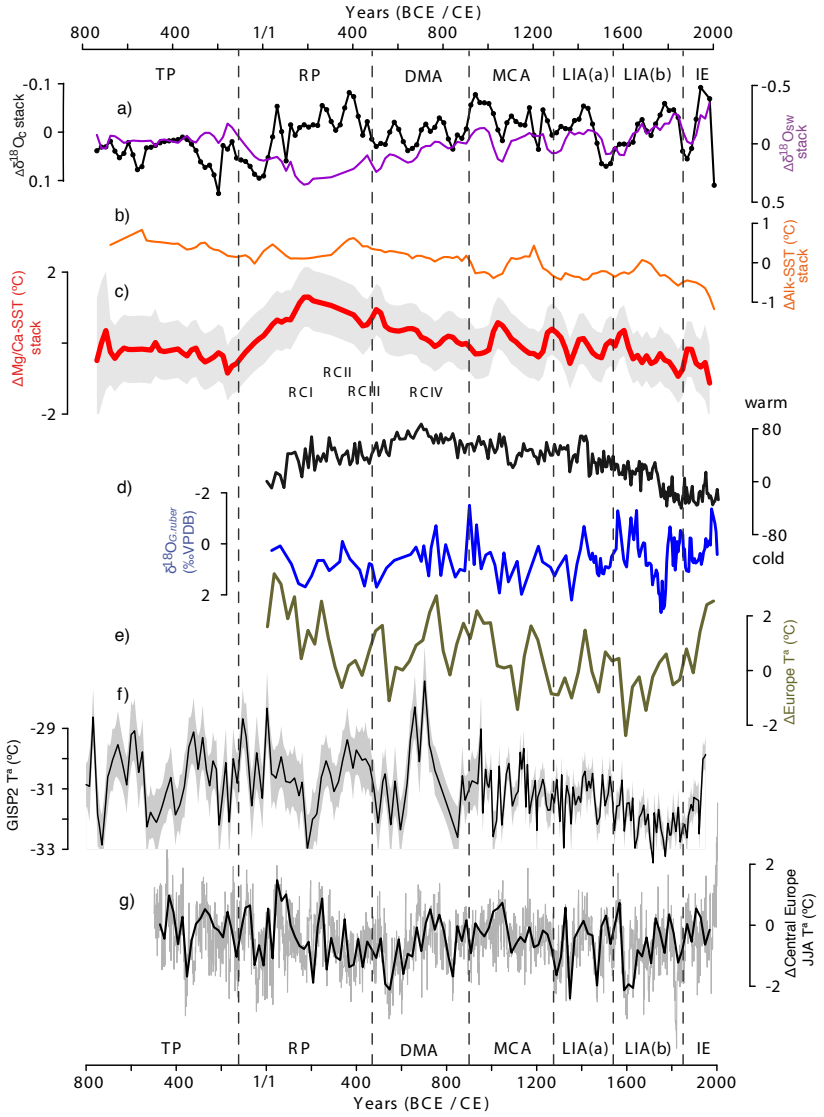

Figure 3.6. Temperature and isotope anomaly records from Minorca (this study) and data from other regions. **(a)** $\delta^{18}O_C$ and $\delta^{18}O_{SW}$ (‰ SMOW) Minorca stacks; **(b)** alkenone–SST anomaly Minorca stack; **(c)** Mg/Ca–SST anomaly Minorca stack; **(d)** warm and cold phases and $\delta^{18}O_{G.ruber}$ recorded by planktonic foraminifera from the southern Tyrrhenian composite core, with RCI to RCIV showing Roman cold periods (Lirer et al., 2014); **(e)** 30-year averages of the PAGES 2k Network (2013) Europe anomaly temperature reconstruction; **(f)** Greenland snow surface temperature (Kobashi et al., 2011); and **(g)** central Europe summer anomaly temperature reconstruction in central Europe (Büntgen et al., 2011). Period DMA (Dark Middle Ages) correspond to EMA (Early Middle Ages).

After the RP, during the whole EMA and until the MCA, the Mg/Ca–SST stack shows a cooling of ~1 °C (0.2 °C 100 yr^{-1}), which is 0.3 °C in the case of the alkenone-SST stack and the E-P rate decreases. This trend contrasts with the general warming trend interpreted from the speleothem records of northern Iberia (Martín-Chivelet et al., 2011) or the transition towards drier conditions observed in Alboran records (Nieto-Moreno et al., 2011). However, SST proxies from the Tyrrhenian Sea show a cooling trend after the second half of the EMA and the Roman IV cold/dry phase (Lirer et al., 2014) that can be tentatively correlated with our SST records (Fig. 3.6). This cooling phase is also

documented in the $\delta^{18}O_{G.ruber}$ record of the Gulf of Taranto (Grauel et al., 2013). These heterogeneities in the signals from the different proxies and regions illustrate the difficulties in characterizing the climate variability during these short periods and reinforce the need for a better geographical coverage of individual proxies.

The medieval period is usually described as a very warm period in numerous regions in the Northern Hemisphere (Hughes and Diaz, 1994; Mann et al., 2008; Martín-Chivelet et al., 2011), but this interpretation is challenged by an increasing number of studies (i.e. Chen et al., 2013). The Minorca SST stacks also show the occurrence of significant temperature variability that does not reflect a specific warm period within the last 2 kyr (Fig. 3.6). An important warming event is observed at ~1000 CE, followed by a later cooling with minimum values at about 1200 CE (Fig. 3.6). Higher temperature variability is found in Greenland records (Kobashi et al., 2011), while an early warm MCA and posterior cooling is also observed in temperature reconstructions from central Europe (Büntgen et al., 2011) and in the European multiproxy 2 kyr stack of the PAGES 2K Consortium (2013). Nevertheless, all these proxies agree in indicating overall warmer temperatures during the MCA than during the LIA. At the MCA–LIA transition, a progressive cooling and a change in oscillation frequency before and after the onset of LIA are recorded. This transition is consistent with the last rapid cli- mate change (RCC) described in Mayewski et al. (2004).

In the context of the Mediterranean Sea, the lake, marine, and speleothem records consistently agree in showing drier conditions during the MCA than during the LIA (Moreno et al., 2012; Chen et al., 2013; Nieto-Moreno et al., 2013; Wassenburg et al., 2013). Examination of the $\delta^{18}O_{sw}$ stack shows several oscillations during the MCA and LIA but no clear differentiation between these periods can be inferred from this proxy, indicating that reduced precipitation also involved reduced evaporation in the basin and that the E-P balance recorded by the $\delta^{18}O_{sw}$ proxy was not modified. The centennial-scale variability found in both the Mg/Ca-SST and $\delta^{18}O_{sw}$ stack reveals that higher E-P conditions existed during the warmer intervals (Fig. 3.6a and c).

According to the Mg/Ca-SST stack, the LIA stands out as a period of high thermal variability in which two substages can be differentiated, a first involving large SST oscillations and warm average temperatures (LIAa) and a second substage with short oscillations and cold average SST (LIAb). We suggest that the LIAa interval could be

linked to the Wolf and Spörer solar minima and that the LIAb corresponds to Maunder and Dalton cold events, in agreement with previous observations (i.e. Vallefuoco et al., 2012).

These two LIA substages are also present in the Greenland record (Kobashi et al., 2011). The intense cooling drop (0.8 °C 100 yr^{-1}) at the onset of the LIAb is in agreement with the suggested coolings of 0.5 and 1 °C in the Northern Hemisphere (i.e. Matthews and Briffa, 2005; Mann et al., 2009). These two steps within the LIA are better reflected in the Mg/Ca-SST stack than in the alkenone-SST stack. This is also the case of the alkenone records in the Alboran Sea (Nieto-Moreno et al., 2011), which may result from smaller SST variability of the alkenone proxies.

In terms of humidity, the LIA represents a period of increased runoff in the Alboran record (Nieto-Moreno et al., 2011). Available lake level reconstructions from southern Spain also show progressive increases after the MCA, reaching maximum values during the LIAb (Martín-Puertas et al., 2008). Different records of flood events in the Iberia Peninsula also report a significant increase in extreme events during the LIA (Barriendos and Martin-Vide, 1998; Benito et al., 2003; Moreno et al., 2008). These conditions are consistent with the described enhanced storm activity over the GoL in this period (Sabatier et al., 2012), explaining the enhanced humidity transport towards the Mediterranean Sea as a con- sequence of the reduced E-P ratio observed in the $\delta^{18}O_{sw}$, particularly during the LIAb (Fig. 3.6a).

The end of the LIA and onset of the IE is marked with a warming phase of about 1 °C in the Mg/Ca-SST stack and a lower-intensity change in the alkenone-SST stack. This initial warm climatic event is also documented in other Mediterranean regions (Taricco et al., 2009; Marullo et al., 2011; Lirer et al., 2014) and Europe (PAGES 2K Consortium, 2013), which is coincident with a total solar irradiance (TSI) enhancement after Dalton minima. The two Minorca SST stacks show a cooling trend by the end of the record, which does not seem to be consistent with the instrumental atmospheric records. In the western Mediterranean, warming has been registered in two main phases: from the mid-1920s to 1950s and from the mid-1970s onwards (Lionello et al., 2006). The Minorca stacks do not show this warming, but they do not cover the second warming period. Nevertheless, the instrumental data from the beginning of the 20th

century in the western Mediterranean do not display any warming trends before the 1980s (Vargas-Yáñez et al., 2010).

Climate forcings mechanisms

The general cooling trend observed in both Mg/Ca-SST and alkenone-SST stacks shows a good correlation with the evolution of summer insolation in the North Hemisphere, which dominates the present annual insolation balance ($r = 0.2$ and 0.8, p value ≤ 0.007, respectively; Fig. 3.7). In numerous records from the Northern Hemisphere (i.e. Wright, 1994; Marchal et al., 2002; Kaufman et al., 2009; Moreno et al., 2012), this external forcing has also been proposed to control major SST trends during the Holocene period. In addition, summer insolation seems to have had significant influence in the decreasing trend of the isotope records during the whole period spanned ($r = 0.4$, p value = 0), as has been suggested in, for example, Ausín et al. (2015). In any case, a different forcing mechanism needs to account for the centennial-scale variability of the records, e.g. increased volcanism in the last millennium (McGregor et al., 2015), although no significant correlations have been observed between our records and volcanic reconstructions (Gao et al., 2008).

Solar variability has frequently been proposed the to be a primary driver of the Holocene millennial-scale variability (i.e. Bond et al., 2001). Several oscillations observed in the TSI record (Fig. 3.7a), but the correlations with the Mg/Ca-SST and alkenone-SST stacks are low, since most of the major TSI drops do not correspond to SST cold events. However, some correlation is observed between TSI and alkenone SSTs ($r = 0.5$, p value = 0). In any case, TSI does not seem to be the main driver of the centennial-scale SST variability in the studied records.

One of the major drivers of the Mediterranean interannual variability in the Mediterranean region is the NAO (Hurrell, 1995; Lionello and Sanna, 2005; Mariotti, 2011). Positive NAO indexes are characterized by high atmospheric pressure over the Mediterranean Sea and increases of the E-P balance (Tsimplis and Josey, 2001).

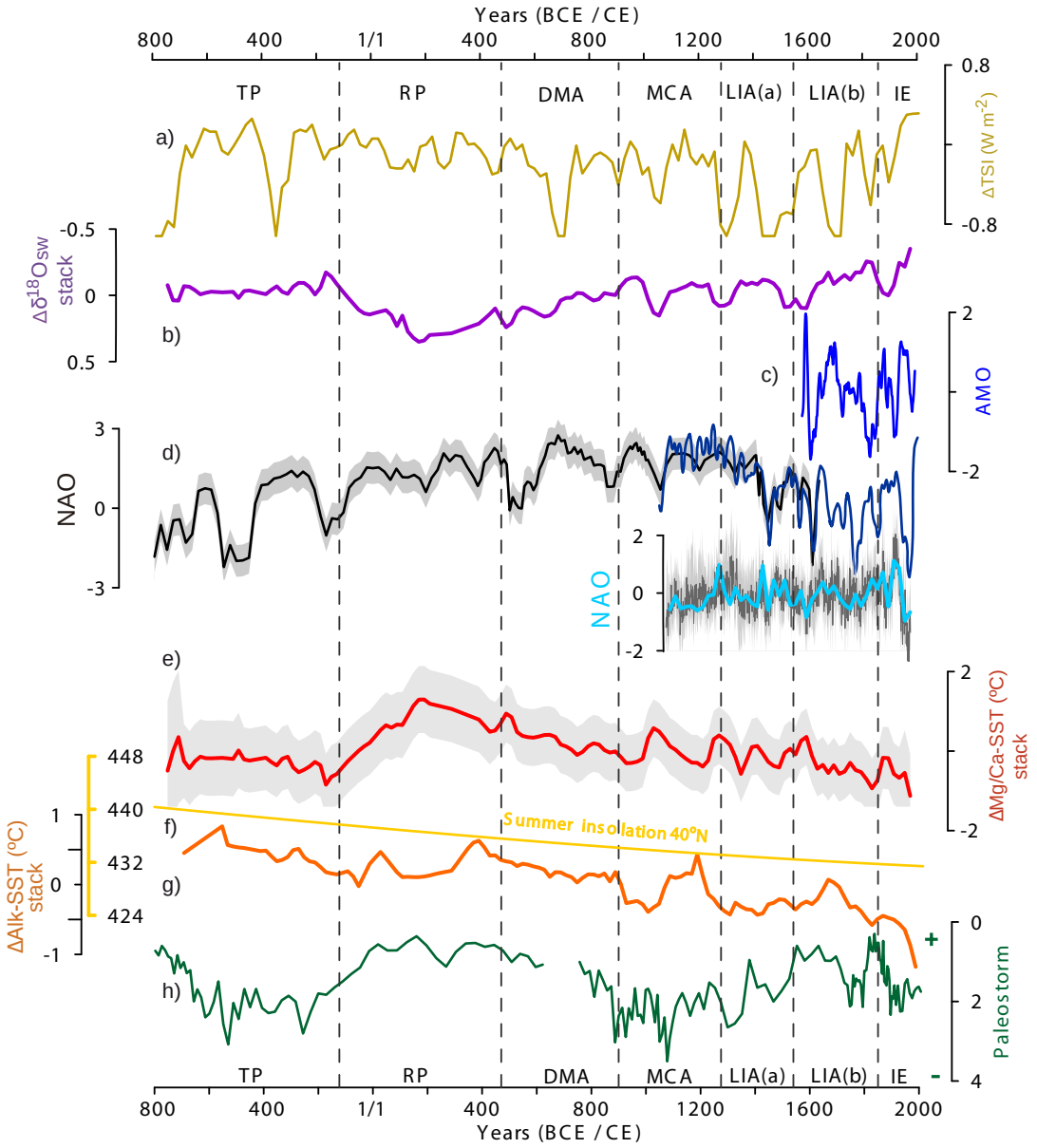

Figure 3.7. Temperature and isotope anomaly records from Minorca (this study) and data from other regions and with external forcings: **(a)** total solar irradiance (Steinhilber et al., 2009, 2012), **(b)** $\delta^{18}O_{SW}$ Minorca stacks, **(c)** Atlantic Multidecadal Oscillation (AMO; Gray et al., 2004), **(d)** North Atlantic Oscillation (NAO) reconstructions (Olsen et al., 2012; Trouet et al., 2009; and, for the last millennium, Ortega et al., 2015), **(e)** Mg/Ca-SST anomaly Minorca stack, **(f)** summer insolation at 40 N (Laskar et al., 2004), **(g)** alkenone-SST anomaly Minorca stack, and **(h)** palaeostorm activity in the Gulf of Lion (Sabatier et al., 2012). Period DMA (Dark Middle Ages) correspond to EMA (Early Middle Ages).

During these positive NAO periods, winds over the Mediterranean tend to be deviated towards the north, overall salinity increases, and formation of dense deep water masses is reinforced as the water exchange through the Corsica Channel is higher and the arrival of northern storm waves decreases (Wallace and Gutzler, 1981; Tsimplis and Baker, 2000; Lionello and Sanna, 2005). The effect of NAO on Mediterranean temperatures is more ambiguous. SST changes during the last decades do not show

significant variability with NAO (Luterbacher et al., 2004; Mariotti, 2011), although some studies suggest an opposite response between the two basins, with cooling responses in some eastern basins and warmings in the western basin during positive NAO conditions (Demirov and Pinardi, 2002; Tsimplis and Rixen, 2002). Although still controversial, some NAO reconstructions on proxy records are starting to become available for the period studied (Lehner et al., 2012; Olsen et al., 2012; Trouet et al., 2012; Ortega et al., 2015). The last millennium is the best-resolved period, and it allows a direct comparison with our data to evaluate the potential link to NAO.

The correlations between our Minorca temperature stacks with NAO reconstructions (Fig. 2.7) are relatively low in the case of Mg/Ca-SST ($r = 0.3$, p value ≤ 0.002) and not significant in the alkenone stack, indicating that this forcing is probably not the driver of the main trends in these records, al- though several uncertainties still exist about the long NAO reconstructions (Lehner et al., 2012). If detailed analysis is performed focussing on the more intense negative NAO phases (Fig. 3.8), they mostly appear to correlate with cooling phases in the Mg/Ca stack. The frequency of these negative events is particularly high during the LIA, and mostly during its second phase (LIAb), when the coldest intervals of our SST stacks were observed. When several different proxy last century records of annual resolution, tested with some model assimilations (Ortega et al., 2015), are compared with the last NAO reconstruction, the observed correlations with $\delta\,^{18}O_{sw}$ are not statistically significant. However, the Welch's test results do not allow for the null hypothesis to be discarded. A coherent pattern of NAO variability with our $\delta\,^{18}O_{sw}$ reconstruction, with high (low) isotopic values mainly dominating during positive (negative) NAO phases, can be observed in the last centuries (Fig. 2.8). This pattern is consistent with the described E-P increase during high NAO phases described for the last decades (Tsimplis and Josey, 2001). The SST stacks also suggest some degree of correlation between warm SST and high NAO values (Fig. 3.7), but a more coherent picture is observed when the SST records are compared to the Atlantic Multidecadal Oscillation (AMO) reconstruction: warm SST dominated during high AMO values (Fig. 3.9). This pattern of salinity changes related to NAO and SST to AMO has also been described in climate studies encompassing the last decades (Mariotti, 2011; Guemas et al., 2014) and confirms the complex but tight response of the Mediterranean to atmospheric and marine changes over the North Atlantic Ocean.

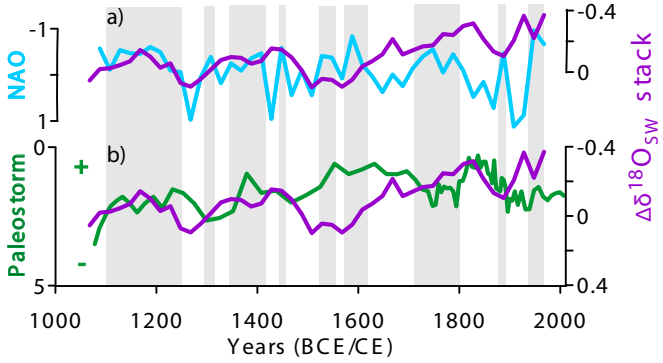

Figure 3.8. $^{18}O_{SW}$ Minorca stack (‰ SMOW) during the last mil- lennium (age is expressed in years CE) plotted with **a)** NAO re- construction (Ortega et al., 2015) and **b)** palaeostorm activity in the Gulf of Lion (Sabatier et al., 2012). Notice that the NAO axis is on a descending scale. Grey vertical bars represent negative NAO phases.

The pattern of high $\delta^{18}O_{sw}$ at dominant positive NAO corresponds to a reduction in the humidity transport over the Mediterranean region as a consequence of high atmospheric pressure (Tsimplis and Josey, 2001). Accordingly, several periods of increased/decreased storm activity in the GoL (Fig. 3.8; Sabatier et al., 2012) correlate with low/high values in the $\delta^{18}O_{sw}$, indicating that, during negative NAO conditions, northern European storm waves arrived more frequently in the Mediterranean Sea (Lionello and Sanna, 2005), contributing to the reduction of the E-P balance (Fig. 3.8). Our data also indicate that, during these enhanced storm periods, cold SST conditions dominated in the region as previously suggested (Sabatier et al., 2012). Nevertheless, not all the NAO oscillations had identical expression in the compared records, which is coherent with recent observations indicating that negative NAO phases may correspond to different atmospheric configuration modes and impact differently over the western Mediterranean Sea (Sáez de Cámara et al., 2015). Regarding the lower part of the record, the maximum SST temperatures and $\delta^{18}O_{sw}$ recorded during the RP (100–300 CE) may suggest the occurrence of persistent positive NAO conditions, which would also be consistent with a high pressure-driven drop in relative sea level as has been reconstructed in the north-western Mediterranean Sea (southern France, 40 ± 10 cm; Morhange et al., 2013).

It is interesting to note that during the EMA a pronounced and intense cooling event is recorded in the Mg/Ca–SST stack at about 500 CE. Several references document in the scientific literature the occurrence of a dimming of the sun at 536–537CE (Stothers, 1984). This event, based on ice core records, has been linked to a tropical volcanic eruption (Larsen et al., 2008). Tree-ring data reconstructions from Europe and also historical documents indicate the persistence during several years (536–550 CE) of what is described as the most severe cooling across the Northern Hemisphere during the last

two millennia (Larsen et al., 2008). Despite the limitations derived from the resolution of our records, the Mg/Ca–SST stack record may have caught this cooling, which would prove the robustness of our multiproxy age models (see 2.9 for age model development).

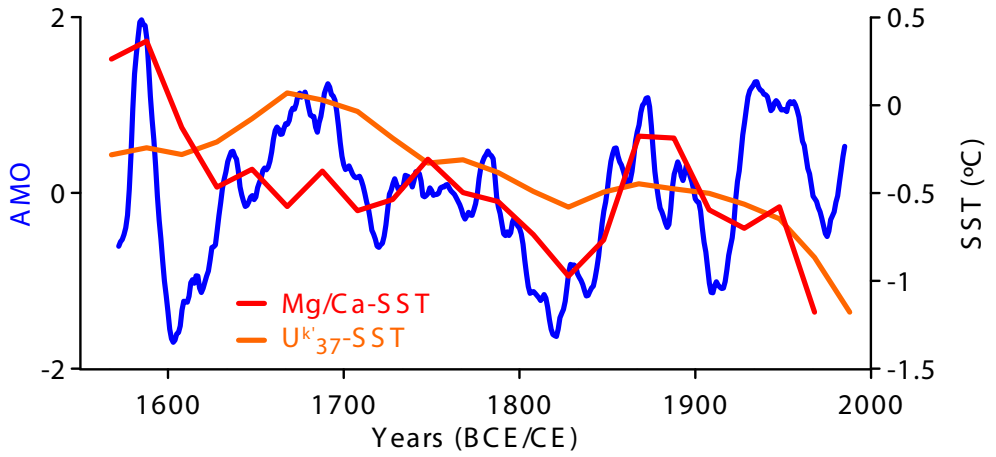

Figure 3.9. Mg/Ca-SST and alkenone–SST Minorca anomaly stacks during the last centuries plotted with AMO reconstruction (Gray et al., 2004).

3.1.8 Summary and conclusions

The review of new core-top data of *G. bulloides* Mg/Ca ratios from the central-western Mediterranean Sea together with previous published data support a consistent temperature sensitivity for the Mediterranean samples and allows for the previous calibrations to be refined. The recorded Mg/Ca–SST signal from *G. bulloides* is interpreted to re- flect April–May conditions from the upper 40 m layer. In contrast, the alkenone–SST estimations are interpreted to in- tegrate a more annually averaged signal, although they are biased toward the winter months since primary productivity during the summer months in the Mediterranean Sea is extremely low. The averaged signal of the alkenone–SST records may explain its relatively smoothed oscillations in comparison to the Mg/Ca–SST records.

After careful construction of a common chronology for the studied multicores, based on several chronological tools, the individual proxy records have been grouped in an anomaly-stacked record to allow a better identification of the main patterns and structures. Both Mg/Ca–SST and alkenone stacks show a consistent cooling trend over the studied period. Since the RP maximum, this cooling has ranged between −1.7 and −2.0ºC kyr^{-1} in the Mg/Ca record and is less pronounced in the alkenone record (−1.1 ºC kyr^{-1}). This cooling trend is consistent with the general lowering of summer insolation.

The overall cooling is punctuated by several SST oscillations at centennial timescales, which represent maximum SST during most of the RP; a progressive cooling during the DMA; a pronounced variability during the MCA with two intense warming phases reaching warmer SST than during the LIA; and a very unstable and rather cold LIA, with two substages–a first one with larger SST oscillations and warmer average temperatures (LIAa) and a second one with shorter oscillations and colder average SST (LIAb). The described two stages within the LIA are clearer in the Mg/Ca–SST stack than in the alkenone–SST record. Comparison of Mg/Ca–SST and $\delta^{18}O_{sw}$ stacks indicates that warmer intervals have been accompanied by higher evaporation–precipitation (E–P) conditions. The E–P balance oscillations over each defined climatic period during the last 2.7 kyr suggest variations in the thermal change and moisture export patterns in the central-western Mediterranean.

Comparison of the Minorca SST stacks with other European palaeoclimatic records suggests a rather heterogeneous thermal response along the European continent and surrounding marine regions. Comparison of the new Mediterranean records with the reconstructed variations in TSI does not support a clear connection with this climate forcing. Nevertheless, changes in the NAO and AMO seem to have in fluenced the regional climate variability. The negative NAO phases correlate mostly with cooling phases of the Mg/Ca stack, although this connection is complex and apparently better defined during the most intense negative phases. Focussing on the last 1 kyr, when NAO reconstructions are bet- ter constrained, provides a more consistent pattern, with cold and particularly fresher $\delta^{18}O_{sw}$ values (reduced E–P balance) during negative NAO phases. Our results are consistent with enhanced southward transport of European storm tracks dur- ing this period and previous reconstructions of storm activity in the GoL. Nevertheless, the SST stacks show a more tied relation to AMO during the last four centuries (the available period of AMO reconstructions) in which warm SST dom- inated during high AMO values. This evidence supports a close connection between Mediterranean and North Atlantic climatology over the last 2 kyr.

Acknowledgements. Cores MINMC06 were recovered by the HERMES 3 cruise in 2006 on R/V Thethys II and HER-MC-MR3 cores were collected by the HERMESIONE expedition onboard R/V Hespérides in 2009. This research was financially supported by OPERA (CTM2013-48639-C2-1-R) and Consolider-Redes

(CTM2014-59111-REDC). We thank Generalitat de Catalunya Grups de Recerca Consolidats for grant 2009 SGR 1305 to GRC Geociències Marines. The Project of Strategic Interest NextData PNR 2011–2013 (www.nextdataproject.it) also collaborated in the financing. We are grateful to M. Guart (Dept. de Dinàmica de la Terra i de l'Oceà, Universitat de Barcelona), M. Romero, T. Padró and J. Perona (Serveis Cientifico-Tècnics, Universitat de Barcelona), J. M. Bruach (Departament de Física, Universitat Autònoma de Barcelona), and B. Hortelano, Y. Gonzalez-Quinteiro, and I. Fernández (Institut de Diagnosi Ambiental i Estudis de l'Aigua, CSIC, Barcelona) for their help with the laboratory work; to D. Amblàs for his collaboration with the artwork of maps; and to Paleoteam for the unconditional support. E. Garcia-Solsona, S. Giralt, and M. Blaauw are acknowledged for their help. We also acknowledge the guest editor and anonymous reviewers for their comments, which contributed to improving this paper. Belen Mar- trat acknowledges funding from CSIC-Ramon y Cajal post-doctoral programme RYC-2013-14073. Mercè Cisneros benefited from a fellowship of the University of Barcelona. Leopoldo D. Pena acknowledges support from the Ramón y Cajal programme (MINECO, Spain). Isabel Cacho thanks the ICREA-Academia programme from the Generalitat de Catalunya.

3.1.9 References

Abrantes, F., Lebreiro, S., Rodrigues, T., Gil, I., Bartels-Jónsdóttir, H., Oliveira, P., Kissel, C., and Grimalt, J. O.: Shallow-marine sediment cores record climate variability and earthquake activity off Lisbon (Portugal) for the last 2000 years, Quaternary Sci. Rev., 24, 2477–2494, doi:10.1016/j.quascirev.2004.04.009, 2005.

Anand, P., Elderfield, H., and Conte, M. H.: Calibration of Mg/Ca thermometry in planktonic foraminifera from a sediment trap time series, Paleoceanography, 18, 1050, doi:10.1029/2002PA000846, 2003.

André, G., Garreau, P., Garnier, V., and Fraunié, P.: Modelled variability of the sea surface circulation in the North-western Mediterranean Sea and in the Gulf of Lions, Ocean Dynam., 55, 294–308, 2005.

Appleby, P. G. and Oldfield, F.: Application of Lead-210 to Sedimentation Studies, Clarendon Press, Oxford, Chapt. 21, 731– 778, 1992.

Ausín, B., Flores, J. A., Sierro, F. J., Cacho, I., Hernández- Almeida, I., Martrat, B., and Grimalt, J. O.: Atmospheric pat- terns driving Holocene productivity in the Alboran Sea (West- ern Mediterranean): a multiproxy approach, Holocene, 25, 1–13, doi:10.1177/0959683614565952, 2015.

Bárcena, M. A., Flores, J. A., Sierro, F. J., Pérez-Folgado, M., Fabres, J., Calafat, A., and Canals, M.: Planktonic response to main oceanographic changes in the Alboran Sea (Western Mediterranean) as documented in sediment traps and surface sediments, Mar. Micropaleontol., 53, 423–445, doi:10.1016/j.marmicro.2004.09.009, 2004.

Barker, S., Greaves, M., and Elderfield, H.: A study of cleaning procedures used for foraminiferal Mg/Ca paleothermometry, Geochem. Geophy. Geosy., 4, 8407, doi:10.1029/2003GC000559, 2003.

Barker, S., Cacho, I., Benway, H., and Tachikawa, K.: Plank- tonic foraminiferal Mg/Ca as a proxy for past oceanic tem- peratures: a methodological overview and data compilation for the Last Glacial Maximum, Quaternary Sci. Rev., 24, 821–834, doi:10.1016/j.quascirev.2004.07.016, 2005.

Barriendos, M. and Martin-Vide, J.: Secular climatic oscillations as indicated by catastrophic floods in the spanish mediterranean coastal area (14th–19th centuries), Climatic Change, 38, 473– 491, 1998.

Bé, A. W. H. and Hutson, W. H.: Ecology of planktonic foraminifera and biogeographic patterns of life and fossil assemblages in the Indian Ocean, Micropaleontology, 23, 369–414, 1977.

Bemis, B. E., Spero, H. J., Bijma, J., and Lea, D. W.: Reevaluation of the oxygen isotopic composition of planktonic foraminifera: Experimental results and revised paleotemperature equations, Paleoceanography, 13, 150–160, doi:10.1029/98PA00070, 1998.

Benito, G., Sopeña, A., Sánchez-Moya, Y., Machado, M. J., and Pérez-González, A.: Palaeoflood record of the Tagus River (Cen- tral Spain) during the Late Pleistocene and Holocene, Quaternary Sci. Rev., 22, 1737–1756, doi:10.1016/S0277-3791(03)00133-1, 2003.

Béthoux, J. P.: Mean water fluxes across sections in the Mediter- ranean Sea, evaluated in the basis of water and salt budgets and of observed salinities, Oceanol. Acta, 3, 79–88, 1980.

Bond, G., Kromer, B., Beer, J., Muscheler, R., Evans, M. N., Showers, W., Hoffmann, S., Lottibond, R., Hajdas, I., and Bonani, G.: Persistent solar influence on North At- lantic climate during the holocene, Science, 294, 2130–2136, doi:10.1126/science.1065680, 2001.

Bosc, E., Bricaud, A., and Antoine, D.: Seasonal and interannual variability in algal biomass and primary production in the Mediterranean Sea, as derived from 4 years of SeaW- iFS observations, Global Biogeochem. Cy., 18, 2003–2034, doi:10.1029/2003GB002034, 2004.

Büntgen, U., Tegel, W., Nicolussi, K., McCormick, M., Frank, D., Trouet, V., Kaplan, J. O., Herzig, F., Heussner, K. U., Wanner, H., Luterbacher, J., and Esper, J.: 2500 years of European cli- mate variability and human susceptibility, Science, 331, 578–82, doi:10.1126/science.1197175, 2011.

Cacho, I., Pelejero, C., Grimalt, J. O., Calafat, A., and Canals, M.: C37 alkenone measurements of sea surface temperature in the Gulf of Lions (NW Mediterranean), Org. Geochem., 30, 557– 566, 1999a.

Cacho, I., Grimalt, J. O., Pelejero, C., Canals, M., Sierro, F. J., Flores, J. A., and Shackleton, N.: Dansgaard-Oeschger and Heinrich event imprints in Alboran Sea paleotemperatures, Paleoceanog- raphy, 14, 698–705, 1999b.

Cacho, I., Grimalt, J. O., Sierro, F. J., Shackleton, N., and Canals, M.: Evidence for enhanced Mediterranean thermohaline circula- tion during rapid climatic coolings, Earth Planet. Sc. Lett., 183, 417–429, doi:10.1016/S0012-821X(00)00296-X, 2000.

Cacho, I., Grimalt, J., Canals, M., Sbaffi, L., Shackleton, N. J., Schönfeld, J., and Zahn, R.: Variability of the western Mediter- ranean Sea surface temperature during the last 25 000 years ans its connection with the Northern Hemisphere climatic changes, Paleoceanography, 16, 40–52, 2001.

Cacho, I., Shackleton, N., Elderfield, H., Sierro, F. J., and Grimalt, J. O.: Glacial rapid variability in deep-water temperature and ^{18}O from the Western Mediterranean Sea, Quaternary Sci. Rev., 25, 3294–3311, doi:10.1016/j.quascirev.2006.10.004, 2006.

Canals, M., Puig, P., De Madron, X. D., Heussner, S., Palanques, A., and Fabres, J.: Flushing submarine canyons, Nature, 444, 354– 357, doi:10.1038/nature05271, 2006.

Chen, L., Zonneveld, K. A. F., and Versteegh, G. J. M.: The Holocene Paleoclimate of the Southern Adriatic Sea re- gion during the “Medieval Climate Anomaly” reflected by organic walled dinoflagellate cysts, Holocene, 23, 645–655, doi:10.1177/0959683612467482, 2013.

Cléroux, C., Cortijo, E., Anand, P., Labeyrie, L., Bassinot, F., Caillon, N., and Duplessy, J. C.: Mg/Ca and Sr/Ca ra- tios in planktonic foraminifera: proxies for upper water col- umn temperature reconstruction, Paleoceanography, 23, PA3214, doi:10.1029/2007PA001505, 2008.

Combourieu Nebout, N., Turon, J., Zahn, R., Capotondi, L., Lon- deix, L., and Pahnke, K.: Enhanced aridity and atmospheric high-pressure stability over the western Mediterranean during the North Atlantic cold events of the past 50 k.y., Geology, 30, 863– 866, 2002.

Combourieu Nebout, N., Peyron, O., Dormoy, I., Desprat, S., Beau- douin, C., Kotthoff, U., and Marret, F.: Rapid climatic variability in the west Mediterranean during the last 25 000 years from high resolution pollen data, Clim. Past, 5, 503–521, doi:10.5194/cp- 5-503-2009, 2009.

Conte, M. H., Sicre, M. A., Rühlemann, C., Weber, J. C., Schulte, S., Schulz-Bull, D., and Blanz, T.: Global temperature calibration of the alkenone unsaturation index (U^{K^0}) in surface waters and comparison with surface sediments, Geochem. Geophy. Geosy., 7, Q02005, doi:10.1029/2005GC001054, 2006.

Coplen, T.: New guidelines for reporting stable hydrogen, carbon, and oxygen isotope-ratio data, Geochim. Cosmochim. Ac., 60, 3359–3360, 1996.

Corella, J. P., Moreno, A., Morellón, M., Rull, V., Giralt, S., Rico, M. T., Pérez-Sanz, A., and Valero-Garcés, B. L.: Climate and human impact on a meromictic lake during the last 6000 years (Montcortés Lake, Central Pyrenees, Spain), J. Palaeolimnol., 46, 351–367, 2011.

Craig, H.: The measurement of oxygen isotope paleotemperatures, in: Stable Isotopes in Oceanographic Studies and Paleotem- peratures, edited by: Tongiorgi, E., Consiglio Nazionale delle Ricerche, Laboratorio di Geologia Nucleare, Pisa, 1–24, 1965.

Dahl-Jensen, D., Mosegaard, K., Gundestrup, N., Clow, G. D., Johnses, S. J., Hansen, A. W., and Balling, N.: Past temperatures directly from the Greenland ice sheet, Science, 282, 268–271, 1998.

Demirov, E. and Pinardi, N.: Simulation of the Mediterranean Sea circulation from 1979 to 1993: Part I. The interannual variability, J. Marine Syst., 33–34, 23–50, 2002.

Di Bella, L., Frezza, V., Bergamin, L., Carboni, M. G., Falese, F., Mortorelli, E., Tarragoni, C., and Chiocci, F. L.: Foraminiferal record and high-resolution seismic stratigraphy of the Late Holocene succession of the submerged Ombrone River delta (Northern Tyrrhenian Sea, Italy), Quaternary Int., 328–329, 287– 300, 2014.

D'Ortenzio, F. and Ribera d'Alcalà, M.: On the trophic regimes of the Mediterranean Sea: a satellite analysis, Biogeosciences, 6, 139–148, doi:10.5194/bg-6-139-2009, 2009.

Eglinton, T. I., Conte, M. H., Eglinton, G., and Hayes, J. M.: Proceedings of a workshop on alkenone-based paleoceanographic indicators, Geochem. Geophy. Geosy., 2, 2000GC000122, doi:10.1029/2000GC000122, 2001.

Elderfield, H. and Ganssen, G.: Past temperature and ^{18}O of surface ocean waters inferred from foraminiferal Mg / Ca ratios, Nature, 405, 442–445, 2000.

Esper, J., Frank, D. C., Büntgen, U., Verstege, A., Luterbacher, J., and Xoplaki, E.: Long-term drought severity variations in Morocco, Geophys. Res. Lett., 34, L17702, doi:10.1029/2007GL030844, 2007.

Esper, J., Düthorn, E., Krusic, P. J., Timonen, M., and Büntgen, U.: Northern European summer temperature variations over the Common Era from integrated tree-ring density records, J. Qua- ternary Sci., 29, 487–494, doi:10.1002/jqs.2726, 2014.

Estrada, M., Vives, F., and Alcaraz, M.: Life and productivity in the open sea, in: Western Mediterranean, edited by: Margalef, R., Oxford, Pergamon Press, 148–197, 1985.

Fanget, A. S., Bassetti, M. A., Arnaud, M., Chioleau, J. F., Cossa, D., Goineau, A.,Fontanier, C., Buscail, R., Jouet, G., Maillet, G. M., Negri, A., Dennielou, B., and Berné, S.: Historical evolu- tion and extreme climate events during the last 400 years on the Rhone prodelta (NW Mediterranean), Mar. Geol., 346, 375–391, doi:10.1016/j.margeo.2012.02.007, 2013.

Ferguson, J. E., Henderson, G. M., Kucera, M., and Rickaby, R. E. M.: Systematic change of foraminiferal Mg / Ca ratios across a strong salinity gradient, Earth Planet. Sc. Lett., 265, 153–166, doi:10.1016/j.epsl.2007.10.011, 2008.

Fleitmann, D., Cheng, H., Badertscher, S., Edwards, R. L., Mudelsee, M., Gktürk, O. M., Fankhauser, A., Pickering, R., Raible, C. C., Matter, A., Kramers, J., and Tüysüz, O.: Timing and climatic impact of Greenland interstadials recorded in sta- lagmites from northern Turkey, Geophys. Res. Lett., 36, L19707, doi:10.1029/2009GL040050, 2009.

Fletcher, W. J. and Sánchez Goñi, M. F.: Orbital and sub-orbital- scale climate impacts on vegetation of the western Mediterranean basin over the last 48000 yr, Quaternary Res., 70, 451–464, 2008.

Fletcher, W. J., Debret, M., and Sanchez Goñi, M.: Mid-Holocene emergence of a low-frequency millennial oscillation in western Mediterranean climate: implications for past dynamics of the North Atlantic atmospheric westerlies, Holocene, 23, 153–166, doi:10.1177/0959683612460783, 2012.

Frigola, J.: Variabilitat climàtica ràpida a la conca occidental del Mediterrani: registre sedimentològic, PhD Thesis, Dept. of Stratigraphy, Paleontology and Marine Geosciences, University of Barcelona, Spain, 2012.

Frigola, J., Moreno, A., Cacho, I., Canals, M., Sierro, F. J., Flores, J. A., Grimalt, J. O., Hodell, D. A., and Curtis, J. H.: Holocene climate variability in the western Mediterranean region from a deepwater sediment record, Paleoceanography, 22, PA2209, doi:10.1029/2006PA001307, 2007.

Frigola, J., Moreno, A., Cacho, I., Canals, M., Sierro, F. J., Flores, J. A., and Grimalt, J. O.: Evidence of abrupt changes in Western Mediterranean Deep Water circulation during the last 50 kyr: a high-resolution marine record from the Balearic Sea, Quaternary Int., 181, 88–104, doi:10.1016/j.quaint.2007.06.016, 2008.

Frisia, S., Borsato, A., Preto, N., and McDermott, F.: Late Holocene annual growth in three Alpine stalagmites records the influence of solar activity and the North Atlantic Oscillation on winter cli- mate, Earth Planet. Sc. Lett., 216, 411–424, 2003.

Ganssen, G. M. and Kroon, D.: The isotopic signature of planktonic foraminifera from NE Atlantic surface sediments: implications for the reconstruction of past oceanic conditions, J. Geol. Soc. London, 157, 693–699, 2000.

Gao, C., Robock, A., and Ammann, C.: Volcanic forcing of cli- mate over the past 1500 years: An improved ice core-based index for climate models, J. Geophys. Res., 113, D23111, doi:10.1029/2008JD010239, 2008.

Giorgi, F.: Climate change hot-spots, Geophys. Res. Lett., 33, L08707, doi:10.1029/2006GL025734, 2006.

González-Álvarez, R., Bernárdez, P., Pena, L. D., Francés, G., Prego, R., Diz, P., and Vilas, F.: Paleoclimatic evolution of the Galician continental shelf (NW of Spain) during the last 3000 years: from a storm regime to present conditions, J. Mar. Syst., 54, 245–260, 2005.

Goudeau, M. L. S., Reichart, G. J., Wit, J. C., de Nooijer, L. J., Grauel, A. L., Bernasconi, S. M., and de Lange, G. J.: Seasonality variations in the Central Mediterranean during climate change events in the Late Holocene, Palaeogeogr. Palaeocl., 418, 304– 318, 2015.

Goy, J. L, Zazo, C., and Dabrio, C. J.: A beach-ridge progradation complex reflecting periodical sea-level and climate variability during the Holocene (Gulf of Almeria, Western Mediterranean), Geomorphology, 50, 251–268, 2003.

Gray, S. T., Graumlich, L. J., Betancourt, J. L., and Pederson, G. T.: A tree-ring based reconstruction of the Atlantic Multidecadal Oscillation since 1567 A. D., Geophys. Res. Lett., 31, L12205, doi:10.1029/2004GL019932, 2004.

Griggs, C., DeGaetano, A., Kuniholm, P., and Newton, M.: A regional high-frequency reconstruction of May–June precipitation in the north Aegean from oak tree rings, AD 1089–1989, Int. J. Climatol., 27, 1075–1089, 2007.

Grauel, A. L., Goudeau, M. L. S., de Lange, G. J., and Bernasconi, S. M.: Climate of the past 2500 years in the Gulf of Taranto, central Mediterranean Sea: a high-resolution climate reconstruc- tion based on ^{18}O and ^{13}C of *Globigerinoides ruber* (white), Holocene, 23, 1440–1446, doi:10.1177/0959683613493937, 2013.

Guemas, V., García-Serrano, J., Mariotti, A., Doblas-Reyes, F., and Caron, L. P.: Prospects for decadal climate prediction in the Mediterranean region, Q. J. Roy. Meteor. Soc., 141, 580–597, doi:10.1002/qj.2379, 2014.

Hernández-Almeida, I., Bárcena, M. Á., Flores, J. A., Sierro, F. J., Sánchez-Vidal, A., and Calafat, A.: Microplankton response to environmental conditions in the Alboran Sea (Western Mediter- ranean): one year sediment trap record, Mar. Micropaleontol., 78, 14–24, doi:10.1016/j.marmicro.2010.09.005, 2011.

Holzhauser, H., Magny, M., and Heinz, J.: Glacier and lake- level variations in west-central Europe over the last 3500 years, Holocene, 15, 789–801, 2005.

Hönisch, B., Allen, K. A., Lea, D. W., Spero, H. J., Eggins, S. M., Arbuszewski, J., DeMenocal, P., Rosenthal, Y., Russell, A. D., and Elderfield, H.: The influence of salinity on Mg / Ca in plank- tic foraminifers – evidence from cultures, core-top sediments and complementary ^{18}O, Geochim. Cosmochim. Ac., 121, 196– 213, 2013.

Hoogakker, B. A. A., Klinkhammer, G. P., Elderfield, H., Rohling, E. J., and Hayward, C.: Mg / Ca paleothermometry in high salinity environments, Earth Planet. Sc. Lett., 284, 583–589, doi:10.1016/j.epsl.2009.05.027, 2009.

Huang, S.: Merging information from different resources for new insights into climate change in the past and future, Geophys. Res. Lett., 31, 1–4, doi:10.1029/2004GL019781, 2004.

Hughes, M. K. and Diaz, H. F.: Was there a “Medieval warm period”, and if so, where and when?, Climatic Change, 26, 109– 142, 1994.

Hurrell, J. W.: Decadal Trends in the North Atlantic Oscillation: regional temperatures and precipitation, Science, 269, 676–679, doi:10.1126/science.269.5224.676, 1995.

Incarbona, A., Ziveri, P., Di Stefano, E., Lirer, F., Mortyn, G., Patti, B., Pelosi, N., Sprovieri, M., Tranchida, G., Vallefuoco, M., Al- bertazzi, S., Bellucci, L. G., Bonanno, A., Bonomo, S., Censi, P., Ferraro, L., Giuliani, S., Mazzola, S., and Sprovieri, R.: The Impact of the Little Ice Age on Coccolithophores in the Cen- tral Mediterranea Sea, Clim. Past, 6, 795–805, doi:10.5194/cp-6- 795-2010, 2010.

Jalut, G., Esteban Amat, A., Mora, S. R., Fontugne, M., Mook, R., Bonnet, L., and Gauquelin, T.: Holocene climatic changes in the western Mediterranean: installation of the Mediterranean climate, CR. Acad. Sci. II, 325, 327–334, 1997.

Jalut, G., Esteban Amat, A., Bonnet, L., Gauquelin, T., and Fontugne, M.: Holocene climatic changes in the Western Mediterranean, from south-east France to south-east Spain, Palaeogeogr. Palaeocl., 160, 255–290, 2000.

Joerin, U. E., Stocker, T. F., Schlu, C., and Physics, E.: Multicen- tury glacier fluctuations in the Swiss Alps during the Holocene, Holocene, 16, 697–704, 2006.

Kaufman, D. S., Schneider, D. P., McKay, N. P., Ammann, C. M., Bradley, R. S., Bria, K. R., Miller, G. H., Otto-Bliesner, B. L., Overpeck, J. P., and Vinther, B. M.: Recent warming reverses long-term arctic cooling, Science, 325, 1236–1239, doi:10.1126/science.1173983, 2009.

Kobashi, T., Kawamura, K., Severinghaus, J. P., Barnola, J. M., Nakaegawa, T., Vinther, B. M., Johnsen, S. J., and Box, J. E.: High variability of Greenland surface temperature over the past 4000 years estimated from trapped air in an ice core, Geophys. Res. Lett., 38, L21501, doi:10.1029/2011GL049444, 2011.

Krishnaswami, S., Lal, D., Martin, J. M., and Meybeck, M.: Geochronology of lake sediments, Earth. Planet. Sc. Lett, 11, 407–414, 1971.

Labuhn, I., Genty, D., Vonhof, H., Bourdin, C., Blamart, D., Dou- ville, E., Ruan, J., Cheng, H., Edwards, R. L., Pons-Branchu, E., and Pierre, M.: A high-resolution fluid inclusion ^{18}O record from a stalagmite in SW France: modern calibration and compar- ison with multiple proxies, Quaternary Sci. Rev., 110, 152–165, doi:10.1016/j.quascirev.2014.12.021, 2015.

Lacombe, H., Gascard, J. C, Cornella, J., and Béthoux, J. P.: Re- sponse of the Mediterranean to the water and energy fluxes across its surface, on seasonal and interannual scales, Oceanol. Acta, 4, 247–255, 1981.

Lacombe, H., Tchernia, P., and Gamberoni, L.: Variable bottom water in the Western Mediterranean basin, Prog. Oceanogr., 14, 319–338, 1985.

Larsen, L. B., Vinther, B. M., Bria, K. R., Melvin, T. M., Clausen, H. B., Jones, P. D., Siggaard-Andersen, M. L., Hammer, C. U., Eronen, M., Grudd, H., Gunnarson, B. E., Hantemirov, R. M., Naurzbaev, M. M., and Nicolussi, K.: New ice core evidence for a volcanic cause of the A.D. 536 dust veil, Geophys. Res. Lett., 35, 1–5, doi:10.1029/2007GL032450, 2008.

Laskar, J., Robutel, P., Joutel, F., Gastineau, M., Correia, A. C. M., and Levrard, B.: A longterm numerical solution for the insolation quantities of the Earth, Astron. Astrophys., 285, 261–285, 2004.

Lea, D. W., Mashiotta, T. A., and Spero, H. J.: Controls on magne- sium and strontium uptake in planktonic foraminifera determined by live culturing, Geochim. Cosmochim. Ac., 63, 2369–2379, 1999.

Lea, D. W., Pak, D. K., and Paradis, G.: Influence of vol- canic shards on foraminiferal Mg/Ca in a core from the Galápagos region, Geochem. Geophy. Geosy., 6, Q11P04, doi:10.1029/2005GC000970, 2005.

Lebreiro, S. M., Francés, G., Abrantes, F. F. G., Diz, P., Bartels- Jónsdóttir, H. B., Stroynowski, Z. N., Gil, I. M., Pena, L. D., Rodrigues, T., Jones, P. D., Nombela, M. A., Alejo, I., Bria, K. R., Harris, I., and Grimalt, J. O.: Climate change and coastal hydrographic response along the Atlantic Iberian margin (Tagus Prodelta and Muros Ría) during the last two millennia, Holocene, 16, 1003–1015, 2006.

Lehner, F., Raible, C. C., and Stocker, T. F.: Testing the ro- bustness of a precipitation proxy-based North Atlantic Os- cillation reconstruction, Quaternary Sci. Rev., 45, 85–94, doi:10.1016/j.quascirev.2012.04.025, 2012.

Lionello, P.: The Climate of the Mediterranean Region: From the Past to the Future, Elsevier Science, Burlington, MA, 2012.

Lionello, P. and Sanna, A.: Mediterranean wave climate variability and its links with NAO and Indian Monsoon, Clim. Dynam., 25, 611–623, doi:10.1007/s00382-005-0025-4, 2005.

Lionello, P., Malanott-Rizzoli, R., Boscolo, R., Alpert, P., Artale, V., Li, L., Luterbacher, J., May, W., Trigo, R., Tsimplis, M., Ulbrich, U., and Xoplaki, E.: The Mediterranean climate: An overview of the main characteristics and issues, in: Mediterranean Climate Variability (MedClivar), Elsevier, Amsterdam, 1–26, 2006.

Lirer, F., Sprovieri, M., Ferraro, L., Vallefuoco, M., Capotondi, L., Cascella, A., Petrosino, P., Insinga, D. D., Pelosi, N., Tambur- rino, S., and Lubritto, C.: Integrated stratigraphy for the Late Quaternary in the eastern Tyrrhenian Sea, Quaternary Int., 292, 71–85, doi:10.1016/j.quaint.2012.08.2055, 2013.

Lirer, F., Sprovieri, M., Vallefuoco, M., Ferraro, L., Pelosi, N., Giordano, L., and Capotondi, L.: Planktonic foraminifera as bio- indicators for monitoring the climatic changes that have occurred over the past 2000 years in the southeastern Tyrrhenian Sea, In- tegr. Zool., 9, 542–54, doi:10.1111/1749-4877.12083, 2014.

Luterbacher, J., Dietrich, D., Xoplaki, E., Grosjean, M., and Wan- ner, H.: European seasonal and annual temperature variabil- ity, trends, and extremes since 1500, Science, 303, 1499–1503, doi:10.1126/science.1093877, 2004.

Malanotte-Rizzoli, P., Artale, V., Borzelli-Eusebi, G. L., Brenner, S., Crise, A., Gacic, M., Kress, N., Marullo, S., Ribera d'Alcalà, M., Sofianos, S., Tanhua, T., Theocharis, A., Alvarez, M., Ashke- nazy, Y., Bergamasco, A., Cardin, V., Carniel, S., Civitarese, G., D'Ortenzio, F., Font, J., Garcia-Ladona, E., Garcia-Lafuente, J. M., Gogou, A., Gregoire, M., Hainbucher, D., Kontoyannis, H., Kovacevic, V., Kraskapoulou, E., Kroskos, G., Incarbona, A., Mazzocchi, M. G., Orlic, M., Ozsoy, E., Pascual, A., Poulain, P.-M., Roether, W., Rubino, A., Schroeder, K., Siokou-Frangou, J., Souvermezoglou, E., Sprovieri, M., Tintoré, J., and Tri- antafyllou, G.: Physical forcing and physical/biochemical variability of the Mediterranean Sea: a review of unresolved issues and directions for future research, Ocean Sci., 10, 281–322, doi:10.5194/os-10-281-2014, 2014.

Mangini, A., Spötl, C., and Verdes, P.: Reconstruction of temper- ature in the Central Alps during the past 2000 yr from a ^{18}O stalagmite record, Earth. Planet. Sc. Lett., 235, 741–751, 2005.

Mann, M. E., Zhang, Z., Hughes, M. K., Bradley, R. S., Miller, S. K., Rutherford, S., and Ni, F.: Proxy-based reconstructions of hemispheric and global surface temperature variations over the past two millennia, P. Natl. Acad. Sci. USA, 105, 13252–13257, 2008.

Mann, M. E., Zhang, Z., Rutherford, S., Bradley, R. S., Hughes, M. K., Shindell, D., Ammann, C., Faluvegi, G., and Ni, F.: Global signatures and dynamical origins of the little ice age and me- dieval climate anomaly, Science, 326, 1256–1260, 2009.

Marchal, O., Cacho, I., Stocker, T. F., Grimalt, J. O., Calvo, E., Mar- trat, B., Shackleton, N., Vautravers, M., Cortijo, E., Van Kreveld, S., Andersson, C., Ko, N., Chapman, M., Sbaffi, L., Duplessy, J., Sarnthein, M., and Turon, J.: Apparent long-term cooling of the sea surface in the northeast Atlantic and Mediterranean during the Holocene, Quaternary Sci. Rev., 21, 455–483, 2002.

Mariotti, A.: Decadal climate variability and change in the Mediter- ranean Region, Sci. Technol. Infus. Clim. Bull., Climate Test Bed Joint Seminar Series, Maryland, US National Oceanic and Atmo- spheric Administration, 1–5, 2011.

Martín-Chivelet, J., Muñoz-García, M. B., Edwards, R. L., Turrero, M. J., and Ortega, A. I.: Land surface tempera- ture changes in Northern Iberia since 4000 yr BP, based on ^{13}C of speleothems, Global Planet. Change, 77, 1–12, doi:10.1016/j.gloplacha.2011.02.002, 2011. Martín-Puertas, C., Valero-Garcés, B. L., Brauer, A., Mata, M. P.,

Delgado-Huertas, A., and Dulski, P.: The Iberian–Roman Hu- mid Period (2600–1600 cal yr BP) in the Zoñar Lake varve record (Andalucía, Southern Spain), Quaternary Res., 71, 108– 120, doi:10.1016/j.yqres.2008.10.004, 2008.

Martínez-Cortizas, A., Pontevedra-Pombal, X., García-Rodeja, E., Nóvoa-Muñoz, J. C., and Shotyk, W.: Mercury in a Spanish Peat Bog: archive of climate change and atmospheric metal deposition, Science, 284, 939–942, 1999.

Martrat, B., Grimalt, J. O., Lopez-Martinez, C., Cacho, I., Sierro, F. J., Flores, J. A., Zahn, R., Canals, M., Curtis, J. H., and Hodell, D. A.: Abrupt temperature changes in the Western Mediter- ranean over the past 250 000 years, Science, 306, 1762–1765, doi:10.1126/science.1101706, 2004.

Marullo, S., Artale, V., and Santoleri, R.: The SST multi-decadal variability in the Atlantic-Mediterranean region and its relation to AMO, J. Climate, 24, 4385–4401, doi:10.1175/2011JCLI3884.1, 2011.

Mashiotta, T. A., Lea, D. W., and Spero, H. J.: Glacial–interglacial changes in Subantarctic sea surface temperature and ^{18}O-water using foraminiferal Mg, Earth Planet. Sc. Lett., 170, 417–432, 1999.

Masqué, P., Fabres, J., Canals, M., Sanchez-Cabeza, J. A., Sanchez- Vidal, A., Cacho, I., Calafat, A. M., and Bruach, J. M.: Accumu- lation rates of major constituents of hemipelagic sediments in the deep Alboran Sea: a centennial perspective of sedimentary dynamics, Mar. Geol., 193, 207–233, 2003.

Matthews, J. A. and Bria, K. R.: The "Little ice age": re-evaluation of an evolving concept, Geogr. Ann. A, 87, 17–36, 2005.

Mauffret, A.: Etude géodynamique de la marge des Illes Baléares, Mémoires de la Société Géologique de France LVI, 1–96, 1979. Mayewski, P. A., Rohling, E. E., Stager, J. C., Karlen, W., Maasch,

K. A., Meeker, L. D., Meyerson, E. A., Gasse, F., van Kreveld, S., Holmgren, K., Lee-Thorp, J., Rosqvist, G. Rack, F., Staub- wasser, M., Schneider, R. R., and Steig, E. J.: Holocene climate variability, Quaternary Res., 62, 243–255, 2004.

McConnell, M. C. and Thunell, R. C.: Calibration of the planktonic foraminiferal Mg/Ca paleothermometer: sediment trap results from the Guaymas Basin, Gulf of California, Paleoceanography, 20, PA2016, doi:10.1029/2004PA001077, 2005.

McGregor, H. V., Evans, M. N., Goosse, H., Leduc, G., Martrat, B., Addison, J. A., Graham Mortyn, P., Oppo, D. W., Seidenkrantz, M.-S., Sicre, M.-A., Phipps, S. J., Selvaraj, K., Thirumalai, K., Filipsson, H. L., and Ersek, V.: Robust global ocean cooling trend for the pre-industrial Common Era, Nat. Geosci., 8, 671–677, doi:10.1038/ngeo2510, 2015.

MEDAR GROUP, MEDATLAS/2002 European Project: Mediter- ranean and Black Sea Database of Temperature Salinity and Bio- Chemical Parameters, Climatological Atlas, Institut Français de Recherche pour L'Exploitation de la Mer (IFREMER), Edition/Instituto Nazionale di Oceanografia e di Geofisica Speri- mentale (OGS), 2002.

Medoc, G.: Observation of formation of Deep Water in the Mediter- ranean Sea, Nature, 227, 1037–1040, 1970.

Millán, M. M., Estrela, M. J., Sanz, M. J., Mantilla, E., Martín, M., Pastor, F., Salvador, R., Vallejo, R., Alonso, L., Gangoiti, G., Ilar- dia, J. L., Navazo, M., Albizuri, A., Artiñano, B., Ciccioli, P., Kallos, G., Carvalho, R. A., Andrés, D., Ho, A., Werhahn, J., Seufert, G., and Versino, B.: Climatic feedbacks and desertifica- tion: the Mediterranean Model, J. Climate, 18, 684–701, 2005.

Millot, C.: Circulation in the Western Mediterranean Sea, J. Mar. Syst., 20, 423–442, 1999.

Morellón, M., Pérez-Sanz, A., Corella, J. P., Büntgen, U., Catalán, J., González-Sampériz, P., González-Trueba, J. J., López-Sáez, J. A., Moreno, A., Pla-Rabes, S., Saz-Sánchez, M. Á., Scus- solini, P., Serrano, E., Steinhilber, F., Stefanova, V., Vegas- Vilarrúbia, T., and Valero-Garcés, B.: A multi-proxy perspective on millennium-long climate variability in the Southern Pyrenees, Clim. Past, 8, 683–700, doi:10.5194/cp-8-683-2012, 2012.

Moreno, A., Cacho, I., Canals, M., Prins, M. A., Sánchez- Goñi, M. F., Grimalt, J. O., and Weltje, G. J.: Saharan Dust Transport and High-Latitude Glacial Climatic Variabil- ity: the Alboran Sea Record, Quaternary Res., 58, 318–328, doi:10.1006/qres.2002.2383, 2002.

Moreno, A., Cacho, I., Canals, M., Grimalt, J. O., Sánchez-Goñi, M. F., Shackleton, N., and Sierro, F. J.: Links between marine and atmospheric processes oscillating on a millennial time-scale. A multi-proxy study of the last 50 000 yr from the Alboran Sea (Western Mediterranean Sea), Quaternary Sci. Rev., 24, 1623– 1636, doi:10.1016/j.quascirev.2004.06.018, 2005.

Moreno, A., Valero-Garcés, B. L., González-Sampériz, P., and Rico, M.: Flood response to rainfall variability during the last 2000 years inferred from the Taravilla Lake record (Cen- tral Iberian Range, Spain), J. Paleolimnol., 40, 943–961, doi:10.1007/s10933-008-9209-3, 2008.

Moreno, A., Pérez, A., Frigola, J., Nieto-Moreno, V., Rodrigo- Gámiz, M., Martrat, B., González-Sampériz, P., Morellón, M., Martín-Puertas, C., Pablo, J., Belmonte, Á., Sancho, C., Cacho, I., Herrera, G., Canals, M., Grimalt, J. O., Jiménez-Espejo, F., Martínez-Ruiz, F., Vegas-Vilarrúbia, T., and Valero-Garcés, B. L.: The Medieval Climate Anomaly in the Iberian Peninsula re- constructed from marine and lake records, Quaternary Sci. Rev., 43, 16–32, doi:10.1016/j.quascirev.2012.04.007, 2012.

Morhange, C., Marriner, N., Excoffon, P., Bonnet, S., Flaux, C., Zi- browius, H., Goiran, J. P., and El Amouri, M.: Relative Sea-Level Changes During Roman Times in the Northwest Mediterranean: the 1st Century AD. Fish Tank of Forum Julii, Fréjus, France, Geoarchaeology, 28, 363–372, doi:10.1002/gea.21444, 2013.

Mulitza, S., Boltovskoy, D., Donner, B., Meggers, H., Paul, A., and Wefer, G.: Temperature: ^{18}O relationships of planktonic foraminifera collected from surface waters, Palaeogeogr. Palaeoecol., 202, 143–152, doi:10.1016/S0031-0182(03)00633- 3, 2003.

Nieto-Moreno, V., Martínez-Ruiz, F., Giralt, S., Jiménez-Espejo, F., Gallego-Torres, D., Rodrigo-Gámiz, M., García-Orellana, J., Ortega-Huertas, M., and de Lange, G. J.: Tracking climate vari- ability in the western Mediterranean during the Late Holocene: a multiproxy approach, Clim. Past, 7, 1395–1414, doi:10.5194/cp- 7-1395-2011, 2011.

Nieto-Moreno, V., Martínez-Ruiz, F., Willmott, V., García-Orellana, J., and Masqué, P.: Organic geochemistry climate conditions in the westernmost Mediterranean over the last two millennia: an integrated biomarker approach, Org. Geochem., 55, 1–10, doi:10.1016/j.orggeochem.2012.11.001, 2013.

Olsen, J., Anderson, N. J., and Knudsen, M. F.: Variability of the North Atlantic Oscillation over the past 5200 years, Nat. Geosci., 5, 808–812, doi:10.1038/ngeo1589, 2012.

Ortega, P., Lehner, F., Swingedouw, D., Masson-Delmotte, V., Raible, C. C., Casado, M., and Yiou, P.: A model-tested North Atlantic Oscillation reconstruction for the past millennium, Nature, 523, 71–74, doi:10.1038/nature14518, 2015.

PAGES: Science Plan and Implementation Strategy, IGBP Report No. 57, IGBP Secretariat, Stockholm, 2009.

PAGES 2K Consortium: Continental-scale temperature variability during the past two millennia, Nature, 6, 339–346, doi:10.1038/NGEO1797, 2013.

Pastor, F.: Ciclogénesis intensas en la cuenca occidental del Mediterráneo y temperatura superficial del mar: modelización y evaluación de las áreas de recarga, PhD Thesis, Dept. of Astronomy and Meteorology, University of Barcelona, Spain, 2012.

Pastor, F., Estrela, M., Peñarrocha, D., and Millán, M.: Torrential rains on the Spanish Mediterranean Coast: modeling the effects of the sea surface temperature, J. Appl. Meteorol., 40, 1180– 1195, 2001.

Patton, G. M., Martin, P. A., Voelker, A., and Salgueiro, E.: Multi- proxy comparison of oceanographic temperature during Heinrich Events in the eastern subtropical Atlantic, Earth Planet. Sc. Lett., 310, 45–58, doi:10.1016/j.epsl.2011.07.028, 2011.

Pena, L. D., Calvo, E., Cacho, I., Eggins, S., and Pelejero, C.: Identification and removal of Mn-Mg-rich contaminant phases on foraminiferal tests: implications for Mg/Ca past temper- ature reconstructions, Geochem. Geophy. Geosy., 6, Q09P02, doi:10.1029/2005GC000930, 2005.

Pena, L. D., Cacho, I., Calvo, E., Pelejero, C., Eggins, S., and Sadekov, A.: Characterization of contaminant phases in foraminifera carbonates by electron micro- probe mapping, Geochem. Geophy. Geosy., 9, Q07012, doi:10.1029/2008GC002018, 2008.

Pena, L. D., Francés, G., Diz, P., Esparza, M., Grimalt, J. O., Nombela, M. A., and Alejo, I.: Climate fluctuations during the Holocene in NW Iberia: High and low latitude linkages, Cont. Shelf. Res., 30, 1487–1496, doi:10.1016/j.csr.2010.05.009, 2010.

Pierre, C.: The oxygen and carbon isotope distribution in the Mediterranean water masses, Mar. Geol., 153, 41–55, 1999.

Pinardi, N. and Masetti, E.: Variability of the large general circula- tion of the Mediterranean Sea from observations and modelling: a review, Palaeogeogr. Palaeocl., 158, 153–173, 2000.

Pinot, J. M., López-Jurado, J., and Riera, M.: The CANALES experiment (1996–1998), Interannual, seasonal, and mesoscale variability of the circulation in the Balearic Channels, Prog. Oceanogr., 55, 335–370, 2002.

Piva, A., Asioli, A., Trincardi, F., Schneider, R. R., and Vigliotti, L.: Late-Holocene climate variability in the Adriatic Sea (Central Mediterranean), Holocene, 18, 153–167, 2008.

Pla, S. and Catalan, J.: Chrysophyte cysts from lake sediments re- veal the submillennial winter/spring climate variability in the northwestern Mediterranean region throughout the Holocene, Clim. Dynam., 24, 263–278, 2005.

Pujol, C. and Vergnaud-Grazzini, C.: Distribution patterns of live planktic foraminifers as related to regional hydrography and productive systems of the Mediterranean Sea, Mar. Micropaleontol., 25, 187–217, 1995.

Reguera, M. I.: Respuesta del Mediterráneo Occidental a los cam- bios climáticos bruscos ocurridos durante el último glacial: es- tudio de las asociaciones de foraminíferos, PhD Thesis, Dept. of Geology, University of Salamanca, Spain, 2004.

Reimer, P. J., Bard, E., Bayliss, A., Beck, J. W., Blackwell, P. G., Bronk Ramsey, C., Buck, C. E., Edwards, R. L., Friedrich, M., Grootes, P. M., Guilderson, T. P., Haflidason, H., Hajdas, I., Hatté, C., Heaton, T. J., Hömann, D. L., Hogg, A. G., Hughen, K. A., Kaiser, K. F., Kromer, B., Manning, S. W., Niu, M., Reimer, R. W., Richards, D. A., Scott, M. E., Southon, J. R., Turney, C. S. M., and van der Plicht, J.: Intcal13 and Marine13 radiocarbon age calibration curves 0–50 000 years cal BP, Radiocarbon, 55, 1869–1887, 2013.

Richter, T. O. and van der Gaast, S.: The Avaatech Core Scanner: technical description and applications to NE Atlantic sediments, in: New Ways of Looking at Sediment Core and Core Data, edited by: Rothwell, R. G., Geological Society Special Publica- tion, London, 39–50, 2006.

Rigual-Hernández, A. S., Sierro, F. J., Bárcena, M. A., Flores, J. A., and Heussner, S.: Seasonal and interannual changes of planktic foraminiferal fluxes in the Gulf of Lions (NW Mediterranean) and their implications for paleoceanographic studies: two 12- year sediment trap records, Deep-Sea Res. Pt. I, 66, 26–40, doi:10.1016/j.dsr.2012.03.011, 2012.

Rigual-Hernández, A. S., Bárcena, M. A., Jordan, R. W., Sierro, F. J., Flores, J. A., Meier, K. J., Beaufort, L., and Heussner, S.: Diatom fluxes in the NW Mediterranean: evidence from a 12- year sediment trap record and surficial sediments, J. Plankton. Res., 35, 1–17, doi:10.1093/plankt/fbt055, 2013.

Roberts, N., Moreno, A., Valero-Garcés, B. L., Corella, J. P., Jones, M., Allcock, S., Woodbridge, J., Morellón, M., Luter- bacher, J., Xoplaki, E., and Türkes¸ M.: Palaeolimnological evidence for an east–west climate see-saw in the Mediter- ranean since AD 900, Global Planet. Change, 84–85, 23–34, doi:10.1016/j.gloplacha.2011.11.002, 2012.

Rodrigo-Gámiz, M., Martínez-Ruiz, S., Rampen, S., Schouten, S., and Sinninghe Damsté, J.: Sea surface temperature variations in the western Mediterranean Sea over the last 20 kyr: a dual-organic proxy (U^{k^0} and LDI) approach, Paleoceanography, 29, 37

87–98, doi:10.1002/2013PA002466, 2014. Rogerson, M., Rohling, E. J., Weaver, P. P. E., and Murray, J. W.: The Azores Front since the Last Glacial Maximum, Earth Planet. Sc. Lett., 222, 779–789, doi:10.1016/j.epsl.2004.03.039, 2004. Rohling, E., Hayes, A., De Rijk, S., Kroon, D., Zachariasse, W. J., and Eisma, D.: Abrupt cold spells in the northwest Mediterranean, Paleoceanography, 13, 316–322,

1998. Sabatier, P., Dezileau, L., Colin, C., Briqueu, L., Bouchette, F., Martinez, P., Siani, G., Raynal, O., and Von Grafenstein, U.: 7000 years of paleostorm activity in the NW Mediterranean Sea in response to Holocene climate events, Quaternary Res., 77, 1–11, doi:10.1016/j.yqres.2011.09.002, 2012.

Sáez de Cámara, E., Gangoiti, G., Alonso, L., and Iza, J.: Daily precipitation in Northern Iberia: understanding the recent changes after the circulation variability in the North Atlantic sector, J. Geophys. Res., 120, 9981–10, doi:10.1002/2015JD023306, 2015.

Sanchez-Cabeza, J., Masqué, P., and Ani-Ragolta, I.: ^{210}Pb and ^{210}Po analysis in sediments and soils by microwave acid diges- tion, J. Radioanal. Nucl. Ch., 227, 19–22, 1998.

Schiebel, R., Schmuker, B., Alves, M., and Hemleben, C.: Tracking the Recent and Late Pleistocene Azores front by the distribution of planktic foraminifers, J. Mar. Syst., 37, 213–227, 2002.

Schilman, B., Bar-Matthews, M., Almogilabin, A., and Luz, B.: Global climate instability reflected by Eastern Mediterranean marine records during the late Holocene, Palaeogeogr. Palaeocl., 176, 157–176, 2001.

Shackleton, N.: Attainment of isotopic equilibrium between ocean water and the benthonic foraminifera genus *Uvigerina*: isotopic changes in the ocean during the last glacial, CNRS, Colloq. Int., 219, 203–209, 1974.

Sicre, A., Ternois, Y., Miquel, J. C., and Marty, J. C.: Alkenones in the Northwestern Mediterranean sea: interannual variability and vertical transfer, Geophys. Res. Lett., 26, 1735–1738, 1999.

Sicre, M. A., Yiou, P., Eiríksson, J., Ezat, U., Guimbaut, E., Dah- haoui, I., Knudsen, K. L., Jansen, E., and Turon, J. L.: A 4500- year reconstruction of sea surface temperature variability at decadal time-scales off North Iceland, Quaternary Sci. Rev., 27, 2041–2047, doi:10.1016/j.quascirev.2008.08.009, 2008.

Sierro, F. J., Hodell, D. A., Curtis, J. H., Flores, J. A., Reguera, I., Colmenero-Hidalgo, E., Bárcena, M. A., Grimalt, J. O., Ca- cho, I., Frigola, J., and Canals, M.: Impact of iceberg melting on Mediterranean thermohaline circulation during Heinrich events, Paleoceanography, 20, 1–13, doi:10.1029/2004PA001051, 2005.

Siokou-Frangou, I., Christaki, U., Mazzocchi, M. G., Montresor, M., Ribera d'Alcalá, M., Vaqué, D., and Zingone, A.: Plankton in the open Mediterranean Sea: a review, Biogeosciences, 7, 1543– 1586, doi:10.5194/bg-7-1543-2010, 2010.

Steinhilber, F., Beer, J., and Fröhlich, C.: Total solar irradi- ance during the Holocene, Geophys. Res. Lett., 36, L19704, doi:10.1029/2009GL040142, 2009.

Steinhilber, F., Abreu, J. A., Beer, J., Brunner, I., Christl, M., Fis- cher, H., Heikkilä, U., Kubik, P. W., Mann, M., McCracken, K. G., Miller, H., Miyahara, H., Oerter, H., and Wilhelms, F.: 9400 years of cosmic radiation and solar activity from ice cores and tree rings, P. Natl. Acad. Sci. USA, 109, 5967–5971, doi:10.1073/pnas.1118965109, 2012.

Stine, S.: Extreme and persistent drought in California and Patago- nia during medieval time, Nature, 369, 546–549, 1994.

Stothers, R. B.: Mystery cloud of AD 536, Nature, 307, 344–345, doi:10.1038/307344a0, 1984.

Stuiver, M. and Reimer, P. J.: Extended ^{14}C data base and revised Calib 3.0 ^{14}C age calibration program, Radiocarbon, 35, 215– 230, 1993.

Taricco, C., Ghil, M., Alessio, S., and Vivaldo, G.: Two millennia of climate variability in the Central Mediterranean, Clim. Past, 5, 171–181, doi:10.5194/cp-5-171-2009, 2009.

Taricco, C., Vivaldo, G., Alessio, S., Rubinetti, S., and Mancuso, S.: A high-resolution ^{18}O record and Mediterranean climate vari- ability, Clim. Past, 11, 509–522, doi:10.5194/cp-11-509-2015, 2015.

Ternois, Y., Sicre, M. A., Boireau, A., Marty, J. C., and Miquel, J. C.: Production pattern of alkenones in the Mediterranean Sea, Geophys. Res. Lett., 23, 3171–3174, 1996.

Thornalley, D. J. R., Elderfield, H., and McCave, I. N.: Holocene oscillations in temperature and salinity of the surface subpolar North Atlantic, Nature, 457, 711–714, doi:10.1038/nature07717, 2009.

Touchan, R., Xoplaki, E., Funkhouser, G., Luterbacher, J., Hughes, M. K., Erkan, N., Akkemik, Ü., and Stephan, J.: Reconstruc- tions of spring/summer precipitation for the Eastern Mediter- ranean from treering widths and its connection to large-scale at- mospheric circulation, Clim. Dynam., 25, 75–98, 2005.

Touchan, R., Akkemik, Ü., Hughes, M. K., and Erkan, N.: May–June precipitation reconstruction of southwestern Anato- lia, Turkey during the last 900 years from tree rings, Quaternary Res., 68, 196–202, 2007.

Trouet, V., Esper, J., Graham, N. E., Baker, A., Scourse, J. D., and Frank, D. C.: Persistent positive North Atlantic Oscillation mode dominated the Medieval Climate Anomaly, Science, 324, 78–80, doi:10.1126/science.1166349, 2009.

Trouet, V., Scourse, J. D., and Raible, C. C.: North Atlantic stormi- ness and Atlantic Meridional Overturning Circulation during the last Millennium: reconciling contradictory proxy records of NAO variability, Global Planet. Change, 84–85, 48–55, doi:10.1016/j.gloplacha.2011.10.003, 2012.

Tsimplis, M. N. and Baker, F.: Sea level drop in the Mediter- ranean Sea: an indicator of deep water salinity and temperature changes?, Geophys. Res. Lett., 27, 1731–1734, 2000.

Tsimplis, M. N. and Josey, S. A.: Forcing of the Mediterranean Sea by atmospheric oscillations over the North Atlantic, Geophys. Res. Lett., 28, 803–806, 2001.

Tsimplis, M. N. and Rixen, M.: Sea level in the Mediterranean Sea: the contribution of temperature and salinity changes, Geophys. Res. Lett., 29, 1–4, doi:10.1029/2002GL015870, 2002.

Vallefuoco, M., Lirer, F., Ferraro, L., Pelosi, N., Capotondi, L., Sprovieri, M., and Incarbona, A.: Climatic variability and an- thropogenic signatures in the Gulf of Salerno (southern-eastern Tyrrhenian Sea) during the last half millennium, Rend Lincei, 23, 13–23, doi:10.1007/s12210-011-0154-0, 2012.

van Raden, U. J., Groeneveld, J., Raitzsch, M., and Kucera, M.: Mg / Ca in the planktonic foraminifera Globorotalia inflata and Globigerinoides bulloides from Western Mediterranean plankton tow and core top samples, Mar. Micropaleontol., 78, 101–112, doi:10.1016/j.marmicro.2010.11.002, 2011.

Vargas-Yáñez, M., Moya, F., García-Martínez, M. C., Tel, E., Zunino, P., Plaza, F., Salat, J., and Pascual, J.: Climate change in the Western Mediterranean Sea 1900–2008, J. Marine Syst., 82, 171–176, doi:10.1016/j.jmarsys.2010.04.013, 2010.

Velasco, J. P. B., Baraza, J., and Canals, M.: La depresión periférica y el lomo contourítico de Menorca: evidencias de la actividad de corrientes de fondo al N del Talud Balear, Geogaceta, 20, 359– 362, 1996.

Versteegh, G. J. M., de Leeuw, J. W., Taricco, C., and Romero, A.: Temperature and productivity influences on U^{K^0} and their possible relation to solar forcing of the 37 Mediterranean winter, Geochem. Geophy. Geosy., 8, Q09005, doi:10.1029/2006GC001543, 2007.

Villanueva, J., Pelejero, C., and Grimalt, J. O.: Clean-up procedures for the unbiased estimation of C_{37} alkenone sea surface temper- atures and terrigenous n-alkane inputs in paleoceanography, J. Chromatogr., 757, 145–151, 1997.

Wallace, J. M. and Gutzler, D. S.: Teleconnections in the geopo- tential height field during the Northern Hemisphere winter, Mon. Weather Rev., 109, 784–812, 1981.

Wassenburg, J. A., Immenhauser, A., Richter, D. K., Niedermayr, A., and Riechelmann, S.: Moroccan

speleothem and tree ring records suggest a variable positive state of the North Atlantic Oscillation during the Medieval Warm Period, Earth Planet. Sc. Lett., 375, 291–302, doi:10.1016/j.epsl.2013.05.048, 2013.

Wright, H. E.: Global Climates since the Last Glacial Maximum, Minnesota University Press, Minneapolis, 1994.

Yu, J., Elderfield, H., Greaves, M., and Day, J.: Preferential dissolution of benthic foraminiferal calcite during laboratory reductive cleaning, Geochem. Geophy. Geosy., 8, Q06016, doi:10.1029/2006GC001571, 2007.

3.1.10 Supplement Information to Cisneros et al., 2016

Supplement of Clim. Past, 12, 849–869, 2016
http://www.clim-past.net/12/849/2016/
doi:10.5194/cp-12-849-2016-supplement

Age model development

^{14}C, ^{210}Pb, ^{137}Cs dates

Absolute dating with radiocarbon dates was focused on cores MIN1, MIN2 and MR3.3 (Table 3.2). According to those dates and assuming the sampling year as the core top age (2006 and 2009, for MIN and MR3 cores respectively), the sedimentation rates of these three cores result in 13 ± 1, 20 ± 3 and 13 ± 5 cm ky^{-1}, respectively (sedimentation rates uncertainties are expressed as 1σ in this section).

In order to evaluate the preservation of the core tops, ^{210}Pb activity profiles were obtained from MIN1, MIN2, MR3.1A and MR3.2 cores (Fig. 3.10). ^{210}Pb concentrations generally decrease with depth in all four cores, down to 3.5 cm in MIN2 core and 3 cm for MIN1, MR3.1A and MR3.2 cores. Excess ^{210}Pb concentrations at the surface and inventories in the MIN cores are in agreement with those published for the Algero- Balear Basin (Garcia-Orellana et al., 2009). However, they were lower in MR3 cores, particularly for MR3.1A core, which we attribute to the loss of the most surficial part of these cores during recovery, corresponding to about 50 yr by comparison to the other cores. The variability in the ^{210}Pb data denotes the high heterogeneity of this sedimentary system in reference to deep-sea hemipelagic sediments, highlighting the relevance of its study on the basis of a multicore approach (e.g. Maldonado et al., 1985; Martin et al., 1989; Calafat et al., 1996; Velasco et al., 1996; Canals et al., 2006; Frigola et al., 2007).

Table 3.2. Radiocarbon dates obtained on monospecific foraminifer *G. inflata* and calibrated ages, these last ones are expressed in years Before Common Era (BCE) and Common Era (CE). MR3.3 dates are presented for the first time in this study. Cores were analysed at the NOSAMS/Woods Hole Oceanographic Institution, USA (OS) and at Direct AMS Radiocarbon Dating Service, USA (D-AMS).

Laboratory Code	Core	Comp. Depth (cm)	^{14}C ages	Cal years BCE/CE (2-σ)
OS-67294	MIN1	7-7.5	895 ± 35	1411 - 1529 CE
OS-67296		19-19.5	2010 ± 35	304 - 544 CE
OS-67291		11-11.5	845 ± 35	1440 - 1598 CE
OS-67297	MIN2	18-18.5	1190 ± 35	1170 - 1312 CE
OS-67324		25-25.5	1540 ± 25	804 - 989 CE
OS-67323		28.5-29	1840 ± 30	520 - 680 CE
D-AMS 004812		3.5-4	938 ± 25	1383 - 1484 CE
OS-87613		6.5-7	1270 ± 35	1063 - 1256 CE
OS-87614	MR3.3	12-12.5	1420 ± 30	911 - 1085 CE
OS-87615		16-17	1900 ± 30	438 - 621 CE
D-AMS 004811		20-21	2350 ± 29	88 BCE - 107 CE
OS-87619		24-25	2620 ± 25	388 BCE - 214 BCE

The concentration profile and inventory of ^{137}Cs in MIN1 core is also in good agreement with the results reported for the western Mediterranean Basin (Garcia-Orellana et al., 2009). Its detection down to 3 cm combined with the excess ^{210}Pb concentration profile suggests the presence of sediment mixing to be accounted for in the calculation of the sediment accumulation rates, which are to be taken as maxima estimates. In doing so, the maxima sedimentation rates for the last 100–150 years are: 27 ± 2 cm kyr^{-1} (MIN1 core), 28 ± 2 cm kyr^{-1} (MIN2), 28 ± 4 cm kyr^{-1} (MR3.1A), and 35 ± 3 cm kyr^{-1} (MR3.2). These sedimentation rates are in agreement with those previously described in a long sediment record recovered within the contouritic system (Frigola et al., 2007 and 2008), but much higher than those found in the literature from

deeper sites of the Balearic Sea, with predominant hemipelagic sedimentation (e.g. Weldeab et al., 2003; Zúñiga et al., 2007; Garcia-Orellana et al., 2009).

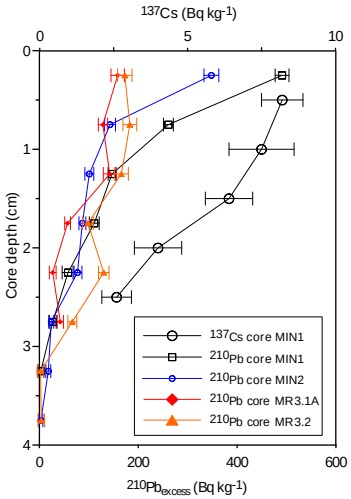

Figure 3.10. Excess ^{210}Pb (Bq kg^{-1}) profiles for MIN1, MIN2, MR3.1A and MR3.2 cores and also ^{137}Cs concentration profile for MIN1 core. Error bars represent 1 σ uncertainty.

Biostratigraphical data based on planktonic foraminifera

Core MR3.3, the best ^{14}C-dates time-constrained, was chosen in order to perform a taxonomic analysis of planktonic foraminifera. The identified species were: (1) *Globigerina bulloides* including *G. falconensis*, (2) *Globigerinoides ruber* pink and white variety, (3) *Orbulina* spp. including both *O. universa* and *O. suturalis*, (4) *Globigerinoides quadrilobatus* and *G. sacculifer*, (5) *Globigerinatella siphoniphera* including *G. calida*, (6) *Globorotalia inflata*, (7) *Turborotalita quinqueloba*, (8) *Globigerinita glutinata*, (9) *Neogloboquadrina pachyderma* right coiled, (10) *Neogloboquadrina dutertrei*, (11) *Globorotalia truncatulinoides* left coiled and (12) *Clavoratorella* spp. The abundance of *G. truncatulinoides* left coiled was also analysed in the top of the core MR3.1A.

In order to improve the time constrain of our cores, percentages records of *G. quadrilobatus* and *G. truncatulinoides* left coiled from MR3.3 core have been correlated with those from a southern Tyrrhenian Sea composite core (Fig. 3.11), with a very robust age-model (Lirer et al., 2013) based on the combination of different dating methods (radionuclides-^{14}C AMS dates and tephra-chronology). The Mediterranean ecobiostratigraphic strength of these taxa has been previously documented by Piva et al. (2008) for the last 370 ky. The pronounced decrease in *G. quadrilobatus* percentages at

the base of MR3.3 core (Fig. 3.11a) can be correlated with the end of the *G. quadrilobatus* acme interval observed in the north and south Tyrrhenian Sea record (Lirer et al., 2013, 2014; Di Bella et al., 2014) from 1750 to 750 BCE and previously documented in the Sicily Channel (Sprovieri et al., 2003) and the Sardinian valley (Budillon et al., 2009). In addition, data on distribution pattern of the leaving planktonic foraminifera, reported in Pujol and Vergnaud-Grazzini (1995), documented that this taxon is present in the whole central and south western Mediterranean (excluding the GoL). This correlation provide to us a control age point in MR3.3 core of 750 ± 48 BCE at about 27 cm, consistent with the ^{14}C dating of 301 ± 87 BCE at 24 cm. In the upper part of the MR3.3 record, another control age point can be obtained from the correlation of the pronounced peak of *G. truncatulinoides* left coiled (~20% in abundance, Fig. 3.11b) with a similar peak previously reported in the central and south Tyrrhenian Sea record during the LIA at 1718 ± 10 CE (Lirer et al., 2013; Margaritelli et al., 2015), and coincident with the Maunder event (Vallefuoco et al., 2012; Lirer et al., 2014; Margaritelli et al., 2015).

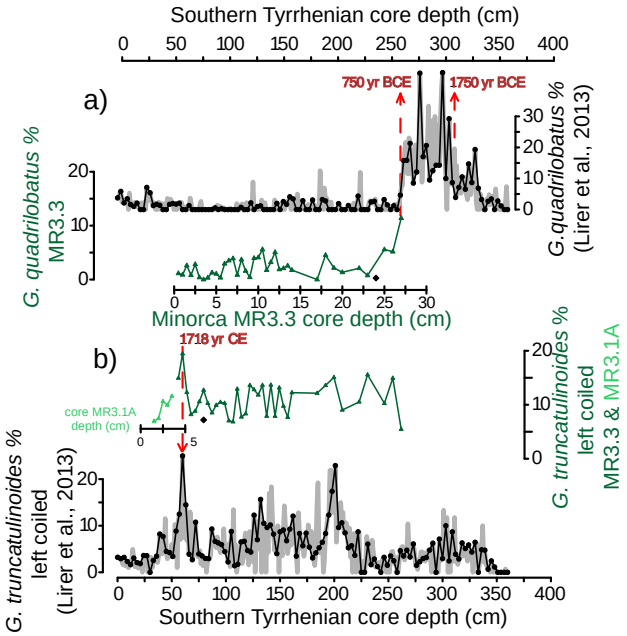

Figure 3.11. Comparison among the quantitative distribution patterns of **(a)** *G. quadrilobatus* and **(b)** *G. truncatulinoides* left coiled with core MR3.3 (dark green plot) and data from the composite core (C90-1m, C90 and C836 cores) studied in the southern Tyrrhenian Sea (Lirer et al., 2013), expressed as 3 point average and with the grey area corresponding to the entire record. The two tie points used in age models (dashed red line) correspond to 1718 CE and 750 BCE. Black diamonds show ^{14}C dates from core MR3.3.

Thunell (1978) documented the occurrence in recent surface sediments of this taxon from Balearic Islands to Sicily channel and Pujol and Vergnaud-Grazzini (1995)

observed this species in leaving abundance foraminifera of the whole western Mediterranean. This age point is also consistent with the obtained ^{14}C date of MR3.3 core at 3.5cm of 1434 ± 51 CE, further supporting the absence of the last two centuries in the MR3.3 core. The absence of these centuries is also suggested by the *G. truncatulinoides* left coiled abundance patterns data from the top (1.5-3.5 cm) of the MR3.1A core (Fig. 3.11b). MR3.1A data is in agreement with the drop of the peak in MR3.3 core and ^{210}Pb measurements (Fig. 3.10) have corroborated the presence of the most recent sediment in core MR3.1A.

Bayesian accumulation models

A preliminary age model for MIN1, MIN2 and MR3.3 cores were initially generated by means of available ^{14}C ages, the two biostratigraphical dates from MR3.3 core and maximum sedimentation rates derived from ^{210}Pb concentration profiles from MIN1 and MIN2 cores. This preliminary age model was built using the Bayesian statistics software Bacon with the statistical package R (Blaauw and Christen, 2011).

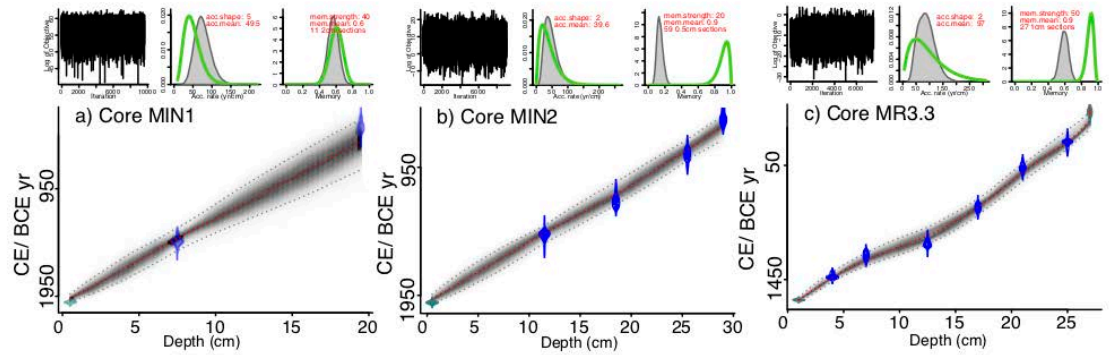

Figure 3.12. Age-depth models based on Bayesian accumulation simulations (Blaauw and Christen, 2011): **a)** MIN, **b)** MIN2 and **c)** MR3.3 cores. The three upper plots in each core show the stable MCMC run achieved (left), the prior (green line) and posterior (grey) distributions of the accumulation rates (middle), and the prior (green line) and posterior (grey) distributions of the memory (right). Each main graphic represents the age–depth model for each core (darker grey indicates more probable calendar ages) based on the prior information, the calibrated radiocarbon dates (purple symbols), sample year for cores MIN (blue symbols) and biostratigraphical dates from MR3.3 core (red symbols).

Considering that the two independent sedimentation rates estimations based on ^{14}C and ^{210}Pb have significant uncertainties inherent to the methods and considering the different sampling resolution, averaged sedimentation rates obtained from the two methods have been taken into account in the Bayesian accumulation models. Regarding the core top ages, it was considered to be the recovering year (2006 ± 10 CE) in MIN

cores and 1718 ± 10 CE for MR3.3 core, coinciding with the peak in the *G. truncatulinoides* record. The program settings for thickness of the sections and memory were chosen to fulfil the criterions of the best mean 95% confidence range and to maintain good correlation between prior and posterior accumulation rates. In addition, it was decided to keep the memory strength values rather high since the sedimentary context, a contouritic drift, is expected to record highly variable accumulation rates, and due to the smother changes induced by lowering the memory strength would no reflect realistic changes in this context.

The best Bayesian models achieved with a confidence mean of 95% provide accumulation rates for MIN1, MIN2 and MR3.3 cores of 14 ± 2, 22 ± 1 and 12 ± 1 cm kyr^{-1}, respectively (uncertainties are expressed as 1σ), which correspond to mean time resolutions of 292, 161, and 200 yr, respectively. It should be noted that the largest errors are obtained for MIN1 core because of the only two ^{14}C dates. These age models reconstruct a rather smooth accumulation history, although significant fluctuations in accumulation rate at centennial or even decadal scale can be expected in this sedimentological context. The posterior outputs for accumulation rate (see Fig. 3.12) and its variability are quite comparable to their prior ones, but in the case of MR3.3 core the posterior output indicates larger memory (more variability) than that assumed a priori. This is due to the strong change in sedimentation rates at about 12 cm (998 CE) that the prior output tends to attenuate, and which could be associated with abrupt changes in sedimentation rates at that time (Fig. 3.12c).

These age models have been then further re-evaluated using other geochemical proxies as stratigraphical tools in order to ensure a common chronological framework for the obtained climate records. Nevertheless, any readjustment has always been kept within the confident rage of the Bayesian models.

Multi-proxy chronostratigraphy

The chronologies of MIN1, MIN2 and MR3.3 cores were finally evaluated and readjusted in base to their Mg/Ca records and taking into account the 95% probability intervals obtained in the Bayesian models.

Mg/Ca measured in *G. bulloides* is a well-established proxy of Sea Surface Temperatures (Barker et al., 2005). The two sampling stations are only separated by 30

km and thus it is a reasonable assumption to expect comparable and synchronous SST changes in all the studied cores. Visual comparison of the MIN1, MIN2 and MR3.3 records of Mg/Ca show several resemblances in some of the main patterns and structures, which are considerably synchronous with the Bayesian age models (Fig. 3.13).

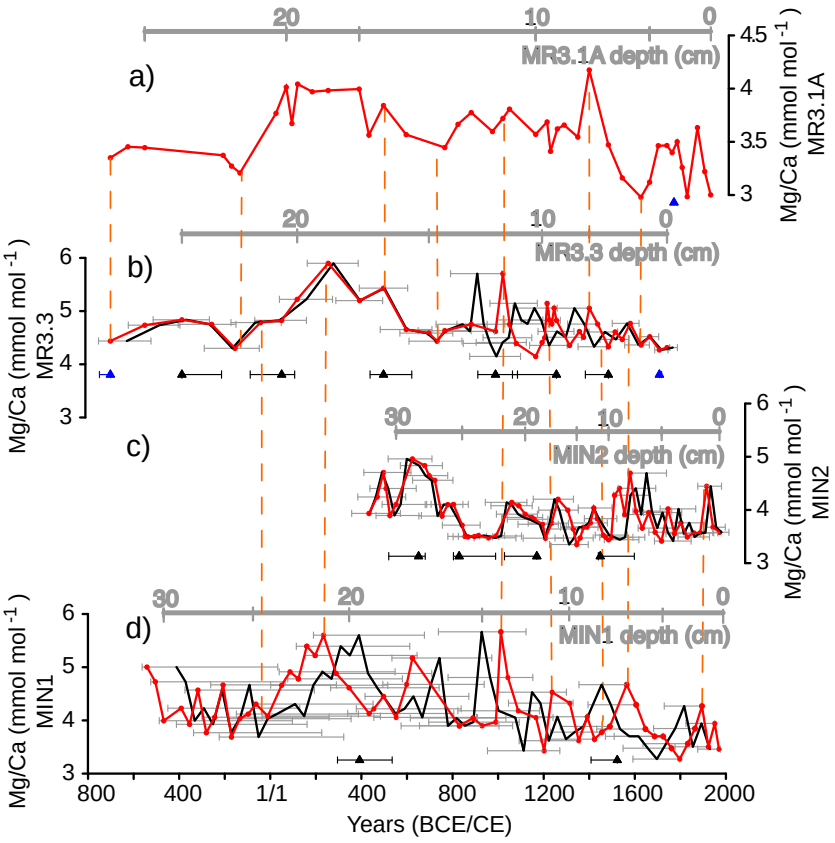

Figure 3.13. Main procedures of multy-proxy chronostratigraphy performed with Mg/Ca records for cores **a)** MR3.1A; **b)** MR3.3; **c)** MIN2, and **d)** MIN1. Final age-depth models are plotted in red. Black plots and grey error bars correspond to Bayesian accumulation age-depth models. Triangles represent to ^{14}C dates (black) and biostratigraphical dates based on planktonic foraminifera (blue), and they are shown below the corresponding core and with their associated 2σ errors. Depths in relation to the final age model can be observed above its corresponding core. Vertical dashed lines (orange) indicate tie points between the different Mg/Ca records (tie points and attendant uncertainties in Table 3.5).

Consequently, the three records have been tuned in base to the main structures and taking into account the 95% confidence of the statistical produced models (Fig. 3.13). The final age-models of MIN1, MIN2 and MR3.3 cores have an average age difference that is below 24 years in reference to the Bayesian models and the 75–63% of the records are into the confidence intervals obtained in the Bayesian models.

The chronology from MR3.3 core has been the base to construct the age model for the

other MR3 cores (MR3.1A, MR3.1B and MR3.2) for which no ^{14}C dates were available (Table 3.3). The chronostratigraphical tools for MR3.1 core have been again the Mg/Ca records (Fig. 3.13; Table 3.5). Additionally, manganese records in all MR3 cores have also been used as an additional chronostratigraphical tool. Mn presence in deep-sea sediments is related to redox processes (Calvert and Pedersen, 1996). Considering that all MR3 cores correspond to the same multicore these Mn rich layers have been used as isochrones. The available Mn records have been measured by two different methods: Mn measured in the bulk sediment by means of XRF Core-Scanner (MR3.1B and MR3.2) and Mn present in the foraminiferal samples and measured by ICP-MS (MR3.3, MR3.1A and MR3.1B). Absolute values were very different between those samples measured with ICP-MS after cleaning the foraminifera with the reductive step (MR3.1A) and those without this cleaning step (MR3.3 and MR3.1B) but the same main features can be correlated between the three cores (Fig. 3.14; Table 3.5).

Table 3.3. Summary of records analysed, and methods utilized in age models.

Core	Records analysed	Age model
MIN1	Mg/Ca-SST, $U^{k'}_{37}$-SST, $\delta^{18}O$	^{14}C, ^{210}Pb, ^{137}Cs, software-simulations, SST-tuning
MIN2	Mg/Ca-SST, $U^{k'}_{37}$-SST, $\delta^{18}O$	^{14}C, ^{210}Pb, software-simulations, SST-tuning
MR3.1A	Mg/Ca-SST, $\delta^{18}O$	^{210}Pb, SST-tuning, geochemical chronostratigraphy, foraminiferal assemblage
MR3.1B	Mg/Ca-SST, $\delta^{18}O$, Geochemical composition	SST-tuning, geochemical chronostratigraphy
MR3.2	Geochemical composition	^{210}Pb, geochemical chronostratigraphy
MR3.3	Mg/Ca-SST, $U^{k'}_{37}$-SST, $\delta^{18}O$	^{14}C, software-simulations, SST-tuning, foraminiferal assemblage

In the case of MR3.1B core (Fig. 3.14b), analysed at ultra-high resolution (0.25 cm slides), the Mn record shows the highest values with peaks over 80 ppb whose Mg/Ca values have been excluded of derived SST records since Mn enrichments can bias Mg/Ca ratios toward higher values and lead to significant overestimation of past

seawater temperatures (Boyle, 1983; Pena et al., 2005, 2008). The top 5 cm of MR3.1A and MR3.2 cores have been dated according to the maxima sedimentation rates using the ^{210}Pb flux.

Final age models and sedimentation rates

According to the obtained chronologies, the period covered by the studied sedimentary sequences is from 759 ± 20 BCE to 1988 ± 18 CE (uncertainties are expressed as the time resolution of the respective core here and in 1σ on the rest of this section), being MR3.1B core the one spanning a longer period (Table 3.4). Total average of mean accumulation rates is 17 ± 4 cm kyr^{-1} with a total mean resolution of 84 ± 18 years.

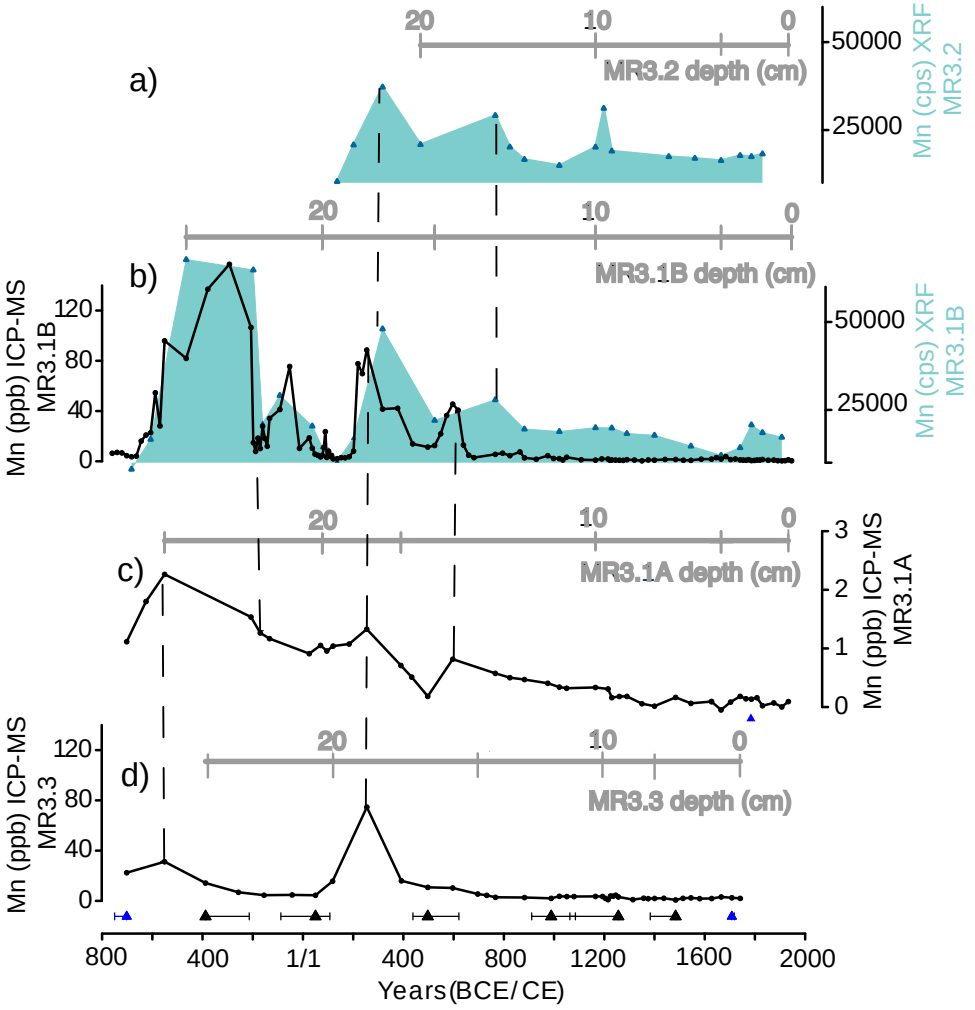

Figure 3.14. Multy-proxy chronostratigraphy performed with Manganese profiles. Blue filled plots represents Mn profiles obtained by XRF Core-Scanner for **a)** MR3.2, and **b)** MR3.1B cores, respectively. Black plots show Mn from trace elements analysed by means of ICP-MS for **b)** MR3.1B, **c)** MR3.1A, and **d)** MR3.3 cores. Vertical dashed lines indicate tie points of geochemical chronostratigraphy (tie points and attendant uncertainties in Table 3.2). Triangles represent to ^{14}C

dates (black) and biostratigraphical dates based on planktonic foraminifera (blue) and they are shown below the corresponding core and with their associated 2σ errors.

Table 3.4. Mean accumulation rates, years covered and mean time resolution of all cores according to final age-depth models.

Core	Mean acc. rate (cm kyr^{-1})	Spanning time (yr)	Mean time resolution (yr cm^{1})
MIN1	14	2528	83
MIN2	25	1538	48
MR3.3	17	2443	78
MR3.1A	15	2635	95
MR3.1B	16	2706	98
MR3.2	15	1797	102

The final mean sedimentation rates obtained in MIN cores, 14 ± 6 and 25 ± 10 cm kyr^{-1}, are very similar with those derivated from Bayesian model simulations, 14 ± 2 and 22 ± 1 cm kyr^{-1}, and those previously published by Moreno et al. (2012), 19 and 23 cm kyr^{-1}. The differences in sedimentation rates between all cores except MIN2 are lower than 3 cm kyr^{-1}, variability that is reasonable due the diverse sediment processes that affect the contouritic system.

Table 3.5. Tie points used on each core to make age models with their attendant errors and indicated in Figures 3.13 and 3.14. Uncertainties correspond to the resolution of each age model on its respective core. Also absolute dates (^{14}C and biostratigraphy based on planktonic foraminiferal assemblage) are indicated. Years are expressed as Before Common Era (BCE) and Common Era (CE).

Core	Composite depth (cm)	Method	Ages (years BCE/CE)	Age-uncertainties interval (years BCE/CE)
MIN1	2-2.5	Mg/Ca	1895 CE	1864-1923 CE
	6.5-7		1564 CE	1523-1606 CE
	7-7.5	^{14}C	1523 CE	1408-1523 CE
	8-8.5		1455 CE	1423-1491 CE
	10.5-11	Mg/Ca	1237 CE	1202-1315 CE
	13.5-14		1012 CE	990-1043 CE
	19-19.2	^{14}C	392 CE	295-535 CE
	20-21	Mg/Ca	234 CE	1970-289 CE
	24-24.5		63 BCE	76-11 BCE
MIN2	1-1.5		1915 CE	1887-1944 CE
	7-7.5	Mg/Ca	1580 CE	1556-1605 CE
	9-9.5		1497 CE	1485-1511 CE
	11-11.5	^{14}C	1448 CE	1440-1598 CE
	16-16.5	Mg/Ca	1263 CE	1235-1306 CE
	18-18.5		1170 CE	1170-1312 CE
	25-25.5	^{14}C	829 CE	804-989 CE
	28.5-29		651 CE	520-680 CE
MR3.3	0.5-1	Foraminiferal Assemblage	1708 CE	1708-1728 CE
	3.5-4		1484 CE	1383-1484 CE
	6.5-7		1256 CE	1063-1256 CE
	12-12.5	^{14}C	989 CE	9111085 CE
	16-17		497 CE	438-621 CE
	20-21		50 CE	88 BCE-107 CE
	24-25		388 BCE	388-214 BCE
	26-27	Foraminiferal Assemblage	702 BCE	798-702 BCE
MR3.1A	5-5.5		1627 CE	1545-1665 CE
	6.5-7	Mg/Ca	1400 CE	1350-1484 CE
	10-10.5		1050 CE	1021-1165 CE
	12.5-13		766 CE	597-824 CE
	13-13.5	Mn ICP-MS	597 CE	497-766 CE
	13.5-14	Mg/Ca	497 CE	433-597 CE
	15-16	Mn ICP-MS	254 CE	184-390 CE
	21-22	Mg/Ca	133 BCE	170 BCE-25 CE
	22-23	Mn ICP-MS	170 BCE	207 -133 BCE
	24-25		551 BCE	625-207 BCE
	26-27	Mg/Ca	702 BCE	779-625 BCE
MR3.1B	13-14	Mn-XRF	618 CE	532-702 CE
	14-14.25	Mn ICP-MS	597 CE	501-683 CE
	15-16	Mn-XRF	317 CE	65-557 CE
	16-16.25	Mn ICP-MS	254 CE	184-506 CE
	23.5-23.75		189 BCE	226-152 BCE
MR3.2	13-14	Mn-XRF	766 CE	468-824 CE
	15-16		317 CE	202-468 CE

3.2 DEEP-WATER FORMATION VARIABILITY IN THE NORTH-WESTERN MEDITERRANEAN SEA DURING THE LAST 2500 YR: A PROXY VALIDATION WITH PRESENT-DAY DATA

Mercè Cisneros[1], Isabel Cacho[1], Jaime Frigola[1], Anna Sanchez-Vidal[1], Antoni Calafat[1], Rut Pedrosa-Pàmies[1], *, Aitor Rumín-Caparrós[1] and, Miquel Canals[1]

[1]GRC Geociències Marines, Departament de Dinàmica de la Terra i de l'Oceà, Facultat de Ciències de la Terra, Universitat de Barcelona, Barcelona, Spain

*Current address: The Ecosystems Center, Marine Biological Laboratory, Woods Hole, USA

Global and Planetary Change 177, 56-68, 2019
https://doi.org/10.1016/j.gloplacha.2019.03.012

3.2.1 Abstract

Here we investigate the sensitivity of deep-water formation in the north-western Mediterranean Sea to climate variability during the last 2500 yr. With this purpose, the grain-size parameter UP10 (fraction >10 μm) is used as a proxy for intensity of deep-water circulation. Such a proxy is first validated through the analysis of oceanographic data collected from October 2012 to October 2014 by means of two deep-water mooring lines equipped with sediment traps and currentmeters in the Gulf of Lion and north of Minorca Island. Enhancements of deep current speed resulted from dense shelf water cascading and open-sea deep convection in February 2013 leading to dense-water formation. The grain-size distribution of settling particles from sediment traps collected during 2012-2013 shows a distinctive particle mode and high UP10 values correlated to deep-water formation. These data are consistent with grain-size values in sediment cores from the north of Minorca, thus supporting the validity of the UP10 parameter to reconstruct changes of intensity in deep-water formation and associated near-bottom currents.

The deep-water sediment record of the north of Minorca for the last 2.5 kyr shows that the strongest deep-water formation events occurred during relatively warm intervals,

such as the Roman Period (123 BCE-470 CE1), the end of the Medieval Climate Anomaly (900-1275 CE) and the first part of the Little Ice Age (1275-1850 CE). By contrast, our data indicate a progressive reduction in the overturning conditions during the Early Middle Ages (470-900 CE) resulting in weaker deep-water formation events during most of the Medieval Climate Anomaly. Intense deep-water formation events appear to be mostly associated with periods of enhanced Evaporation-Precipitation balance rather than to buoyancy loss due to winter cooling only. Our results suggest that warm sea surface temperature during spring months could have played an important role by increasing the Evaporation–Precipitation balance and favouring buoyany loss by increased of salinity.

The comparison our data with other oceanographic and climatic records indicates a change in the proxy relation before and after the Early Middle Ages. Western Mediterranean Deep Water and Levantine Intermediate Water behave in opposite way after the Early Middle Ages, thus indicating that the previously proposed Mediterranean see-saw pattern in the Evaporation-Precipitation balance also influenced convection patterns in the basins during the last 1500 yr. These changes are discussed in the frame of different configurations of the North Atlantic Oscillation and East Atlantic/ West Russian modes of atmospheric variation.

3.2.2 Introduction

The western Mediterranean Sea, particularly the Gulf of Lion (GoL), is one of the few marine regions where deep-water formation (DWF) takes place and it occurs almost each winter through two oceanographic processes: dense shelf water cascading and open-sea deep convection (MEDOC Group, 1970; Canals et al., 2006; Durrieu et al., 2013; among others). These two processes are driven by intense sea-atmosphere heat exchanges, and the subsequent buoyancy loss of offshore waters, induced by cold, dry, and persistent N–NW winds, resulting in the formation of the Western Mediterranean Deep Water (WMDW) (Fig. 3.15).

The WMDW mass is an important component of the Mediterranean thermohaline circulation. It fills the deep basin locating in depths below the Levantine Intermediate

[1] BCE: Before Common Era years. CE: Common Era years.

Water (LIW), and partly contributes in determining the characteristics of the Mediterranean outflow water (MOW) (Stommel et al., 1973; Lionello et al., 2006). Finally, changes in MOW could influence the Atlantic thermohaline circulation by enhancing the general salinity of the north Atlantic region (Bryden and Stommel, 1984; Lionello et al., 2006). In addition, the Mediterranean acts as a heat loss region from the Atlantic, since outcoming waters are colder than the incoming surface waters through the Strait of Gibraltar (Wu et al., 2007). Besides, changes in the strength of the Mediterranean thermohaline circulation associated with climate changes would also impact Mediterranean Sea Surface Temperature (SST) with immediate consequences in climate conditions of the adjacent areas (Somot et al., 2006). Changes in the SST would also have an impact on dense water formation rates and thus on hydrographic properties (Beuvier et al., 2010). Consequently, changes in DWF in the GoL could have oceanographic and climatic consequences at regional but also at large scales.

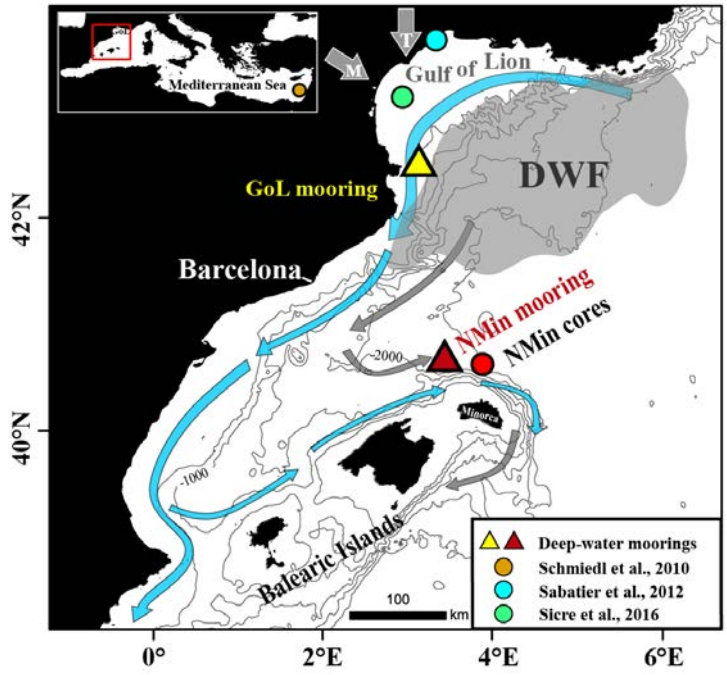

Figure 3.15. Central-western Mediterranean Sea. Circles locate sediment cores. Red circle: NMin cores (this study); Green circle: KSGC-31 and GolHo-1B cores; blue circle: PB06 core; orange circle: SL 112 core in the Eastern Mediterranean. Triangles indicate NMin mooring (red, this study) and GoL mooring (yellow, Sanchez-Vidal et al., 2015). Grey short arrows: Tramuntana and Mistral winds. Blue and grey arrows: surface and deep sea circulation, respectively; the shadow area in the Gulf of Lion (GoL) indicates where the deep-water formation (DWF) occurs.

During the last years an intense effort has been carried out to increase the understanding on DWF in the western Mediterranean Sea and complete the existing instrumental data series (e.g.: Houpert et al., 2016; Somot et al., 2016; Estournel et al., 2016; Bosse et al.,

2016, 2017; Durrieu de Madron et al., 2017). Long, high-quality and homogenised instrumental time-series covering the past few centuries exist for climate parameters like air temperature, precipitation and sea level pressure (Lionello et al., 2006 and references therein). Nevertheless, instrumental data on deep-water environments is still relatively short. In this way, paleorecords suppose a valuable contribution to enhance our temporal view of DWF evolution and better understand its connection with climate variability.

Some previous paleoceanographical studies have reconstructed changes in western Mediterranean DWF, particularly in relation to the last glacial millennial scale climate variability, when the GoL DWF weakened in relation to Dansgaard-Oeschger warm insterstadials (Cacho et al., 2000, 2006; Sierro et al., 2005; Frigola et al., 2008; Rodrigo-Gámiz et al., 2011). Or even, it has also been proposed that dense shelf water cascading may have played an important role during the Messinian salinity crisis (Rovieri et al., 2014). Few evidences indicate some centennial scale Holocene oscillations in the intensity of deep-water currents associated with WMDW formation (Frigola et al., 2007) but these records lack the resolution for a detailed characterization of the historical record, especially the last two millennia. Past changes in deep convection in the eastern Mediterranean Sea have been intensively studied in relation to Sapropel deposition, particularly for the Holocene Sapropel 1 (Rohling et al., 2015 and references therein), but very little information exists for the last two millennia (Schmiedl et al., 2010; Incarbona et al., 2016).

The overall goal of this study is: i) to validate the application of the UP10 parameter in the Minorca promontory as a proxy of DWF in the GoL in base to oceanographical data, and then ii) to characterize the DWF evolution in the GoL during the last 2.5 kyr, to better understand its long-term variability and its relation with regional climate conditions. With this aim the generated records allow us to analyse the high frequency variability for climate/historical moments of the two millennium of the Common Era. The different climatic periods have been defined as follows (BCE=years before Common Era and, CE=Common Era): Talaiotic Period (TP, until 123 BCE), Roman Period (RP; 123 BCE-470 CE), “Early Middle Ages” (EMA; 470-900 CE), Medieval Climate Anomaly (MCA; 900-1275 CE), Little Ice Age (LIA; 1275-1850 CE) and, the Industrial Era (IE) as the most recent period (see Cisneros et al., 2016 for further

information; EMA is equivalent to Dark Middle Ages)

The UP10 parameter has been analysed in two deep-sea multicores recovered north of Minorca Island (NMin) (Fig. 3.15). UP10 records with a preliminary age model were already published in Moreno et al. (2012). These age models were complemented and improved following a multiproxy chronology by Cisneros et al. (2016), where a 2 kyr SST stack record from a larger group of multicores was discussed.

3.2.3 Study area

Oceanographic settings

The Mediterranean Sea has been described as a 'miniature ocean' (Stanley, 1972; Margalef, 1985) that operates as a concentration basin (Bethoux et al., 1999), where the freshwater input does not compensate the overall evaporation. Consequently, Mediterranean dense waters are formed in specific basins filling intermediate and deep depths. Levantine Intermediate Water (LIW) forms in the eastern Mediterranean while Western Intermediate Water and Tyrrhenian Dense Water (MEDOC, 1970; Millot, 1999) form in the Western Mediterranean Basin at intermediate depths. DWF processes also take place in both basins forming the Eastern and Western Mediterranean Deep Water Masses (EMDW and WMDW, respectively).

The two main factors that seem to explain >70 % of the interannual variance of the DWF phenomenon are: i) the interannual variability of the winter-integrated buoyancy loss driven by the heat loss; and ii) the water column preconditioning before the convection mostly driven by both the heat and salt contents of the surface layer (Somot et al., 2016). Water mass properties in the western basin can be also related to variations in the characteristics of the surface and intermediate waters like Atlantic waters and LIW (Schroeder et al., 2011; Somot et al., 2016; Estournel et al., 2016).

The exchange of energy between the atmosphere and the sea surface takes place through net air-sea heat exchange, which is the sum of four fluxes: latent and sensible heat fluxes (linearly proportional to the wind speed and the air-sea temperature or humidity difference) and, short and long-wave radiation fluxes (function of air temperature, humidity, and cloudiness) (Deser et al., 2010).

In addition, dense waters in the GoL can be also originated by dense shelf water cascading process (Canals et al., 2006), flowing down the slope towards the deep basin, interacting with the open-sea convected waters (Bethoux et al., 2002; Durrieu de Madron et al., 2013, 2017). These cascading events are also linked to cold, dry, and persistent N–NW winds that induce sea-atmosphere heat losses. Although major open-sea convection events can occur while cascading is weak (Durrieu de Madron et al., 2017) and, the WMDW mass is mainly renovated by the open-sea convection process, the cascading contribution has also been proposed as a relevant contributor (Bethoux et al., 2002; Puig et al., 2013; Durrieu de Madron et al., 2013).

Controls on Mediterranean inter-annual climate variability

The Mediterranean climate is influenced by both mid-latitude and tropical dynamics (Lionello et al., 2006), constituting a transitional zone, high sensitive to climate variations. The seasonal variability is characterized by mild wet winters and warm to hot, dry summers. Processes of annual formation of WMDW are very much related to specific local atmospheric configuration (López-Jurado et al., 2005). Direct observations during recent years describe four main winter modes of interannual atmospheric variability in the North Atlantic/Europe region that exert a control on air-sea heat exchange in the Mediterranean Sea: i) the North Atlantic Oscillation (NAO); ii) the East Atlantic (EA); iii) the Scandinavian (SCAN); and iv) the East Atlantic/West Russian (EA/WR) patterns (Cassou et al., 2010; Josey et al., 2011). i) The NAO can be defined as a large-scale meridional see-saw on atmospheric pressures along the North Atlantic sector (Hurrell, 1995). The remaining modes of atmospheric variability present a less clear picture due to have signature only during part of the year, among another factors (Trigo et al., 2006). ii) The EA pattern, first described by Wallace and Gutzler (1981), consists of a north-south pressure dipole structurally similar to NAO but with the centres spanning from east to west in the North Atlantic and showing a stronger subtropical connection in the lower-latitude center (Barnston and Livezey, 1987). iii) The SCAN pattern has a southwest-northeast pressure dipole with the stronger pole centred to the east of Scandinavia. It influences the generation of northern European precipitation anomalies (Bueh and Nakamura, 2007) and in the Mediterranean region has been considered to have weaker influence than the other modes (Josey et al., 2011). Lastly, iv) the EA/WR pattern has been proposed to impact the Mediterranean region

rainfall (Krichak and Alpert, 2005) and its heat loss in winter, creating an east-west dipole structure over the Mediterranean stronger than that from the NAO.

Different combinations between the atmospheric patterns can cause distinct effects on the present-day climate. For instance, NAO/EA configurations with the same (opposite) sign have been coincident with homogeneous (heterogeneous) spatial correlations of both precipitation and temperature (Comas-Bru and McDermott, 2014). In particular, during years with numerous days of predominant EA patterns and only a few number of NAO- days, correspond to years of intense DWF in the north-western Mediterranean (NWMed) region (Bethoux et al., 2002; Puig et al.; 2013; Durrieu de Madron et al., 2013).

3.2.4 Material and methods

Mooring measurements and sediment cores

Present and past deep-sea conditions have been evaluated combining data from two mooring lines and two sediment cores from the same area (Fig. 3.15).

The first mooring (CCC1000) was deployed in the GoL margin in the axis of the Cap de Creus Canyon at 968 m of water depth (henceforth GoL-mooring; 42º18.88'N, 3º33.52'E) during October 2012-May 2014. The mooring was equipped with a Nortek Aquadopp currentmeter placed at 23 m above the bottom (mab). Sampling intervals were set at 20 min during the period 2012-13 and at 15 min during 2013-2014, respectively. This mooring also included a Technicap PPS 4/3 cylindro-conical sediment trap at 25 mab, with a sampling period of 15 days (Table 3.6). More details about this mooring are described in Sanchez-Vidal et al. (2015).

The second mooring (MIN-I) was deployed in the sediment drift built by the action of the southward branch of the WMDW north of Minorca at 2052 m of water depth (henceforth NMin-mooring; 40º28.05'N, 03º40.64'E) during October 2012-October 2014. The mooring was equipped with a Nortek Aquadopp currentmeter placed at 5 mab and with a SBE37 at 5 mab (2012-2013) or 25 mab (2013-2014). Sampling intervals were set at 15 min (SBE37 and Aquadopp) in 2012-2013, and 10 min (SBE37) and 30 min (Aquadopp) in 2013-2014. It was also equipped with a Technicap PPS 3/3

cylindro-conical sediment trap at 25 mab, with a sampling period ranging from one or two months (Table 3.6).

MINMC06-1 and MINMC06-2 multicores (henceforth NMin1 and NMin2; 40º29' N, 04º01' E; 2391 m water depth; 31 cm and 32.5 cm core length, respectively) were recovered in the north Minorca sediment drift in the path of the southward branch of the S-SE flowing WMDW, very close to the NMin-mooring location (Fig. 3.15). The suitability of this location for detailed paleoceanographic reconstructions was already pointed out by previous studies (Sierro et al., 2005; Frigola et al., 2007, 2008; Cisneros et al., 2016). More detailed information on the sediment drift formation and characteristics can be found in Velasco et al. (1996) and Frigola et al. (2007).

Table 3.6. Sediment trap samples from the GoL (Cap de Creus Canyon; CCC1000) and NMin (MIN-I) calculated in this study to validate UP10. "t" corresponds to the total grain-size fraction and "dc" to de-carbonated. TMF: Total Mass Flux. UP10 proxy integrates the grain-size fraction coarser than 10 µm.

Sample	Opening day	Closing day	TMF (mg m^{-2} d^{-1})	UP10	Near-bottom current velocity peaks (cm s^{-1})	Hydrological situation
CCC1000-III-3 (t)	16/1/12	1/2/12	3639.4	27.5	11	Pre-cascading
CCC1000-III-4 (t)	1/2/12	16/2/12	68156.9	51.2	126	Cascading (start)
CCC1000-V4 (dc)	1/2/13	15/2/13	3102.0	21.5	13	Pre-cascading
CCC1000-V5 (dc)	15/2/13	1/3/13	64130.1	42.2	84	Cascading
CCC1000-V6 (dc)	1/3/13	16/3/13	25674.1	29.3	82	Post-cascading
MIN-I-6 (t)	1/3/13	1/4/13	479.4	31.4	24	Pre-open sea deep convection (and start)
MIN-I-6 (dc)	1/3/13	1/4/13		33.7		
MIN-I-8 (t)	1/4/13	1/6/13	896.3	42.4	23	Open sea deep convection (and post)
MIN-I-8 (dc)	1/4/13	1/6/13		38.2		

Particle size-characterization

The grain-size distribution of the total and de-carbonated fractions was analysed in both NMIN cores (0.5 cm resolution) and in the settling particles collected with the sediment traps of the two moorings. The analysed settling particles corresponds to periods comprised into 2012-2013 (see Table 3.6) and represent conditions of before, during and after a DWF event.

Grain size analyses were performed using a Coulter LS230 Laser Diffraction Particle Size Analyser (CLS). Prior to analysis, on the one hand, organic matter from dried

samples was removed with a 10% H_2O_2 solution, thus allowing to obtain the total fraction grain size distribution. On the other hand, the lithic grain-size particle distribution was obtained after 1M HCl treatments of samples for carbonates removal, thus obtaining the de-carbonated fraction. In core NMin2 both total and de-carbonated fractions were analysed while in NMin1, the longest core, only the total fraction was analysed. For settling particle samples a combination of both total and de-carbonated fraction was analysed (Table 3.6). The total fraction of the sediment integrates the lithic fraction, including detrital carbonates, but also carbonate tests representing local biological production. By these reason, the de-carbonated fraction is considered to better represent the bottom currents intensity, since the local pelagic productivity signal has been removed with the carbonates (McCave et al., 1995). However, carbonates removal also affects those from detrital origin, mostly fines, and consequently the grain-size percentages of the de-carbonated fraction use to show higher values, due to the closure effect to 100%. In addition, differences between total and de-carbonate fractions from the same core can also be affected by down-core differences in carbonate content. Thus, the down-core discussion and interpretations are centred in the results obtained with the de-carbonated fraction from core NMin2. However, total fraction results from NMin1 are also incorporated in the discussion since it allows the extension of the record to the RP. This is supported by the relatively good correlation between total and de-carbonate fractions from core NMin2 (Fig. 3.21 in Supplementary material).

CLS measures sizes between 0.04 μm and 2000 μm determining grain-size distributions as volume percentages based on diffraction laws (McCave et al., 1986; Agrawal et al., 1991). It is assumed that this diffraction is given by spherical particles and the particle size is provided as an ‘‘equivalent spherical diameter’’. For this reason, laser diffraction methods are claimed to underestimate plate-shaped clay mineral percentages. To correct this underestimation, content of clays included sizes until 8 μm, as proposed by Konert and Vandenberghe (1997). CLS accuracy and repeatability (precision) were tested by running the standard LS size control G15 and using glass beads with pre-defined parameters, which gave standard deviations of 2.4% and coefficients of variation better than 0.3%, respectively.

Particle size distributions are discussed considering the grain-size fraction coarser than 10 μm (UP10 fraction), which was previously applied as an indicator of deep currents

variability in this area (Frigola et al., 2007). Other grain-size parameters different to the UP10 are often used in the literature for the study of deep-water currents intensity, as is the case of the sortable silt (SS) fraction (McCave et al., 1995; 2017) and the silt/clay ratio (Hall and McCave, 2000). The SS fraction (10-63 μm) is defined as the coarser fraction of the silt with noncohesive behaviour during transport and deposition (McCave et al., 1995). Thus, neither the SS nor the silt/clay parameters take into account the fine sand subpopulation (>63 μm), which is integrated in the UP10 fraction that, as discussed below, could be reworked by strong contour currents (Frigola et al., 2007; 2008). Nevertheless, we have compared the results for the three mentioned grain-size parameters in both studied cores and settling particles measurements from NMin and the results are comparable (Fig. 3.21).

3.2.5 Results and Discussion

Winter 2013: dense shelf water cascading and open-sea deep convection

Deep oceanographic conditions (temperature and current velocity) obtained by the moored instruments in the GoL and NMin (comprised into October 2012-October 2014), presented by first time in the present study, are shown in Fig. 3.16 together with meteorological data. The average deep-water temperature recorded during October 2012-May 2014 in both sites is very similar, around 13.2 °C (Fig. 3.16f-g). However, the GoL-mooring time serie shows important changes in winter 2013 in contrast to the rather stable temperatures from the NMin-mooring. These GoL temperature changes involved a drop of 1.63 ºC (from 13.07 to 11.44 ºC) by the end of February 2013 in the Cap de Creus canyon axis, while downcanyon near-bottom current speeds enhanced up to 84 cm s^{-1} (Fig. 3.16f-g). Both temperature drop and downcanyon flow evidences the occurrence of a dense shelf water cascading event. Cold and dry northerly winds produced cooling and densification of surface waters in the continental shelf (Fig. 3.16b-c) and, subsequently, waters sunk, overflowed the shelf edge, and cascaded downslope through south-west GoL's submarine canyons to at least 1000 m depth where the mooring was located. The winter 2013 cascading event has been described as a reemergence of the stronger one occurring in winter 2012 (1-3 ºC drop and currents up to 125 cm s^{-1}) (Durrieu de Madron et al., 2013; Sanchez-Vidal et al., 2015). 'Reemergence' refers to the easy reproduction of a deep and cold mixed layer because of the thermal anomalies of the previous year (Somavilla et al., 2009).

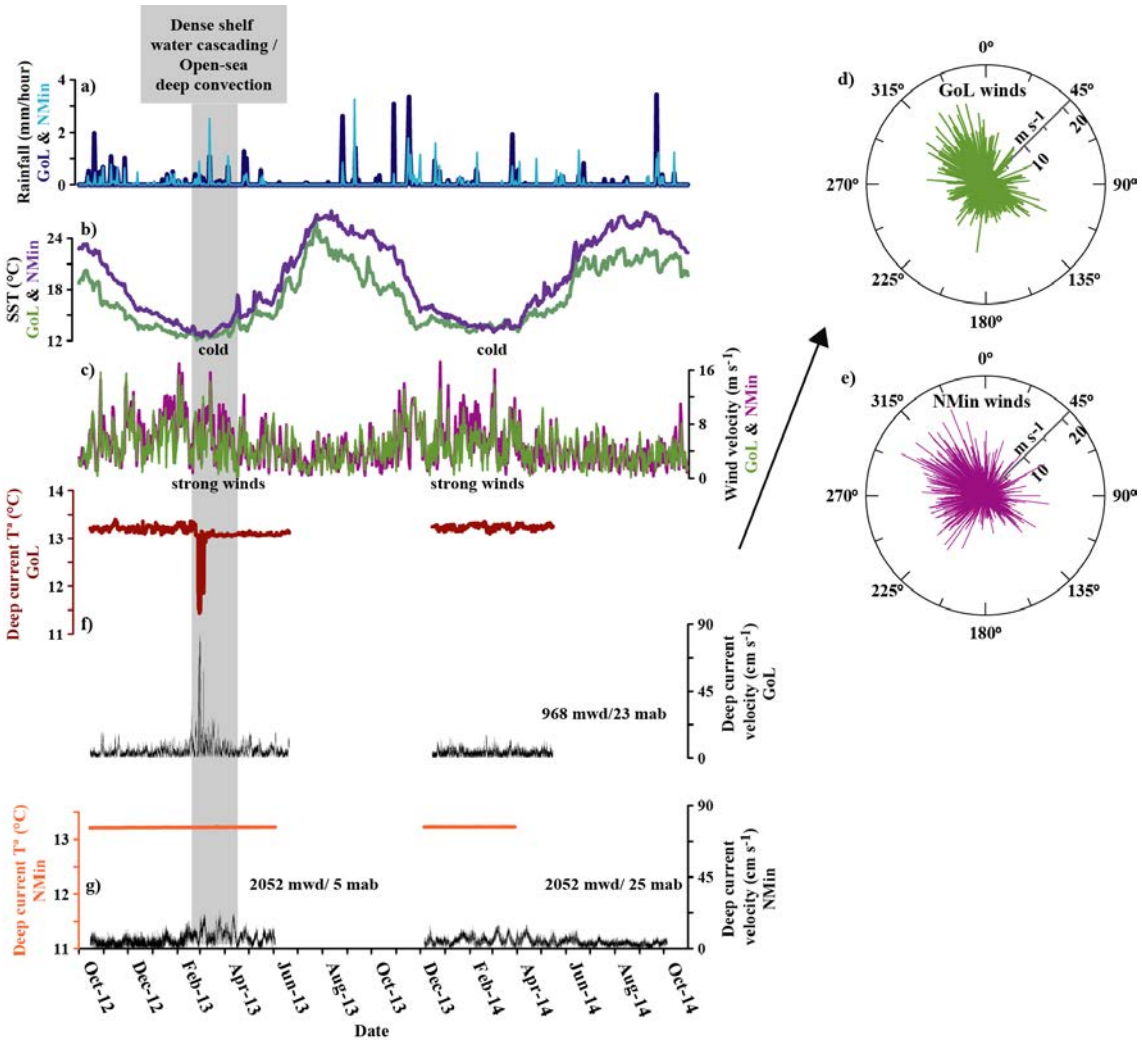

Figure 3.16. Meteorological conditions and mooring measurements during October 2012-October 2014 in the Gulf of Lion (GoL) and north Minorca (NMin). Meteorological data: a) Precipitation in GoL (http://www.esrl.noaa.gov/psd/in) and Mallorca Island (www.balearsmeteo.com/sant_lorenzo); b-e) Sea Surface Temperature (SST), wind velocity and direction (http://www.esrl.noaa.gov/psd/in). Oceanographic data obtained from GoL and NMIN moorings (this study): f-g) Near-bottom current temperature and velocity in each mooring site. Depths of the moorings (mwd: m water depth) and of the currentmeters (mab: meters above the bottom) are also indicated. The grey vertical bar indicates the period of deep-water formation (dense shelf water cascading/open-deep sea convection).

The same intense atmospheric forcings in February 2013 also triggered open-sea convection offshore (Waldman et al., 2017; Durrieu de Madron et al. 2017; Houpert et al., 2016), after increase air–sea heat fluxes (Fig. 3.22 in Supplementary material). Sea surface cooling and destabilization of the water column involved deep vertical mixing and an exceptional bottom reaching convection event, as also shown as a very low chlorophyll patch in February 2013 (Fig. 3.23 left in Supplementary mateial). After this intense convective episode, long-lived mesoscale eddies were formed and the new WMDW was advected southwestwards towards the north of Minorca (Testor and Gascard, 2006; Bosse et al., 2016, 2017; Waldman et al., 2017; Margirier et al., 2017).

A series of peaks in near-bottom currents, up to 24 cm s^{-1} were detected in the NMin-mooring during February-April 2013 and one of them is coincident with the described event in the GoL-mooring (Fig. 3.16g). These NMin highest velocities are in agreement with those maxima (28 cm s^{-1}) recorded by the LION-mooring line located in the centre of open-ocean convection zone during the end of February 2013 (Durrieu de Madron et al., 2017). Therefore, spreading of bottom-reaching open-sea convection may have reached north Minorca as well.

Overall, the same atmospheric forcing triggered dense water formation in the continental shelf and open-sea convection, and both lead to increased near-bottom current speeds. In any case, both DWF processes have demonstrated to produce active resuspension and redistribution of deep sediments (Canals et al., 2006; Stabholz et al., 2013; Puig et al., 2013). Therefore, we hypothesise that sediment cores from the NMin sediment drift are sensitive to the described changes in deep currents associated with WMDW production processes and we propose their applicability to reconstruct the operation mode of this convection cell during the last 2.5 kyr.

UP10: proxy for DWF in the past

We have evaluated the effects of increased bottom currents during DWF events on present-day sediment transport and particle grain-size distributions in the GoL and NMin, and investigated their linkage to the grain-size of the sedimentary record for the study of DWF in the recent past.

On the one hand, grain-size distributions of settling particles in both investigated areas when no DWF occurred show 3 main modes at 0.3, 5-10 (dominant class) and 20-40 μm, and UP10 values ranging from 21.5-33.7% (Fig. 3.17a-b). In contrast, during DWF there is a shift in grain-size towards coarser values, characterized by the appearance of a mode >40 (and ~ <100 μm), which is hardly present in the other samples (Fig. 3.17a-b). Thus, maxima UP10 values occurred during the period of DWF (38.2-51.2 %) together with maxima particle fluxes and the highest variability in the grain-size distribution (Fig. 3.17a; Table 3.6). In fact, transport of large amounts of suspended coarse sediments from the continental shelf down-canyon towards the deep basin was already previously described during GoL cascading currents (Canals et al., 2006; Puig et al., 2008; Sanchez-Vidal et al., 2008). Furthermore, the intensification of deep currents

NMin due to DWF should be able to resuspend and transport coarse particles (Martín et al., 2010; Stabholz et al., 2013). Overall, this evidences that DWF, either through cascading or convection, has a direct impact on the grain-size distribution and the UP10 of settling particles in both regions.

On the other hand, grain-size distributions from sediment core samples recovered in the NMin sediment drift show similar modes to those described for settling particles. Thus, samples with the finest/coarsest grain-size distributions from NMin1 and NMin2 cores have a comparable grain-size distribution of setting particles when no DWF occurred/during DWF, respectively (Fig. 3.17c-f). The good resemblance in the grain-size distribution of settling particles and the sedimentary record supports the interpretation of high UP10 values from samples of the NMin sediment drift as a proxy of increased current velocities near the seafloor related to DWF (Fig. 3.18). Most of the analysed sediment core samples show very similar distributions to that of settling particles corresponding to relatively calmed conditions. However, some intervals from the sediment cores are characterized by the appearance of sediment mode populations well above 40 μm, between 100 and120 μm and up ~220 μm, and in some specific intervals arrive up to ~300 and 400 μm. These very coarse samples also show high mode variability, minor sorting, and high UP10 values (Fig. 3.17 and 3.18). Such coarse grain populations were not detected in settling particle, possibly because sediment core samples may reflect deep current speeds from stronger DWF events than those from year 2013 but also it needs to be considered that sediment traps collect particles several meters above the bottom (25 mab) and may not have the same intensity than those at the actual sea floor. These coarser sediment mode populations could possibly correspond to lag deposits, like a consequence of armouring processes (Hüneke et al., 2008; Gambacort et al., 2014).

Maximum near bottom current speeds recorded during the spreading of dense water during winter 2013 (24 cm s^{-1}, at 25 mab) exceed the threshold to transport particles up to 40 μm, as calculated by the Sedtrans model (Li and Amos, 2001). However, some of

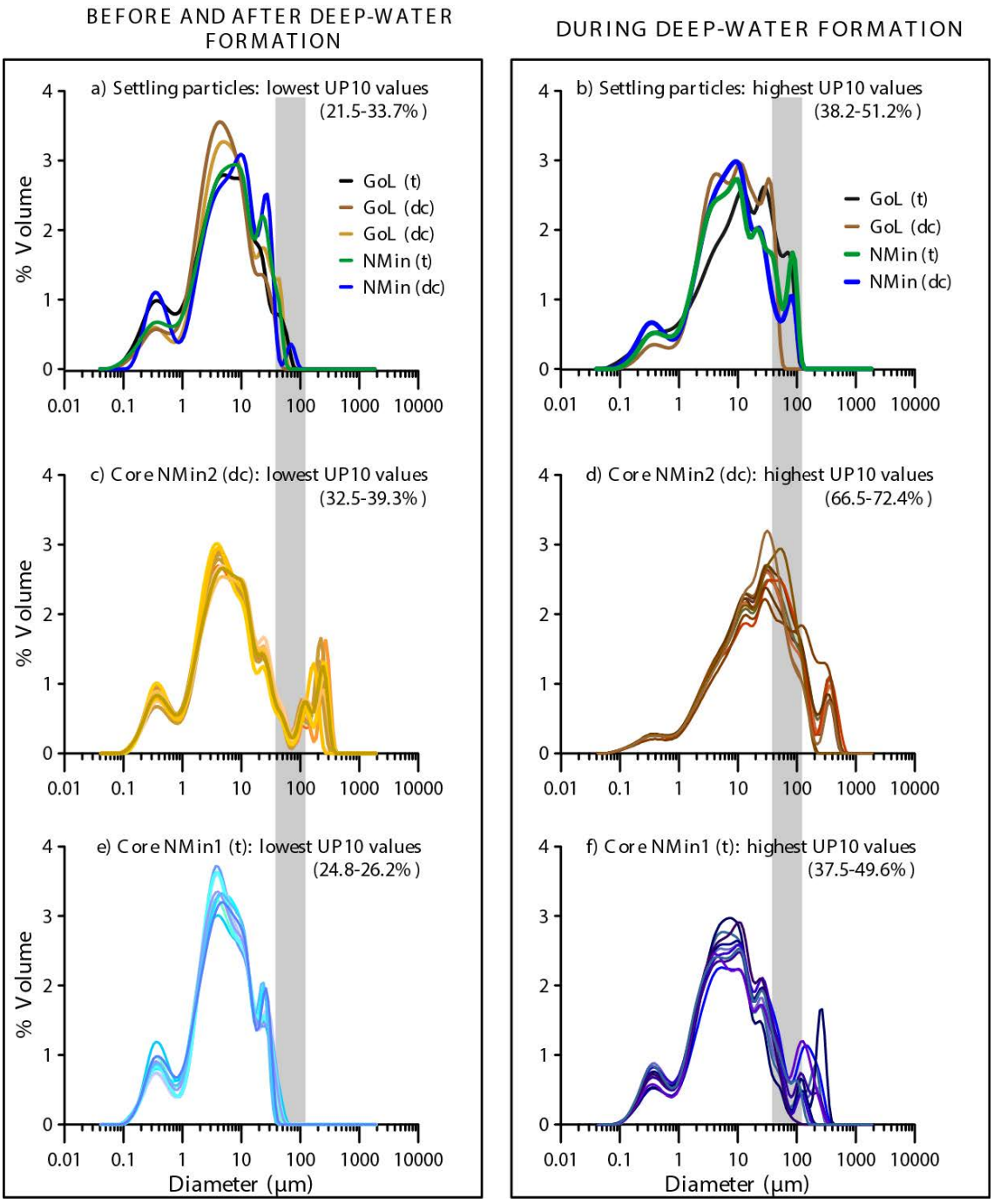

Figure 3.17. Grain-size modal distributions from settling particles (a-b) and multicores (c-f). Figures of the left correspond to periods before and after the Deep-Water Formation (DWF) and those in the right to periods during DWF. (t) corresponds to total grain-size fraction and (dc) to de-carbonated. GoL samples correspond to Mooring CCC1000 and NMin samples to Mooring MIN-I (see Table 3.6 for entire code of samples). c-d) the 10 highest and 10 lowest UP10 values of NMin2 core (dc), respectively and; e-f) the 10 highest and 10 lowest UP10 values of NMin1 core (t). Vertical grey bars indicate grain-size particle band from ~40 to 100 μm.

the down-core sediment samples with modes up to 220 μm, would require currents up to 39 cm s^{-1} at the bottom and 61 cm s^{-1} at 25 mab to start their transport. This difference in the transport capacity of bottom currents and those at 25 mab may explain

in part the general coarser modes found in the sediment cores. The coarsest grain-size distributions of these down-core samples are ~300 and 400 μm and would require bottom-currents up to 45 and 47 cm s^{-1} respectively, to start their transport at the sea bottom. Although these calculated bottom velocities were not recorded in 2013 by the NMin mooring, they are comparable to the maximum velocities detected in the centre of the basin (45 cm s^{-1} at 30 mab) during the 2013 DWF event (Durrieu de Madron et al., 2017). Overall, this suggests that during some periods of the past, DWF events could have been more energetic than that recorded in 2013, although most of the studied time period were of similar intensity or even weaker (Fig. 3.18).

Consequently, these results supports that currents in the studied region can be strong enough to transport fine sand particles and, in consequence, the UP10 fraction better represent transport changes in the whole particle size spectrum of the region and thus, this is a reliable proxy for deep-water intensity currents related to DWF events in the GoL (Frigola et al., 2007).

DWF variability: the last 2500 years

Long-term trends from the UP10 record of the de-carbonated fraction of NMin2 core and that of the total fraction of NMin1 core present a significant correlation for the common spanned period (r = 0.3, p value ≤ 0.0465) (Fig. 3.18). The major differences between both cores are observed during the EMA. UP10 percentages are always higher in the de-carbonated than in the total samples, likely due to removal of fine carbonate particles and the closure effect of 100%. For this reason, differences in absolute values between the two cores (Fig. 3.17) mainly reflect different sample treatment and not different sensitivity to the speed changes. Note that UP10% are very comparable between the two records measured in the total fraction (Fig. 3.21). Consequently, oscillations in the UP10 record of the total fraction from NMin1 core can be mainly derived from deep current intensity changes, thus allowing expanding the studied period to 500 BCE. Thus, both de-carbonate and total UP10 records from NMin2 and NMin1 cores, respectively, will be discussed in parallel.

Two main intervals with high values of the UP10 fraction suggest intense DWF in the GoL during the last 2.5 kyr. The first time interval includes the RP and the EMA (~0-900 CE), while the second one corresponds to the end of the MCA and the LIAa

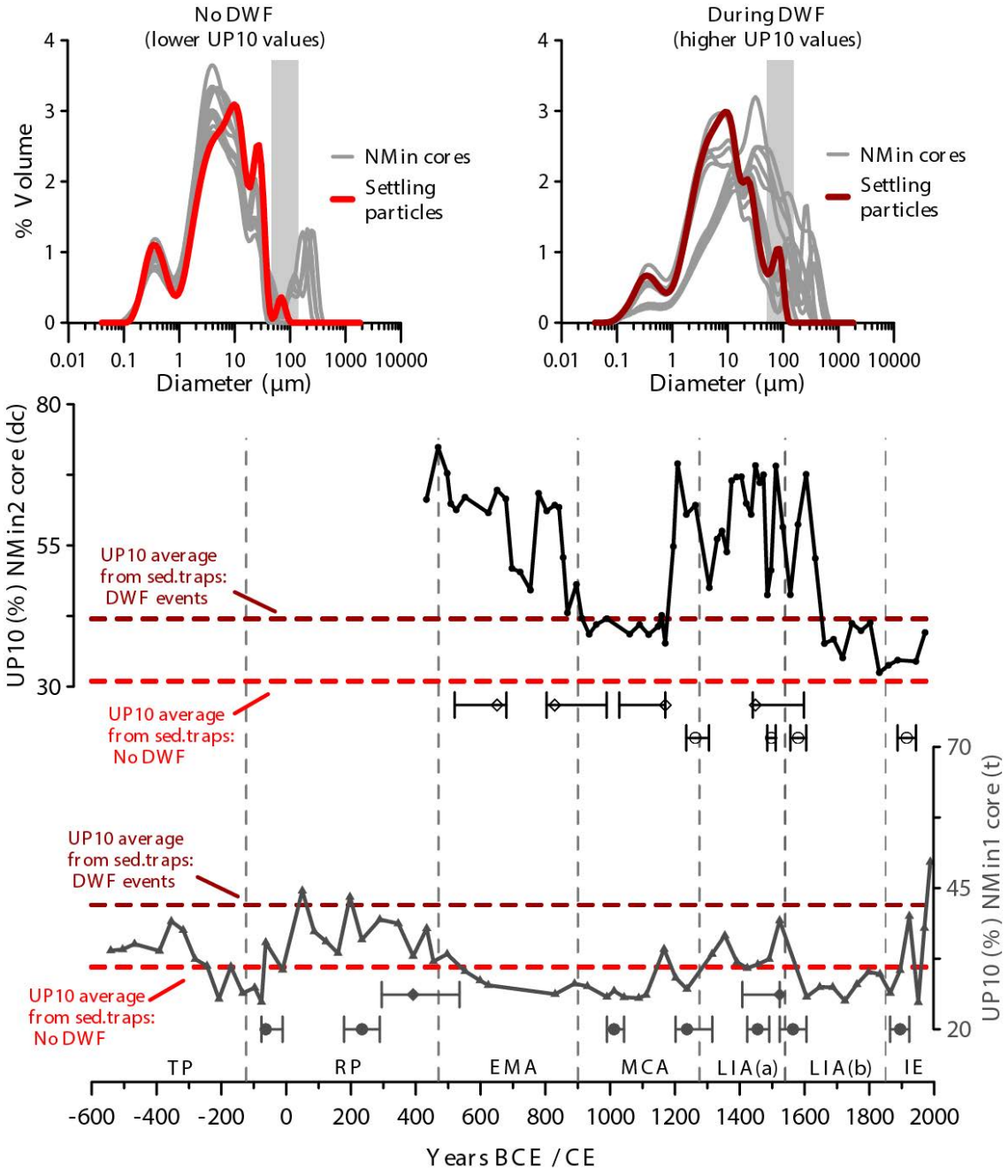

Figure 3.18. Upper panels: grain-size distribution from NMin sediment cores (grey) and from the de-carbonated fraction from settling particles (red) in NMin during deep-water formation (DWF; right) and during periods without DWF (left). Data from MIN cores represent the 10 samples with highest (right) and the 10 lowest (left) UP10 values. Vertical grey bars indicate grain-size particle band from ~40 to 100 µm. **Lower panel:** UP10 proxy records (total fraction >10 µm) for NMin2 cores (black) and NMin1 (grey) during the last 2.5 kyr. (dc) corresponds to the de-carbonated grain-size fraction and (t) to the total grain-size fraction. Age control points with their associated error bars are shown below each core, diamonds represent absolute calibrated ^{14}C AMS dates and circles represent tie points using different chrono-stratigraphic markers (Cisneros et al., 2016 for details). Horizontal dashed lines represent average UP10 values obtained during DWF (dark red) and before or after DWF (light red) in settling particle from NMin. Years are expressed as Before Common Era (BCE; negative years) and Common Era (CE). Vertical dashed lines indicates the limits of the discussed periods: TP: Talaiotic Period; RP: Roman Period, 123 BCE-470 CE; EMA: Early Middle Ages, 470-900 CE; MCA: Medieval Climate Anomaly, 900-1275 CE; LIA: Little Ice Age, 1275-1850 CE; IE: Industrial Era.

(~1150-1600 CE). Relative low values of the UP10 fraction during the MCA, and especially those during the end of the LIAb and the beginning of the IE, suggest reduced DWF conditions. During RP and EMA remarkable winter vertical mixing has been already suggested by Margaritelli et al. (2018) through observations of foraminiferal assemblages studied in cores recovered in NMin.

The role of SST and humidity conditions

Considering that cold and dry northerly winds promote DWF events in the GoL, it could be expected that cold winters were coincident with intense DWF. This relation can be reviewed for the past using our GoL-DWF record and an alkenone-SST record from the GoL (Sicre et al., 2016) (Fig. 3.19a). The alkenone-SST record is interpreted to mostly reflect annual average temperatures, although slightly biased towards the cold season since no alkenone production occurs during summer months in the Mediterranean (Cacho et al., 1999; Sicre et al., 2016; Cisneros et al., 2016). Relatively cold SST in the GoL are coincident with high UP10 (r = -0.3, p value ≤ 0.0270) during the last 1.5 kyr (Fig. 3.19a). However, focusing on the multi-centennial trends, not significant correlations have been observed during each of the spanned periods except for the RP (r = 0.5, p value ≤ 0.0175).

A further insight in the past connection between GoL-DWF and SST conditions can be performed through the study of two additional SST-stack records alkenone and Mg/Ca proxies derived, respectively, which were produced in a multi-core collection from the NMin region, including those cores used in our UP10 records (Cisneros et al., 2016). Correlation of the NMin alkenone-SST and Mg/Ca-SST records with the DWF record (r = 0.4, p value ≤ 0.0002 and r = 0.6, p value = 0, respectively) suggests that strongest DWF events occurred preferentially during periods with relatively warm SST (Fig. 3.19a and b). According to that, the strongest DWF events preferably occurred during relatively warm periods such as the RP (r = 0.7, p value = 0), or the end of the MCA and LIAa. The Mg/Ca-SST drop during the EMA is also accompanied by a relative reduction in the intensity of the DWF events (r = 0.8, p value = 0). In this case, the record comparison does not have any time uncertainty since both records share the same chronology (Cisneros et al., 2016). This relation is surprising since Mg/Ca-SST record from the planktonic foraminifera *Globigerina bulloides* has been interpreted in this region to reflect mostly spring season conditions (Cisneros et al., 2016) and it is not

reflecting any cooling intensification associated with the strong DWF periods. Therefore, this proxy comparison suggests that SST was not the main factor controlling past changes in GoL-DWF.

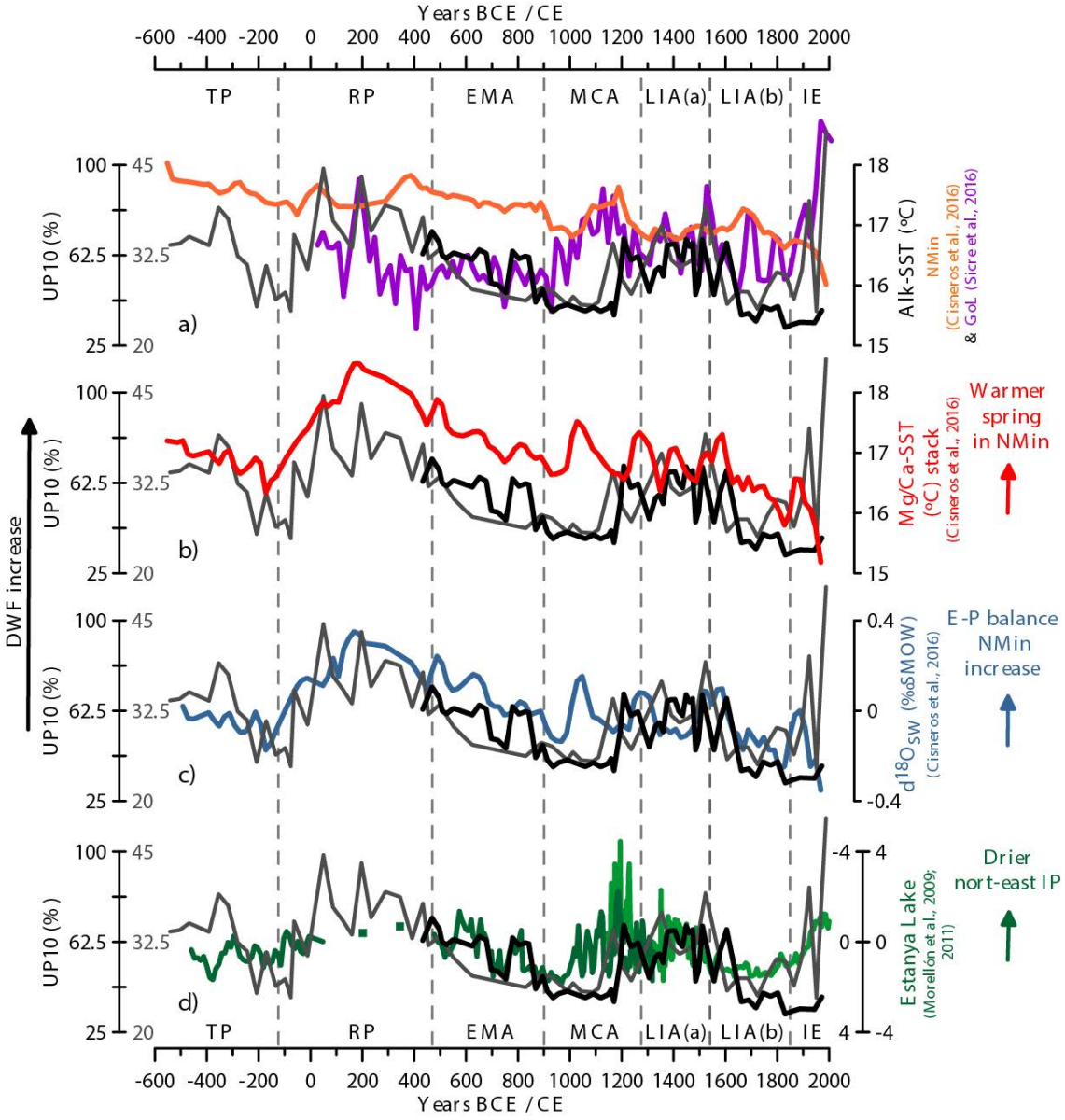

Figure 3.19. UP10 record from NMin2 core (de-carbonated grain-size fraction) and from NMin1 core (total grain-size fraction) are represented in black and grey, respectively, using left axes and compared to: a) Alk-SST from Gulf of Lion (GoL) plotted at 20 yr-time steps (Sicre et al., 2016) and, Alk-SST from NMin (Cisneros et al., 2016); b) Mg/Ca-SST from NMin (Cisneros et al., 2016); c) Evaporation-Precipitation (E-P) balance reconstructed by $\delta^{18}O_{SW}$ in NMin cores (Cisneros et al., 2016); d) Salinity reconstruction in the north-east Iberian Peninsula (IP) from Estanya Lake salinity (PCA 2) (Morellón et a., 2009; 2011).

Changes in the hydrological cycle can also be critical determining surface salinity and thus the intensity of DWF. In order to explore this, we have compared the $\delta^{18}O_{sw}$ stack record, based on the Mg/Ca-SST stack reconstruction discussed above (Fig. 3.19b)

(Cisneros et al., 2016), with our UP10 record (Fig. 3.19c). The $\delta^{18}O_{sw}$ record is interpreted to reflect Evaporation-Precipitation (E-P) balance, which in this case would potentially integrate a wide region from the Western Mediterranean Basin. At multi-centennial time-scale and for the last 1.5 kyr, they show a good correlation (r = 0.6, p value = 0) indicating intensification (weakening) of DWF in the GoL generally during increased (decreased) E-P sea-water balances. This positive relation is particularly clear for the EMA (r = 0.7, p value ≤ 0.0001) and the LIAb (r = 0.8, p value ≤ 0.0008) as well as for the RP (r = 0.6, p value ≤ 0.0011). An additional humidity/aridity record, in this case more sensitive to local precipitation, is the salinity reconstruction from Estanya Lake, north-eastern Iberian Peninsula (Morellón et al., 2009; 2011). Despite time uncertainties between the records (Fig. 3.19d), they show a coherent pattern of stoked DWF (high UP10 values) during drier conditions (saltier waters) in Estanya Lake (r = 0.4, p value ≤ 0.0004). This is the case for the second half of the MCA and LIA(a) while the more humid conditions of the LIA(b) are coincident with weaker DWF. The low resolution of the record for the RP does not allow analysing this time interval.

Overall, strong DWF (maximum UP10 values) occurred during both cold and relatively warm periods in the GoL. This could be partly explained by the fact that net heat flux during wintertime, which is mainly dominated by the latent heat flux (Houpert et al., 2016), is not directly reflected in the SST records. Latent heat flux, and to a lesser extent sensible heat, control anomalies in the winter net heat exchanges in the GoL (Josey, 2003; Schroeder et al., 2010). Regarding to the remarkable similarity between our DWF and the Mg/Ca-SST records (Fig. 3.19b), warm spring SST could be also related to drier conditions, thus both favouring E-P balance and a subsequent increase of salinity. For example, this can be observed at the end of the MCA, with a relative increase in SST coincident with drier conditions in the north-east Iberia, thus allowing an intensification of DWF. More research is needed in order to better understand the relationship between changes in SST and hydrology conditions on DWF in this region. However, similar results have been also observed in south-west Australia, a region that is also located in a Mediterranean climate zone (Pattiaratchi et al., 2011). Consequently, these results further support that SST have not been the only critical factor determining the intensification of DWF during the last 2.5 kyr, and point that buoyancy loss, although might be ultimately triggered by SST cooling, is highly controlled or modulated by E-P balance and thus hydrological conditions in the north-western

Mediterranean region. This is consistent with the discussed changes in regional humidity patterns which could contribute to the buoyancy-loss and preconditioning of the Mediterranean waters by enhancing E-P balance. This preconditioning has been considered the second driving factor in deep water convection (Somot et al., 2016), favouring the weakening of the vertical stratification due to reduced freshwater inputs and subsequent increases in surface salinities (Stommel, 1972). This preconditioning mechanism has been proposed to occur towards late-summer early-autumn, when storm winds and water cooling contribute to mix the surface layer and to progressively erode the seasonal thermocline (Puig et al., 2013). Further research in needed regarding past changes in surface salinity conditions in the paleoceanographic record in order to disentangle the relationship between surface conditions and deep-water convection.

Atmospheric teleconnections and links with the Eastern Mediterranean Basin

In order to assess potential connections between our reconstructed GoL-DWF record with changes in the wind system over the GoL during the last 1.5 kyr, we compare it with a storm activity record based on lagoon sediments from the GoL (Sabatier et al., 2012). Both records show certain similarity ($r = -0.3$, p value ≤ 0.0249) indicating that periods of enhanced storm activity were generally coincident with strong DWF activity (Fig. 3.20a). The higher coherence between high/low UP10 values and high/low GoL-storm activity is observed during EMA ($r = -0.8$, p value ≤ 0.001). Correlation is also remarkable during RP ($r = -0.5$, p value ≤ 0.0032), MCA ($r = -0.5$, p value ≤ 0.0191) and LIAa ($r = -0.6$, p value ≤ 0.0236) but lower or even opposite correlation occurs during the LIAb and IE. Frequently, eastern storms are related to northerly storms, but depending on atmospheric conditions, northerly winds in this region do not always promote eastern storms and vice versa. At present, eastern storms in the NWMed region are responsible of very high wave heights (i.e. significant wave heights of 8 m and maxima of 14 m) and important erosive episodes (Palanques et al., 2006; Sanchez-Vidal et al., 2012). Possibly, during periods of high correlation and a remarkable storminess (like RP, EMA and LIAa) both kind of storms were coupled and could have been enhanced intensity or more frequent occurrence. The confluence of both kinds of storms frequently can provoke maxima transport of suspended sediment towards the deep sea (e.g.: Rumín-Caparrós et al., 2013). However, during moments with no correlation, these two types of storms could have been rather decoupled, observing stronger storms in the GoL during the periods of minimum DWF such as the LIAb (Fig. 3.20a).

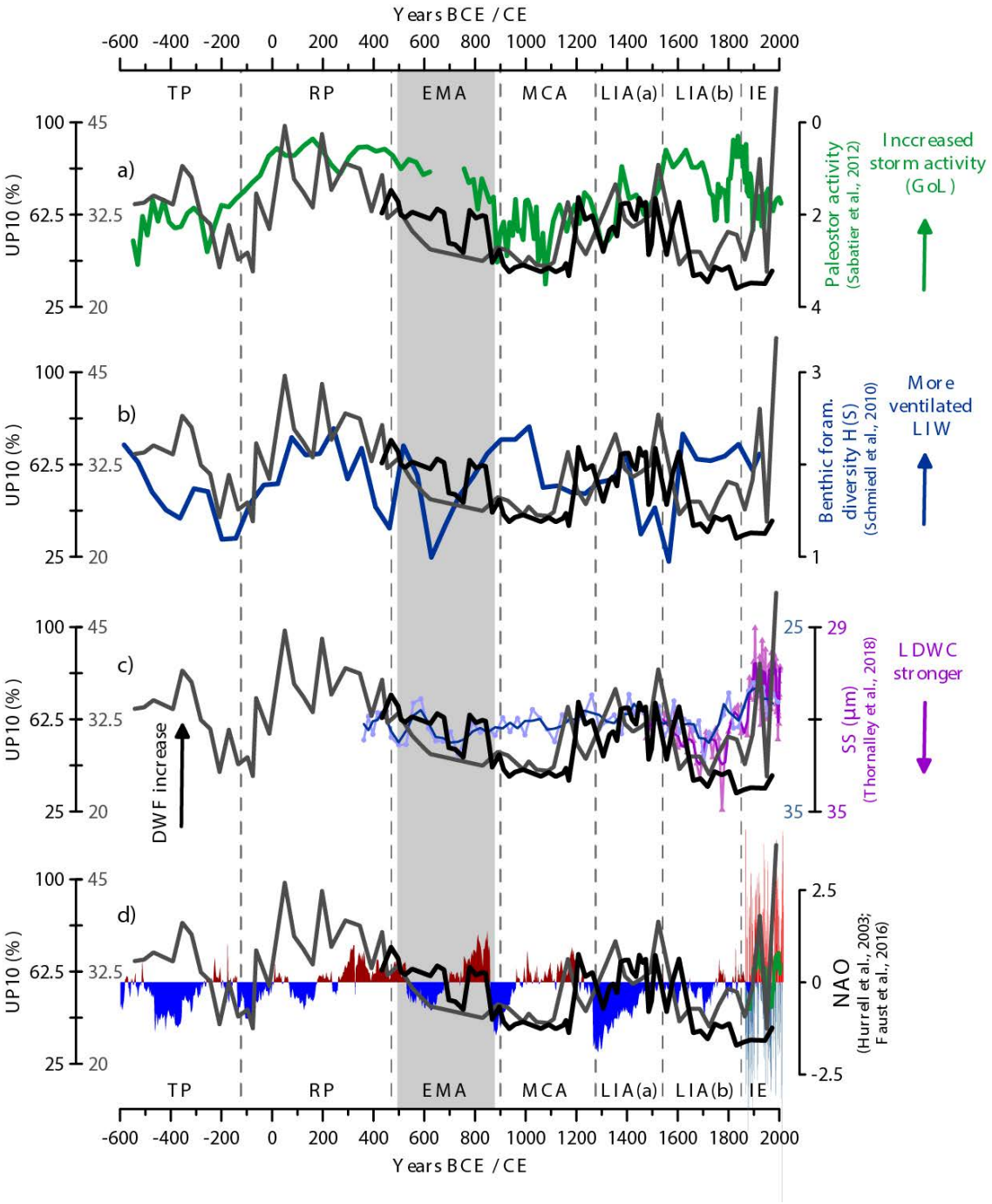

Figure 3.20. UP10 record from NMin2 core (de-carbonated fraction) and from NMin1 core (total fraction) are represented in black and grey, respectively, using left axes and compared to: a) Paleostorm activity (Sabatier et al., 2012) in the Gulf of Lion (GoL); b) Benthic foraminifera diversity in the eastern Mediterranean Sea (Schmiedl et al., 2010); LIW: Levantine Intermediate Water. c) Labrador Deep-Water Current (LDWC) reconstructed by Sortable silt (SS) mean grain-size (Thornalley et al., 2018); d) North Atlantic Oscillation (NAO) for the instrumental period (green plot: running averaged 20 yr; Hurrell et al., 2003) and reconstruction for the last 2.5 kyr (Faust et al., 2016).

The relationship between GoL-DWF and LIW is explored in base to the records of benthic foraminifera diversity index in SL 112 core from the Liguriam Sea (892 m water depth; Schmiedl et al., 2010) (Fig. 3.20b). An almost opposite behaviour between

the two records can be identified for the periods before and after the EMA (Fig. 3.20b). During the TP and RP maximum ventilation in LIW coexisted with strong GoL-DWF ($r = 0.6$, p value = 0), supporting a contribution of the LIW salt content promoting deep convection in the GoL during these periods. During the EMA low oxygenation values in the LIW may indicate reduced contribution of this water mass to the NWMed that probably led to the recorded progressive slowdown of GoL-DWF. In a general way, it should be noted that during the last 1.5 kyr, both basins records show a rather opposite trend (Fig. 3.19b) suggesting a decoupling between the two water masses ($r = -0.5$, p value = 0). Interestingly, an east-west Mediterranean climate sea-saw pattern has been previously described for the last 1.1 kyr (Roberts et al., 2012). Thus, the opposite trends described in the hydro-climatic conditions between Iberia and Turkey during the MCA and LIA could also induce opposite response in the convection cells of the WMDW and the LIW. This Mediterranean bipolar see-saw has been associated with the combination of different climate modes proposing a complex non stationary behaviour of the NAO with other atmospheric modes (Josey et al., 2011; Roberts et al., 2012).

The relationship between DWF in the GoL and the North Atlantic Ocean has previously been established for the last glacial period, at millennial scale, when an opposite correlation was described between the two thermohaline overturning cells. A weakening of North Atlantic DWF occurred during cold stadial phases, associated with surface freshening driven by ice melting events, while GoL-DWF was enhanced, associated with enhanced Mediterranean dry conditions and Northwesterlies intensity over the GoL (Cacho et al., 2000, 2006; Sierro et al., 2005). The comparison of our results to the SS mean size record from the Labrador Sea as a proxy of DWF in this region (Thornalley et al., 2018), also shows a relative opposite trend for the last 1.5 kyr (Fig. 3.19c). In particular, at sub-centennial scale, this relation is significant during the MCA ($r = -0.5$, p value ≤ 0.0248). The DWF reduction in the Labrador Sea during IE has been associated with surface water freshening, but the forcing mechanism for the previous 1.5 kyr changes remain unclear (Thornalley et al., 2018). Studies focussed on the last decades observations have directly connected Labrador Sea water properties to NAO conditions,, through an enhanced westerlies cooling associated with NAO+ (i.e: Kieke and Yashayaev 2015; Ortega et al. 2017). Nevertheless, other factors such as the precise location of the pressure cells can complicate this relation (Kim et al., 2016).

Thus, we explore the potential role of NAO conditions on GoL-DWF for the last 2.5 kyr by comparing our record with the NAO reconstruction from Faust et al.(2016). This comparison suggests again different behaviour during the intervals before and after the EMA (Fig. 3.19d). During the TP and RP, positive NAO phases are mainly related to GoL-DWF increments, while negative NAO phases are related to rather weak DWF events ($r = 0.3$, p value ≤ 0.0271). For the last 1.5 kyr, although a tempting opposite trend can be observed, no-significant correlation has been obtained, and thus a decrease or increase in DWF occurred indistinctly during both positive and negative NAO phases. For instance, intense negative NAO values during the LIAa coincide with DWF increases, a relation previously suggested for Holocene millennial-centennial time-scale events (Ausín et al., 2015). But, in contrast, during the LIAb weaker negative NAO phases occurred during DWF decreases. These results suggest that GoL-DWF and the NAO do not present a stationary relationship and other mechanisms should interact in the transference of the atmospheric signal from high to medium latitudes. During recent positive NAO phases,, a reinforced atmospheric high-pressure system over the western Mediterranean Sea enhances westerly winds circulation, enhancing the E-P balance of the region (Tsimplis and Josey, 2001). However, at annual and multidecadal scales the strength and location of the NAO dipole can be also modulated by the EA and the SCAN patterns (Comas-Bru and McDermott, 2014). Moreover, negative states of the EA pattern can favour the influence of cold and dry winds over the Mediterranean Sea, modulating the air-sea heat exchange (Josey et al., 2011).

In this way, the DWF changes observed in the NWMed region cannot be explained by a single factor such as storm intensity in the GoL, changes in LIW formation or NAO phases and intensity. One of the most remarkable and consistent observation is the rather opposite relationship prior and post the EMA between our GoL-DWF record and both LIW and NAO reconstructions. The EMA climate conditions have been described by several studies as cold and unstable in the northern hemisphere and especially in Europe (Helama et al., 2017 and references therein). Consequently, we propose that these changes during the EMA responded to a variation in the interplay of different atmospheric modes. Such a change has also been described by Sánchez-López et al. (2016) over the Iberian Peninsula, who proposed the dominance of opposite/similar signs in the NAO/EA phases before/after the EMA. Interestingly, changes in the EA/WR and NAO patterns produce opposite hydrological responses in the western-

eastern basins of the Mediterranean Sea (Josey et al., 2011). Such a situation could explain the described Mediterranean see-saw in both hydrological conditions (Roberts et al., 2012) and GoL-DWF and LIW intensity after the EMA (Fig. 3.19b). This would support an enhancement in the influence of the EA/WR patterns over the Mediterranean after the EMA (Roberts et al., 2012). A negative state of EA/WR pattern would enhance GoL-DWF and reduce LIW formation and vice versa for a positive pattern (Josey et al., 2011).

3.2.6 Conclusions

The evolution of DWF in the Gulf of Lion (GoL) during the last 2.5 kyr is analysed using the grain-size parameter "UP10" (fraction >10 μm) from two multicores recovered at the sediment drift north of Minorca (NMin). The suitability of the UP10 parameter to track the intensity of deep-water currents related to DWF events has been tested through data from two moorings deployed in the GoL and the NMin regions during 2012-2014. Events of DWF are detected in both moorings by increases in deep-water currents, which reached up to 24 cm s^{-1} in the NMin location, the closest one to the studied sediment cores. Grain-size analyses of settling particles from sediment traps, reveal the appearance of a particular mode (40-100 μm) in samples related to DWF events, a distribution that agrees with those from sediment samples with high UP10 values and interpreted to reflect enhanced deep sea currents.

The sediment core results characterized the Roman Period (RP; 123 BCE-470 CE) like a period of intense DWF. After that, during the Early Middle Ages (EMA; 470-900 CE) intense DWF also occurred but a progressive decrease has been observed until the Medieval Climate Anomaly (MCA; 900-1275 CE), which is mostly characterized by relatively weak overturning conditions with the exception of the ending century. Our data depict the Little Ice Age (LIA; 1275-1850 CE) in two substages: i) The LIAa with enhanced overturning that started by the end of the MCA ii) LIAb with reduced GoL overturning. Thus, strongest DWF rates took place during rather warm periods, as RP as well as the LIAa, and according to the SST records from the NMin region. When the UP10 is compared to the SST evolution from the GoL, intense DWF occurred during both cold and relatively warm periods.

Therefore, these observations point out that SST was not the only critical factor

determining the DWF during the last 2.5 kyr and thus, buoyancy loss was not only driven by SST cooling. Based on our NMin-SST data, we propose that warmer springs played an important role in DWF by increasing the Evaporation-Precipitation balance and favouring buoyancy loss by increased salinity. Such a connection between GoL-DWF and regional hydrological conditions is further supported by coherent covariation between our record and a humidity record from the Iberian Peninsula during the last 1.5 kyr. However, exploring sea surface salinity changes during the past by means of independent proxies to SST reconstructions would likely provide clues in the control of deep water overturning at millennial and centennial, or even, decadal time scales.

The comparison of our GoL-DWF record with other oceanographic-climatic records highlights a complex interaction of different regional atmospheric and oceanic factors to explain the DWF evolution of the last 2.5 kyr. Overall, we describe a major change in the behaviour of the GoL-DWF during the EMA. Previously to the EMA, strong GoL-DWF occurred coincident to strong LIW ventilation and positive NAO phases. In contrast, after the EMA GoL-DWF and LIW present opposite trends and any clear relation is evident with the NAO index. This post-EMA situation is consistent with a previous described east-west climate sea-saw in the Mediterranean region and could respond to a stronger influence of the EA/WR pattern that would complicate the NAO influence over the region.

Acknowledgments. We thank the anonymous reviewers for their very useful comments and discussions on this work. ERC-Consolidator Grant TIMED (683237), CHIMERA (CTM2016-75411-R), Consolider-Redes (CTM2014-59111-REDC) and PERSEUS (FP7-OCEAN-2011-3-287600) financially supported this research. We thank Generalitat de Catalunya Grups de Recerca Consolidats for grant 2017 SGR 315 to GRC Geociències Marines. MINMC06 cores were recovered during the HERMES 3 cruise in 2006 on board R/V Thethys II. We are in debt with the crew and scientists onboard SOCIB and Lluerna for their help in the mooring deployment and recovery.

We are grateful to M. Guart (Dept. de Dinàmica de la Terra i de l'Oceà, Universitat de Barcelona) for her help in the laboratory. Mercè Cisneros benefited from a fellowship of the University of Barcelona. Isabel Cacho thanks the ICREA-Academia programme from the Generalitat de Catalunya.

Data Availability

Datasets related to this article can be found at https://data.mendeley.com/datasets/mymcnbhkpm/draft? a=1182c022-4439-46ed-8404-322e6262eb02, an open-source online data repository hosted at Mendeley Data.

3.2.7 References

Agrawal, Y. C., McCave, I. N., Riley, J. B., 1991. Laser diffraction size analysis. In: Syvitski, J. P.M. (Ed.), Principles, Methods, and Application of Particle Size Analysis. Cambridge University Press, Cambridge, 119–129.

Ausín, B., Flores, J.A., Sierro, F.J., Cacho, I., Hernández-Almeida, I., Martrat, B. Grimalt, J.O., 2015. Atmospheric patterns driving Holocene productivity in the Alboran Sea (Western Mediterranean): a multiproxy approach. Holocene 25, 1-13, doi:10.1177/0959683614565952.

Barnston, A. G., and Livezey, R.E., 1987. Classification, seasonality and persistence of low-frequency atmospheric circulation patterns, Mon. Weather Rev., 115, 1083–1126. doi:10.1175/1520-0493(1987)115<1083:CSAPOL>2.0.CO;2.

Bethoux, J., Gentili, B., Morin, P., Nicolas, E., Pierre, C., Ruiz-Pino, D., 1999. The Mediterranean Sea: a miniature ocean for climatic and environmental studies and a key for the climatic functioning of the North Atlantic. Progress in Oceanography 44, 131–146. doi:10.1016/S0079-6611(99)00023-3

Bethoux, J.P., Durrieu de Madron, X., Nyffeler, F., Tailliez, D., 2002. Deep water in the western Mediterranean: Peculiar 1999 and 2000 characteristics, shelf formation hypothesis, variability since 1970 and geochemical inferences. Journal of Marine Systems 33–34, 117–131. doi:10.1016/S0924-7963(02)00055-6.

Beuvier, J., F. Sevault, M. Herrmann, H. Kontoyiannis, W. Ludwig, M. Rixen, E. Stanev, K. Béranger, and S. Somot (2010), Modeling the Mediterranean Sea interannual variability during 1961–2000: Focus on the Eastern Mediterranean Transient, J. Geophys. Res., 115, C08017, doi:10.1029/2009JC005950.

Bosse, A., Testor, P., Houpert, L., Damien, P., Prieur, L., Hayes, D., Taillandier, V., Durrieu de Madron, X., d'Ortenzio, F., Coppola, L., Karstensen, J., Mortier, L., 2016. Scales and dynamics of Submesoscale Coherent Vortices formed by deep convection in the northwestern Mediterranean Sea: Vortices in the NW Mediterranean Sea. Journal of Geophysical Research: Oceans 121, 7716–7742. doi:10.1002/2016JC012144

Bosse, A., Testor, P., Mayot, N., Prieur, L., D'Ortenzio, F., Mortier, L., Le Goff, H., Gourcuff, C., Coppola, L., Lavigne, H., Raimbault, P., 2017. A submesoscale coherent vortex in the Ligurian Sea: From dynamical barriers to biological implications. Journal of Geophysical Research: Oceans. doi:10.1002/2016JC012634

Bryden, H. L., and Stommel, H. M., 1984. Limiting processes that determine basic features of the circulation in the Mediterranean Sea. Oceanol. Acta 7(3), 289–296.

Bueh, C., Nakamura, H., 2007. Scandinavian pattern and its climatic impact, Q. J. R. Meteorol. Soc. 133, 2117–2131. doi:10.1002/qj.173.

Cacho, I., Grimalt, J.O., Pelejero, C., Canals, M., Sierro, F. J., Flores, J. A., Shackleton, N. J., 1999. Dansgaard-Oeschger and Heinrich event imprints in Alboran Sea temperatures. Paleoceanography 14, 698–705.

Cacho, I., Grimalt, J.O., Sierro, F.J., Shackleton, N., Canals, M., 2000. Evidence for enhanced Mediterranean thermohaline circulation during rapid climatic coolings. Earth and Planetary Science

Letters 183, 417–429.

Cacho, I., Shackleton, N., Elderfield, H., Sierro, F.J., Grimalt, J.O., 2006. Glacial rapid variability in deep-water temperature and δ18O from the Western Mediterranean Sea. Quaternary Science Reviews 25, 3294–3311. doi:10.1016/j.quascirev.2006.10.004

Canals, M., Puig, P., de Madron, X.D., Heussner, S., Palanques, A., Fabres, J., 2006. Flushing submarine canyons. Nature 444, 354–357. doi:10.1038/nature05271

Cassou, C., Minvielle, M., Terray, L., Périgaud, C., 2010. A statistical dynamical scheme for reconstructing ocean forcing in the Atlantic. Part I: weather regimes as predictors for ocean surface variable, Climate Dynamics 36(1–2), 19–39.

Cisneros, M., Cacho, I., Frigola, J., Canals, M., Masqué, P., Martrat, B., Casado, M., Grimalt, J.O., Pena, L.D., Margaritelli, G., Lirer, F., 2016. Sea surface temperature variability in the central-western Mediterranean Sea during the last 2700 years: A multi-proxy and multi-record approach. Climate of the Past 12, 849–869. doi:10.5194/cp-12-849-2016

Comas-Bru, L., McDermott, F., 2014. Impacts of the EA and SCA patterns on the European twentieth century NAO-winter climate relationship: Impacts of EA and SCA patterns on NAO-winter climate relationship. Quarterly Journal of the Royal Meteorological Society 140, 354–363. doi:10.1002/qj.2158

Deser, C., Alexander, M. A., Xie, S. P., Phillips, A. S., 2010. Sea Surface Temperature Variability: Patterns and Mechanisms. Ann. Rev. Mar. Sci., 2, 115–143. doi:10.1146/annurev-marine-120408-151453

Durrieu de Madron, X., Houpert, L., Puig, P., Sanchez-Vidal, A., Testor, P., Bosse, A., Estournel, C., Somot, S., Bourrin, F., Bouin, M.N., Beauverger, M., Beguery, L., Calafat, A., Canals, M., Cassou, C., Coppola, L., Dausse, D., D'Ortenzio, F., Font, J., Heussner, S., Kunesch, S., Lefevre, D., Le Goff, H., Martín, J., Mortier, L., Palanques, A., Raimbault, P., 2013. Interaction of dense shelf water cascading and open-sea convection in the northwestern Mediterranean during winter 2012: Shelf Cascading and open-sea convection. Geophysical Research Letters 40, 1379–1385. doi:10.1002/grl.50331

Durrieu de Madron, X., Ramondenc, S., Berline, L., Houpert, L., Bosse, A., Martini, S., Guidi, L., Conan, P., Curtil, C., Delsaut, N., Kunesch, S., Ghiglione, J.F., Marsaleix, P., Pujo-Pay, M., Séverin, T., Testor, P., Tamburini, C., the ANTARES collaboration, 2017. Deep sediment resuspension and thick nepheloid layer generation by open-ocean convection: BNL generation by open-oean convection.. Journal of Geophysical Research: Oceans 122, 2291–2318. doi:10.1002/2016JC012062

Estournel, C., Testor, P., Damien, P., D'Ortenzio, F., Marsaleix, P., Conan, P., Kessouri, F., Durrieu de Madron, X., Coppola, L., Lellouche, J.-M., Belamari, S., Mortier, L., Ulses, C., Bouin, M.-N., Prieur, L., 2016. High resolution modeling of dense water formation in the north-western Mediterranean during winter 2012-2013: Processes and budget: Modeling of dense water convection. Journal of Geophysical Research: Oceans 121, 5367–5392. doi:10.1002/2016JC011935

Faust, J.C., Fabian, K., Milzer, G., Giraudeau, J., Knies, J., 2016. Norwegian fjord sediments reveal NAO related winter temperature and precipitation changes of the past 2800 years. Earth and Planetary Science Letters 435, 84–93. doi:10.1016/j.epsl.2015.12.003

Frigola, J., Moreno, A., Cacho, I., Canals, M., Sierro, F.J., Flores, J.A., Grimalt, J.O., 2008. Evidence of abrupt changes in Western Mediterranean Deep Water circulation during the last 50kyr: A high-resolution marine record from the Balearic Sea. Quaternary International 181, 88–104. doi:10.1016/j.quaint.2007.06.016

Frigola, J., Moreno, A., Cacho, I., Canals, M., Sierro, F.J., Flores, J.A., Grimalt, J.O., Hodell, D.A., Curtis, J.H., 2007. Holocene climate variability in the western Mediterranean region from a deepwater sediment record. Paleoceanography 22. doi:10.1029/2006PA001307.

Gambacort, G., Bersezio, R., Erba, E., 2014. Sedimentation in the Tethyan pelagic realm during the Cenomaniam: Monotonous settling or active redistribution? Palaeogeography, Palaeoclimatology, Palaeoecology 409, 301-319.

Hall, I. R., and McCave, I. N., 2000. Palaeocurrent reconstruction, sediment and thorium focussing on the Iberian margin over the last 140 ka. Earth and Planetary Science Letters 178, 151–164.

Helama, S., Jones, P.D., Briffa, K.R., 2017. Dark Ages Cold Period: A literature review and directions for future research. The Holocene 1-7. doi:10.1177/0959683617693898.

Houpert, L., Durrieu de Madron, X., Testor, P., Bosse, A., D'Ortenzio, F., Bouin, M.N., Dausse, D., Le Goff, H., Kunesch, S., Labaste, M., Coppola, L., Mortier, L., Raimbault, P., 2016. Observations of open-ocean deep convection in the northwestern Mediterranean Sea: Seasonal and interannual variability of mixing and deep water masses for the 2007-2013 Period: DEEP CONVECTION OBS. NWMED 2007-2013. Journal of Geophysical Research: Oceans 121, 8139–8171. doi:10.1002/2016JC011857

Hüneke, H., Stow, D.A.V., 2008. Identification of ancient contourites: problems and palaeoceanographic significance. In: Rebesco, M., Camerlenghi, A. (Eds.), Contourites, developments in Sedimentology 60, Elsevier, Amsterdam, 323-344.

Hurrell, J. W., 1995. Decadal Trends in the North Atlantic Oscillation: regional temperatures and precipitation. Science 269, 676–679, doi:10.1126/science.269.5224.676.

Hurrell, J.W., Kushnir, Y., Ottersen, G., Visbeck, M., 2003. The North Atlantic Oscillation: Climate Significance and Environmental Impact. Geophysical Monograph Series 134, doi:10.1029/134GM01

Incarbona, A., Martrat, B., Mortyn, P.G., Sprovieri, M., Ziveri, P., Gogou, A., Jordà, G., Xoplaki, E., Luterbacher, J., Langone, L., Marino, G., Rodríguez-Sanz, L., Triantaphyllou, M., Di Stefano, E., Grimalt, J.O., Tranchida, G., Sprovieri, R., Mazzola, S., 2016. Mediterranean circulation perturbations over the last five centuries: Relevance to past Eastern Mediterranean Transient-type events. Scientific Reports 6. doi:10.1038/srep29623

Josey, S. A., 2003. Changes in the heat and freshwater forcing of the Eastern Mediterranean and their influence on DeepWater Formation. Journal Geophysical Research 108, 3237, doi:10.1029/2003JC001778

Josey, S.A., Somot, S., Tsimplis, M., 2011. Impacts of atmospheric modes of variability on Mediterranean Sea surface heat exchange. Journal of Geophysical Research 116. doi:10.1029/2010JC006685

Kieke, D., Yashayaev, I., 2015. Studies of Labrador Sea Water formation and variability in the subpolar North Atlantic in the light of international partnership and collaboration. Progress in Iceanography 132, 220-232. doi:10.1016/j.pocean.2014.12.010

Kim, W.M., Yeager, S., Chang, P., Danabasoglu, G., 2016. Atmospheric Conditions Associated withLabrador Sea Deep Convection: New Insights from a Case Study of the 2006/07 and 2007/08 Winters. American Meteorological Society 29, 5281-5297. doi:10.1175/JCLI-D-15-0527.1

Konert, M., Vandenberghe, J., 1997. Comparison of laser grain-size analysis with pipette and sieve analysis: a solution for the underestimation of the clay fraction. Sedimentology 44, 523–535.

Krichak, S. O., and Alpert, P., 2005. Decadal trends in the east Atlantic west Russia pattern and Mediterranean precipitation. Int. J. Climatol., 25, 183–192. doi:10.1002/joc.1124.

Li, M.Z., Amos, C.L., 2001. SEDTRANS96: the upgraded and better calibrated sediment-transport model for continental shelves. Computers and Geosciences 27, 619–645.

Lionello, P., Malanott-Rizzoli, R., Boscolo, R., Alpert, P., Artale, V., Li, L., Luterbacher, J., May,W., Trigo, R., Tsimplis, M., Ulbrich, U., Xoplaki, E., 2006. The Mediterranean climate: An overview of the main characteristics and issues. In: Mediterranean Climate Variability (MedClivar), Elsevier, Amsterdam, 1–26.

López-Jurado, J.L., González-Pola, C., Vélez-Belchi, P., 2005. Observation of an abrupt disruption of the long-term warming trend at the Balearic Sea, western Mediterranean Sea, in summer 2005. Geophysical

Research Letters 32, 1–4. doi:10.1029/2005GL024430

Margalef, R., 1985. Introduction to the Mediterranean. A Western Mediteranean. Margalef, R. (eds). Oxford, Pergamon Press, 1-16.

Margaritelli, G., Cisneros, M., Cacho, I., Vallefuoco, M., Rettori, R., Lirer, F., 2018. Climatic variability over the last 3000 years in the central-western Mediterranean Sea (Menorca Basin) detected by planktonic foraminifera and stable isotope records. Glob. and Planet. Changes 169, 179-187. https://doi.org/10.1016/j.gloplacha.2018.07.012

Margirier F., Testor, P., Bosse, A., L'Hévéder, L., Mortier, L., Smeed, D., 2017. Characterization of Convective Plumes Associated With Oceanic Deep Convection in the Northwestern Mediterranean From High-Resolution In Situ Data Collected by Gliders. Journal of Geophysical Research: Oceans 122, 1-13 https://doi.org/10.1002/2016JC012633.

Martín, J., Miquel, J. C., Khripounoff, A., 2010. Impact of open sea deep convection on sediment remobilization in the western Mediterranean. Geophys. Res. Lett., 37, L13604, doi:10.1029/2010GL043704.

McCave, I. N., Bryant, R. J., Cook, H. F., Coughanowr, C. A., 1986. Evaluation of a laser-diffraction-size analyzer for use with natural sediments. Journal of Sedimentary Research 56, 561–564.

McCave, I. N., Manighetti, B., Robinson, S. G., 1995. Sortable silt and fine sediment size/ composition slicing: Parameters for paleocurrent speed and paleoceanography. Paleoceanography 10, 593–610.

McCave, I.N., Thornalley, D.J.R., Hall, I.R, 2017. Relation of sortable silt grain-size to deep-sea current speeds: Calibration of the 'Mud Current Meter'. Deep-Sea research Part I, Oceanographic research Papers. doi:10.1016/j.dsr.2017.07.003

MEDOC Group. 1970: Observation of formation of Deep Water in the Mediterranean Sea. Nature 227, 1037–1040.

Millot, C., 1999. Circulation in the Western Mediterranean Sea. Journal of Marine Systems 20, 423–442.

Morellón, M., Valero-Garcés, B., Vegas-Vilarrúbia, T., González-Sampériz, P., Romero, Ó., Delgado-Huertas, A., Mata, P., Moreno, A., Rico, M., Corella, J.P. 2009. Lateglacial and Holocene palaeohydrology in the western Mediterranean region: the Lake Estanya record (NE Spain). Quaternary Science Reviews 28, 2582-2599. doi:10.1016/j.quascirev.2009.05.014

Morellón, M., Valero-Garcés, B., González-Sampériz, P., Vegas-Vilarrúbia, T., Rubio, E., Rieradevall, M., Delgado-Huertas, A., Mata, P., Romero, Ó., Moreno, A., Engstrom, D.R., López-Vicente, M., Navas, A., Soto, J. 2011. Climate changes and human activities recorded in the sediments of Lake Estanya (NE Spain) during the Medieval Warm Period and Little Ice Age. Journal of Paleolimnology 46, 423-452. doi: 10.1007/s10933-009-9346-3

Moreno, A., Pérez, A., Frigola, J., Nieto-Moreno, V., Rodrigo-Gámiz, M., Martrat, B., González-Sampériz, P., Morellón, M., Martín-Puertas, C., Corella, J.P., Belmonte, A., Sancho, C., Cacho, I., Herrera, G., Canals, M., Grimalt, J.O., Jiménez-Espejo, F., Martínez-Ruiz, F., Vegas-Vilarrúbia, T., Valero-Garcés, B.L., 2012. The Medieval Climate Anomaly in the Iberian Peninsula reconstructed from marine and lake records. Quaternary Science Reviews 43, 16–32. doi:10.1016/j.quascirev.2012.04.007

Ortega, P., Robson, J., Sutton, R.T., Andrews, M.B., 2017. Mechanisms of decadal variability in the Labrador Sea and the wider North Atlantic in a high-resolution climate model. Clim Dyn 49, 2625-2647. doi:10.1007/s00382-016-3467-y

Palanques, A., Durrieu de Madron, X., Puig, P., Fabres, J., Guillén, J., Calafat, A., Canals, M., Heussner, S., and Bonnin, J., 2006. Suspended sediment fluxes and transport processes in the Gulf of Lions submarine canyons, The role of storms and dense water cascading. Mar. Geol., 234, 43–61 doi:10.1016/j.margeo.2006.09.002.

Pattiaratchi, C.,Hollings, B., Woo, M., Welhena, T., 2011. Dense shelf water formation along the south-west Australian inner shelf, Geophys. Res. Lett. 38, L10609, doi:10.1029/2011GL046816.

Puig, P., Palanques, A., Orange, D.L., Lastras, G., Canals, M., 2008. Dense shelf water cascades and sedimentary furrow formation in the Cap de Creus Canyon, northwestern Mediterranean Sea. Continental Shelf Research 28, 2017–2030.

Puig, P., Madron, X.D. de, Salat, J., Schroeder, K., Martín, J., Karageorgis, A.P., Palanques, A., Roullier, F., Lopez-Jurado, J.L., Emelianov, M., Moutin, T., Houpert, L., 2013. Thick bottom nepheloid layers in the western Mediterranean generated by deep dense shelf water cascading. Progress in Oceanography 111, 1–23. doi:10.1016/j.pocean.2012.10.003

Roberts, N., Moreno, A., Valero-Garcés, B.L., Corella, J.P., Jones, M., Allcock, S., Woodbridge, J., Morellón, M., Luterbacher, J., Xoplaki, E., Türkeş, M., 2012. Palaeolimnological evidence for an east–west climate see-saw in the Mediterranean since AD 900. Global and Planetary Change 84–85, 23–34. doi:10.1016/j.gloplacha.2011.11.002

Rodrigo-Gámiz, M., Martínez-Ruiz, F., Jiménez-Espejo, F.J. Gallego-Torres, D., Nieto-Moreno, V., Romero, O., Ariztegui, D., 2011. Impact of climate variability in the western Mediterranean during the last 20,000 years: oceanic and atmospheric responses. Quat Sci Rev 30, 2018–2034. doi:10.1016/j.quascirev.2011.05.011

Rohling, E.J., Marino, G., Grant, K.M., 2015. Mediterranean climate and oceanography, and the periodic development of anoxic events (sapropels). Earth-Science Reviews 143, 62–97. doi:10.1016/j.earscirev.2015.01.008

Roveri, M., Manzi, V., Bergamasco, A., Falcieri, F.M., Gennari, R., Lugli, S., Schreiber, B.C., 2014. Dense shelf water cascading and Messinian canyons: a new scenario for the Mediterranean salinity crisis. American Journal of Science 314, 751–784.

Rumín-Caparrós, A., Sanchez-Vidal, A., Calafat, A., Canals, M., Martín, J., Puig, P., Pedrosa-Pamies, R., 2013. External forcings, oceanographic processes and particle flux dynamics in Cap de Creus submarine canyon, NW Mediterranean Sea. Biogeosciences 10, 3493–3505. doi:10.5194/bg-10-3493-2013

Sabatier, P., Dezileau, L., Colin, C., Briqueu, L., Bouchette, F., Martinez, P., Siani, G., Raynal, O., Von Grafenstein, U., 2012. 7000 years of paleostorm activity in the NW Mediterranean Sea in response to Holocene climate events. Quaternary Research 77, 1–11. doi:10.1016/j.yqres.2011.09.002

Sánchez-López, G., Hernández, A., Pla-Rabes, S., Trigo, R.M., Toro, M., Granados, I., Sáez, A., Masqué, P., Pueyo, J.J., Rubio-Inglés, M.J., Giralt, S., 2016. Climate reconstruction for the last two millennia in central Iberia: The role of East Atlantic (EA), North Atlantic Oscillation (NAO) and their interplay over the Iberian Peninsula. Quaternary Science Reviews 149, 135–150. doi:10.1016/j.quascirev.2016.07.021

Sanchez-Vidal, A., Pascual, C., Kerherveé, P.A., Calafat, A., Heussner, S., Palanques, A., Durrieu de Madron, X., Canals, M., Puig. P, 2008. Impact of dense shelf water cascading on the transfer of organic matter to the deep Western Mediterranean Basin. Geo. phys. Res. Lett., 35, L05605, doi:10.1029/2007GL032825.

Sanchez-Vidal, A., Canals, M., Calafat, A., Lastras, G., Pedrosa-Pàmies, R., Menéndez, M., Medina, R., Company, J. B., Hereu, B., Romero. J., Alcoverro, T., 2012. Impacts on the Deep-Sea Ecosystem by a Severe Coastal Storm, PLoS one, 7, e30395, doi:10.1371/journal.pone.0030395.

Sanchez-Vidal, A., Llorca, M., Farré, M., Canals, M., Barceló, D., Puig, P., Calafat, A., 2015. Delivery of unprecedented amounts of perfluoroalkyl substances towards the deep-sea. Science of the Total Environment 526, 41–48. doi:10.1016/j.scitotenv.2015.04.080

Schmiedl, G., Kuhnt, T., Ehrmann, W., Emeis, K.-C., Hamann, Y., Kotthoff, U., Dulski, P., Pross, J., 2010. Climatic forcing of eastern Mediterranean deep-water formation and benthic ecosystems during the past 22 000 years. Quaternary Science Reviews 29, 3006–3020. doi:10.1016/j.quascirev.2010.07.002

Schroeder, K., Josey, S.A., Herrmann, M., Grignon, L., Gasparini, G.P., Bryden, H.L., 2010. Abrupt warming and salting of the Western Mediterranean Deep Water after 2005: Atmospheric forcings and lateral advection. Journal of Geophysical Research 115. doi:10.1029/2009JC005749

Schroeder, K., Haza, A. C., Griffa, A., Özgökmen, T. M., Poulain, P., Gerin, R., Peggion, G., Rixen, M., 2011. Relative dispersion in the liguro-provencal basin: from sub-mesoscale to mesoscale. Deep-Sea Research Part I, 58, 861–882.

Sicre, M.-A., Jalali, B., Martrat, B., Schmidt, S., Bassetti, M.-A., Kallel, N., 2016. Sea surface temperature variability in the North Western Mediterranean Sea (Gulf of Lion) during the Common Era. Earth and Planetary Science Letters 456, 124–133. doi:10.1016/j.epsl.2016.09.032

Sierro, F.J., Hodell, D.A., Curtis, J.H., Flores, J.A., Reguera, I., Colmenero-Hidalgo, E., Bárcena, M.A., Grimalt, J.O., Cacho, I., Frigola, J., Canals, M., 2005. Impact of iceberg melting on Mediterranean thermohaline circulation during Heinrich events: Impact of Iceberg melting in the Mediterranean. Paleoceanography 20, PA2019. doi:10.1029/2004PA001051

Somavilla, R., González-Pola, C., Rodriguez, C., Josey, S.A., Sánchez, R.F., Lavín, A., 2009. Large changes in the hydrographic structure of the Bay of Biscay after the extreme mixing of winter 2005, J. Geophys. Res. 114, C01001, doi:10.1029/2008JC004974.

Somot, S., Houpert, L., Sevault, F., Testor, P., Bosse, A., Taupier-Letage, I., Bouin, M.-N., Waldman, R., Cassou, C., Sanchez-Gomez, E., Durrieu de Madron, X., Adloff, F., Nabat, P., Herrmann, M., 2016. Characterizing, modelling and understanding the climate variability of the deep water formation in the North-Western Mediterranean Sea. Climate Dynamics. doi:10.1007/s00382-016-3295-0

Somot, S., Sevault, F., Déqué, M., 2006. Transient climate change scenario simulation of the Mediterranean Sea for the twenty-first century using a high-resolution ocean circulation model. Climate Dynamics 27, 851–879.

Stabholz, M., Durrieu de Madron, X., Canals, M., Khripounoff, A., Taupier-Letage, I., Testor, P., Heussner, S., Kerhervé, P., Delsaut, N., Houpert, L., Lastras, G., Dennielou, B., 2013. Impact of open-ocean convection on particle fluxes and sediment dynamics in the deep margin of the Gulf of Lions. Biogeosciences 10, 1097-1116. doi:10.5194/bg-10-1097-2013

Stanley, D. J. Ed., 1972. The Mediterranean Sea: a natural sedimentation laboratory. Dowden, Hutchinson & Ross, Stroudsbourg, PA., 765.

Stommel, H., Bryden, H., Mangelsd, P., 1973. Does some of Mediterranean outflow come from great depth? Pure and Applied Geophysics 105 (4), 879-889.

Stommel, H., 1972. Deep winter-time convection in the Western Mediterranean Sea. In: Studies in physical oceanography, a tribute to Georg Wiist on his 80th birthday, A.L. GORDON, editor, Gordon & Breach, 2, 207-218.

Testor, P., Gascard, J.C., 2006. Post-convection spreading phase in the Northwestern Mediterranean Sea. Deep-Sea Research Part I: Oceanographic Research Papers 53, 869–893. doi:10.1016/j.dsr.2006.02.004

Thornalley, D.J.R., Oppo, D.W., Ortega, P., Robson, J.I., Brierley, C.M., Davis, R., Hall, I.R., Moffa-Sanchez, P., Rose, N.L., Spooner, P.T., Yashayaev., I., Keigwin, Ll. D., 2018. Anomalously weak Labrador Sea convection and Atlantic overturning during the past 150 years. Nature 556, 227-230. https://doi.org/10.1038/s41586-018-0007-4

Trigo, R., Xoplaki, E., Zorita, E., Lutherbacher, J., Krichak, S.O., Alpert, P., Jacobeit, J., Sáenz, J., Fernández, J., González-Rouco, F., Garcia-Herrera, R., Rodo, X., Brunetti, M., Nanni, T., Maugeri, M., Tükes, M., Gimeno, L., Ribera, P., Brunet, M., Trigo, I.F., Crepon, M., Mariotti, A., 2006. Relations between variability in the Mediterranean Region and Mid-Latitude Variability. In: Mediterranean Climate Variability (MedClivar), Elsevier, Amsterdam, 178-226.

Tsimplis, M. N., Josey, S.A., 2001. Forcing of the Mediterranean Sea level by atmospheric oscillations

over the North Atlantic. Geophys. Res. Lett. 28, 803–806. doi:10.1029/2000GL012098.

Velasco, J. P. B., Baraza, J., Canals, M., 1996. La depresión periférica y el lomo contourítico de Menorca: Evidencias de la actividad de corrientes de fondo al N del Talud Balear. Geogaceta, 20, 359–362.

Waldman, R., Somot, S., Herrmann, M., Bosse, A., Caniaux, G., Estournel, C., Houpert, L., Prieur, L., Sevault, F., Testor, P., 2017. Modeling the intense 2012-2013 dense water formation event in the northwestern Mediterranean Sea: Evaluation with an ensemble simulation approach. Journal of Geophysical Research 122, 2, 1297-1324.

Wallace, J.M., Gutzler, D.S., 1981. Teleconnections in the geopotential height field during the Northern Hemisphere winter. Mon. Wea.Rev. 109, 784-812.

Wu, W., Danabasoglu, G., Large, W. G., 2007. On the effects of parameterized Mediterranean Overflow on North Atlantic ocean circulation and climate. Ocean Modell., 19(1–2), 31–52, doi:10.1016/j.ocemod.2007.06.003.

3.2.8 Supplementary material to Cisneros et al., 2019

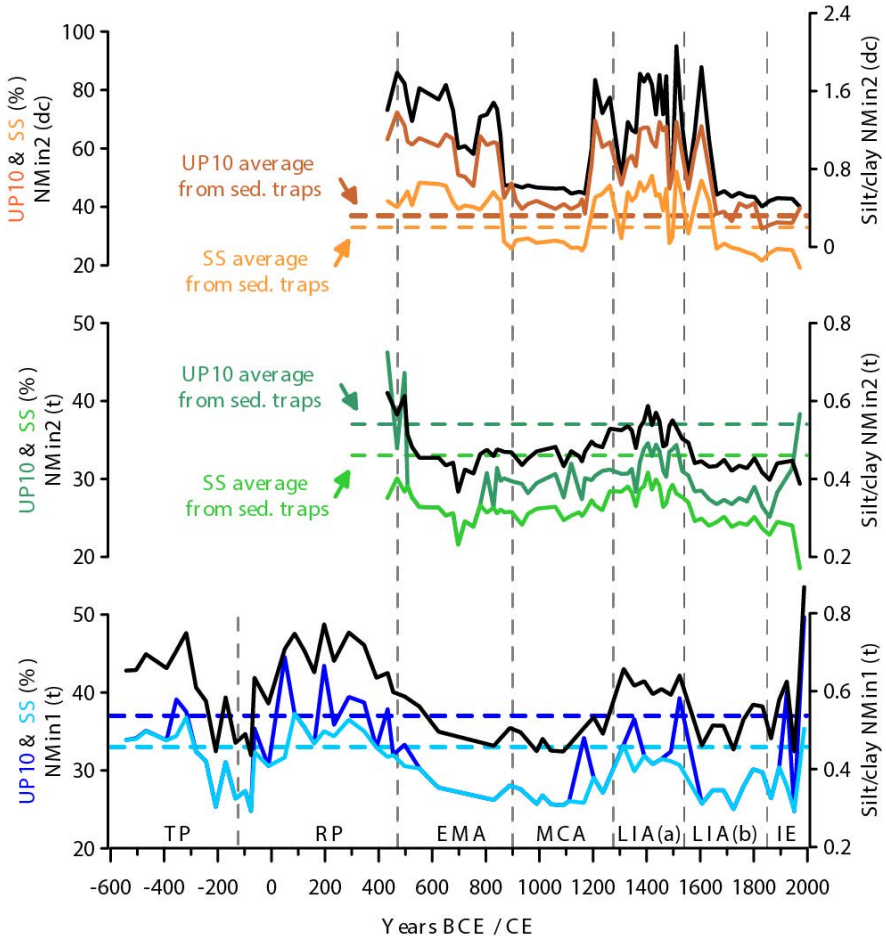

Figure 3.21. Comparison between UP10 (> 10 µm), Sortable Silt (SS; 10-63 µm) and Silt/clay (8-63 µm / < 8 µm**)** obtained by means of grain-size analyses performed on NMin1 and NMin2 cores; "t" corresponds to the total grain-size fraction and "dc" to de-carbonated. Dashed lines correspond to UP10 and SS averages obtained from NMin sediment traps, respectively. Years are expressed as Before Common Era (BCE; negative years) and Common Era (CE). Vertical dashed lines indicates the limits of the discussed periods: TP: Talaiotic Period; RP: Roman Period, 123 BCE-470 CE; EMA: Early Middle Ages, 470-900 CE; MCA: Medieval Climate Anomaly, 900-1275 CE; LIA: Little Ice Age, 1275-1850 CE; IE: Industrial Era.

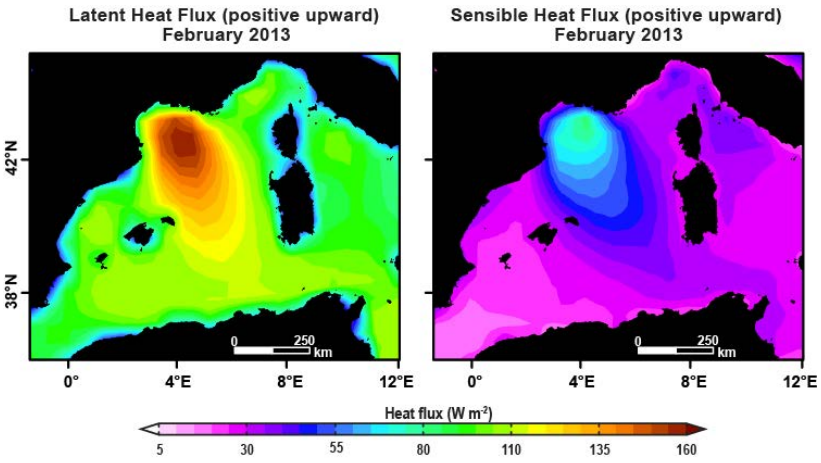

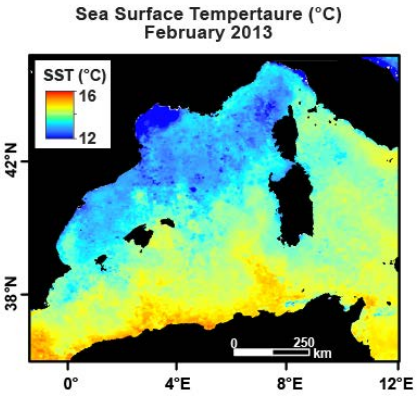

Figure 3.22. Latent and Sensible heat flux in the western Mediterranean Sea during February 2013 obtained from Giovanni.gsfc.nasa.gov. Positive values representing sensible heat flux from the ocean to the atmosphere given in the Western Mediterranean Deep Water formation region (Gulf of Lion). Sea Surface Temperature (SST) during February 2013 are also shown.

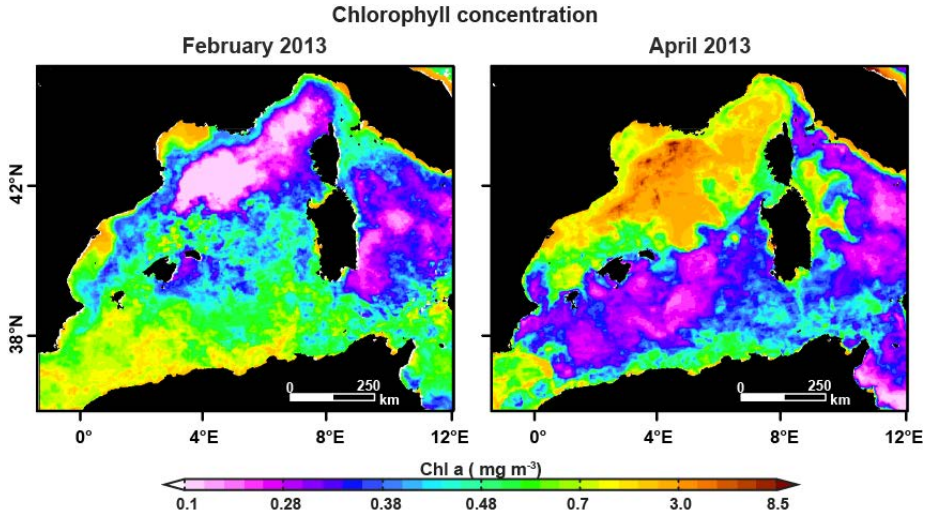

Figure 3.23. Satellite images showing surface mass concentration of Chlorophyll-a in sea-water for the western Mediterranean Sea provided by Ocean Biology Processing Group. 2003. MODIS Aqua Level 3 Global Monthly Mapped 4 km Chlorophyll a. Ver. 6. PO.DAAC, CA, USA. **Left panel)** Period corresponding to the Western Mediterranean Deep Water (WMDW) formation when very low chlorophyll-a values in the open-sea convection area are given, indicating that deeper waters are emerging (water-column mixing). **Right panel)** Period after WMDW formation when high chlorophyll-a values are observed, which suggest an important bloom (associated with the water-column mixing).

3.3 WESTERN MEDITERRANEAN HYDROCLIMATE VARIABILITY DURING THE LAST 2700 YEARS BASED IN STALAGMITE MULTI-PROXY RECORDS

Keywords: speleothems; paleohydrology; western Mediterranean; Micro-CT scanning; XRF.

3.3.1 Abstract

This study presents for the last 2.7 kyr (653 yr BCE-1880 yr CE) the first hydrological reconstruction of the western Mediterranean based on five stalagmites from two Mallorca island caves. The paleohydrological information from the stalagmites has been tested by a multi-proxy strategy that has included the description of the architectural elements, mineralogical X-Ray Diffraction characterization, $\delta^{18}O$, $\delta^{13}C$ and trace element analyses, high resolution digital pictures and qualitative elemental composition using a XRF core-scanner system, Micro-CT scanning, U/Th dates and cave monitoring. This combined methodology, has proved the paleohydrological value of these archives and has allowed the interpretation of enriched (depleted) $\delta^{18}O$ values as drier (wetter) conditions in the region.

General wet conditions have been obtained for the early Roman Period (RP), the first half of the Early Middle Ages (EMA) and the entire Little Ice Age (LIA) while drier conditions have characterized the late RP, the late EMA and the entire Medieval Climate Anomaly. The recorded $\delta^{18}O$ values for the LIA are the most depleted ones for the studied period including also those of the farmed calcite, highlighting this period as the wettest one. Although some multidecadal LIA variability indicate relatively drier (wetter) conditions coincident with cold (warm) temperatures and positive (negative) North Atlantic Oscillation modes. These Mallorca wet periods corresponded to heavy rainfalls events in the northeast Iberian Peninsula and higher storminess activity in the Gulf of Lion. Overall, humidity muticentennial trends observed in our study area seem to be coincident to those described in the Iberian Peninsula and in Central Europe by previous studies.

3.3.2 Introduction

Water availability has been a key aspect in the historic development of the Mediterranean area, a region that supports a high population pressure, which keeps

increasing in spite of its limited water resources. Besides, this region is one of the most vulnerable regarding the current situation of global warming (Giorgi et al., 2006). The time response of the precipitation patterns to the climate change associated to CO_2 rising can be slow (decades-centuries) but also fast (few years) (Ceppi et al., 2018). Future global climate change scenarios based on climate models point this region as a hot spot in hydrological terms, where significant reduction in precipitation could happen (Gibelin and Deque, 2003; Giorgi et al., 2006; Ulbrich et al 2006; Giorgi and Lionello, 2008; Sheffield and Wood, 2008; Mariotti et al., 2008). During the last few decades intense rain events in the western Mediterranean basin have occurred from late summer to winter and, they have caused numerous catastrophic floods with human casualties (Pastor et al., 2001). Particularly, climate change over the Balearic Islands is evident by a temperature increase and a precipitation reduction during the second half of the XX century and beginning of XXI with larger amplitude than in most parts of the globe (Homar et al., 2010).

Previous works using Mediterranean speleothem records have concentrated in older periods than the Holocene or frequently only span the last 3 kyr partially (Bar-Matthews et al., 2003; Frisia et al., 2003, 2005, 2006; McMillan et al., 2005; Mangini et al., 2005; Domínguez-Villar et al., 2008; Verheyden et al., 2008; Fleitmann et al., 2009; Martín-Chivelet et al., 2011; Railsback et al., 2011; Rudzka et al., 2012; Wassenburg .et al., 2013; Cheng et al., 2015; Labuhn et al., 2015). However, existent speleothem records for the last 3kyr is scarce for the western Mediterranean region and even lower if we focus in the central-western Mediterranean. In particular context of the Mallorca Island, the available speleothem studies concentrate in overgrowths reconstructing past sea-levels (Vesica et al., 2001; Polyak et al., 2018; Dumitru et al., 2019) or in stalagmites but from older periods like the Last Interglacial (Hodge, 2004; Hodge et al., 2008; Dumitru et al., 2018).

Available paleoclimatic records from last few millennia reveal a significant regional heterogeneity in the climatic patterns (Neukom et al., 2019). This study aims characterise the hydroclimate variability of the last millennia in Mallorca. The suitability of the stalagmites for high precision U/Th chronologies provides a further great advantage to these archives. It applies a muti-proxy strategy combining geochemical, petrological, textural tools and also includes Micro-CT scanning in one of

the studied stalagmites, whose application on stalagmites studies is very limited so far (Vanghi et al., 2015; Walczack et al., 2015).

The studied spelothem records span the last 3kyr and covering the following climate/historical periods (years expressed as BCE, before common era, and CE, common era): the Talaiotic Period (TP; until 123 yr BCE), the Roman Period (RP; 123 yr BCE-470 yr CE), the Early Middle Ages (EMA; 470-900 yr CE), the Medieval Climate Anomaly (MCA; 900-1275 yr CE), and the Little Ice Age (LIA; 1275-1850 yr CE), with the Industrial Era (IE) as the most recent period (more details in Cisneros et al., 2016).

3.3.3 Cave and climatic settings

The studied speleothem were recovered from *Sa Balma des Quartó* cave (Feni, Ciara, Multieix and Séan stalagmites) and *Ses Coves del Pirata* (Constantine stalagmite) located in the south-east of Mallorca (Balearic Islands) in the central-western Mediterranean Sea. The two caves are formed by Upper-Miocene reef limestone (Ginés et al., 2014; Fig. 3.24), which is very porous and encourage dripping predominantly by seepage. The frequent presence of soda-straws stalactites in both caves and monitoring performed in *Sa Balma* since 2013 cave corroborates this kind of drip. Both caves are near and under the same type of vegetation and climate conditions. Currently, the surrounded landscape consists in a forest formed by Mediterranean vegetation, which is rather undisturbed by human activities.

Sa Balma des Quartó cave (*Balma* hereinafter) seems to have been used by humans since prehistoric times as a burial place (Bermejo et al., 2014). It is located parallel to the coast, in a cliff of a 20 m maximum height. It consists basically in a wide spacious chamber formed by collapse, the bottom of which is 10.5 m above sea level and 12.5 m from the surface (Fig. 3.24b). The chamber has a rich decoration of speleothems, including an abundance of straw stalactites of remarkable length. The height of the cave in some points reaches few meters from the outside and its length is 70 m (Bermejo et al., 2014). The access to the cave consists in a small and vertical hole in the outside rock-shelter and, during cold (warm) season is when the cave is more (less) ventilated.

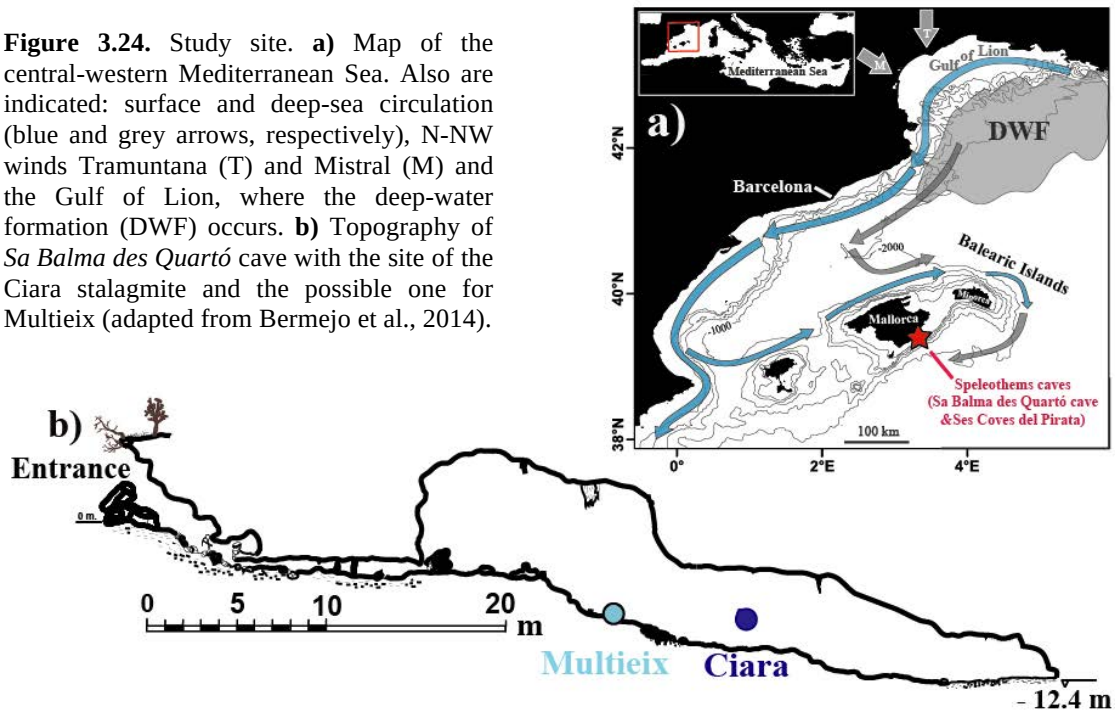

Figure 3.24. Study site. **a)** Map of the central-western Mediterranean Sea. Also are indicated: surface and deep-sea circulation (blue and grey arrows, respectively), N-NW winds Tramuntana (T) and Mistral (M) and the Gulf of Lion, where the deep-water formation (DWF) occurs. **b)** Topography of *Sa Balma des Quartó* cave with the site of the Ciara stalagmite and the possible one for Multieix (adapted from Bermejo et al., 2014).

Ses Coves del Pirata (*Pirata* hereinafter) were partially prepared to receive touristic visits at the end of the XIX century, although graffiti inside the cave allude to 1614 yr CE (Pasqual and Nicolau, 2006). *Pirata* cave is part of a system together with the *cova del Pont* and *the cova de sa Piqueta*, with a current total length of 3020 m, of which 1190 m are subaquatic. Several lakes can be found in the cave at level height located below the phreatic level (-32 m regarding the entrance). The cave, which is divided in numerous chambers by columns and stalagmite walls, is characterized by a complicated topography. In addition, many of these stalagmitic massifs and flowstones have been broken by an important local subsidence (Ginés and Ginés, 1976; Gràcia et al., 2006). Its tour-length is approximately ~800 m and it consists in two main sectors: the Classic Sector (Martel et al., 1903; Ginés and Ginés, 1976) and the Ignored Sector (discovered at 1986 yr CE; Garcia et al., 1986). The first sector is conformed by a big chamber of 140 m lenght and a maxima width of ~70 m and it is divided in two portions that extended in direction north and south, respectively. Constantine stalagmite was found in the south portion, which is the biggest one and remarkably ornamented by stalagmites and columns of big dimensions (Gràcia et al., 2006).

Balearic Islands present a typical Mediterranean climate configuration, which is characterized by mild wet winters and warm to hot, dry summers (Lionello et al., 2006). During autumn occurs the maxima rainfall and it decreases during the winter and spring with a very dry summer season. One peculiarity of the western Mediterranean is that

almost each winter is formed the Western Mediterranean Deep Water in the Gulf of Lion (Fig. 3.24).

Important climate indices that have been associated to the Western Mediterranean region and its rainfall patterns are the NAO and the MOI (Mediterranean Oscillation Index). The NAO is a major source of interannual variability in the atmospheric circulation of the North Atlantic/Europe region, which consists in a difference of atmospheric pressure between Iceland low and Azores high. Positive (negative) NAO phases suppose more and stronger winter storms crossing the Atlantic on a more northerly track, which results in warm and wet (cold and dry) winters in Europe and dry (wet) conditions over the Mediterranean (Hurrell et al., 1995; 2003; Trigo et al., 2002). Regarding to the MOI, which is mainly active during the boreal winter, is consequence of the dipole behaviour of the atmosphere in the area between the western and eastern Mediterranean and it refers to the difference in pressure between the mid-northern Atlantic (regulated from permanent pressure centres-the Azores high and the Iceland low) and the southeastern Mediterranean (probably under the influence of the permanent southeast Mediterranean low) (Grbec et al., 2003). MOI is calculated by Conte et al. (1989) and Palutikof et al. (1996) as the normalized pressure difference between Algiers and Cairo. Another definition calculates this index from Gibraltar's Northern Frontier and Lod Airport in Israel (Palutikof et al., 2003). It has been observed significant correlation during the cold season between the (negative/positive) MO index and (high/low) total precipitation over the entire western Mediterranean region, including large areas of the Iberian Peninsula, France, Italy, Morocco and Algeria (Corella et al., 2016).

3.3.4 Material and methods

The five studied stalagmites are: Feni, Ciara, Multieix and Séan (from *Balma* cave) and Constantine (from *Pirata* cave). Feni (15.5-cm-length), Multieix (30.5-cm-length) Constantine (9-cm-length) and Seán (12-cm-length) were found not in situ of their original growth sites into their respective caves. The particular morphology of Multieix reproduced by several stalagmites of the basal sector of *Balma* cave suggests that it was recovered close of its growth position although its base not identified (Fig. 3.24). Ciara (42.5-cm-length) grew up in the main chamber of *Balma* cave.

Stalagmites were cut into two halves and, from the axial part of these halves fabrics were studied by means of thin sections or acetate peels observations (Feldmann et al., 1989) by optical microscopy. Four thin sections were prepared for Multieix covering the next cm: 6-3.4, 11.5-6, 20-15, 23.5-20.5 and, for Seán between cm 4-6.5. These thin sections were selected in order to characterise some apparent discontinuities and/or fabric changes. Acetate peels observations (Feldmann et al., 1989) were performed on Multieix stalagmite from cm 3.4 to 0 and from bottom to cm 23.5 and also along all the other speleothems. XRD (X-Ray Diffraction) measurements were performed on Multieix (cm 28.5, 23, 19, 11.5, 6.5 and 3.5) and Constantine (cm 7.5, 6 and 3.5) with a Bruker D8-A25 diffractometer at the Institut de Ciències de la Terra Jaume Almera, Barcelona, Spain. The diffractometer was equipped with a Cu tube (l=1.5405 Å) and an ultrafast position sensitive detector (PSD). XRD scans were collected over the 2θ range between 3.5° and 65° with steps of 0.05° and an equivalent integration time of 576 s per step. A voltage (current) of 30 kV (40 mA) was applied to the x-ray generator. The phases in the samples were identified with Bruker's software package Diffrac.Suite™ together with the PDF-2 database from the International Centre for Diffraction Data (ICDD).

Stalagmites age models are based on a total of 62 U/Th absolute ages (Table 3.10 in Supplementry Material) performed according to the uranium and thorium separating chemical procedure described in Edwards et al. (1987). Ages in Constantine stalagmite for cm 6.6 to 1.3 were performed in Xi'an Jiaotong University (China). The rest of dates were preàred and measured at the University of Minnesota (USA) laboratories. Analyses were conducted with a multicollector ICP-MS (Neptune Thermo Finnigan). After dissolved with nitric acid the calcite powder, a mixed $^{229}Th/\ ^{233}U/^{236}U$ spike was added. Sample was dried down and an iron chloride solution added. Iron precipitation was achieved by the addition of NH_4OH, drop by drop. Centrifugation was used to separate the iron from the rest of solution and the supernatant liquid removed. Sample was then loaded into columns containing anion resin and, HCl and water was added to elute Th and U, respectively. Once both elements were separated, each sample was dried down, and dilute nitric acid was added. Every age model has been produced using U/Th dates on the Bchron package (Parnell et al., 2008) in the free R software.

Samples for trace elements $\delta^{18}O$ and $\delta^{13}C$ analyses were microdrilled at 1 mm

resolution following the growth axis. Trace elements were measured on an inductively coupled plasma mass spectrometer (ICP-MS, Perkin Elmer ELAN 6000) in the Scientific and Technological Centres of the University of Barcelona (CCiT- UB). Samples were dissolved in 5 mL of dilute nitric acid (Tracepur) immediately before analyses. A standard solution with known elemental ratios was used for sample standard bracketing (SSB) as a correction for instrumental drift. Taking into account the known standard solutions concentrations, the average reproducibility for Sr/Ca, Mg/Ca and Ba/Ca ratios was better than 80, 97 and 88 %, respectively. It should be noted that analytical difficulties were detected in the measurements of samples from Constantine stalagmite, related to the theoric [Sr/Ca] in the standard solutions. If these samples are not taking into account the average reproducibility for Sr/Ca is 97 %. In order to calibrate the obtained intensity ratios, six solutions with a different trace element ratios values and a constant concentration of 100 ppm of Ca were used. Stable isotopes values were measured using a Finnigan MAT 252 mass spectrometer fitted with a Kiel-II carbonate microsampler in the CCiT-UB. The reproducibility was of 0.02 ‰ for $\delta^{13}C$ and 0.06 ‰ for $\delta^{18}O$. Calibration to Vienna Pee Dee Belemnite (VPDB) was carried out by means of NBS-19 standards.

In addition, Seán stalagmite has been further studied using Micro-Computed Tomography (Micro-CT scanning) and Avaatech XRF core-scanner system. The Micro-CT scanning was performed with a Multitom CORE X-ray CT system in the CORELAB from the University of Barcelona. The CT-scanner was operated at a tube voltage of 140 kV and an intensity of 33 W. The exposition time was 800 ms, the voxel size 32.99 µm and, the number of projections 1500. Reconstructed images of the relative density values were exported as 16-bit using the AVIZO (FEI) software. This technique allows obtaining topographies with resolution between 5 and 300 µm (Frigola et al., 2015). The Micro-CT scanning results are expressed in this study as 2D images in a colourmap with the distribution and quantification of relative density values and porosity.

The XRF analyses (CORELAB, University of Barcelona) were performed in the 4.5-7.5 cm section of Seán stalagmite. Scanning took place at the split stalagmite directly at 200 µm resolution. Major elements (atomic weight between aluminium and iron) were analysed in 10 kV potential, a tub intensity of 1.95 mA and a 60 s time exposure and,

minor elements (atomic weight between iron and lead) in 30 kV, 1.95 mA and a 90 s. The measurement amplitude was reduced to 8 mm in order to adjust it to the laminae of the stalagmite.

Colour measurements from the high resolution 70 µm pictures were performed along the whole Seán stalagmite. Results are expressed in this study as L*a*b* values (colour coordinates), which are a scale of uniform colour defined by the Commission Internationale de l'Eclairage (CIE; Muñoz et al., 2015). L* corresponds to lightness and ranged values from 0 (black) to 100 (white). The proxies a* and b* represent variations between red-green and yellow-blue, respectively, ranging values between -120 and 120 (Westland, 2012). Colour coordinates can allow recognizing changes in the carbonate, iron and clay content (Mix et al., 1992; Nederbragt i Thurow, 2004; Rogerson et al., 2006; Debret et al., 2011).

3.3.5 Results

Fabrics and Architectural elements

In base to the thin sections or acetate peels, a carefully analysis of the fabrics and architectural structures has been preformed for each of the stalagmites that had allow defining some unconformities bounded units (UBUs) following the methodology proposed by Martin-Chivelet et al. (2017). The results are presented in detail in the Supplementary Material and Figures 3.33-3.35. In summary, Feni and Ciara stalagmites have been described by only one UBU, and the rest of stalagmites have been characterized as follows: Multieix, UBU3 (302 BCE-279 CE), UBU2 (279-858 CE) and UBU1 (1501-1844 CE); Constantine, UBU4 (423-548 CE), UBU3 (548-789 CE), UBU2 (789-1017) and UBU1 (1017-1102 CE); Seán, UBU2 (1421-1622 CE) and UBU1 (1622-1880 CE). A particularly remarkable feature found in Seán stalagmite is the presence of a brown layer at 1622 CE that marks the boundary between the two defined UBUs in this stalagmite. This brown layer is characterise by the presence of micrite carbonate but does not involve dissolution and/or erosion of the underlayer calcite crystals. It should be noted the presence of a gastropod test around the mentioned brown layer (Fig. 3.36 in Supplementary Material).

Age models

Age models for the oldest stalagmites, Feni, Ciara, Constantine and cm 30.5-5 of Multieix, were respectively performed taking in account the whole data set of U/Th ages within Bchrom (Parnell et al., 2008) (Table 3.10 in Supplementary Material). Age models for Ciara, the stalagmite dated at the highest resolution, and Constantine result from averaging all models provided by Bchrom. The age models of Feni and the lower part of Multieix (cm 30.5-5) stalagmites have been performed using their U/Th ages and according to the best fit to Ciara. The age model for Seán, the most recent stalagmite, was performed in two batches to minimize uncertainties, from the top to the unconformity at cm 6 and from there to the bottom. One of the nine U/Th dates of this stalagmite was excluded sine it enhanced the outlier probability of the adjacent dates. The Seán age model also corresponds to the average of the entire whole set of models provided by Bchrom. The age model for the upper 5 cm of Multieix was selected from those provided by Bchrom that had the best fit to Seán, since this stalagmite had a more solid age model for this section.

Table 3.7. Average growth rates, mean time resolutions and spanned periods for each stalagmite. More detailed information about growth rates can be consulted in Supplementary Material. *Considering the sampling resolution (1 mm). **Ranged from 37 to 1 years.

Stalagmite	Average growth rate (mm yr^{-1})	Mean time resolution (yr)*	Spanned years	Spanned period
FENI	0.8	2.0	653-301 yr BCE	TP
CIARA	0.7	2.2	537 yr BCE-398 yr CE	TP, RP
MULTIEIX (cm 30.5-5)	0.4	4.6	302 yr BCE-858 yr CE	TP, RP, EMA
CONSTANTINE	0.1	7.6	423-1102 yr CE	EMA, MCA
SEÁN	0.4	3.8	1421-1880 yr CE	LIA
MULTIEIX (cm 5-0)	0.3	6.8**	1503-1844 yr CE	LIA

Mg/Ca, Sr/Ca and Ba/Ca records

Mg/Ca, Sr/Ca and Ba/Ca ratios results (averages and range values) for each stalagmite are shown in Table 3.8 and correlations between the three ratios for each stalagmite in Table 3.9. Mg/Ca, Sr/Ca and Ba/Ca ratios have been analysed in every stalagmite (Fig 3.25) andd Al/Ca was additionally analysed in Constantine (Fig. 3.34 in Supplementary Material).

In Feni and Ciara stalagmites, Mg/Ca, Sr/Ca and Ba/Ca ratios show good correlation between them (Table 3.9). Maxima values in Feni were recorded during 450 BCE, high values have been obtained at 300 yr BCE (corresponding to the top of the stalagmite). In Ciara, low values characterize several moments of the BCE centuries, while higher values have been observed towards the end of the RP.

Table 3.8. Summary of the geochemical results indicating the average and range values for stable isotopes and trace elements ratios for each stalagmite

Proxy	**Averages and ranges**				
	Feni	Ciara	Multieix	Constantine	Seán
Mg/Ca (mMol mol^{-1})	5.1 [3.5-9.6]	7.1 [4.9-17.3]	8.7 [5.2-14.2]	4.4 [2.8-6.0]	6.5 [4.3-9.0]
Sr/Ca (mMol mol^{-1})	0.05 [0.02-0.12]	0.12 [0.06-0.23]	0.08 [0.04-0.13]	0.01 [0.01 10^{-2}-0.41 10^{-2}]	0.08 [0.03-0.13]
Ba/Ca (mMol mol^{-1})	0.003 [0.002-0.008]	0.005 [0.002 10^{-2}-0.011]	0.004 [0.0223 10^{-2}-0.011]	0.001 [0.002 10^{-2}-0.002]	0.004 [0.005 10^{-2}-0.009]
$\delta^{18}O$ (‰)	-4.6 [-5.4 - -3.4]	-4.7 [-5.5 - -3.2]	-4.0 [-5.2 - -2.9]	-4.2 [-5.1 - -3.3]	-5.0 [-5.9 - -4.0]
$\delta^{13}C$ (‰)	-7.3 [-9.3 - -5.0]	-7.6 [-9.2 - -4.2]	-6.4 [-8.9 - -2.5]	-6.6 [-8.8 - -4.5]	-8.5 [-10.0 - -6.3]

In Constantine stalagmite, the averages of all ratios are remarkable lower than those for the coeval parts of the Multieix stalagmite because trace element ratios of this stalagmite were not corrected like the other cases, given irregularities in the measurements related to the theoretical concentrations in the standard solutions. Mg/Ca, Sr/Ca and Ba/Ca record trends show good correlation (Table 3.9). However, the three ratios present certain differences depending on the UBU. The period 789-1017 yr CE (UBU2) is the most stable one with relatively high Mg/Ca values. The 1017-1101 yr CE (UBU1) period presents the highest Mg/Ca variability.

The three studied ratios in Multieix stalagmite show a good correlation, although is weaker between Mg/Ca vs. Ba/Ca (Table 3.9). During the TP-RP transition (143-16 yr BCE; UBU3), Mg/Ca and Sr/Ca show certain differences in their trends. During 279-449 yr CE Mg/Ca and Ba/Ca values are high, while during 449-858 yr CE the three ratios show the lowest average values. During 1503-1844 yr CE (UBU1), Mg/Ca and

Sr/Ca ratios increase until the maxima values about 1722-1803 yr CE and decreasing from here to the most recent years (Fig. 3.25).

In Seán stalagmite, the Mg/Ca ratios obtained for 1421-1622 yr CE (UBU2) are slightly lower than those obtained for 1622-1880 yr CE (UBU1) (Fig. 3.25). Sr/Ca and Ba/Ca ratios do not show significant differences in averages between both periods. However, Ba/Ca variability is less remarkable in the oldest period than in the most recent one. The ratios enhance from its base until 1615 yr CE (the end of UBU2 ca. the brown layer) and after that a decrease can be observed. Although no significant correlation has been obtained for the entire record of Seán between Mg/Ca and Sr/Ca (Table 3.9), it should be noted that correlation during 1421-1622 yr CE (UBU2) is r = 0.3, p value = 0.0376 while it is not significant during 1622-1880 yr CE (UBU1). It should be also noted that into these years (1700-1850 yr CE) is when differences between Seán and Multieix have been observed, with higher Mg/Ca ration in Multieix (Fig. 3.25).

Table 3.9. Correlations between the three trace element ratios for each stalagmite.

Stalagmite	Mg/Ca vs. Sr/Ca		Mg/Ca vs. Ba/Ca		Sr/Ca vs. Ba/Ca	
	r	***p* value**	**r**	***p* value**	**r**	***p* value**
Feni	0.80	0.00	0.80	0.00	0.80	0.00
Ciara	0.70	0.00	0.70	0.00	0.70	0.00
Constantine	0.60	0.02	0.60	0.02	0.60	0.02
Multieix	0.6	0.00	0.3	0.00	0.6	0.00
Seán	no significant		0.4	0.01	0.7	0.00

One of the most remarkable features of this multi-stalagmite reconstruction is the general good agreement between the trace element records provided by different stalagmites during the overlapping periods, particularly for the Mg/Ca ratios.

$\delta^{18}O$ and $\delta^{13}C$ records

A summary of the $\delta^{18}O$ and $\delta^{13}C$ results for each stalagmite is shown in Table 3.8 and the whole records plotted against age in Fig. 3.25. Correlations between both isotope ratios are significant positive for each stalagmite (Fig. 3.26; $r \geq 0.7$, p *value* = 0) and for this reason their patterns along the records are described jointly. Both stable isotopes for each stalagmite also present significant positive correlation to Mg/Ca (Fig. 3.27).

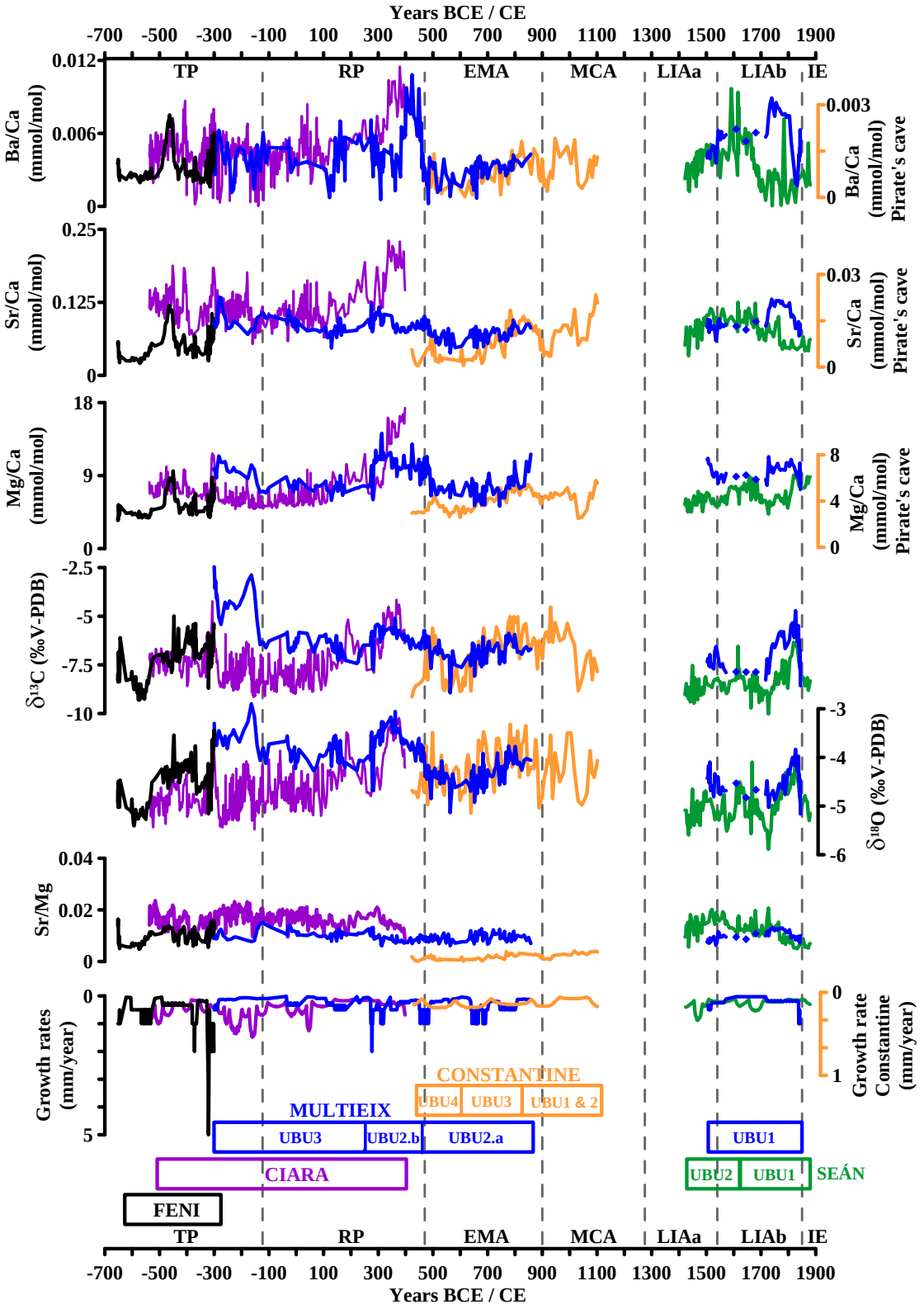

Figure 3.25. From up to bottom, Ba/Ca, Sr/Ca, Mg/Ca, $\delta^{13}C$, $\delta^{18}O$, Sr/Mg records and, growth rates for stalagmites: Feni (black line); Ciara (purple line); Multieix (blue line,); Constantine (orange line) and Seán (green line). Note that trace elements of Constantine, which is from a different cave (*Ses Coves del Pirata*) than the rest of stalagmites (*Sa Balma des Quartó* cave), are plotted in different scale-axis (right axis). Horizontal axis are expressed in years Before Common Era (BCE) / Common Era (CE). The climate/historical periods are also indicated: Talaiotic Period (TP); Roman Period (RP); Early Middle Ages (EMA); Medieval Climate Anomaly (MCA); Little Ice Age (LIA) and Industrial Era (IE). The 50 U/Th ages used in the four age models can be consulted in Table 3.10. Unconformity Bounded Units (UBU) for each stalagmite are also indicated.

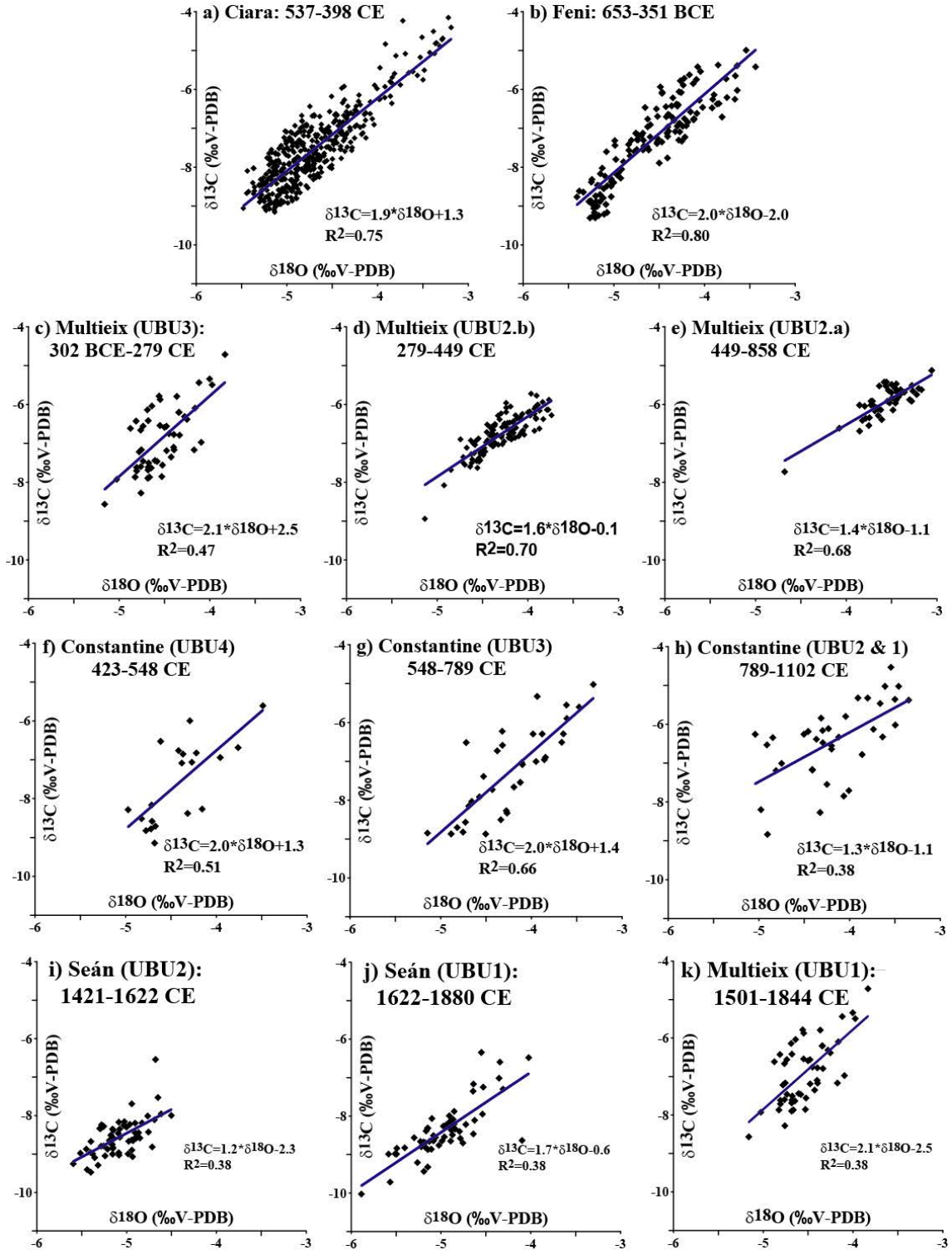

Figure 3.26. Correlations between $\delta^{13}C$ and $\delta^{18}O$ for the different stalagmites and their respective Unconformity Bounded Units (UBUs). **a)** Feni. **b)** Ciara. Multieix: **c)** cm 30.5-22, UBU3; **d)** cm 22-17, UBU2.B; **e)** cm 17-5, UBU2.A. Constantine: **f)** cm 9-7, UBU4; **g)** cm 7-3.5, UBU3; **h)** cm 3.5-0, UBU2 and UBU1. Seán: **i)** cm 12-6, UBU2; **j)** cm 6-top, UBU1. **k)** The top 5 cm of Multieix (UBU1).

$\delta^{18}O$ and $\delta^{13}C$ values in both Feni and Ciara stalagmites present very similar average ranges. In Feni stalagmite presents remarkable depleted values in the base with enriched

values between 489-322 yr BCE. Ciara stalagmite shows high frequency variability (<decadal time-scale) with the most depleted values before 100 CE and the most enriched values from 100 to 398 yr CE.

Multieix stalagmite did not grow continuous but it is a particular relevant in this study since it overlaps with most of the other studied stalagmites. During its lower unit (UBU3; 302 yr BCE-279 yr CE), isotope records present remarkable enriched values, which are higher than those obtained in the coeval stalagmite, Ciara. After that, stable isotope values become more depleted for the second unit (UBU2; 279-858 yr CE). Stable isotopes correlations for this UBU2 have been analysed in two different sections (UBU2.b from 279 to 449 yr CE and UBU2.a from 449 to 858 yr CE) because a more enriched and more depleted sector previous and after 449 yr CE can be differentiated (Fig. 3.26).

Stalagmite or UBU	**Mg/Ca vs. $\delta^{18}O$**		**Mg/Ca vs. $\delta^{13}C$**	
	r	***p* value**	**r**	***p* value**
Feni	0.61	0.00	0.51	0.00
Ciara	0.76	0.00	0.82	0.00
Constantine	0.57	0.00	0.75	0.00
Multieix	0.48	0.00	0.47	0.00
Seán	0.39	0.00	0.49	0.00
All stalagmites	**0.53**	**0.00**	**0.57**	**0.00**
Constantine UBU1-2	0.58	0.00	0.46	0.01
Constantine UBU3	0.66	0.00	0.86	0.00
Constantine UBU4	no significant		0.81	0.00
Mutieix UBU1	0.28	0.05	0.35	0.01
Multieix UBU2	0.81	0.00	0.79	0.00
Multieix UBU3	0.66	0.00	0.66	0.00
Seán UBU1	0.38	0.00	0.54	0.00
Seán UBU2	no significant		0.32	0.01

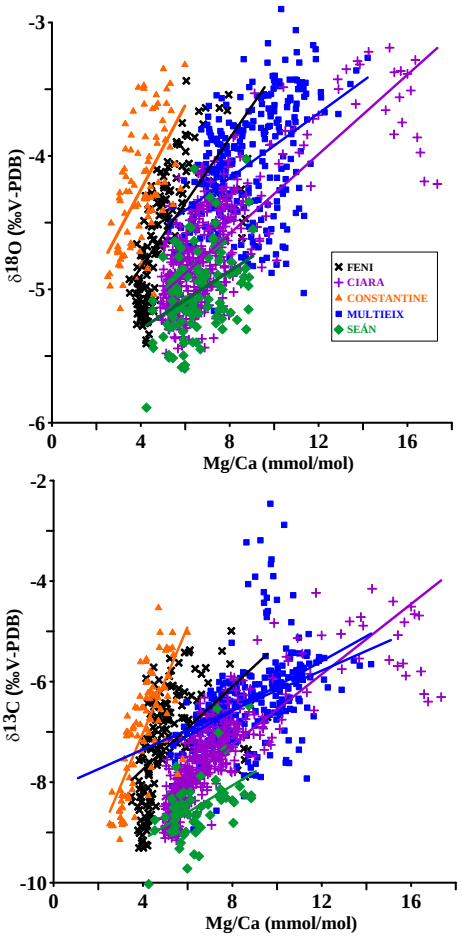

Figure 3.27. Correlations between Mg/Ca and $\delta^{13}C$ and $\delta^{18}O$, respectively, for each stalagmite. In the Table are shown also these correlations for the different UBUs of the stalagmites.

The most recent part of the stalagmite (UBU1; 1503-1844 yr CE), show contrasting values with very depleted values in the early part that enrich significantly after 1700 yr CE. Isotope records in Constantine stalagmite agree well with those patterns detected in the overlapping period of Multifeix even though they belong to different caves. Most

depleted values concentrate in the lower part (423-650 yr CE) while they became heavier toward the upper part. Regarding to Seán stalagmite, the two defined UBUs are comparable isotopic values being more depleted at the base and increase upwards from 1645 yr CE.

Micro-CT scanning and XRF results: Seán stalagmite

Micro-CT scanning was only applied in the Seán stalagmite in order to better characterise the boundary between the two UBUs and corresponding to the previously described brown layer. Micro-CT scanning results are expressed in a colour-map density (Fig. 3.28 left panel). Growing laminates are well represented in the image by the alternation of denser (25081-15673.5 HU) and more porous (15673.5-6266 HU) layers. Colour-map densities values < 6266 HU correspond to void spaces. The UBU boundary or brown layer is very well identified in the Micro-CT image by very low values (~ 6266 HU) indicating a void space.

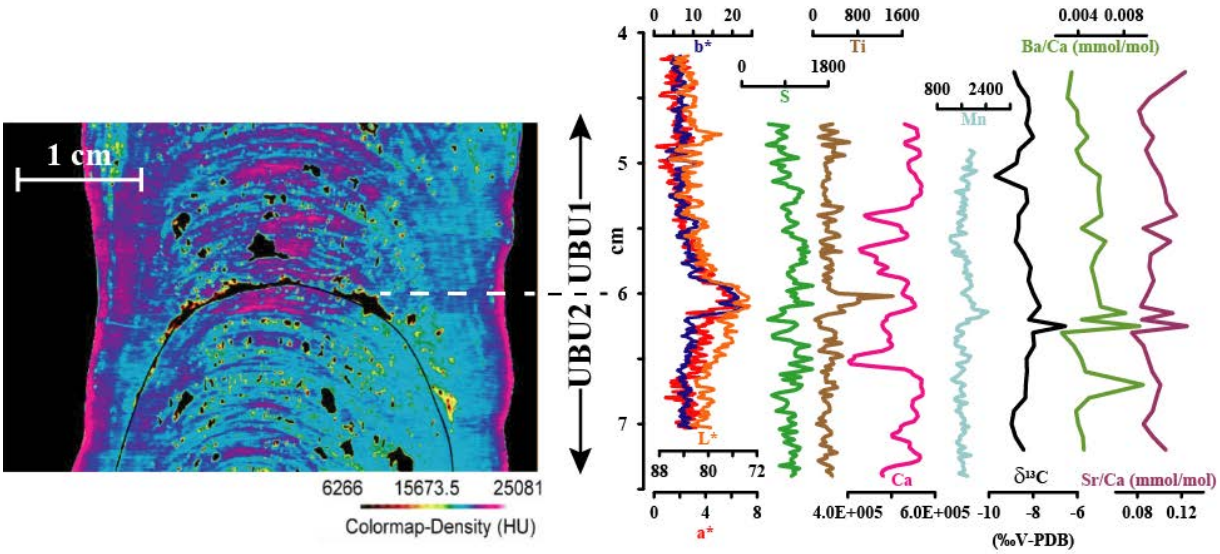

Figure 3.28. Left panel: Micro-CT Colour map from the upper part of Seán stalagmite (4.5 – 6cm), HU = Hounsfield units; Right panel (from left to right): Coordinates of colour CIE-L (Lightness)*a*b*; S, Ti, Ca and Mn elements measured with the XRF-scanner and $\delta^{13}C$, Ba/Ca and Sr/Ca measured in discreet samples.

Among the several elements in the XRF core-scanner measurements were also performed in Seán covering the UBUs limit including S, Ti, Mn and Ca (Fig. 3.28 right panel). S record shows several oscillations but without any significant change associated to the UBUs limit. In contrast Ti record shows an abrupt enhancement coincident with the brown layer. The Mn profile shows a little maximum below the

UBUs irregularity while Ca shows several oscillations but none differentiates the UBU's boundary.

Colour measurements (L*a*b* values-colour coordinates) were obtained from the high-resolution scanner pictures (Fig. 3.28 right panel) and define an abrupt change in the boundary between both Seán's UBUs. Parameters b* (yellow-blue) and L* (lightness) indicate more differences in the boundary than parameter a* (red-green).

3.3.6. Discussion

Control factors on partitioning

Mg/Ca Sr/Ca and Ba/Ca ratios in dripwater can provide information about the two dominant factors controlling dripwater chemistry: 1) Bedrock dissolution; 2) mixing of post-evaporative salt solutions accumulated in the soils; and 3) hydrochemistry evolution through the karst pathways dominated by the amount of *prior calcite precipitation* (PCP) above the drip sites (Tremaine and Froelich, 2013). PCP takes place in the limestone aquifer during transit of water in aerated channels, upstream of the stalagmite formation and, it can be a major mechanism controlling the trace element composition of stalagmites (Fairchild et al., 2000; Hori et al 2013). PCP (Fairchild et al., 2000; Fairchild and Treble, 2009; Stoll et al., 2012) occurs when the water finds a gas phase characterized by a lower pCO_2 and then, CO_2 degassing takes place, which will lead to super-saturate the water for $CaCO_3$ and a tendency for calcite precipitation. The effect of PCP results in an increase in the ratio of trace element to Ca in solution due to the removal of the cations from the water in the proportion in which they are incorporated into the calcite (Holland et al., 1964; Fairchild and Treble, 2009). PCP can increase under dry climate conditions since led to longer water residence time in the epikarst and decreased drip rates that enhance CO2 degasing (Fairchild et al., 2000). The studied stalagmites present positive correlation between Mg/Ca, Sr/Ca and also Ba/Ca during most of the records (Table 3.9), which points out an important PCP control on our trace elements. The dominant seepage flow described in the caves with the formation of large soda-straws stalactites supports the dominance PCP control on the cave drip waters chemistry.

The only no significant correlation between trace elements ratios has been obtained during the end of the LIAb (Seán UBU1; between Sr/Ca and Mg/Ca; Table 3.9). Also

during 1700-1850 yr CE is when differences between Seán and Multieix have been observed, with higher Mg/Ca ration in Multieix (Fig. 3.25). Ratios differences can be explained by changes in the growth rates, in the source elements (when here is not a single source of elements, eolian dust) or variations in the pCO2 (Fairchild et al., 2009). Growth rates have demonstrated to produce a strong control on both Sr and Ba. Differences between these elements lay in their different partitioning factor into the growing calcite, this result in a strong kinetic effect in both Sr and Ba that has not been observed in Mg (Stoll et al., 2012) as a consequence, enhanced speleothem growth rates result on significant enhancement in the Sr/Ca and Ba/Ca which is not detected in Mg/Ca. Anyway, in order to use Sr/Ca and Mg/Ca in stalagmites like paleoclimate proxies, the Sr/Mg ratio must be constant in stalagmites through time (Tremaine and Froelich, 2013) and the Sr/Mg ratio variability in the Mallorca stalagmites is not remarkable (Fig. 3.25).

Control factors on isotopic speleotem signals

As it has been mentioned in the previous subsection, PCP seems to be a dominant control in partitioning. High correlations between $\delta^{13}C$ signatures and Mg/Ca and Sr/Ca in speleothems have been related to PCP (Fairchild and Treble, 2009). All Mallorca stalagmites and their corresponding UBUs presented in this study show a significant positive correlation between $\delta^{13}C$ and Mg/Ca (Fig. 3.27). Thus, the relationship between PCP and degassing seems to results in systematic rises in $\delta^{13}C$ Mallorca stalagmite values. Model experiments also demonstrate that $\delta^{13}C$ in drip waters increases proportional to Mg/Ca ratios under enhanced PCP conditions (Owen et al., 2018). Thus, drier intervals can lead increased PCP leading to the similarity between higher Mg and Sr concentrations and higher speleothem $\delta^{13}C$ (Treble et al., 2003).

Regarding to the Mallorca stalagmites correlation between $\delta^{18}O$ and Mg/Ca, is also significant positive for all the stalagmites but not for all the UBUs analysed separately (Fig. 3.27), which could point out weaker PCP influence in $\delta^{18}O$ than in $\delta^{13}C$.

Oxygen isotopes are the most commonly used proxy in speleothem studies and have long been utilized to reconstruct cave temperature (particularly in high latitudes in continental interiors) or precipitation properties of meteoric water, which can be influenced by factors like the moisture source effect, the amount effect (particularly in

the semi-arid regions) and synoptic meteorology (Fairchild and Treble, 2009). A criterion to accept stable isotope speleothem records like useful paleoclimate proxies is the no presence of a positive correlation in both isotopes on samples taken along the growth axis (Goede et al., 1986; Desmarchelier et al., 2000). Other studies argue that his positive correlation is due to environmental changes, which can simultaneously influence both isotopes (e.g.: Genty et al., 2003; Paulsen et al., 2003). However, Mickler et al. (2006) showed, following the theory of Hendy (1971), that a positive $\delta^{18}O$-$\delta^{13}C$ covariation can occur from non-equilibrium isotope effects, independent of environmental variations, driven during progressive CO_2 degassing and calcite precipitation by the isotopic evolution of the dissolved inorganic carbon reservoir. This study also found that among 165 published speleothem stable isotope records with a global distribution, most of them presented positive covariation between both isotopes.

All the stalagmites presented in this study show significant positive $\delta^{18}O$-$\delta^{13}C$ covariance (Fig. 3.26). The $\delta^{18}O$-$\delta^{13}C$ covariance on the stalagmite through time can be explained taking into account that increase (decrease) in precipitation amount, which would cause depletion (enrichment) of $\delta^{18}O$, also encourage plant productivity and increased soil CO_2 production, driving more depleted $\delta^{13}C$ in dripwaters (Hodge, 2004). Overall, despite on positive $\delta^{18}O$-$\delta^{13}C$ covariance, possibly from non-equilibrium isotope effects, speleothem stable isotope records can still be useful tools to provide paleoclimatic information (e.g., Spötl and Mangini, 2002; Mickler et al 2006).

Cave precipitates and model data have demonstrate that under low rate drip locations typically of seepage, like is the case of our study cave, oxygen and carbon isotopes tend to precipitate in disequilibrium resulting in heavier $\delta^{13}C$ and $\delta^{18}O$ values than those predicted in equilibrium (Riechelmann et al., 2013). Processes that can drive isotopic disequilibrium for $\delta^{18}O$ resulting in heavier values are: (i) high rates of calcite precipitation; (ii) prolonged residence times of the thin solution layer on the surface of the stalagmite as a consequence of low drip rates (iii) evaporation. So although $\delta^{18}O$ is not directly modified by PCP changes, the drier conditions that enhance PCP also can extend the thin solution layer residence time on the surface of the stalagmite. Karst hydrology influences both the drip rate and the abundance of PCP. The last one has direct influence on $\delta^{13}C$, but trough the influence on the saturation Index with respect to the calcite, $\delta^{18}O$ is indirectly also affected by PCP (Riechelmann et al., 2013).

Covariance of $\delta^{18}O$ with Mg/Ca and Sr/Ca has also been argued to distinguish 'rainfall amount' versus 'rainfall source' in speleothem $\delta^{18}O$ records (Tremaine and Froelich, 2013). But under constant speleothem Sr/Mg conditions, coherent and in-phase variations in speleothem $\delta^{18}O$, Sr/ Ca and Mg/Ca may be confidently attributed to wet vs. dry rainfall amount (Tremaine and Froelich, 2013). Mallorca stalagmites present relatively constant Sr/Mg ratio (Fig. 3.25). In addition, the relationship between speleothem Mg and $\delta^{18}O$ is also used to argue that Mg is an indicator of effective water excess where speleothem $\delta^{18}O$ is assumed to largely reflect changes in rainfall (Fairchild 2009). Overall and also taking into account the similarity between the long-term trends of the $\delta^{18}O$ records from the coeval stalagmites (Frisia, 2015) considered in this study, adequacy of these paleoarchives to perform hydroclimate interpretations for the spanned period and in this context can be corroborated.

Climate evolution: the last 2.7kyr

The general trends of the $\delta^{18}O$ records indicate rather wet conditions during TP, the beginning of the RP, the EMA and the LIA. In contrast, drier conditions have been observed during the last part of the RP and the EMA and, the MCA. Climate interpretation during the TP and the RP is based on Ciara and Feni stalagmites and the $\delta^{18}O$ records from centimetres of the Multieix base (until 146 yr CE) have not been taking into account. The most depleted $\delta^{18}O$ values for the whole studied period occurred during the LIA (Fig. 3.29) pointing this as the wettest period. None of the stalagmites fully covers the MCA and early LIA, a period that represents a hiatus in Multieix stalagmite.

During the TP general wet conditions dominated although with several minor oscillations pointing the occurrence of some short drier episodes (Fig. 3.30). The stalagmites microstratigraphy support the dominance of homogeneous drip rates indicating hydric stability during this period when climate conditions were relatively cold according to a Sea Surface Temperatures (SST) reconstruction in the central-western Mediterranean Sea (Cisneros et al., 2016). During the RP occurred a major transition from relatively humid conditions, comparable to those from the TP, to one of the apparently driest periods of the record. This transition occurred around 200 yr CE when SST reached the maximum values of he last three millennia (Cisneros et al., 2016).

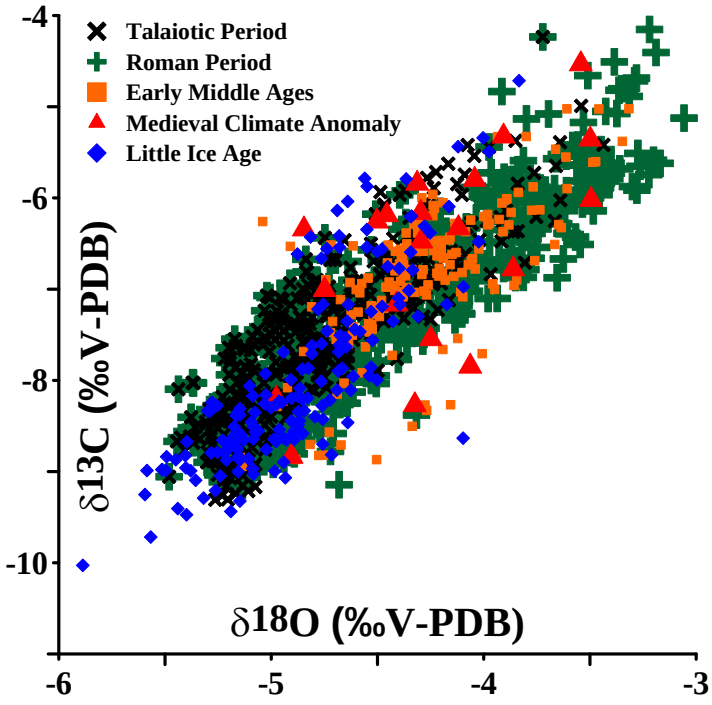

Figure 3.29. $\delta^{13}C$ vs. $\delta^{18}O$ from all the Mallorca stalagmites during each of the climatic periods of the last 2.7 kyr.

During the RP-EMA transition climate became wetter, conditions that dominated during the early EMA to change toward drier conditions after 650 yr CE and maintained during the second half of the EMA while SST record indicates an overall cooling trend along the whole EMA (Cisneros et al., 2016). These cold and wet conditions during the early EMA are in agreement with those described in the Gulf of Lion (Jalali et al., 2018) and in the central Mediterranean (Bassetti et al., 2016) by coastal and deltaic records, respectively.

The MCA is only partially represented by Constantine stalagmite that shows relatively heavy isotope values and minima growth rates before it definitely stopped its growth at about 1100 yr CE. Multieix stopped its growth right before the onset of the MCA and restarted it at the early LIA. These evidences suggest that climate conditions during the MCA were particularly dry, probably the most extreme arid conditions of the whole studied period, in agreement with previous observation based on record compilation from the Iberian Peninsula (Moreno et al., 2012).

During the LIA, both Multieix and Seán stalagmites agree showing relatively light values, although with several minor oscillations the overall values are mostly lighter than during previous intervals, pointing out this as one of the wettest periods of the

studied record although after 1700 yr CE a trend towards drier conditions appear in agreement with the slower drip and growth rates. The record ends with a short $\delta^{18}O$ depletion after 1880 yr CE indicating an improvement of the hydrological availability during the IE although this period is not entirely covered by the records.

Overall, humidity and thermal conditions observed in our study area seem to be coincident to those described in the Iberian Peninsula (Desprat et al., 2003; Álvarez et al., 2005; Moreno et al., 2008; 2012; Martín-Puertas et al., 2009; 2010; Morellón et al, 2009; 2011; 2012; Rodrigues et al., 2009; Martín-Chivelet et al., 2011; Nieto-Moreno et al., 2011; Pérez-Sanz et al., 2013; Corella et al., 2016) and in Central Europe (Büntgen et al., 2011; Luterbacher et al., 2016). However, the hidroclimate variability reconstruction from Mallorca speleothemes present differences regarding those reconstructions from the Iberian Peninsula and Central Europe in some moments during periods likes the RP and the EMA (Fig. 3.30).

Extreme episode during 1622 yr CE?

One of the characteristics of the Seán stalagmite during the LIA is the presence of a brown layer centred at 1622 yr CE that marks the limit between the two described UBUs (Fig. 3.31) and is associated to a remarkable Ti peak and it is also accompanied by abrupt changes in the colour parameters (Fig. 3.31). The brown layer follows the general lamination, no important signs of erosion or stops in the deposition haven been detected and thus, Seán apparently grew quite continuously and this layer did not involve a hiatus in the record. Overall, this unconformity consists in a minor an eventual event, which does not seem answer to variations in drip rates or changes in the growth rates. The presence of high Ti values and also of micrite carbonate suggests the enhanced arrival of terrigenous particles, corresponding to an allogenic horizon.

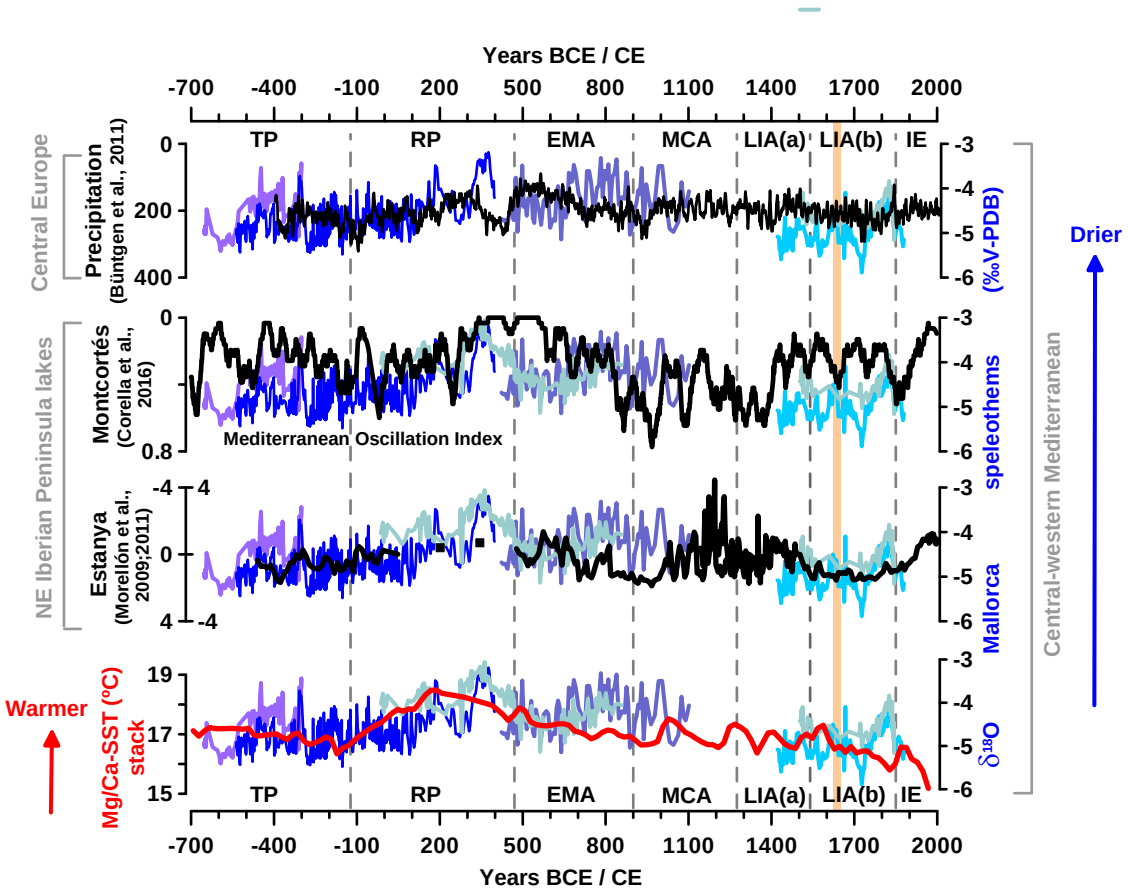

Figure 3.30 Comparison between the paleohydrological Mallorca records ($\delta^{18}O$ stalagmites in blue) and thermal and hydrological recosntructions from Iberian Peninsula and Central Europe. Sea Surface Temperatures (SST; in red) correspond to the central-western Mediterranean Sea (Cisneros et al., 2016). The vertical brown line indicates the brown layer in Seán stalagmite.

Among the potential sources of this distinctive layer it has been considered the influence of a large volcanic eruption since the dominant LIA cold temperatures have frequently been attributed to such events (Crowley, 2000; Robock, 2000; Bertler et al 2011; (Miller et al., 2012; McGregor et al., 2015). Nevertheless, this layer is not related to any sulphur (S) peak or $\delta^{13}C$ enrichment (Fig. 3.31) that typically are detected in records associated to volcanic eruption (Frisia et al., 2008; Badertscher et al., 2014). Thus the remarkable Ti peak in the brown layer may indicate the arrival of detrital material. One mechanism able to transport this king of material to our cave is the supply of dust aerosols. Numerous studies have demonstrated the influence of the Saharan dust in our study area (Goudie and Middleton, 2001; Moreno et al 2002) and the big importance in the red Mediterranean soils (Muhs et al., 2010). In addition, it has been detected in the cave soil sediments in Mallorca (Fornós et al., 2009) and in stalagmites from the Eastern Mediterranean through Sr and U isotopes (Frumkin and Stein, 2004). Saharan dust is mostly supplied by wet deposition (‘muddy rain’), when the air mass becomes fresh after to be in contact to the sea, while dry deposition only takes place

occasionally (Fiol et al., 2005). In addition, although aerosols interaction with radiative forcing is still quite controversial, recent works correlate aerosols enhancement with drops in SST and argued that positive NAO phases can also favour the aerosol enhancement in our study area (Nabat et al., 2015a; 2015b; 2016). Nevertheless, despite on the relatively more enriched stable isotopes in our brown layer and the coincidence with a drop in SST and an isolated period of positive NAO phase (Fig. 3.31), it can be possible to conclude neither that this episode correspond to a dry or wet dust deposition.

Previous studies have traced cave floods in the form of detrital layer recorded in stalagmites (Borsato et al., 2003; Dorale et al., 2005; Dasgupta et al., 2010). Elevated Ti compared to the calcite matrix have been used to identify paleofloods events for instance in southern Greece (Finné et al., 2015). Thus, speleothems can be used as proxies for extreme rainfall or other hydrologic drivers of cave flooding. (Denniston and Luetscher, 2017). The lower part of the *Balma* cave, presents evidences of inundation possibly after an extreme rain events. Although the cave is dominated by seepage flow, one side of the cave shows evidences of episodic water flows that may led the inundation of the base which easily could cover the six cm of Seán where the brown layer is located. This hypothesis is in agreement with the fact that the micrite layer is filling the gaps between the older columnar fabric and it also could explain the presence of a gastropod test (Fig. 3.36 in Supplementary Material). The Miocene carbonates of the karst system are rich in these marine microfossils, which could arrive in suspension to the stalagmite and fixed by the next calcite growth.

During the entire LIA period, frequent rain extreme events have been described in previous studies: an increment in the run-off in the Alboran sea (Nieto-Moreno et al., 2011) and in the central-western Mediterranean sea (Margaritelli et al., 2018); humid episodes in the north-western Mediterranean sea (Bassetti et al., 2016); the most important flood of the last millennia in the Ebro river basin (Balasch et al., 2019); increase in the lake levels in the southern Spain (Martín-Puertas et al., 2008); enhance in flood events in the Iberian Peninsula (Barriendos and Martin-Vide, 1998; Benito et al, 2003; Moreno et al, 2008). Thus, the brown layer from Seán stalagmite may represent the occurrence of a major flooding event at 1622 yr CE related to an extreme rain event in Mallorca. It should be noted the low uncertainties obtained in the U/Th ages that are closest to the cm 6 in Seán: cm 5.4, 1660 ± 15.1 yr CE and cm 6.6, 1602.4

± 7.7 yr CE (Table 3.10). Previous studies based on historical documents have pointed out remarkable floods around Mallorca Island during the XVII century and particularly, during the autumn of the years CE: 1618, 1620, 1655, 1635 and 1683 (Campaner, 1881).

Forcings and climate variability during the LIA

The LIA climate variability has been attributed to a series of factors such as increased volcanic activity changes in the thermohaline circulation and solar activity minima (Broecker 2000, 2001; Lund et al. 2006). In order to better understand the potential causes of the detected hydrological changes recorded by the studied Mallorca stalagmites, their LIA signal is compared with existing records (Fig. 3.32) from the in the Balearic Sea, positive (negative) NAO modes, positive (negative) MOI and higher (lower) storminess activity in the Gulf of Lion (Fig. 3.32). However, correlations between the different considered records are not always constant suggesting a non-stationary patterns behaviour over time. For instance, regarding to the Solar Minima (Bard et al. 2000; Mayewski et al. 2004, 2006; Ammann et al., 2007; Vallefuoco et al., 2012), during the Spörer (1450-1550 yr CE) and the Maunder Solar Minima (1645-1715 yr CE), wet conditions or trends to wet are represented by overall lighter $\delta^{18}O$ values in Mallorca stalagmites (Fig. 3.32). In contrast, during the Dalton Minimum (1790-1820 yr CE) stalagmites indicate one of the driest LIA intervals in Mallorca.

Regarding to NAO, the predominant wet conditions observed by our stalagmites were coincident with the frequent negative NAO phases reconstruct for the LIA, which has also been observed in records from the Iberian Peninsula for the same period (Ramos-Román et al., 2018). However, during some moments this relation does not exist, like ~1850 yr CE. Recent observations indicate that negative NAO modes may correspond to different configuration of the pressure cells with different consequences in the hydrology of the western Mediterranean Sea (Comas-Bru et al., 2014; Sáez de Cámara et al, 2015; Comas-Bru et al., 2016). Examples of these different combinations of climate modes would be different signs of the NAO/East Atlantic Pattern (Sánchez-López et al., 2016) or the influence of the Western Russian Pattern (Josey et al., 2011).

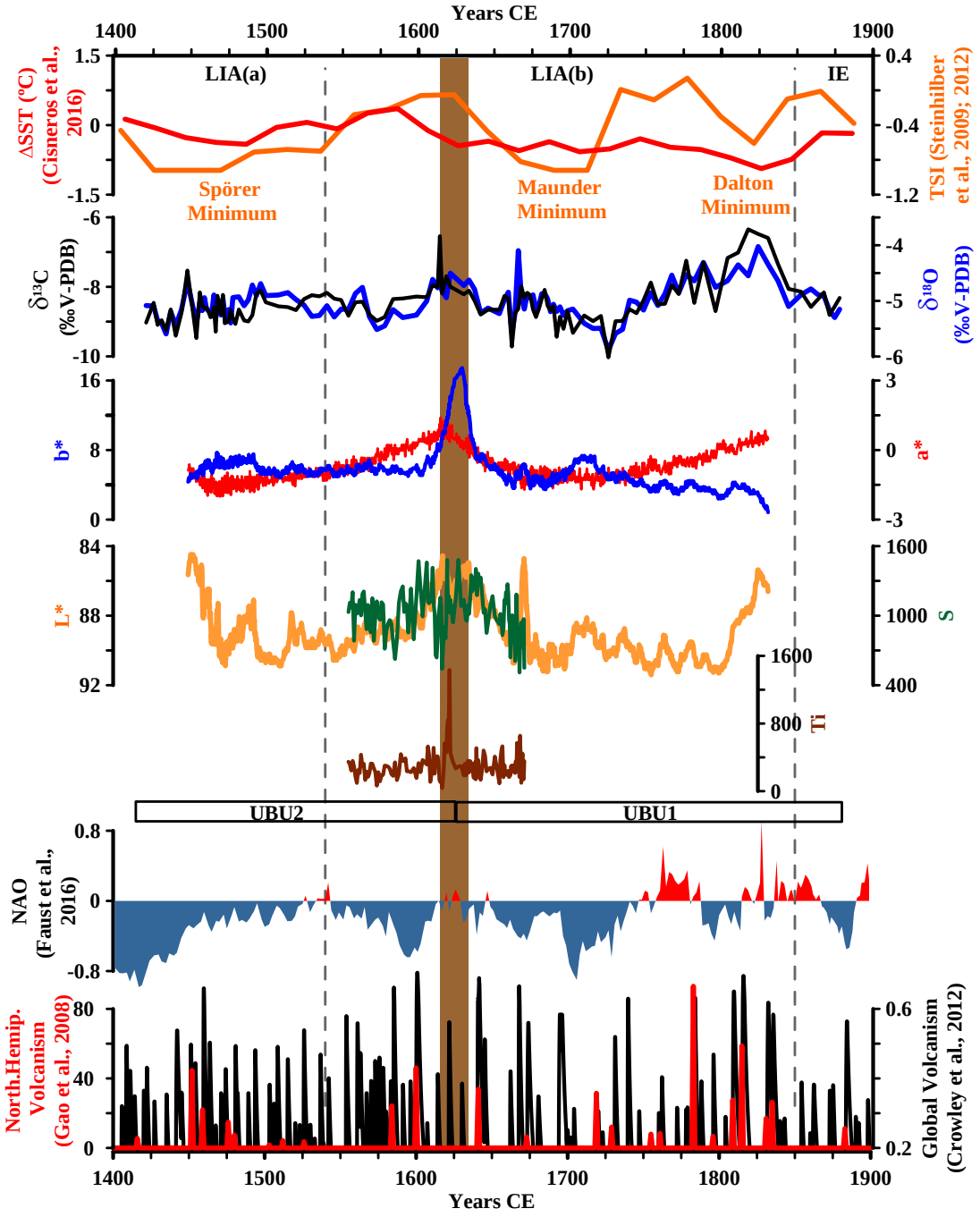

Figure 3.31. Records from Seán stalagmite compared to SST, TSI, North Atlantic Oscillation (NAO) reconstruction and volcanism activity. From top to bottom: Mg/Ca-Sea Surface Temperature (SST) from north Minorca (Cisneros et al., 2016); Total Solar Irradiance (TSI; Steinhilber et al., 2009; 2012); $\delta^{13}C$ and $\delta^{18}O$ records; Coordinates of colour CIE-L (Lightness)*a*b*; Sulphur (S) and Titanium (Ti) from XRF analyses; North Atlantic Oscillation (NAO) reconstruction; Northern and Global Volcanism (Gao et al., 2008; Crowley et al., 2012). Brown vertical band indicates discontinuity and brown layer observed in Seán (~cm 6), which corresponds to the limit between both UBUs in this stalagmite.

Total Solar Irradiance (TSI; Steinhilber et al., 2009; 2012), the NAO (Faust et al., 2016), the MOI (Corella et al., 2016) and the storminess in the Gulf of Lion (Sabatier et al., 2012). Accordingly to this comparison, most of the multidecadal periods representing drier (wetter) conditions in Mallorca are coincident with cold (warm) SST

In reference to the MOI, multidecadal trends to drier conditions in Mallorca are mostly coincident with more heavy rainfalls in the northeast Iberian Peninsula (Fig. 3.32). Nevertheless, certain mismatch in the trends and magnitude of the oscillation of MOI and $\delta^{18}O$ records has been observed during some moments like after the three solar minima and even during the Dalton Minimum (Fig. 3.32) when fewer Heavy Rainfalls in northern east Iberian Peninsula are coincident with drier conditions in the central-western Mediterranean region. It should be noted that the brown layer observed in Seán is coincident with an enhancement of heavy rain events in northern Iberian Peninsula (Fig. 3.32), which is in agreement with the hypothesis of a punctual flood caused by extreme rain event and suggested here like cause of the brown layer.

3.3.7 Conclusions and future perspectives

This study presents five stalagmite records from two Mallorca Island caves that represent the first speleothem-based hydrological reconstruction for the central-western Mediterranean during the last 2.7 kyr (653 yr BCE-1880 yr CE). The carefully observation of the architectural elements has been combined with mineralogical X-Ray Diffraction characterization, $\delta^{18}O$, $\delta^{13}C$ and trace element analyses (Mg/Ca, Sr/Ca and Ba/Ca), and complemented in one stalagmite with high resolution optical parameters, qualitative elemental composition using a XRF core-scanner system and Micro-CT scanning. Chronologies have been produced with accurate U/Th dates. This multi-proxy combination methodology has proved that stalagmites from central-western Mediterranean region can be adequate tools to provide paleohydrological information and the $\delta^{18}O$ proxy is a valid proxy to define in drier and wetter periods this context.

None of the studied stalagmites cover the whole studied period but a good overlap exists between them which allows to reproduce most of the discussed climatic intervals by two independent stalagmite records with the exception of the Medieval Climate Anomaly (MCA) that correspond to an hiatus in the record. General wet conditions dominated for the Talaiotic Period (TP) and the early Roman Period (RP), the first half of the Early Middle Ages (EMA) and the entire Little Ice Age (LIA), while dry conditions characterized the late RP, the late EMA and the entire MCA. The fossil $\delta^{18}O$ values obtained for the LIA represent the most depleted ones for the studied period, which points out this period as the wettest one.

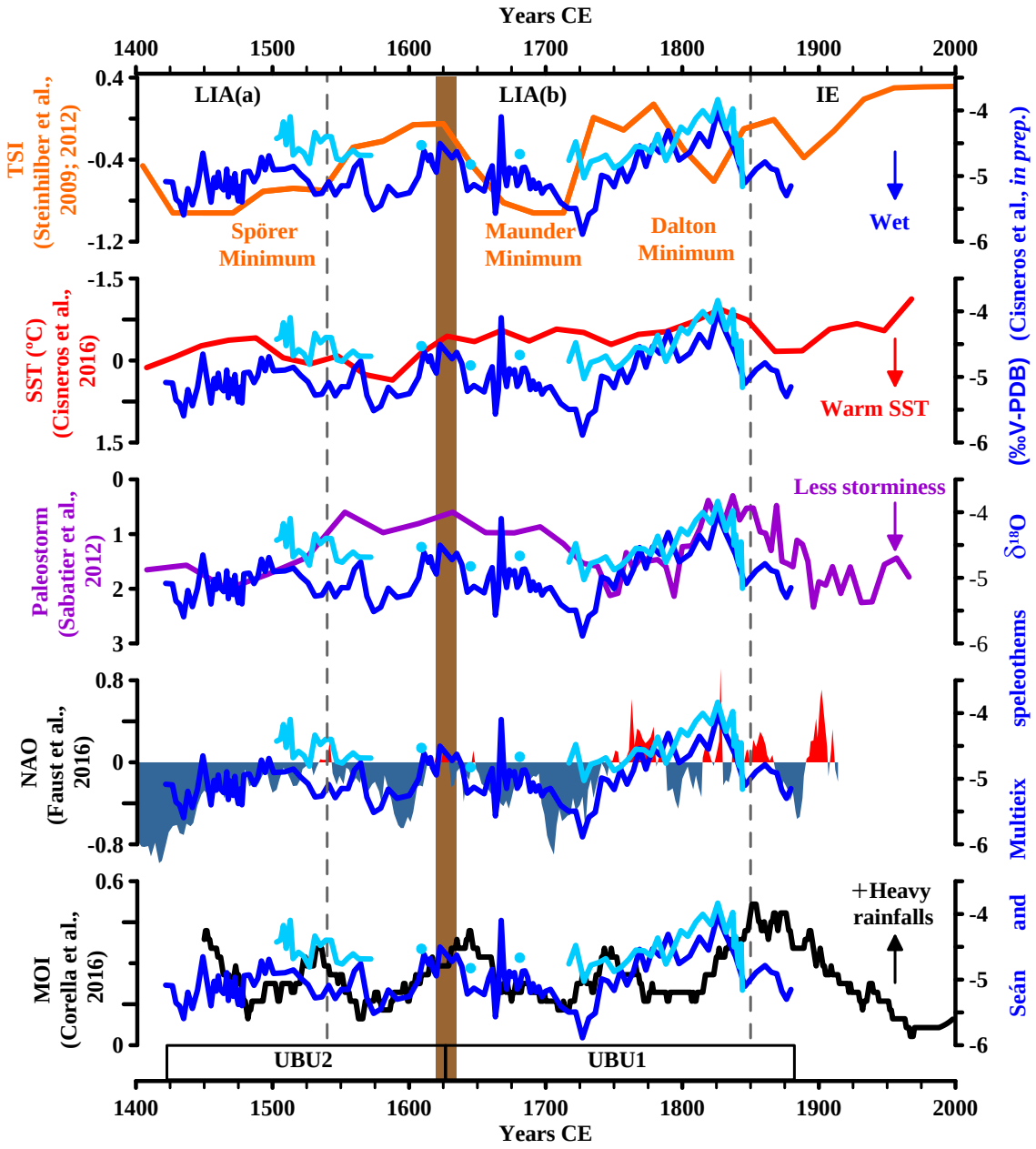

Figure 3.32. Oxygen stable isotope records for Seán (darker blue) and Multieix (less intense blue) stalagmites compared to data from another studies for the spanned period of the LIA. From top to bottom: Total Solar Irradiance (TSI; Steinhilber et al., 2009; 2012); Mg/Ca-Sea Surface Temperature (SST) from north Minorca (Cisneros et al., 2016); Paleostorm activity in the Gulf of Lion (Sabatier et al., 2012); North Atlantic Oscillation (NAO; Faust et al., 2016); Mediterranean Oscillation Index (MOI) from northeast Iberian Peninsula (Corella et al., 2016). Unconformity Bounded Units (UBU) for Seán stalagmite are indicated and the vertical brown band corresponds to the limit between them (brown layer ca. cm 6).

An extreme flooding event during the LIA, ca. 1622 yr CE, has been interpreted from a distinctive "detrital" brown layer defined in Seán stalagmite which corresponds to elevated Ti values and to the presence of micrite crystals filling the porosity from the older columnar crystals and also associated to a gastropod test. The LIA record presents multidecadal oscillations corresponding to drier (wetter) conditions and coincident with

cold (warm) SST in the Balearic Sea, positive (negative) NAO indexes, more (less) Heavy Rainfalls in the northeast Iberian Peninsula and higher (lower) storminess activity in the Gulf of Lion. Nevertheless, some exceptional periods exist to this overall correlation suggesting non-stationary patterns during some moments. Further research is needed in order to better understand the complex mechanisms that modulated climate patterns in the past and the Mallorca stalagmites potential like paleohydrological archives and information derived from historic climate records can be very helpful.

Acnowledgements. We thank financial support from ERC-Consolider Grant TIMED (683237); OPERA (CTM2013-48639-C2-1-R); PLIOKAR (CGL2013-48441-P); CHIMERA (CTM2016-75411-R); PLIOKAR-II (CGL2016-79246-P, AEI-FEDER, EU) and Generalitat de Catalunya, Grups de Recerca Consolidats (2017 SGR 315) to GRC Geociències Marines. We are grateful to M. Guart and A. Gallardo (Dept. de Dinàmica de la Terra i de l'Oceà, Universitat de Barcelona), J. Perona, T. Bullich, M. Aulet and À. San Martín for their collaboration in the laboratory tasks and, A. Pilares for his collaboration in the fieldwork. M. Cisneros benefited from a fellowship of the UB.

3.3.8 References

Álvarez, M.C., Flores, J.A., Sierro, F.J., Diz, P., France, G., Pelejero, C. and Grimalt, J., 2005. Millennial surface water dynamics in the Ría de Vigo during the last 3000 years as revealed by coccoliths and molecular biomarkers. Palaeogeo., Palaeoclim., Palaeoeco. 218, 1e13. http://dx.doi.org/10.1016/j.palaeo.2004.12.002

Ammann, C.M., Joos, F., Schimel, D.S., Otto-Bliesner, B.L. and Tomas, R.A., 2007. Solar influence on climate during the past millennium: results from transient simulations with the NCAR climate system model. Proceedings National Academy of Sciences of the USA 104, 3713–3718.

Badertscher, S., Borsato, A., Frisia, S., Cheng, H., Edwards, R.L., Tüysüz, O. and Fleitmann, D., 2014. Speleothems as sensitive recorders of volcanic eruptions – the Bronze Age Minoan eruption recorded in a stalagmite from Turkey. Earth and Planetary Science Letters 392, 58–66. https://doi.org/10.1016/j.epsl.2014.01.041

Balasch, J.C., Pino, D., Ruiz-Bellet, J.L., Tuset, J., Barriendos, M., Castelltort, X. and Peña, J.C., 2019. The extreme floods in the Ebro River basin since 1600 CE. Science of the Total Environment 646, 645-660. https://doi.org/10.1016/j.scitotenv.2018.07.325

Bard, E., Raisbeck, G., Yiou, F. and Jouzel, J., 2000. Solar irradiance during the last 1200 years based on cosmogenic nuclides. Tellus B 52, 985–992.

Barriendos, M. and Martin-Vide, J., 1998. Secular climatic oscillations as indicated by catastrophic floods in the spanish Mediterranean coastal area (14th–19th centuries), Climatic Change 38, 473– 491.

Bassetti, M.A, Berné, S., Sicre, M.A., Dennielou, B., Alonso, Y., Buscail, R., Jalali, J., Hebert, B. and

Christophe Menniti, C., 2016. Holocene hydrological changes of the Rhone River (NW Mediterranean) as recorded in the marine mud belt. Climate of the past 12, 1539–1553.

Benito, G., Sopeña, A., Sánchez-Moya, Y., Machado, M. J. and Pérez-González, A., 2003. Palaeoflood record of the Tagus River (Central Spain) during the Late Pleistocene and Holocene. Quaternary Science Reviews 22, 1737–1756, doi:10.1016/S0277-3791(03)00133-1.

Bermejo, J., Mateu, T., López, B., Minguillón, R., Herráez, G. and Villar, A., 2014. Cova de sa Balma des Quartó (Manacor, Mallorca). Endins: publicació d'espeleologia, 59–64.

Bertler, N.A.N, Mayewski, P.A., Carter, L., 2011. Cold conditions in Antarctica during the Little Ice Age: implications for abrupt climate change mechanisms. Earth and Planetary Science Letters 308, 41–51.

Blaauw, M., 2010. Methods and code for 'classical' age-modelling of radiocarbon sequences. Quat. Geochronology 5, 512–518. doi.org/10.1016/j.quageo.2010.01.002

Borsato, A., Quinif, Y., Bini, A. and Dublyansky, Y., 2003. Open-system alpine speleothems: implications for U-series dating and paleoclimate reconstructions. Studi Trentini di Scienze Naturali, Acta Geologica, 80: 71-83.

Broecker, W.S., 2000. Was a change in thermohaline circulation responsible for the Little Ice Age? Proceedings National Academy of Sciences of the USA 97, 1339–1342.

Broecker, W.S., 2001. Paleoclimate: was the medieval warm period global? Science 291, 1497–1499.

Büntgen, U., Tegel, W., Nicolussi, K., McCormick, M., Frank, D., Trouet, V., Kaplan, J.O., Herzig, F., Heussner, K.U., Wanner, H., Luterbacher, J. and Esper, J., 2011. 2500 years of European climate variability and human susceptibility. Science 331, 578–82, doi:10.1126/science.1197175.

Campaner y Fuertes, A., 1881. Cronicón Mayoricens. J. Colomer y Salas. Palma. XVI+611 pp.

Cheng, H., Edwards, L.R., Chou Shen, C., Polyak, V.J., Asmerom, Y., Woodhead, Jon, Hellstrom, J., Wang, Y., Kong, X., Spötl, C., Wang, X. and Calvin Alexander Jr., E., 2013. Improvements in 230Th dating, 230Th and 234U half-life values, and U-Th isotopic measurements by multi-collector inductively coupled plasma mass spectrometry. Earth Planetary Science Letters 371–372, 82–91.

Cisneros, M., Cacho, I., Frigola, J., Canals, M., Masqué, P., Martrat, B., Casado, M., Grimalt, J.O., Pena, L.D., Margaritelli, G. and Lirer, F., 2016. Sea surface temperature variability in the central-western Mediterranean Sea during the last 2700 years: a multi-proxy and multi-record approach. Climate of the Past 12, 849–869. https://doi.org/10.5194/cp-12-849-2016

Comas-Bru, L. and McDermott, F., 2014. Impacts of the EA and SCA patterns on the European twentieth century NAO-winter climate relationship: Impacts of EA and SCA patterns on NAO-winter climate relationship. Quarterly Journal of the Royal Meteorological Society 140, 354–363. https://doi.org/10.1002/qj.2158

Comas-Bru, L., McDermott, F. and Werner, M., 2016. The effect of the East Atlantic pattern on the precipitation δ18O-NAO relationship in Europe. Climate Dynamics 47, 2059–2069. https://doi.org/10.1007/s00382-015-2950-1

Conte, M., Giuffrida, A. and Tedesco, S., 1989. The Mediterranean Oscillation. Impact on precipitation and hydrlogy in Italy Climate Water. Publications of the Academy of Finland, Helsinki.

Corella, J.P., Valero-Garcés, B.L., Vicente- Serrano, S.M., Brauer, A. and Benito, G., 2016. Three millennia of heavy rainfalls in Western Mediterranean: frequency, seasonality and atmospheric drivers. Scientific Reports 6. https://doi.org/10.1038/srep38206

Criado-Aldeanueva, F., Soto-Navarro, F. J. and García-Lafuente, J., 2014. Large-Scale Atmospheric Forcing Influencing the Long-Term Variability of Mediterranean Heat and Freshwater Budgets: Climatic Indices. Journal of Hydrometeorology 15, 650–663.

Crowley, T.J., 2000. Causes of Climate Change Over the Past 1000 Years. Science 289, 270–277. https://doi.org/10.1126/science.289.5477.270

Dasgupta, S., Saar, M.O., Edwards, R.L., Shen, C.C., Cheng, H. and Alexander, E.C., 2010. Three thousand years of extreme rainfall events recorded in stalagmites from Spring Valley Caverns, Minnesota. Earth and Planetary Science Letters 300, 46-54. http://dx.doi.org/10.1016/j.epsl.2010.09.032

Debret, M., Sebag, D., Desmet, M., Balsam, W., Copard, Y., Mourier, B., Susperrigui, A.S., Arnaud, F., Bentaleb, I., Chapron, E., Lallier-Vergès, E. and Winiarski, T. 2011. Spectrocolorimetric interpretation of sedimentary dynamics: The new "Q7/4 diagram". Earth-Science Reviews 109, 1-19.

Denniston, R.F. and Luetscher, M., 2017. Speleothems as high-resolution paleoflood archives. Quat. Sci. Rev. 170, 1-13. http://dx.doi.org/10.1016/j.quascirev.2017.05.006

Desmarchelier, J.M., Goede, A., Ayliffe, L.K., McCulloch, M.T. and Moriarty, K., 2000. Stable isotope record and its palaeoenvironmental interpretation for a late Middle Pleistocene speleothem from Victoria Fossil Cave, Naracoorte, South Australia. Quaternary Science Reviews 19, 763–774.

Desprat, S., Sanchez Goñi, M.F. and Loutre, M., 2003. Revealing climatic variability of the last three millennia in northwestern Iberia using pollen influx data. Earth and Planetary Science Letters 213, 63e78.

Dorale, J.A., Lepley, S.W. and Edwards, R.L., 2005. The ultimate flood recorder: flood deposited sediments preserved in stalagmites. Geophysical Research Abstracts 7, 09901.

Dumitru, O.A., Onac, B.P., Polyak, V.J., Wynn, J.G., Asmeron, Y. and Fornós, J.J., 2018. Climate variability in the western Mediterranean between 121 and 67 ka derived from a Mallorcan speleothem record. Palaeogeography, Palaeoclimatology, Palaeoecology 506, 128-138. https://doi.org/10.1016/j.palaeo.2018.06.028

Dumitru, O.A., Austermann, J., Polyak, V.J., Fornós, J.J., Asmerom, Y., Ginés, J., Ginés, A. and Onac, B.P., 2019. Constraints pn global mean sea level during Piocene warmth. Nature. Doi: 10.1038/s41586-019-1543-2

Edwards, R.L., Chen, J.H. and Wasserburg, G.J., 1987. 238U234U230Th232Th systematics and the precise measurement of time over the past 500,000 years. Earth and Planetary Science Letters 81, 175–192.

Fairchild, I.J., Borsato, A., Tooth, A.F., Frisia, S., Hawkesworth, C.J., Huang, Y.M., McDermott, F. and Spiro, B., 2000. Controls on trace elements (Sr-Mg) compositions of carbonate cave waters: implications for speleothem climatic records. Chemical Geology 166, 255–269.

Fairchild, I.J. and Treble, P.C., 2009. Trace elements in speleothems as recorders of environmental change. Quaternary Science reviews 28, 449-468.

Fairchild, I.J. and Baker, A., 2012. Speleothem science: from process to past environments. John Wiley & Sons. Oxford, UK. http://dx.doi.org/10.1002/9781444361094

Faust, J.C., Fabian, K., Milzer, G., Giraudeau and J., Knies, J., 2016. Norwegian fjord sediments reveal NAO related winter temperature and precipitation changes of the past 2800 years. Earth and Planetary Science Letters 435, 84–93. doi:10.1016/j.epsl.2015.12.003

Feldmann, R.M, Chapman, R.E. and Hannibal, J.T., 1989 (eds). Paleotechniques. The Paleontological

Society, Special Publication, 4.

Finné, M., Kylander, M., Boyd, M., Sundqvist, H.S. and Löwemark, L., 2015. CanXRF scanning of speleothems be used as a non-destructive method to identify paleoflood events in caves? Int. J. Speleol. 44 (1), 17e23.

Fiol, L., Fornós, J.J., Gelabert, B., and Guijarro, J.A., 2005. Dust rains in Mallorca (Western Mediterranean): Their occurrence and role in some recent geological processes: Catena 63, 64–84.

Fornós, J.J., Ginés, J. and Gràcia, F., 2009. Present-day sedimentary facies in the coastal karst caves of Mallorca island (western Mediterranean). Journal of Cave and Karst Studies, v. 71, no. 1, p. 86–99.

Frigola, J., Canals, M. and Mata, P., 2015. Techniques for the non-destructive and continuous analysis of sediment cores. Application in the Iberian continental margin. Boletín Geológico y Minero 126(2-3), 609–634.

Frisia, S., Borsato, A., Fairchild, I.J. and McDermott, F., 2000. Calcite fabrics, growth mechanisms, and environments of formation in speleothems from the Italian Alps and southwestern Ireland. Journal of Sedimentary Research 70, 1183–1196.

Frisia, S., Badertscher, S., Borsato, A., Susini, J., Göktürk, O.M., Cheng, H., Edwards, R.L., Kramers, J., Tüysüz, O. and Fleitmann, D., 2008. The use of stalagmite geochemistry to detect past volcanic eruptions and their environmental impacts. PAGES news 16, 25–26.

Frisia, S., 2015. Microstratigraphic logging of calcite fabrics in speleothems as tool for palaeoclimate studies. International Journal of Speleology 44, 1.

Frumkin, A. and Stein, M., 2004. The Sahara-East Mediterranean dust and climate connection revealed by strontium and uranium isotopes in a Jerusalem speleothem. Earth and Planetary Science Letters 217, 451-464. doi:10.1016/S0012-821X(03)00589-2

Garcia, J.; Delgado, X. i Ferrreres, J., 1986. Recull de cavitats de l'illa de Mallorca.

Genty, D., Blamart, D., Ouahdi, R., Gilmour, M., Baker, A., Jouzel, J. and van Exter, S., 2003. Precise dating of Dansgaard-Oeschger climate oscillations in western Europe from stalagmite data. Nature 421, 833– 837, doi: 10.1038/nature01391.

Gibelin, A.L. and Deque, M., 2003. Anthropogenic climate change over the Mediterranean region simulated by a global variable resolution model. Climate Dynamics 20, 237–339.

Ginés, J. and Ginés, A, 1976. Ses Coves del Pirata. Endins 3, 41-45

Ginés, J., Fornós, J., Ginés, A., Merino, A. and Gràcia, F., 2014. Geologic constraints and speleogenesis of Cova des Pas de Vallgornera, a complex coastal cave from Mallorca Island (Western Mediterranean). International Journal of Speleology 43(2), 105-124.

Giorgi, F., 2006. Climate change hot-spots. Geophysical Research Letters 33. https://doi.org/10.1029/2006GL025734

Giorgi, F. and Lionello, P., 2008. Climate change projections for the Mediterranean region. Global and Planetary Change 63, 90–104.

Goede, A., Green, D.C. and Harmon, R.S., 1986. Late Pleistocene palaeotemperature record from a Tasmanian speleothem. Australian Journal of Earth Sciences 33, 333–342. https://doi.org/10.1080/08120098608729370

Goudie, A.S. and Middleton, N.J., 2001. Saharan dust storms: nature and consequences. Earth-Science

Reviews 56, 179e204.

Gràcia, F., Clamor, B., Fornós, J.J., Jaume, D. and Febrer, M., 2006. El sistema Pirata-Pont-Piqueta (Manacor, Mallorca): geomorfología, espeleogènesi, hidrologia, sedimentologia i fauna. Endins 29, 25-64.

Grbec, B., Morović, M. and Zore-Armanda, M., 2003.Mediterranean Oscillation and its relationship to salinity fluctuation in the Adriatic Sea. Acta Adriatica 44, 1, 61-76.

Hodge, E.J., 2004. Palaeoclimate of the Western Mediterranean Region: Results From Speleothems. Ph.D. Thesis. University of Bristol, Bristol (Unpublished).

Hodge, E. J., Richards, D. A., Smart, P. L., Ginés, A. and Mattey, D. P., 2008. Sub-millennial climate shifts in the western Mediterranean during the last glacial period recorded in a speleothem from Mallorca, Spain. Journal of Quaternary Science 23, 713–718. doi: 10.1002/jqs.1198

Holland, H.D., Kirsipu, T.V., Huebner, S. and Oxburgh, U.M., 1964. On some aspects of the chemical evolution of cave waters. Journal of Geology 72, 36–67.

Homar, V., Ramis, C., Romero, R. and Alonso, S., 2010. Recent trends in temperature and precipitation over the Balearic Islands (Spain). Climatic Change 98, 199-211. doi: 10.1007/s10584-009-9664-5

Hori, M., Ishikawa, T., Nagaishi, K., Lin, K., Wang, B.-S., You, C.-F., Shen, C.-C. and Kano, A., 2013. Prior calcite precipitation and source mixing process influence Sr/Ca, Ba/Ca and 87Sr/86Sr of a stalagmite developed in southwestern Japan during 18.0–4.5ka. Chemical Geology 347, 190–198. https://doi.org/10.1016/j.chemgeo.2013.03.005

Hurrell, J.W., 1995. Decadal Trends in the North Atlantic Oscillation: Regional Temperatures and Precipitation. Science 269, 676–679. https://doi.org/10.1126/science.269.5224.676

Hurrell, J.W., Kushnir, Y., Ottersen, G. and Visbeck, M., 2003. An overview of the North Atlantic Oscillation, in: Hurrell, J.W., Kushnir, Y., Ottersen, G., Visbeck, M. (Eds.), Geophysical Monograph Series. American Geophysical Union, Washington, D. C., 1–35. https://doi.org/10.1029/134GM01

Jaffey, A.H., Flynn, K.F., Glendenin, L.E., Bentley, W.C. and Essling, A.M., 1971. Precision measurements of half-lives and specific activities of 235U and 238U. Physical Review C. 4, 1889–1906.

Jalali, B., Sicre, M.-A., Klein, V., Schmidt, S., Maselli, V., Lirer, F., Bassetti, M.-A., Toucanne, S., Jorry, S. J., Insinga, D.D., Petrosino, P., Châles, F., 2018. Deltaic and Costal Sediments as Recorders of Mediterranean Regional Climate and Human Impact Over the Past Three Millennia. Paleoceanography and Paleoclimatology 33. https://doi. org/10.1029/2017PA003298

Josey, S.A., Somot, S. and Tsimplis, M., 2011. Impacts of atmospheric modes of variability on Mediterranean Sea surface heat exchange. Journal of Geophysical Research 116. https://doi.org/10.1029/2010JC006685

Lionello, P. and Sanna, A., 2005. Mediterranean wave climate variability and its links with NAO and Indian Monsoon. Climate Dynamics 25, 611–623. https://doi.org/10.1007/s00382-005-0025-4

Lionello, P., Malanotte-Rizzoli, P. and Boscolo, R., 2006. Mediterranean climate variability. Elsevier.

Lund, D.C., Lynch-Stieglitz, J. and Curry, W.B., 2006. Gulf Stream density structure and transport during the past millennium. Nature 444:601–604.

Luterbacher, J., Werner, J.P., Smerdon, J.E., Fernández-Donado, L., González-Rouco, F.J., Barriopedro, D., Ljungqvist, F.C., Büntgen, U., Zorita, E., Wagner, S., Esper, J., McCarroll, D., Toreti, A., Frank, D., Jungclaus, J.H., Barriendos, M., Bertolin, C., Bothe, O., Brázdil, R., Camuffo, D., Dobrovolný, P.,

Gagen, M., García-Bustamante, E., Ge, Q., Gómez-Navarro, J.J., Guiot, J., Hao, Z., Hegerl, G.C., Holmgren, K., Klimenko, V.V., Martín-Chivelet, J., Pfister, C., Roberts, N., Schindler, A., Schurer, A., Solomina, O., von Gunten, L., Wahl, E., Wanner, H., Wetter, O., Xoplaki, E., Yuan, N., Zanchettin, D., Zhang, H. and Zerefos, C., 2016. European summer temperatures since Roman times. Environmental Res. Lett. 11, 24001. https://doi.org/10.1088/1748-9326/11/2/024001

Margaritelli, G., Cisneros, M., Cacho, I., Vallefuoco, M., Rettori, R. and Lirer, F., 2018. Climatic variability over the last 3000 years in the central-western Mediterranean Sea (Menorca Basin) detected by planktonic foraminifera and stable isotope records. Global and Planetary Changes 169, 179-187. https://doi.org/10.1016/j.gloplacha.2018.07.012

Mariotti, A., Zeng, N., Yoon, J.-H., Artale, V., Navarra, A., Alpert, P. and Li, L.Z.X., 2008. Mediterranean water cycle changes: transition to drier 21st century conditions in observations and CMIP3 simulations. Environmental Research Letters 3, 044001. https://doi.org/10.1088/1748-9326/3/4/044001

Martel, E.A., 1903: "Les cavernes de Majorque". Spelunca 32 (5). Paris.

Martín-Chivelet, J., Muñoz-García, M.B., Cruz, J.A., Ortega, A.I. and Turrero, M.J., 2017. Speleothem Architectural Analysis: Integrated approach for stalagmite-based paleoclimate research. Sedimentary Geology 353, 28–45. https://doi.org/10.1016/j.sedgeo.2017.03.003

Martín-Puertas, C., Valero-Garcés, B.L., Brauer, A., Mata, M.P., Delgado-Huertas, A. and Dulski, P., 2009. The Iberian–Roman Humid Period (2600–1600 cal yr BP) in the Zoñar Lake varve record (Andalucía, southern Spain). Quaternary Research 71, 108–120. https://doi.org/10.1016/j.yqres.2008.10.004

Martín-Puertas, C., Jiménez-Espejo, F., Martínez-Ruiz, F., Nieto-Moreno, V., Rodrigo, M., Mata, M.P. and Valero-Garcés, B.L., 2010. Late Holocene climate variability in the southwestern Mediterranean region: an integrated marine and terrestrial geochemical approach. Climate of the Past 6, 807-816. https://doi.org/10.5194/cp-6-807-2010.

Mayewski, P.A., Rohling, E., Stager, C., Karlén, K., Maasch, K., Meeker, L.D., Meyerson, E., Gasse, F., van Kreveld, S., Holmgren, K., Lee-Thorp, J., Rosqvist, G., Rack, F., Staubwasser, M. and Schneider, R., 2004. Holocene climate variability. Quaternary Research 62, 243–255.

Mayewski, P.A., Maasch, K., Yan, Y., Kang, S., Meyerson, E., Sneed, S, Kaspari, S, Dixon, D., Morgan, V., van Ommen, T. and Curran, M., 2006. Solar forcing of the polar atmosphere. Annals of Glaciology 41, 147–154.

McDermott F., Frisia S., Huang Y., Longinelli A., Spiro B., Heaton T.H.E., Hawkesworth C.J., Borsato A., Keppens E., Fairchild I.J., Van der Borg K., Verheyden S. and Selmo E., 1999. Holocene climate variability in Europe: Evidence from δ18O, textural and extension-rate variations in three speleothems. Quaternary Science Reviews 18, 1021-1038. http://dx.doi.org/10.1016/S0277-3791(98)00107-3

McGregor, H.V., Evans, M.N., Goosse, H., Leduc, G., Martrat, B., Addison, J.A., Mortyn, P.G., Oppo, D.W., Seidenkrantz, M.-S., Sicre, M.-A., Phipps, S.J., Selvaraj, K., Thirumalai, K., Filipsson, H.L. and Ersek, V., 2015. Robust global ocean cooling trend for the pre-industrial Common Era. Nature Geoscience 8, 671–677. https://doi.org/10.1038/ngeo2510

Mickler, P.J., Stern, L.A. and Banner, J.L., 2006. Large kinetic isotope effects in modern speleothems. Geological Society of America Bulletin 118, 65–81. https://doi.org/10.1130/B25698.1

Miller, G.H., Geirsdóttir, Á., Zhong, Y., Larsen, D.J., Otto-Bliesner, B.L., Holland, M.M., Bailey, D.A., Refsnider, K.A., Lehman, S.J., Southon, J.R., Anderson, C., Björnsson, H. and Thordarson, T., 2012. Abrupt onset of the Little Ice Age triggered by volcanism and sustained by sea-ice/ocean feedbacks. Geophysical Research Letters 39, L02708, https://doi.org/10.1029/2011GL050168

Mix, A.C., Rugh, W., Pisias, N.G. and Veirs, S., 1992. Leg 138 Shipboard Sedimentologists, the Leg 138

Scientific Party, 1992. Color reflectance spectroscopy: A tool for rapid characterization of deep-sea sediments. In: Mayer, L., Pisias, N., Janecek, T, et al. (Eds.), Proc. Ocean Drilling Program, Initial Reports, 138, 1, 67–77.

Morellón, M., Valero-Garcés, B., Vegas-Vilarrúbia, T., González-Sampériz, P., Romero, Ó., Delgado-Huertas, A., Mata, P., Moreno, A., Rico, M. and Corella, J.P., 2009. Lateglacial and Holocene palaeohydrology in the western Mediterranean region: the Lake Estanya record (NE Spain). Quat. Sci. Rev. 28, 2582-2599. doi:10.1016/j.quascirev.2009.05.014.

Morellón, M., Valero-Garcés, B., González-Sampériz, P., Vegas-Vilarrúbia, T., Rubio, E., Rieradevall, M., Delgado-Huertas, A., Mata, P., Romero, Ó., Moreno, A., Engstrom, D.R., López-Vicente, M., Navas, A. and Soto, J., 2011. Climate changes and human activities recorded in the sediments of Lake Estanya (NE Spain) during the Medieval Warm Period and Little Ice Age. Journal of Paleolimnology 46, 423-452. doi: 10.1007/s10933-009-9346-3.

Morellón, M., Pérez-Sanz, A., Corella, J.P., Büntgen, U., Catalán, J., González-Sampériz, P., González-Trueba, J.J., López-Sáez, J.A., Moreno, A., Pla-Rabes, S., Saz-Sánchez, M. Á., Scussolini, P., Serrano, E., Steinhilber, F., Stefanova, V., Vegas-Vilarrúbia, T. and Valero-Garcés, B., 2012. A multi-proxy perspective on millennium-long climate variability in the Southern Pyrenees. Clim. Past. 8, 683-700, doi:10.5194/cp-8-683-2012.

Moreno, A., Cacho, I., Canals, M., Prins, M.A., Sánchez-Goñi, M.F., Grimalt, J.O. and Weltje, G.J., 2002. Saharan dust transport and high latitude glacial climatic variability: the Alboran Sea record. Quaternary Research 58, 318e328.

Moreno, A., Valero-Garcés, B.L., González-Sampériz, P. and Rico, M., 2008. Flood response to rainfall variability during the last 2000 years inferred from the Taravilla Lake record (Central Iberian Range, Spain). Journal of Paleolimnology 40, 943–961. https://doi.org/10.1007/s10933-008-9209-3

Moreno, A., Pérez, A., Frigola, J., Nieto-Moreno, V., Rodrigo-Gámiz, M., Martrat, B., González-Sampériz, P., Morellón, M., Martín-Puertas, C., Pablo, J., Belmonte, Á., Sancho, C., Cacho, I., Herrera, G., Canals, M., Grimalt, J.O., Jiménez-Espejo, F., Martínez-Ruiz, F., Vegas-Vilarrúbia, T. and Valero-Garcés, B.L., 2012. The Medieval Climate Anomaly in the Iberian Peninsula reconstructed from marine and lake records. Quaternary Sci. Rev. 43, 16-32, doi:10.1016/j.quascirev.2012.04.007.

Muñoz, A., Bartolomé, M., Muñoz, A., Sancho, C., Moreno, A., Hellstrom, M.C.J., Osácar, C.M. and Cacho, I., 2015. Solar influence and hydrological variability during the Holocene from a speleothem annual record (Molinos Cave, NE Spain). Terra Nova 0, 0, 1–12.

Muñoz-García, M.B., Cruz, J., Martín-Chivelet, J., Ortega, A.I., Turrero, M.J. and López-Elorza, M., 2016. Comparison of speleothem fabrics and microstratigraphic stacking patterns in calcite stalagmites as indicators of paleoenvironmental change. Quaternary International 407, 74–85. https://doi.org/10.1016/j.quaint.2016.02.036

Muhs, D.R., Budahn, J., Avila, A, Skipp, G., Freeman, J. and Patterson, D., 2010. The role of African dust in the formation of Quaternary soils on Mallorca, Spain and implications for the genesis of Red Mediterranean soils. Quaternary Science Reviews 29, 2518-2540. doi:10.1016/j.quascirev.2010.04.013

Nabat, P., Somot, S., Mallet, M., Sevault, F., Chiacchio, M., and Wild, M., 2015a. Direct and semi direct aerosol radiative effect on the Mediterranean climate variability using a Regional Climate System Model, Clim. Dynam. 44, 1127–1155, doi:10.1007/s00382-014-2205-6.

Nabat, P., Somot, S., Mallet, M., Michou, M., Sevault, F., Driouech, F., Meloni, D., di Sarra, A., Di Biagio, C., Formenti, P., Sicard, M., León, J.F. and Bouin, M.N., 2015b. Dust aerosol radiative effects during summer 2012 simulated with a coupled regional aerosol–atmosphere–ocean model over the Mediterranean. Atmospheric Chemistry and Physics 15, 3303-3326. doi:10.5194/acp-15-3303-2015

Nabat, P., Somot, S., Mallet, M., Sevault, F. and Michou, M., 2016. Aerosol Variability and Weather

Regimes over the Mediterranean Region. In.: Air Pollution Modeling and its Application XXIV. Eds.: Steyn, D.G. and Chaumerliac, N. Springer International Publishing. DOI: 10.1007/978-3-319-24478-5_15

Nederbragt, A.J. and Thurow, J., 2004. Digital sediment colour analysis as a method to obtain high resolution climate proxy records. In: Francus, P. (ed.), Image analysis, sediments and paleoenvironments. Kluwer Academic PublishersDordrecht, The Netherlands, 105-124.

Nieto-Moreno, V., Martínez-Ruiz, F., Giralt, S., Jiménez-Espejo, F., Gallego-Torres, D., Rodrigo-Gámiz, M., García-Orellana, J., Ortega-Huertas, M. and de Lange, G. J., 2011. Tracking climate variability in the western Mediterranean during the Late Holocene: a multiproxy approach. Clim. Past. 7, 1395–1414, doi:10.5194/cp-7-1395-2011

Nieto-Moreno, V., Martínez-Ruiz, F., Willmott, V., García-Orellana, J., Masqué, P. and Sinninghe Damsté, J.S., 2013. Climate conditions in the westernmost Mediterranean over the last two millennia: An integrated biomarker approach. Organic Geochemistry 55, 1–10. https://doi.org/10.1016/j.orggeochem.2012.11.001

Neukom, R., Steiger, N., Gómez-Navarro, J.J., Wang, J. and Werner, J.P., 2019. No evidence for globally coherent warm and cold periods over the pre-industrial Common Era. Nature Let. Res. 571, 550-554. https://doi.org/10.1038/s41586-019-1401-2

Owen, R., Day, C.D. and Henderson, G.M., 2018. CaveCalc: A new model for speleothem chemistry & isotopes. Computers and Geosciences 119, 115-122.https://doi.org/10.1016/j.cageo.2018.06.011

Palutikof, J.P., Conte, M., Casimiro Mendes, J., Goodess, C.M. and Espirito Santo, F., 1996. Climate and climate change. In: Brandt, C.J., Thornes, J.B., (eds) Mediterranean desertification and land use. John Wiley and Sons, London

Palutikof, J., 2003. In Mediterranean Climate: Variability and Trends (ed Hans- Jürgen Bolle) 125–132, Springer Berlin Heidelberg.

Pasqual, A. and Nicolau, M. E., 2006. Anàlisi dels grafits de sa Cova des Pirata i de sa Cova des Pont. Endins 29, 65-74.

Parnell, A.C., Haslett, J., Allen, J.R.M., Buck, C.E. and Huntley, B., 2008. A flexible approach to assessing synchroneity of past events using Bayesian reconstructions of sedimentation history. Quaternary Science Reviews 27, 1872–1885. https://doi.org/10.1016/j.quascirev.2008.07.009.

Pastor, F., Estrela, M.J., Peñarrocha, D. and Millán, M.M., 2001. Torrential rains on the Spanish Mediterranean coast: Modelling the effects of the sea surface temperature. Journal of Applied Meteorology 40, 1180–1195.

Paulsen, D.E., Li, H.-C. and Ku, T.L., 2003. Climate variability in central China over the last 1270 years revealed by high-resolution stalagmite records. Quaternary Science Reviews 22, 691–701.

Pérez-Sanz, A., González-Sampériz, P., Moreno, A., Valero-Garcés, B., Gil-Romera, G., Rieradevall, M., Tarrats, P., Lasheras-Álvarez, L., Morellón, M., Belmonte, A., Sancho, C., Sevilla-Callejo, M. and Navas, A., 2013. Holocene climate variability, vegetation dynamics and fire regime in the central Pyrenees: the Basa de la Mora sequence (NE Spain). Quat. Sci. Rev. 73, 149-169. https://doi.org/10.1016/j.quascirev.2013.05.010

Polyak, V.P., Onac, B.P., Fornós, J.J., Hay, C., Asmeron, Y., Dorale, J.A., Ginés, J., Tuccimei, P. and Ginés, A., 2018. A highly resolved record of relative sea level in the western Mediterranean Sea during the last interglacial period. Nature Geoscience 11, 860-864. https://doi.org/10.1038/s41561-018-0222-5

Ramos-Román, M.J., Jiménez-Moreno, G., Camuera, J., García-Alix, A., Anderson, R.S., Jiménez-

Espejo, F.J. and Carrión, J.S., 2018. Holocene climate aridification trend and human impact interrupted by millennial- and centennial-scale climate fluctuations from a new sedimentary record from Padul (Sierra Nevada, southern Iberian Peninsula). Climate of the Past 14, 117-137. https://doi.org/10.5194/cp-14-117-2018

Richards, D.A. and Dorale, J.A., 2003. Uranium-series chronology and environmental applications of speleothems. Rev. Mineral. Geochem. 52, 407–460. http://dx.doi. org/10.2113/0520407

Riechelman, D.F.C., deiniger, M., Scholz, D., Riechelman, S., Schröder-Ritzrau, A., Spötl, C., Richter, D.K., Mangini, A. and Immenhauser, A., 2013. Disequilibrium carbon and oxygen isotope fractionation in recent cave calcite: Comparison of cave precipitates and model data. Geochemica et Cosmochimica Acta 103, 232-244. http://dx.doi.org/10.1016/j.gca.2012.11.002

Robock, A., 2000. Volcanic eruptions and climate. Reviews of Geophysics 38, 191–219.

Rodrigues, T., Grimalt, J.O., Abrantes, F.G., Flores, J.A. and Lebreiro, S.M., 2009. Holocene interdependences of changes in sea surface temperature, productivity, and fluvial inputs in the Iberian continental shelf (Tagus mud patch): Holocene Changes in the Iberian Continental Shelf. Geochem., Geophys., Geosyst. 10. doi.org/10.1029/2008GC002367

Rogerson, M., Weaver, P.P.E., Rohling, E.J., Lourens, L.J., Murray, J.W. and Hayes, A., 2006. Color logging as a tool in high-resolution paleoceanography, In: Rothwell, R.G. (Ed.), New techniques in sediment core analysis. Geological Society, Special Publications 267, London, 99-112.

Sabatier, P., Dezileau, L., Colin, C., Briqueu, L., Bouchette, F., Martinez, P., Siani, G., Raynal, O. and Von Grafenstein, U., 2012. 7000 years of paleostorm activity in the NW Mediterranean Sea in response to Holocene climate events. Quaternary Research 77, 1–11. https://doi.org/10.1016/j.yqres.2011.09.002

Sáez de Cámara, E., Gangoiti, G., Alonso, L. and Iza, J., 2015. Daily precipitation in Northern Iberia: understanding the recent changes after the circulation variability in the North Atlantic sector. Journal of Geophysical Research 120, 9981–10, doi:10.1002/2015JD023306

Sánchez-López, G., Hernández, A., Pla-Rabes, S., Trigo, R.M., Toro, M., Granados, I., Sáez, A., Masqué, P., Pueyo, J.J., Rubio-Inglés, M.J. and Giralt, S., 2016. Climate reconstruction for the last two millennia in central Iberia: The role of East Atlantic (EA), North Atlantic Oscillation (NAO) and their interplay over the Iberian Peninsula. Quaternary Science Reviews 149, 135–150. https://doi.org/10.1016/j.quascirev.2016.07.021

Schimpf, D., Kilian, R., Kronz, A., Simon, K., Spötl, C., Wörner, G., Deininger, M. and Mangini, A., 2011. The significance of chemical, isotopic, and detrital components in three coeval stalagmites from the superhumid southernmost Andes (53°S) as high-resolution palaeo-climate proxies. Quat. Sci. Rev. 30, 443-459. doi.org/10.1016/j.quascirev.2010.12.006

Sheffield, J. and Wood, E.F., 2008 Projected changes in drought occurrence under future global warming from multi-model, multi scenario, IPCC AR4 simulations. Climate Dynamics 31, 79–105.

Spötl, C. and Mangini, A., 2002. Stalagmite from the Austrian Alps reveals Dansgaard–Oeschger events during isotope stage 3: Implications for the absolute chronology of Greenland ice cores. Earth and Planetary Science Letters 203, 507–518.

Steinhilber, F., Beer, J. and Fröhlich, C., 2009. Total solar irradiance during the Holocene. Geophysical Research Letters 36. https://doi.org/10.1029/2009GL040142

Steinhilber, F., Abreu, J.A., Beer, J., Brunner, I., Christl, M., Fischer, H., Heikkilä, U., Kubik, P.W., Mann, M. and McCracken, K.G., 2012. 9,400 years of cosmic radiation and solar activity from ice cores and tree rings. Proceedings of the National Academy of Sciences 109, 5967–5971.

Stoll, H.M., Muller, W. and Prieto, M., 2012. I-STAL, a model for interpretation of Mg/Ca, Sr/Ca and Ba/Ca variations in speleothems and its forward and inverse application on seasonal to millennial scales. Geochemistry, Geophysics, Geosystems 13, 27.

Treble, P., Shelley, J.M.G. and Chappell, J., 2003. Comparison of high-resolution subannual records of trace elements in a modern (1911–1992) speleothem with instrumental climate data from southwest Australia. Earth and Planetary Science Letters 216, 141–153.

Tremaine, D.M. and Froelich, P.N., 2013. Speleothem trace element signatures: A hydrologic geochemical study of modern cave dripwaters and farmed calcite. Geochimica et Cosmochimica Acta 121, 522–545. https://doi.org/10.1016/j.gca.2013.07.026

Trigo, I.F., Bigg, G.R. and Davies, T.D., 2002. Climatology of cyclogenesis mechanisms in the Mediterranean. Monthly Weather Review 130, 549–569.

Tsimplis, M. N. and Josey, S. A., 2001. Forcing of the Mediterranean Sea by atmospheric oscillations over the North Atlantic. Geophysical Research Letters 28, 803–806.

Ulbrich, U., W. May, L. Li, P. Lionello, J. G. Pinto and S. Somot, 2006. The Mediterranean climate change under global warming. In: P. Lionello, P. Malanotte-Rizzoli & R. Boscolo (Eds), Mediterranean Climate Variability, Amsterdam: Elsevier, 398-415.

Vallefuoco, M., Lirer, F., Ferraro, L., Pelosi, N., Capotondi, L., Sprovieri, M. and Incarbona, A., 2012. Climatic variability and anthropogenic signatures in the Gulf of Salerno (southern-eastern Tyrrhenian Sea) during the last half millennium. Rendiconti Lincei 23, 13–23. https://doi.org/10.1007/s12210-011-0154-0

Vanghi, V., Iriarte, E. and Aranburu, A., 2015. High Resolution X-Ray Computed Tomography for Petrological Characterization of Speleothems. Journal of Cave and Karst Studies 77, 75–82. https://doi.org/10.4311/2014ES0102

Vesica, P.L., Tuccimei, P. Turi, B., Fornós, J.J., Ginés, A. and Ginés, J. 2001. Late Pleistocene Paleoclimates and sea-level change in the Mediterranean as inferred from stable isotope and U-series studies of overgrowths on speleothems, Mallorca, Spain. Quaternary Science Reviews 19, 865-879.

Walczak, I.W., Baldini, J.U.L., Baldini, L.M., McDermott, F., Marsden, S., Standish, C.D., Richards, D.A., Andreo, B. and Slater, J., 2015. Reconstructing high-resolution climate using CT scanning of unsectioned stalagmites: A case study identifying the mid-Holocene onset of the Mediterranean climate in southern Iberia. Quaternary Science Reviews 127, 117–128. https://doi.org/10.1016/j.quascirev.2015.06.013

Westland, S., 2012. Frequently Asked Questions About Colour Physics. Kindle Edition.

3.3.9 Supplementary material to Cisneros et al., in prep.

Fabrics and architectural elements observations

The characterization of the internal microstratigraphy of the stalagmites has been done following the methodology and the nomenclature proposed by Martín-Chivelet et al. (2017) and the observations are synthesized in Figures 3.33-3.35. Interpretations of calcite fabrics have followed Frisia et al. (2000). Feni, Ciara, Constantine and Seán

stalagmites have an external surface quite regular and a cylindrical shape. Multieix is the less regular, presenting three different growth axes.

Speleothems Feni and Ciara (Fig. 3.33a-b) do no show strict unconformity bounded units (UBUs). Along their growth axis white and translucent surfaces has been observed. The type of morphostratigraphic units that presents Feni is mostly flat-topped ('puff-pastry' subtype) and from cm 7-4, growth layers show in some cases small concave down geometries, which remember the type rimmed ('flame-like' subtype). The upper 0.5 cm are formed by a patchy type of morphostratigraphy unit ('mottled' subtype). The entire stalagmite presents basically an aggradational stacking pattern, columnar fabrics and a remarkable lamination (single growth layers ≤ 1 mm).

Ciara stalagmite is mostly composed by flat-topped and presents different subtypes: 'meseta' from cm 35-32 and the rest 'puff-pastry'. It should be noted certain change in the direction of growth ca. cm 22. This cm also supposes a change in the stacking patterns sets: generally aggradational and, from cm 22 to the ~cm 2.5 to progradational. The top 2.5 cm show again aggradational patterns. Fabrics seem to be columnar and the lamination is remarkable and differentiated (single growth layers ≤ 1 mm).

Constantine stalagmite (Fig. 3.34b) is the least translucent of all the pieces and can be described in four UBUs. UBU4 (cm 9-7) presents chaotic type in its morphostratigraphic units ('cerebroid' subtype), progradational geometries and pervasive internal dissolution in the top. UBU3 (cm 7-3.5) shows rimmed morphostratigraphic units ('flame-like' subtype), retractional stacking patterns and predominant dendritic fabrics accompanied by some preserved columnar fabric. UBU3, as well as UBU2, seems to finish with allogenic horizons, respectively, where darker laminae have been observed. UBU2 (cm 3.5-0.8) and UBU1 present flat-topped ('puff-pastry subtype) morphostratigraphic units, aggradational geometries and columnar fabrics. The presence of aragonite has been discarded by the characterization performed at cm 7.5, 6 and 3.5.

Multieix stalagmite presents three different UBUs and the two boundaries (UBU3 and UBU1) show translucent layers while the UBU2 becomes white (Fig. 3.34a). UBU3 (cm 30.5-22), which is the most translucent, presents a flat-topped shape ('puff-pastry' subtype), an aggradational geometry, is mostly composed by columnar fabric and by a

remarkable lamination and, it seems to have stopped growing during a non-deposition (and condensation) hiatus. After that, starts UBU2 (cm 22-5), which is mostly composed by a rimmed mosphostratigraphic unit ('flame-like' subtype) and tendency to progradational geometry. Different types of calcite fabrics composes this UBU2 (Fig. 3.34a): mostly open columnar between cm 22-17; columnar microcrystalline type at cm 15; dendritic ca. cm 9.5 and, columnar fabric with some dendritic branches between cm 11.5-6, approximately. Columnar microcrystalline type has been observed in different parts, showing variations in the size of the crystals: enhancement at cm 20; decrease ca. cm 17.5 and enhancement again at cm 15.5. Fabrics show changes about cm 10 and become dendritic at cm 9.5, which immediately present bigger crystals that coexist until cm 5 with some isolated areas composed by dendritic fabrics. UBU2 ends with a dissolution (corrosion) hiatus at cm. 5, that correspond to a brown layer (~ 30 μm) formed by micrite. In UBU1 (cm 5-top), morphostratigraphic units can be classified as flat-topped with dominance of aggradational stacking pattern sets. However, in the upper 0.5 cm the stacking pattern sets seem to consist in progradational. Regarding to the fabrics, columnar type is predominant. However, the brown laminae (~30 μm) ca. cm 5 is formed by micrite fabric and, around this layer isolated areas of mosaic and dendritic have been also observed. XRD characterizations performed at cm 28.5, 23, 19, 11.5, 6.5 and 3.5 have discarded the presence of aragonite.

Along the growth axis of Seán, a white and translucent surface has been observed. It can be considered that Seán consists in two UBUs: UBU2 from the base to cm 6 and UBU1 from cm 6 to the top. Both UBUs are separated by a brown millimetric layer ca. cm 6 that follows the general lamination, which could be defined as an allogenic horizon. On the one hand, the morphostratigraphic units could be described in a general way, as flat-topped with well-defined and subhorizontal growth layers. On the other hand, it should be noted that two areas with different morphostratigraphic units have been also observed ca. cm 9-8 and cm 1.5-0. Although aggradational stacking pattern sets (Muñoz-García et al., 2016) are generalized along this stalagmite, retractional patterns have been also observed related to these different units ca. cm 9-8 and cm 1.5-0. In reference to ca. cm 9-8, we have described patchy morphostratigraphic units (stacked-hay subtype). Regarding to the cm 1.5-0, we have observed pointed morphostratigraphic

Figure 3.33. Schematic description of (from left to right) the architectural elements, stalagmites pictures, growth rates, U/Th age models and, stable isotopes and trace element ratios records againt cm for **a)** Feni **b)** Ciara stalagmites. U/Th age models performed on Bchrom. Red plots are the final age models. Black diamonds represent the U/Th ages (error 2 sigma). Grey dashed lines correspond to uncertainties derived from all the age models obtained with Bchrom, which have statistically the same significance. Ages are expressed in Before Common Era years (BCE) and Common Era years (CE). Historical/climatic periods are also indicated.

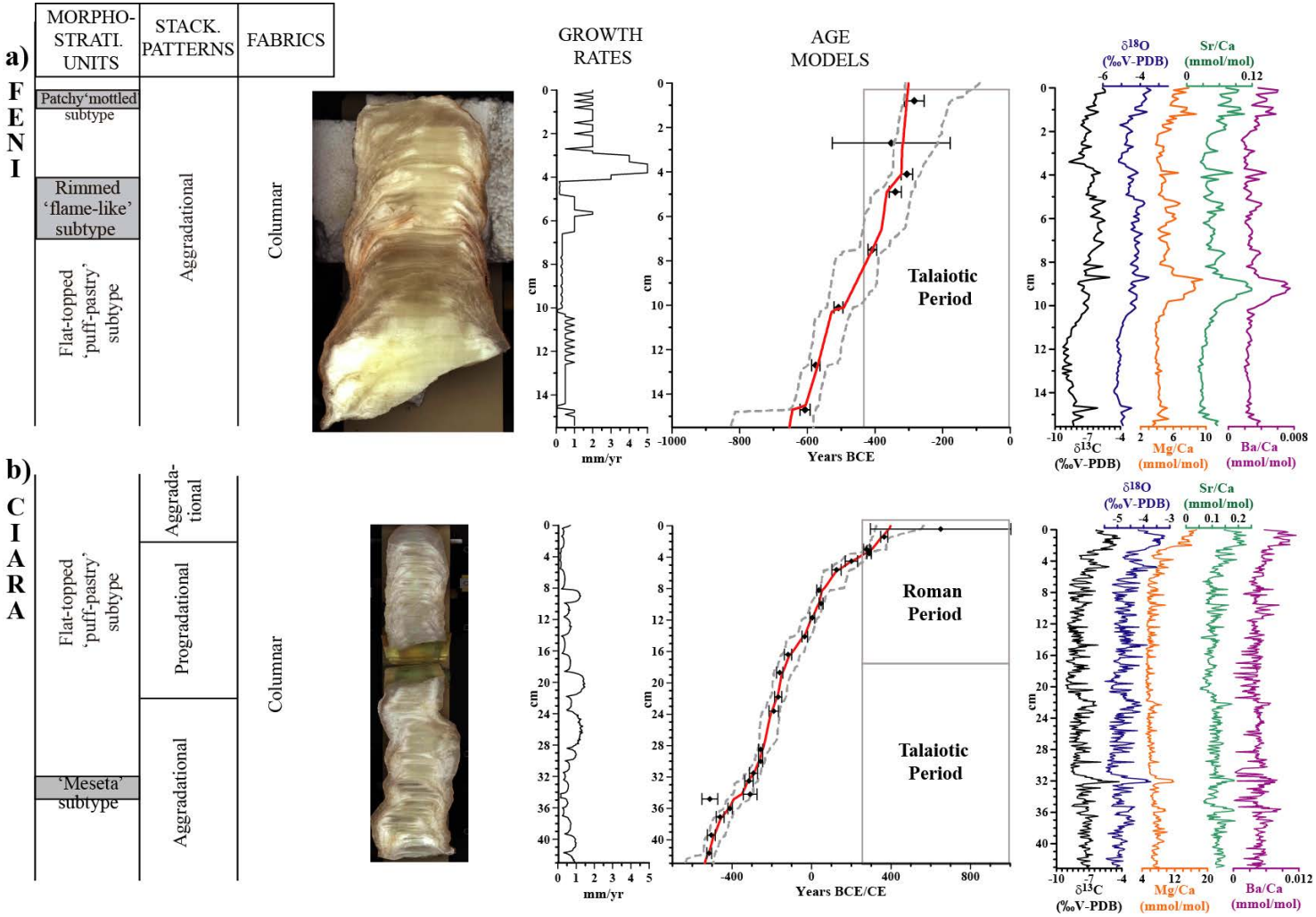

Figure 3.34. Schematic description of (from left to right) the architectural elements, stalagmites pictures, growth rates, U/Th age models and, stable isotopes and trace element ratios records againt cm for **c)** Multieix **d)** Constantine stalagmites. Regarding to the fabrics of Multieix stalagmite (from bottom to top): Columnar fabric ('C', cm 23.5), PPL; Open columnar fabric ('C', cm 17), XPL; Columnar microcrystalline ('Cm', cm 15), XPL; Dendritic fabrics ('d', cm 9.5), PPL; Columnar fabric with dendritic branches (cm 7), XPL; Scale bar: 2 mm. (XPL = Cross Polarized Light; PPL = Plane Polarized Light). U/Th age models performed on Bchrom. Red plots are the final age models. Black diamonds represent the U/Th ages (error 2 sigma). Grey dashed lines correspond to uncertainties derived from all the age models obtained with Bchrom, which have statistically the same significance. Ages are expressed in Before Common Era years (BCE) and Common Era years (CE). Historical/climatic periods are also indicated. *Description of the architectural elements and details about U/Th dates of the top 5 cm in Multieix can be found in Fig. 3.35.

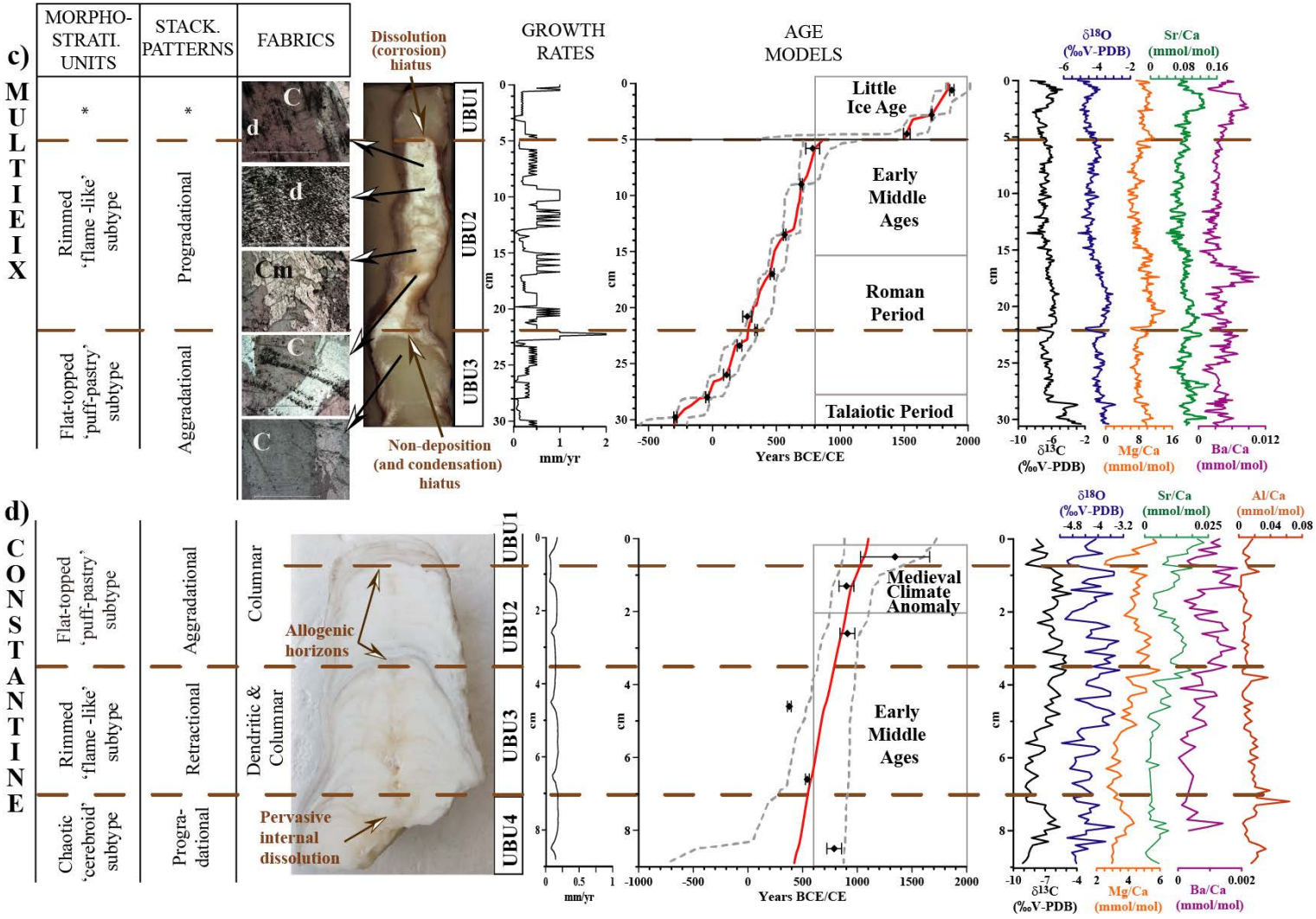

units (arrow-head subtype) with growth layers showing retraction plus aggradation. Columnar calcite fabrics (Frisia et al., 2000) have been observed in most of the speleothem Seán. Nevertheless, at cm 6 from the top, the millimetric brown layer shows micrite fabric and, above this layer some isolated mosaic fabrics have been also observed. Around cm 6, skeletal components have been distinguished, which could correspond to gastropods of 1400 μm length (Fig. 3.36). Seán shows a remarkable and uniform lamination (< 1 mm) along the growth axis that becomes more translucent every some cm.

Growth rates

In Feni stalagmite, the lowest time resolution was 25 yr during ~492 yr BCE (ca. cm 10) and 22 years at ~622 yr BCE (ca. 14.6 cm). Maxima extension rates have been 5 mm/yr at ~321 yr BCE (around cm 3.8). In the case of Ciara, the lowest time resolution has been higher than the lowest of Feni (8.4 mm yr-1). Minima growth rates seem to have been given in some points after 172 yr CE (cm 5) and also at 350 yr BCE (~0.1 mm yr-1, ca. cm 35). Extension rates in Feni are also quite low around this moment. Maxima growth rates (1.5 mm yr-1) are remarkable at ~157 yr BCE (ca. cm 20) and at ~214 yr BCE (cm 25) and also considerable during ~45 yr CE (ca. cm 9).

In the oldest parts of Multieix stalagmite (cm 30.5-5; UBU3 and UBU2), the maxima values (2 mm yr-1) are reached at 277 CE yr (cm 22.2). Growth rates are also remarkable during ~483 yr CE (ca. cm 15) and at ~680 yr CE (cm 10). Minima extension rate corresponds to 36 yr BCE (cm 28) and to 222 yr CE (cm 23.3). It should be noted several periods with sustained low extension rates like 208-36 yr BCE (cm 29-28) and 40-108 yr CE (cm 26.5-26). Slightly differences have been observed between growth rates averages of both UBUs: 0.3 mm yr-1 during 302 yr BCE-279 CE (UBU3) and, 0.5 mm yr-1 during 279-858 yr CE (UBU2). The U/Th date at cm 22 is older than the adjacent dates (Table 3.10) and it seems to correspond to a growing that is different than those of the central axis. *In the most recent part of Multieix (top 5 cm; UBU1): The minima growth rates have been obtained between 1600-1700 yr CE (~cm 3). Seán also showed relative low rates around 1630-1660 yr CE. The Multieix model provided remarkable maxima extension rates of 0.4 mm yr-1 before 1515 yr CE (~cm 4.5). These maxima rates are in agreement with those obtained in Seán, although in Multieix are

Figure 3.35. For both Seán (upper panel) and Multieix (bottom panel) stalagmites (from left to right): U/Th age models, section and fabrics pictures, schematic description of the architectural elements and growth rates. The age models were obtained with Bchrom (Parnell et al., 2008) and black diamonds represent the U/Th ages (error 2 sigma). Red plots are the final models. Grey dashed lines correspond to uncertainties derived from all the models, which have the same significance statistically. Brown dashed line in Seán represents the layer/unconformity ca. cm 6. In relation to the fabrics pictures, for Seán are shown those around cm 6 (from up to bottom): Isolated mosaics fabrics (Mo) above the micrite layer (m), columnar fabric below (C), XPL; Columnar (C), mosaic (Mo) and micrite (m) fabrics, PPL. For the top 5 cm of stalagmite Multieix: Columnar fabric, XPL; Unconformity at cm 5 formed by micrite (m) and isolated mosaic (Mo) areas. XPL. (XPL=Cross Polarized Light; PPL=Plane Polarized Light). Regarding to description of the architectural elements, concepts in vertical corresponds to general characterizations and those in horizontal (and into grey squares) indicate particular features.

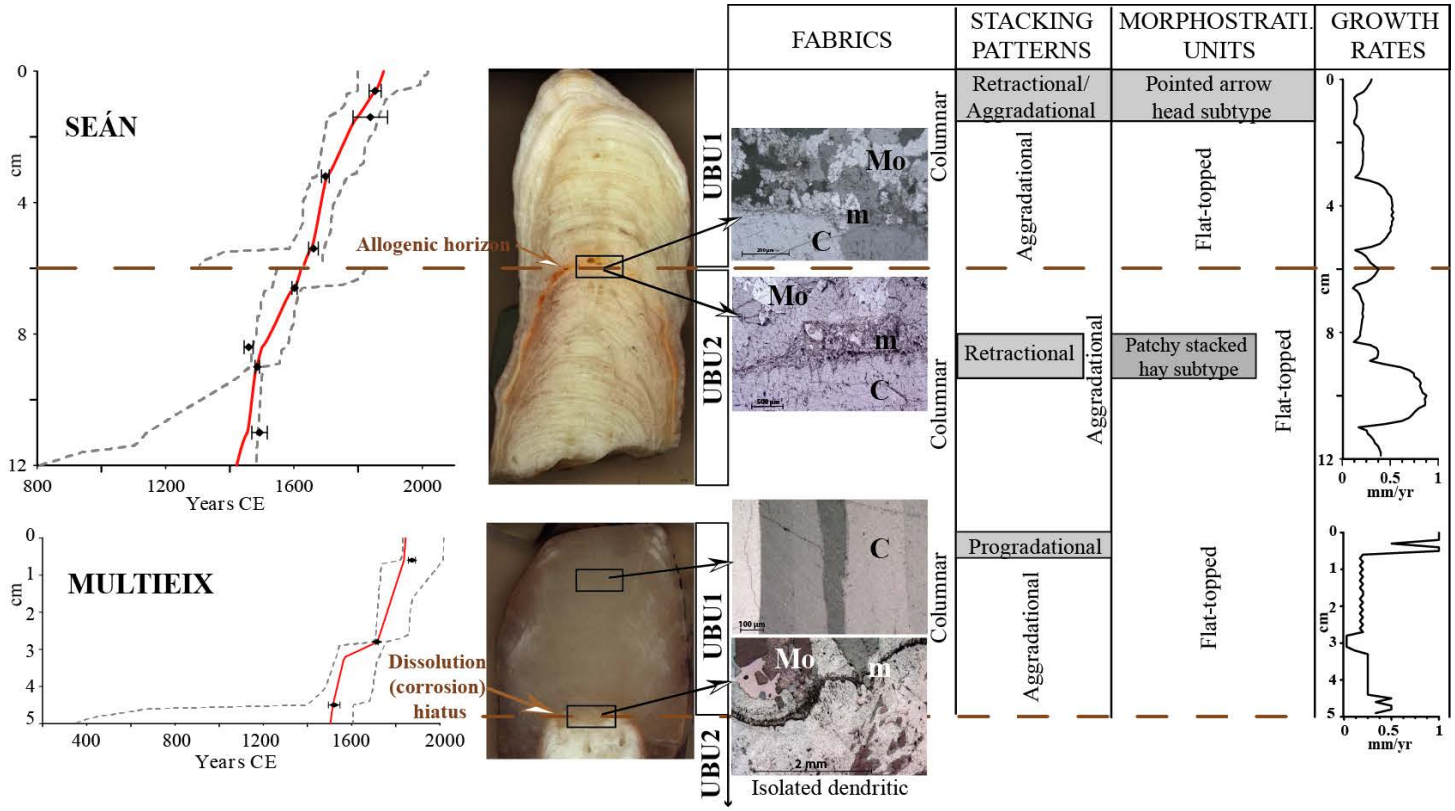

slightly lower. A remarkable increase in the growth rates has been observed in at the end of the spanned period of this stalagmite (~cm 0.5).

In Constantine stalagmite, the best time resolution has been 5.3 yr around 515 yr CE (ca. cm 8,) with a maxima extension rate of 0.2 mm/yr. Considerable growth rate have been also obtained at ~672-617 yr CE (ca. cm 6-5). The lowest time resolutions seem to have occurred since 900 yr CE approximately, reaching 18 yr (top first cm), which correspond to the minima extension rates of 0.06 mm/yr. Slightly differences have been found in the growth rates averages of the different UBUs of Constantine. Extension rates during the oldest period (423–789 yr CE; UBU4 and UBU3) show averages (0.2 mm yr-1) slightly higher than the most recent period (789–1102 yr CE; 0.1 mm yr-1; UBU2 and UBU1).

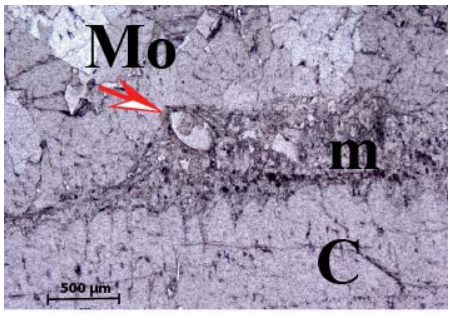

Figure 3.36. Fabric picture of Seán stalagmite at 1622 yr CE (brown layer ca. cm 6). Columnar (C), mosaic (Mo) and micrite (m) fabrics, PPL. The arrow indicates the Gastropod test.

In Seán stalagmite, Growth rate is 0.4 mm yr-1 for the oldest period 1421-1622 yr CE (UBU2, from the base to cm 6) and 0.3 mm yr-1 for the most recent period 1622-1844 yr CE (UBU1, from cm 6 to the top). Minima growth rates in both UBUs are similar (0.1 mm yr-1) and are given ca. 1591 yr CE (cm 7; UBU2) and ca. 1805 yr CE (cm 1; UBU1). Maxima growth rates present differences between both UBUs: 0.9 mm yr-1 at ~1469 yr CE (cm 10, UBU2) and 0.5 mm yr-1 at ~1680 yr CE (cm 4, UBU1), respectively. In this way, the extension rate of the oldest period 1421-1622 yr CE (UBU2) presents higher variability than the most recent period 1622 to 1880 yr CE (UBU1). Regarding to the micrite layer at cm 6, growth rates are similar to the average obtained in the UBU2, which would be indicating no important signs of erosion.

Paleodripping and growth rates: interpreting speleo-microstratigraphy, age-models and non-destructive techniques (Micro-CT and XRF)

All three stalagmites covering the TP (Feni, Ciara and Multieix) show common

microstratigraphic with flat-topped ‘puff-pastry’ subtype and aggradational stacking patterns (Fig. 3.33 and 3.34a) suggesting moderate stability in the main drip rates. However, particular microstratigraphic features have been observed at sub-centennial time-scale. From 393 to 322 yr BCE the rimmed morphostratigraphic units (‘flame-like’ subtype) of Feni (~cm 7-4) point out moderate to high drip rates, which could have been varied seasonally. This is accompanied by an increase in growth rate. During 395-304 yr BCE, Ciara also shows, after its minima growth rate (~0.1 mm yr^{-1}; cm 35), a variation in its morphostratigraphic units (meseta subtype, cm 35-32). In contrast, Feni’s microstratigraphy towards the end of that century (~300 BCE), present patchy type unit (‘mottled’ subtype) and aggradational patterns with columnar fabrics, indicating low dripping and possible evaporation. This is accompanied by a decrease in growth rates. Around 176 yr BCE, Ciara presents variation in the direction of growth and changes from aggradational to progradational patterns suggesting a slight change to increasing drip rates. In this moment, occurred the maxima growth rates in Ciara (1.5 mm yr^{-1}).

During most of the RP, the microstratigraphic features of Ciara and Multieix (flat-topped puff-pastry; Fig. 3.33b and 3.34a) indicate a general moderate stability in the drip rates. However, certain differences have been observed between the beginning and the end of the RP. Before and after ~200 yr CE, the stacking patters of Ciara change from progradational (pointing out increasing drip rates) to aggradational (pointing out more uniform drip rates). The minima growth rates in Ciara and the relative low ones in Multieix accompanied the first years after the 200 yr CE. In addition, the rimmed ‘flame-like’ morphostratigraphic units of Multieix could be in agreement with moderate drip rates. However, by ~300 yr CE CE Multieix shows its maxima growth rates although it could be an artefact due to the non-deposition (and condensation) hiatus observed ~279 yr CE (top UBU3), which possibly suggests a temporal cessation of dripping in the Multieix site.

The RP-EMA transition is characterized by progradational stacking patterns in Constantine (423-548 yr CE; UBU4), which could be indicating increasing drip rates from the end of RP to the beginning of the EMA. The predominant dendritic fabrics could be formed after sudden fast drips that dissolve the pre-existing fabric developing the dendritic fabrics (Fairchild and Baker, 2012; Frisia, 2015), which reinforce the

increasing drip rates during the RP-EMA transition. In addition, the trends to chaotic type and the top pervasive internal dissolution ~548 yr CE can be indicating irregular drip rates and a change in the water saturation, respectively. It should be noted that despite the increase in drip rates interpreted from stacking patterns and fabrics, the morphostratigraphic 'cerebroid' subtype could be indicating low drip rates during 423-548 yr CE. Multieix also seem to have grown up during the end of the RP and most of the EMA (279-858 yr CE) under unstable and increasing drip rates due its microstratigraphic features (UBU2; rimmed mosphostratigraphic units 'flame-like' subtype) and progradational geometry. This stalagmite shows remarkable growth rates during 471-773 yr CE. Unstable and increasing drip rates during most of the EMA are in agreement with the conditions indicated by the microstratigraphic features of Constantine during 548-789 yr CE (UBU3). The rimmed units, which have been observed in both stalagmites spanning EMA, are usually associated to moderate or high drip rates (Martín-Chivelet et al., 2017).

However, the end of the EMA seems to have been characterized in a different way, after 789 yr CE, the architectural elements of Constantine (UBU2; flat-topped units and aggradational stacking patterns) can be associated to more stable drip rates. On the other hand, the micrite layer of Multieix at 858 yr CE and the following hiatus could be interpreted like lower drip rates. It appears plausible to infer that micrite development in speleothems consisting of calcite is favoured by bio-mediation in a regime of relatively low discharge (Frisia et al., 2012; Frisia, 2015).

Regarding to the EMA-MCA transition (UBU 2; 789-1017 yr CE) and the onset of the MCA (UBU1; 1017-1102 yr CE), Constantine has been described by flat-topped morphostratigraphic units ('puff-pastry' subtype) and aggradational geometries, which could be indicating rather uniform drip rates through time. About 1017 yr CE, an allogenic horizon has been observed in UBU2, which is is accompanied by a relative high Al/Ca content, depleted $\delta^{18}O$ values and low Mg/Ca ratios (Fig. 3.34). An increase in drip rates, consistent with depleted $\delta^{18}O$ values and low Mg/Ca ratios, could favoured the enhancement of detritus material input (Schimpf et al., 2011), which would increase the Al/Ca content. After that, Constantine presents the minima growth rates during 1017-1102 yr CE. It should be noted that average growth rates in Constantine (0.1 mm yr^{-1}) has been the lowest comparing to the other stalagmites: Feni,

Ciara and Multieix (0.8, 0.7 and 0.4 mm yr^{-1}, respectively). No more stalagmites growths have been detected in any of the two caves during MCA. Although the absence of growing cannot be conclusive evidence, it results significant and it could indicate that drip rates during MCA were the minimum of the whole studied period.

The period covered by Seán stalagmite, 1421-1880 yr CE, is generaly represented by flat-topped morphostratigraphic units, aggradational stacking pattern sets, columnar fabric and, uniform lamination along the growth axis. The top 5 cm of Multieix (1503-1844 yr CE) is similarly characterized by flat-topped morphostratigraphic units and aggradational stacking pattern sets (Fig. 3.35). The interpretation of all of these general features (Frisia et al., 2000; Muñoz-García et al., 2016; Martín-Chivelet et al., 2017) points out a moderate stability in the drip rates that reinforce a rather continuous growth of both stalagmites also supported by the respective age models,

Seán stalagmite between 1483 and 1526 yr CE (UBU2), is characterized by patchy morphostratigraphy. These kinds of units combined with open columnar, dendritic and/or microcrystalline fabrics, could be suggesting slower drip rates and probably higher calcite saturation than in the previous growth layers (Martín-Chivelet et al., 2017). The acetate peels performed along Seán does not show dendritic or microcrystalline fabrics. Overall, the transition between 1483 and 1526 yr CE seems to indicate slower drip rates than in the rest of the time period covered by Seán stalagmite. A drop in growth rates of Seán accompanies these apparent slower drip rates

Multieix started to grow at ~1503 yr CE, after a hiatus of several centuries, forming isolated areas of mosaic and dendritic fabrics (above the cm 5) (Fig. 3.35). These kinds of fabrics could be developed by the dissolution of the pre-existing fabric due to sudden fast drips (Fairchild and Baker, 2012; Frisia, 2015), which could be indicating the end of slow drip rates during transition between 1483 and 1526 yr CE observed in Seán.

Dendritic fabric can develop by the influence of bio-influenced precipitation, degassing and hydrological instability (Frisia, 2015). On one hand, more depleted $\delta^{13}C$ values in the dendritic fabric than those in columnar fabrics could indicate that kinetic processes did not modify the signal in dendritic fabric. On the other hand, when dendritic the fabric present heavier $\delta^{13}C$ values relative to columnar fabric layers in the same specimen, it can indicate enhanced CO_2 degassing during the formation of dendritic

Table 3.10. Results of U/Th analyses of stalagmites (2 σ error). U decay constants: $\lambda_{238} = 1.55125 \times 10^{-10}$(Jaffey et al., 1971) and $\lambda_{234} = 2.82206 \times 10^{-6}$ (Cheng et al., 2013). Th decay constant: $\lambda_{230} = 9.1705 \times 10^{-6}$ (Cheng et al., 2013). Corrected ^{230}Th ages assume the initial $^{230}Th/^{232}Th$ atomic ratio of $4.4 \pm 2.2 \times 10^{-6}$. These values are those for material at secular equilibrium, with the bulk earth $^{232}Th/^{238}U$ value of 3.8 (Richards and Dorale, 2003). The errors are arbitrarily assumed to be 50%. A) $\delta^{234}U = ([^{234}U/^{238}U]_{activity} - 1) \times 1000$. B) $\delta^{234}U_{initial}$ was calculated based on ^{230}Th age (T), i.e., $\delta^{234}U_{initial} = \delta^{234}U_{measured} \times e^{\lambda^{234}xT}$. C) BCE/CE stands for "Before Common Era"/Common Era" years. Negative years correspond to BCE years. Ages in italics are not included in the age model making-up.

Sample & distance from the top (cm)	^{238}U (ppb)	^{232}Th (ppt)	^{230}Th / ^{232}Th (atomic x10^{-6})	$\delta^{234}U^{A}$ (measured)	^{230}Th / ^{238}U (activity)	^{230}Th Age (yr) (uncorrected)	^{230}Th Age (yr) (corrected)	$\delta^{234}U_{Initial}{}^{B}$ (corrected)	BCE/CE yr (corrected)^{C}
FENI-0.8	242.3 ± 0.5	313.9 ± 6.3	301.9 ± 6.4	120.5 ± 1.9	0.0237 ± 0.0002	2331.7 ± 16.2	2298.1 ± 28.7	121.3 ± 1.9	-284.1 ± 28.7
FENI-2.7	366.2 ± 0.4	3436.4 ± 68.9	46.4 ± 1.0	116.9 ± 1.5	0.0264 ± 0.0001	2608.5 ± 14.5	2363.9 ± ###	117.7 ± 1.5	-351.9 ± 173.6
FENI-4	412.5 ± 0.8	242.5 ± 4.9	663.4 ± 13.8	116.9 ± 1.6	0.0237 ± 0.0001	2333.2 ± 12.9	2317.9 ± 16.8	117.6 ± 1.6	-305.9 ± 16.8
FENI-5.1	428.0 ± 0.7	89.9 ± 1.8	1862.5 ± 40.4	109.1 ± 1.8	0.0237 ± 0.0002	2357.4 ± 17.9	2351.9 ± 18.3	109.8 ± 1.9	-339.9 ± 18.3
FENI-7.6	388.3 ± 0.5	68.7 ± 1.4	2291.2 ± 48.4	117.6 ± 1.5	0.0246 ± 0.0001	2424.2 ± 12.8	2419.6 ± 13.2	118.4 ± 1.5	-407.6 ± 13.2
FENI-10.2	376.4 ± 0.7	65.7 ± 1.4	2423.8 ± 54.2	119.1 ± 1.6	0.0256 ± 0.0001	2526.3 ± 13.1	2521.7 ± 13.5	119.9 ± 1.6	-507.7 ± 13.5
FENI-12.5	473.3 ± 0.9	66.7 ± 1.4	3056.4 ± 63.6	116.9 ± 1.6	0.0261 ± 0.0001	2580.8 ± 12.2	2577.1 ± 12.4	117.8 ± 1.7	-565.1 ± 12.4
FENI-14.5	509.8 ± 1.1	212.7 ± 4.3	1054.8 ± 21.8	119.6 ± 1.7	0.0267 ± 0.0001	2629.5 ± 13.2	2618.7 ± 15.3	120.5 ± 1.7	-606.7 ± 15.3
CIARA-0.4	13.7 ± 0.0	25.1 ± 0.7	139.0 ± 34.9	204.4 ± 1.7	0.0154 ± 0.0039	1406.5 ± 352.9	1362.3 ± ###	205.2 ± 1.8	649.7 ± 354.2
CIARA-1.4	246.9 ± 0.4	158.9 ± 3.2	468.0 ± 10.3	205.7 ± 1.6	0.0183 ± 0.0001	1663.8 ± 13.7	1648.3 ± 17.6	206.7 ± 1.7	365.7 ± 17.6
CIARA-3	437.9 ± 0.6	165.3 ± 3.4	834.9 ± 18.4	203.0 ± 1.6	0.0191 ± 0.0001	1746.3 ± 13.3	1737.2 ± 14.7	204.0 ± 1.6	276.8 ± 14.7
CIARA-3.2	424.8 ± 0.7	91.1 ± 1.9	1455.7 ± 30.6	203.2 ± 1.6	0.0189 ± 0.0001	1728.5 ± 8.8	1723.3 ± 9.6	204.2 ± 1.6	288.7 ± 9.6
CIARA-3.5	435.4 ± 0.6	52.2 ± 1.1	2589.2 ± 58.5	198.9 ± 1.5	0.0188 ± 0.0001	1724.8 ± 11.0	1721.9 ± 11.2	199.8 ± 1.5	290.1 ± 11.2
CIARA-4.5	4752.3 ± 5.8	7575.5 ± 151.8	209.9 ± 4.5	206.1 ± 1.6	0.0203 ± 0.0002	1849.8 ± 14.6	1811.3 ± 30.9	207.1 ± 1.6	200.7 ± 30.9
CIARA-5.6	366.2 ± 0.5	332.4 ± 6.7	379.6 ± 8.4	202.9 ± 1.5	0.0209 ± 0.0002	1910.0 ± 17.4	1888.1 ± 23.3	204.0 ± 1.5	125.9 ± 23.3
CIARA-8.2	408.9 ± 0.6	81.7 ± 1.7	1786.0 ± 38.0	202.7 ± 1.6	0.0217 ± 0.0001	1980.2 ± 9.9	1975.4 ± 10.5	203.8 ± 1.7	36.6 ± 10.5
CIARA-9.9	420.7 ± 0.7	36.0 ± 0.7	4154.6 ± 87.8	204.2 ± 1.7	0.0215 ± 0.0001	1967.0 ± 10.2	1964.9 ± 10.3	205.4 ± 1.7	47.1 ± 10.3
CIARA-11.7	420.6 ± 0.7	45.3 ± 1.0	3373.7 ± 75.1	205.5 ± 1.6	0.0220 ± 0.0001	2010.4 ± 12.0	2007.8 ± 12.1	206.6 ± 1.6	4.2 ± 12.1
CIARA-14.1	432.7 ± 0.6	47.7 ± 1.3	3349.0 ± 92.4	202.5 ± 1.5	0.0224 ± 0.0001	2050.4 ± 13.8	2047.8 ± 13.9	203.7 ± 1.6	-33.8 ± 13.9
CIARA-16.4	339.1 ± 0.5	156.3 ± 3.3	838.2 ± 18.5	203.8 ± 1.6	0.0234 ± 0.0002	2142.6 ± 16.1	2131.5 ± 17.9	205.0 ± 1.6	-117.5 ± 17.9
CIARA-18.7	423.3 ± 0.6	108.7 ± 2.4	1530.5 ± 35.3	203.7 ± 1.5	0.0238 ± 0.0002	2180.6 ± 15.5	2174.4 ± 16.1	204.9 ± 1.5	-160.4 ± 16.1
CIARA-21.8	401.6 ± 0.5	118.4 ± 2.6	1340.9 ± 31.4	205.3 ± 1.6	0.0240 ± 0.0002	2189.1 ± 17.5	2182.0 ± 18.2	206.6 ± 1.6	-168.0 ± 18.2
CIARA-23.6	438.8 ± 0.6	177.2 ± 3.7	989.2 ± 22.9	204.8 ± 1.7	0.0242 ± 0.0002	2214.0 ± 22.7	2204.3 ± 23.7	206.0 ± 1.7	-190.3 ± 23.7
CIARA-28.5	446.7 ± 0.8	116.6 ± 2.4	1577.7 ± 32.7	208.7 ± 1.8	0.0250 ± 0.0001	2274.9 ± 9.9	2268.6 ± 10.8	210.1 ± 1.8	-256.6 ± 10.8
CIARA-30	461.0 ± 0.8	60.6 ± 1.2	3114.7 ± 64.8	204.5 ± 1.6	0.0248 ± 0.0001	2271.8 ± 10.3	2268.6 ± 10.5	205.9 ± 1.6	-256.6 ± 10.5
CIARA-31.5	417.3 ± 0.7	278.2 ± 5.6	628.4 ± 13.4	206.4 ± 1.8	0.0254 ± 0.0002	2319.7 ± 17.0	2303.7 ± 20.5	207.8 ± 1.8	-291.7 ± 20.5
CIARA-32.5	476.0 ± 0.7	47.2 ± 1.6	4242.6 ± 150.9	206.6 ± 1.6	0.0255 ± 0.0002	2329.6 ± 20.8	2327.2 ± 20.9	208.0 ± 1.6	-315.2 ± 20.9
CIARA-34.2	468.9 ± 0.7	892.2 ± 17.9	224.3 ± 4.6	205.2 ± 1.7	0.0259 ± 0.0001	2366.6 ± 12.4	2320.7 ± 34.7	206.5 ± 1.7	-308.7 ± 34.7

CIARA-34.8	429.9 ± 0.6	930.4 ± 18.8	214.2 ± 4.5	203.5 ± 1.7	0.0281 ± 0.0002	2576.7 ± 15.4	2524.4 ± 40.0	204.9 ± 1.7	-512.4 ± 40.0
CIARA-36	492.1 ± 0.7	31.6 ± 0.7	6799.2 ± 153.8	203.7 ± 1.6	0.0265 ± 0.0001	2423.8 ± 10.8	2422.2 ± 10.8	205.1 ± 1.6	-410.2 ± 10.8
CIARA-37.1	385.0 ± 0.5	254.1 ± 5.2	676.2 ± 14.4	198.1 ± 1.5	0.0271 ± 0.0002	2490.5 ± 15.5	2474.5 ± 19.2	199.4 ± 1.5	-460.5 ± 19.2
CIARA-39.4	394.7 ± 0.5	282.3 ± 5.7	638.8 ± 13.5	204.8 ± 1.5	0.0277 ± 0.0002	2535.1 ± 15.4	2517.9 ± 19.6	206.3 ± 1.5	-503.9 ± 19.6
CIARA-41.7	461.5 ± 1.0	94.4 ± 2.0	2239.6 ± 47.8	208.7 ± 1.8	0.0278 ± 0.0001	2534.1 ± 11.6	2529.1 ± 12.1	210.2 ± 1.8	-515.1 ± 12.1
CONSTANTINE-0.5	118.0 ± 0.2	2002.2 ± 40.1	11.0 ± 0.4	116.2 ± 1.7	0.0113 ± 0.0004	1113.9 ± 36.5	670.7 ± ###	116.5 ± 1.7	1345.3 ± 315.7
CONSTANTINE-1.3	129.2 ± 0.1	124.3 ± 2.9	199.3 ± 12.3	118.4 ± 1.4	0.0116 ± 0.0007	1139.8 ± 65.3	1114.8 ± 67.7	118.8 ± 1.4	901.2 ± 67.7
CONSTANTINE-2.6	111.5 ± 0.1	167.0 ± 3.6	128.8 ± 7.9	119.3 ± 1.2	0.0117 ± 0.0007	1146.3 ± 66.3	1107.4 ± 71.8	119.6 ± 1.2	908.6 ± 71.8
CONSTANTINE-4.6	116.7 ± 0.2	76.0 ± 1.7	438.4 ± 10.0	148.5 ± 2.3	0.0173 ± 0.0001	1655.2 ± 11.9	1638.8 ± 16.7	149.1 ± 2.3	378.2 ± 16.7
CONSTANTINE-6.6	99.0 ± 0.1	54.3 ± 1.3	480.8 ± 12.6	178.5 ± 1.3	0.0160 ± 0.0001	1487.8 ± 14.0	1474.3 ± 17.0	179.2 ± 1.3	542.7 ± 17.0
CONSTANTINE-8.5	115.6 ± 0.1	197.7 ± 4.1	127.2 ± 6.5	137.2 ± 1.9	0.0132 ± 0.0006	1271.8 ± 59.9	1228.1 ± 67.4	137.6 ± 1.9	787.9 ± 67.4
MULTIEIX-0.6	245.2 ± 0.5	150.0 ± 3.1	45.5 ± 3.7	178.5 ± 2	0.00169 ± 0.00013	156.2 ± 12.3	141.1 ± 16.3	178.6 ± 1.8	1872.9 ± 16.3
MULTIEIX-3	611.7 ± 1.3	59.4 ± 1.2	546.9 ± 14.0	172.7 ± 2	0.00322 ± 0.00005	299.7 ± 4.6	297.3 ± 4.9	172.8 ± 2.0	1714.7 ± 4.9
MULTIEIX-4.5	351.2 ± 0.4	371.0 ± 7.5	87.1 ± 3.5	175.2 ± 1.7	0.00558 ± 0.00019	519.1 ± 17.8	492.9 ± 25.7	175.4 ± 1.7	1521.1 ± 1.7
MULTIEIX-5.8	271.1 ± 0.3	755.1 ± 15.2	82.2 ± 2.2	174.7 ± 1.7	0.0139 ± 0.0002	1297.1 ± 22.8	1228.1 ± 53.8	175.3 ± 1.7	783.9 ± 53.8
MULTIEIX-9	372.0 ± 0.5	63.2 ± 1.3	1372.1 ± 29.3	173.7 ± 1.6	0.0141 ± 0.0001	1321.0 ± 8.9	1316.8 ± 9.4	174.4 ± 1.6	695.2 ± 9.4
MULTIEIX-13.5	376.6 ± 0.5	98.5 ± 2.0	981.9 ± 20.7	175.2 ± 1.6	0.0156 ± 0.0001	1454.5 ± 8.8	1448.0 ± 9.9	175.9 ± 1.6	564.0 ± 9.9
MULTIEIX-17	324.4 ± 0.5	30.9 ± 0.6	2878.5 ± 65.5	178.3 ± 1.6	0.0166 ± 0.0002	1547.6 ± 15.0	1545.3 ± 15.1	179.0 ± 1.7	466.7 ± 15.1
MULTIEIX-20.8	328.4 ± 0.5	610.7 ± 12.3	170.2 ± 3.8	180.7 ± 1.7	0.0192 ± 0.0002	1787.5 ± 16.7	1741.7 ± 36.4	181.6 ± 1.7	272.3 ± 36.4
MULTIEIX-22	426.1 ± 0.6	52.4 ± 1.1	2412.8 ± 51.1	180.2 ± 1.5	0.0180 ± 0.0001	1674.4 ± 9.8	1671.4 ± 10.0	181.0 ± 1.6	340.6 ± 10.0
MULTIEIX-23	363.5 ± 0.5	108.4 ± 2.4	1070.0 ± 25.5	176.6 ± 1.7	0.0193 ± 0.0002	1807.0 ± 17.4	1799.7 ± 18.1	177.5 ± 1.8	212.3 ± 18.1
MUTIEIX-26	396.6 ± 0.6	483.8 ± 9.7	279.4 ± 5.8	177.4 ± 1.6	0.0207 ± 0.0001	1931.2 ± 9.9	1901.0 ± 23.5	178.4 ± 1.6	111.0 ± 23.5
MULTIEIX-28	371.3 ± 0.6	59.5 ± 1.2	2266.9 ± 47.9	179.7 ± 1.7	0.0220 ± 0.0001	2055.6 ± 12.4	2051.6 ± 12.7	180.8 ± 1.7	-39.6 ± 12.7
MULTIEIX-29.8	349.7 ± 0.5	69.8 ± 1.5	2025.1 ± 45.3	168.9 ± 1.5	0.0245 ± 0.0001	2309.4 ± 12.7	2304.4 ± 13.2	170.0 ± 1.5	-290.4 ± 13.2
SEÁN-0.6	420.2 ± 0.6	429.4 ± 8.7	37.3 ± 2.3	365.0 ± 2	0.00231 ± 0.00013	184.9 ± 10.8	163.1 ± 18.8	365.2 ± 1.9	1852.9 ± 18.8
SEÁN-1.4	364.8 ± 0.5	1107.2 ± 22.2	14.7 ± 0.6	176.0 ± 1	0.00271 ± 0.00010	251.2 ± 9.0	176.1 ± 53.9	176.1 ± 1.4	1837.9 ± 53.9
SEÁN-3	603.2 ± 1.1	305.5 ± 6.2	115.6 ± 3.7	187.8 ± 2	0.00355 ± 0.00009	326.5 ± 8.0	314.1 ± 11.8	187.9 ± 1.7	1697.9 ± 11.8
SEÁN-5.4	729.3 ± 1.3	598.3 ± 12.0	79.2 ± 1.8	157.2 ± 2	0.00394 ± 0.00004	372.1 ± 3.8	351.4 ± 15.1	157.3 ± 1.6	1660.6 ± 15.1
SEÁN-6.6	585.8 ± 1.0	87.4 ± 1.8	480.7 ± 12.8	150.1 ± 2	0.00435 ± 0.00008	413.4 ± 7.2	409.6 ± 7.7	150.3 ± 1.7	1602.4 ± 7.7
SEÁN-8.4	669.0 ± 1.0	121.2 ± 2.8	540.4 ± 17.6	156.3 ± 2	0.00594 ± 0.00014	561.5 ± 13.1	556.9 ± 13.5	156.6 ± 1.7	1459.1 ± 13.5
SEÁN-9	703.3 ± 1.1	212.2 ± 4.3	307.1 ± 6.5	150.7 ± 2	0.00562 ± 0.00004	533.7 ± 3.8	526.0 ± 6.6	150.9 ± 1.5	1486.0 ± 6.6
SEÁN-10	765.8 ± 1.2	146.7 ± 3.2	984.8 ± 33.6	143.5 ± 2	0.01144 ± 0.00030	1096.2 ± 28.8	1091.3 ± 29.0	143.9 ± 1.7	*924.7 ± 29.0*
SEÁN-11	426.9 ± 1.0	530.0 ± 10.7	76.6 ± 1.8	140.3 ± 2	0.00577 ± 0.00008	552.7 ± 7.5	521.0 ± 23.6	140.5 ± 1.8	1493.0 ± 23.6

fabric (McDermott et al., 1999). The dendritic fabrics of Multieix presents more depleted $\delta^{13}C$ values (-7.3 ‰) than the average values in the stalagmite (-6.9 ‰) but the most depleted values (-8.6 ‰) correspond to other intervals. Therefore, bio-influenced mineralisation and kinetic processes seem not to have modified largely the studied signal in these fabrics. It should be noted that dendritic fabrics have been observed in isolated areas. All of this points out that probably dendritic fabrics are not affecting the geochemical signal as much as to influence the paleoclimate interpretation.

Seán stalagmite presents a brown layer at around 1622 yr CE (allogenic horizon), which represent a less important unconformity than that around 1503 ca. cm 5 of Multieix (dissolution hiatus). Allogenic horizons usually are micro- to millimetric in thickness that can represent from minor, eventual episodes to major unconformities. This kind of horizons frequently contain allochtonous material, which can have a variable provenance like an influx of detritic material from outside the cave, biological activity, cave floodings events, etc. (Martín-Chivelet et al., 2017). On the one hand, our age models indicate that Seán grew quite continuously up between 1421 to 1880 yr CE and growth rates in its brown layer are similar to the average obtained in the UBU2, which would be indicating no important signs of erosion or stops in the deposition (Fig. 3.28, right panel). In addition, as indicated by the colour-map density provided by the Micro-CT scanning, the brown layer follows the general lamination, which is quite continuous along the growth axis. Overall, seems to indicate that the allogenic horizon observed ca. 1622 yr CE consisted in a minor an eventual event. On the other hand, the brown lamina is characterized by high content of air, an abrupt change in the colour measurements and, according to the XRF results, enhancements Ti concentrations (Fig. 3.31). These features could be pointing out that the allogenic horizon of Seán ~1622 yr CE was generated by accumulation of terrigenous material input (Ti peak).

The LIAb-IE transition (1790 to 1880 yr CE) has been characterized by pointed morphostratigraphic units with aggradational plus retractional patterns (cm 1.5-0, UBU1, Seán) (Fig. 3.35). If it was coincident with dendritic and/or microcrystalline fabrics, possibly could be indicating trends to slower drip rates (Martín-Chivelet et al., 2017). However, acetate peels do not seem to indicate this kind of fabrics and then, slow drips cannot be corroborated in this way. Regarding to minima growth rates in Seán, have been obtained around 1805 yr CE.

Lastly, towards the end of the period spanned by Multieix (1838-1844 yr CE, cm 0.5) the progradational stacking patterns and the remarkable enhancement in the growth rates indicate an isolated event when drip rates seem to have increased in the site of this stalagmite.

During all the studied period, drip rates present a moderate stability and stalagmites grew up quite continuously, while in those moments with peculiarities in the micro-stratigraphy slower drip rates mostly accompanied drops in the growth rates.

3.4. RESUM DELS RESULTATS

En la present tesi hom presenta un seguit de reconstruccions paleoceanogràfiques i paleoclimàtiques pels darrers 2.700 anys a la regió central de la Mediterrània occidental. Així, hom ha reconstruït les condicions de les aigües superficials i properes al fons mitjançant l'estudi d'indicadors analitzats en testimonis profunds de sediments marins. També s'han reconstruït les condicions atmosfèriques (variabilitat hidroclimàtica) a través de l'estudi d'estalagmites de coves de Mallorca. El lapse de temps abastat inclou els següents períodes climàtics i històrics: el Període Talaiòtic (TP, fins el 123 BCE), el Període Romà (RP, 123 BCE-470 CE[2]), l'Alta Edat Mitjana (EMA, 470 a 900 CE), l'Anomalia Climàtica Medieval (MCA, 900 a 1275 CE), la Petita Edat de Gel (LIA, 1275 a 1850 CE) i l'Era Industrial (1850-present). Els resultats obtinguts s'han plasmat en dos articles científics publicats en revistes indexades, més una tercer article que és actualment en preparació.

.Les condicions ambientals de la superfície del mar han estat estudiades mitjançant cinc testimonis de sediment provinents de dues localitats (testimonis MIN i MR3). En primer lloc s'han reconstruït les temperatures superficials del mar (SST) derivades de la ràtio Mg/Ca analitzada al foraminífer planctònic *Globigerina bulloides*. També s'ha treballat amb els canvis en el balanç d'evaporació-precipitació (E-P) regional, reconstruïts a partir de la combinació de la ràtio Mg/Ca i mesures de $\delta^{18}O$ sobre el mateix foraminífer. Pel que fa a la ràtio Mg/Ca, i per avaluar la variabilitat interna dels resultats de les anàlisis, hom ha comparat els obtinguts en les dues seccions del testimoni MR3.1 (MR3.1A i MR3.1B), les quals foren analitzades per separat. La

[2] BCE: anys abans de l'era comú. CE: anys de l'era comú.

variabilitat interna mitjana obtinguda entre els esmentats registres de Mg/Ca ha estat de ±0,09 mmol mol^{-1} (Fig. 3.36), aproximadament equivalent a <0,15°C i molt propera a les dades publicades per Elderfield et al. (2002).

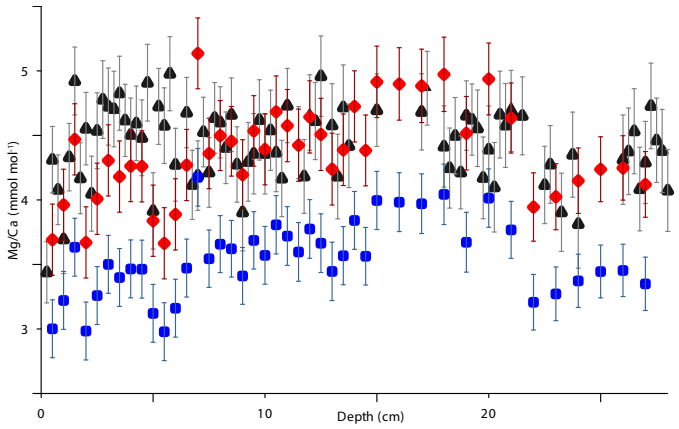

Figura 3.36. Comparació dels registres de Mg/Ca derivats de dues seccions del testimoni de sediment MR3.1: MR3.1B (triangles negres), MR3.1A (quadrats blaus, amb protocol de neteja reductiva) i MR3.1A després de la correcció del 23 % (rombes vermells, amb la correcció del protocol de neteja reductiva), la qual està relacionada amb la realització del pas reductiu durant la neteja de les mostres de foraminífers (veure detalls a l'apartat 3.1.4). Les barres verticals representen les incerteses Mg/Ca a la reproductibilitat de cada anàlisi.

D'altra banda, el calibratge de la SST-Mg/Ca en *G. bulloides* ha estat revisat i reajustat emprant mesures en sediments superficials d'un conjunt de testimonis mostrejats a la mar Mediterrània occidental. Aquest estudi també ha permès, a partir de l'anàlisi de dades oceanogràfiques regionals, establir que la ràtio Mg/Ca a *G. bulloides* reflecteix principalment condicions de SST primaverals. En aquest punt, cal notar que el rang de SST obtingudes en calibratges previs no reflectia condicions oceanogràfiques coherents per la zona d'estudi (Taula 3.11). Els resultats de Mg/Ca-SST s'han pogut contrastar amb reconstruccions de SST basades en l'anàlisi d'alquenones en els mateixos testimonis, compostos que segons diverses interpretacions reflecteixen principalment el senyal anual. La interpretació de l'evolució de les SST s'ha centrat en l'anàlisi d'una corba "stack" construïda a partir de l'apilament dels registres individuals dels cinc testimonis esmentats més amunt. Aquesta estratègia permet obtenir una bona representació de les estructures més robustes i eliminar possibles oscil·lacions menors representades pobrament a escala regional. Segons la corba composta o "stack" obtingut amb les SST-Mg/Ca, el període càlid més sostingut tingué lloc durant el RP, seguit immediatament per una tendència cap al refredament interrompuda per vàries oscil·lacions a escala secular. Durant la MCA hi hagué algunes fases amb SST

particularment càlides, mentre que la LIA estigué marcada per la inestablitat, amb alguns esdeveniments caracteritzats per SST molt fredes, sobretot durant la segona meitat d'aquest període.

Taula 3.11. SST mitjanes obtingudes als primers centímetres de 10 testimonis de sediment mostrejats a la regió central de la Mediterrània occidental. Les SST han estat obtingudes després d'aplicar diferents calibratges per *G.bulloides* ja publicats. El rang de SST descrit pels diferents calibratges és massa ampli per la zona d'estudi i pel període de l'any durant el qual hom espera la floració de *G.bulloides*.

Mg/Ca = A exp (B * SST)	A	B	SST mitjana (ºC) dels primers cm del testimoni
Mashiotta et al. (1999)	0,474	0,107	21,7
Lea et al.,(1999)	0,53	0,1	19,4
Elderfield and Ganssen (2000)	0,56	0,1	18,6
McConnell i Thunell (2005)	1,2	0,057	6,3
Cléroux et al. (2008)	0,78	0,082	12,6
Thornalley, Elderfield i McCave (2009)	0,794	0,1	15,1
Patton et al. (2011)	0,97	0,066	8,7
Aquest estudi	0,7045	0,0939	15,3

.Les condicions ambientals de les aigües profundes s'expressen a través de la variabilitat en la formació d'aigua fonda (DWF) a la regió septentrional de la Mediterrània occidental, estudiada a partir del paràmetre de mida de gra UP10 (fracció >10 μm) als testimonis de sediment MIN. La validesa d'aquest paràmetre per reconstruir canvis en la intensitat de la DWF en el passat ha quedat reforçada per un seguit de dades oceanogràfiques obtingudes *in situ* entre l'octubre de 2012 i l'octubre de 2014 mitjançant dos ancoratges instrumentats (*moorings*) fondejats en aigües profundes del golf de Lleó i el nord de la illa de Menorca, respectivament, i equipats amb trampes de sediment i correntòmetres. Les dades dels ancoratges mostren augments de la velocitat dels corrents marins profunds contemporanis amb episodis de cascades d'aigües denses de plataforma i de convecció a mar obert durant el febrer de 2013. La distribució de la mida de gra de les partícules decantades a les trampes de sediment durant aquest episodi mostra una moda distintiva i valors alts d'UP10, validant així l'aplicació d'aquest paràmetre com a indicador d'augments de DWF.

El registre de DWF pels últims 2.500 anys obtingut a partir de sediments del nord de Menorca mostra que els esdeveniments més forts van ocórrer durant intervals relativament càlids, com el RP, el final de la MCA i la primera part de la LIA. En canvi, les dades indiquen una reducció progressiva de la convecció durant l'EMA, la qual acaba resultant en esdeveniments més febles de DWF durant la major part de la MCA. Esdeveniments intensos de DWF apareixen majoritàriament associats a períodes d'increment del balanç E-P, i no tant a la pèrdua de flotabilitat provocada pel refredament hivernal de les aigües superficials. Els resultats suggereixen que SST càlides durant els mesos de primavera podrien haver tingut un paper important en l'increment del balanç E-P, afavorint la pèrdua de flotabilitat de les aigües de superfície degut a l'increment induït de la seva salinitat.

.Les condicions atmosfèriques comprenen la variabilitat hidroclimàtica reconstruïda a partir de l'anàlisi de cinc estalagmites tot i integrant diferents paràmetres geoquímics i texturals. Aquesta metodologia combinada dóna suport a la validesa d'aquestes estalagmites per proveir informació hidroclimàtica. Els valors de $\delta^{18}O$ més enriquits en l'isòtop pesat ha estat interpretat com indicador de condicions més seques, mentre que els empobriments s'han associat a condicions més humides. La integració dels registres derivats de les cinc estalagmites ha permès elaborar la primera reconstrucció regional de la variabilitat hidroclimàtica pels últims 2.700 anys, només amb una interrupció de 250 anys al final de la MCA i inicis de LIA, que s'ha interpretat com causada per condicions d'aridesa extrema. D'altra banda, destaquen unes condicions generals més humides a començaments del RP, la primera meitat de l'EMA i la LIA, particularment a finals de la LIAb. En canvi, les condicions climàtiques foren més seques al final del RP, a la segona meitat de l'EMA i durant tota la MCA. La presència d'una capa detrítica enriquida en Ti en una de les estalagmites s'ha interpretat com evidència d'una inundació extraordinària associada a un esdeveniment extrem de pluja al voltant de l'any 1622 CE, dins la LIA.

La informació derivada de l'estudi dels sediments marins i de les estalagmites per a la totalitat del període cobert és integrada i discutida tot seguit, al Capítol 4.